A THEORETICAL AND EXPERIMENTAL STUDY

OF LIQUID METAL ION SOURCES

AND THEIR APPLICATION TO FOCUSED ION BEAM TECHNOLOGY

Joseph Puretz
B.A., Ithaca College, Ithaca, New York, 1971

A dissertation submitted to the faculty
of the Oregon Graduate Center
in partial fulfillment of the
requirements for the degree
Doctor of Philosophy
in
Applied Physics

December 1988

The dissertation "A Theoretical and Experimental Study of Liquid Metal Ion Sources and Their Application to Focused Ion Beam Technology" by Joseph Puretz has been examined and approved by the following Examination Committee:

Jonathan H. Orloff, Advisor
Professor

A. E. Bell
Research Associate Professor

L. W. Swanson
Professor

Ronald A. Burghard
Intel Corporation

This dissertation is dedicated to my wife, Sue,

for her love, patience, and support.

ACKNOWLEDGMENTS

I wish to express my gratitude to all those who have had a positive influence on my scientific and technical education. Certainly, there are several outside of OGC. I would like to thank Dr. Murray Steinberg, formerly of the Ithaca College Physics Department, whose anecdotes about famous scientists in real situations, showed me that scientists are human beings first. This was quite a revelation at the time. I also owe my appreciation to Ron Draftz of the Illinois Institute of Technology Research Institute (IITRI) whose knowledge, analytical skill and technique in various "microscopies" were truly impressive. To George Yamate, of IITRI, I owe my thanks for his friendship and for sharing his immense storehouse of knowledge of technical chemistry. I could always get an instant reply to questions like: "What's an example of an oil and water soluble black dye?" or "Is this adhesive soluble in hexane?" I would also like to thank Dr. Reg Davies, formerly of IITRI and probably still at DuPont, for his interest and for enabling me to work on many and varied research projects. Prof. Thomas Erber of the Physics Department of IIT deserves my gratitude for enthusiastically teaching the most difficult advanced physics courses in a unique and creative manner. I cannot recall leaving a lecture without thinking: "I wonder why I never heard or thought of it that way before." He has inspired me to look at old things in new ways.

At OGC, I feel particularly fortunate to have been at the right place at the right time. This is undoubtedly due to the efforts of Professors Tony Bell, Jon Orloff and Lyn Swanson whose research on electron and ion sources and the optical systems

used for beam production and focusing has brought considerable recognition to our group. Their work has made it possible for me to contribute some "firsts" to this area of research. Without them, none of the work reported here would have been done. I would like to thank my advisor, Jon Orloff, who allowed me to pursue my own interests (within reason). Though the road has been a long one, it has been worthwhile. I would also like to express my appreciation to Dr. Al Milgram, formerly of the Univ. of Portland and Tektronix, Inc. for an enjoyable and productive collaboration on the lithography work. I wish to thank Prof. Jürgen Schroeer of the Illinois State University Physics Department for the time spent at OGC working together on the SIMS system. Though we spent a bit too much time calibrating it to get any real data, the work was very enjoyable. Maybe some other time. I also wish to acknowledge the financial assistance of Prof. Dick Elliott and Dr. Rick DeFreez of OGC for supporting me during the period of our collaboration on the optoelectronics micromachining research... my thanks to Rick also for providing much needed help on all the UNIX related stuff. His assistance was invaluable.

I'd like to thank my parents for providing me with a college education, for their unfailing confidence in me over the years and for their love. They always knew I could do it. But who knew it would take so long? Finally I owe my deepest debt of appreciation to my wife Sue to whom this work is dedicated. Mere words cannot sufficiently express my gratitude for her love, support and tolerance to her husband's meager income for much too long. I could not have done it without her.

Table of Contents

APPROVAL ii

DEDICATION iii

ACKNOWLEDGEMENT iv

LIST OF TABLES xi

LIST OF FIGURES xii

ABSTRACT xvii

1. INTRODUCTION 1

2. SOME THEORETICAL CONSIDERATIONS FOR LIQUID METAL ION SOURCES 12

2.1 Introduction 12

2.2 Principle behind the model 14

2.3 Model 18

2.3.1 Space Charge versus Flow Impedance 25

2.3.1.1 Perveance 28

2.3.2 Hydrodynamics and fluid flow 29

2.3.3 Threshold Voltage 37

2.3.4 Emission Area 41

2.3.5 Discussion and Comments relating to I(V) 44

2.4 Energy Broadening in Particle Beams 45

2.4.1 Dimensional Analysis and Energy Broadening Expressions 47

2.5 Summary and Conclusions 50

2.6 Appendices 53

2.6.1 Appendix 2a: Poisson Equation 53

2.6.2 Appendix 2b: Child-Langmuir Law 56

2.6.3 Appendix 2c: Result of Stern, Gossling, Fowler 58

3. THE GALLIUM LIQUID METAL ION SOURCE 60

3.1 Introduction 60

3.2 Fabrication of the LMIS 62

3.2.1 Cleaning the tungsten wire substrate 62

3.2.2 Etching the tungsten wire 65

3.2.2.1 " Blunting back " the emitter 68

3.2.3 Substrates other than tungsten 69

3.2.3.1 Molybdenum 69

3.2.3.2 Molybdenum/Rhenium alloy 71

3.2.3.3 Tantalum 74

3.3 Wetting and testing the emitter 74

3.4 Source Contamination 74

3.4.1 Contamination during wetting and testing 77

3.4.2 Contamination during operation 82

3.4.2.1 Contamination due to backsputtering 83

3.4.2.2 Effect of oxygen 85

3.4.2.3 Effect of chlorine 85

3.4.2.4 Effect of carbon bearing gases 88

3.5 An example of LMIS source contamination 89

4. OVERVIEW OF ION / SOLID INTERACTIONS 97

4.1 The various phenomena in general 97

4.2 The specific effects of ion bombardment 98

4.2.1 Energy loss and ion stopping 101

4.2.2 Penetration depth and straggle 101

4.2.3 Incident ion channeling 104

4.2.4 Radiation damage 105

5. SURFACE TOPOGRAPHY INDUCED BY FOCUSED ION BEAM BOMBARDMENT OF GaAs AND AlGaAs 107

5.1 Background 107

5.2 Introduction to the present work 110

5.3 Experimental 112

5.4 Results and Observations 114

5.5.1 Micrographs 118

5.5.1.1 Effect of substrate temperature 123

5.5.1.2 Threshold dose 123

5.5.1.3 Micrographs A 124

5.5.1.4 Micrographs B 129

5.5.1.5 Micrographs C 129

5.5.1.6 Micrographs D 135

5.5 Discussion 135

5.6.1 Ion Source Current Effects 138

5.6.2 Droplet size 139

5.6.3 Droplet Motion 141

5.6.4 Beam Heating Effects 142

5.6.5 A simple model of droplet formation onset (is too simple) 146

5.7. Sputter cone topography 148

5.7.1 Experimental Sputter Cone Production 150

5.8 Conclusions 150

6. MICROMACHINING 155

6.1 Introduction 155

6.1.1 Ion bombardment induced erosion and redeposition 156

6.2 Micromachining with a focused ion beam (FIBM) 159

6.2.1. The basic equations of FIBM 161

6.2.2 Beam scanning considerations 163

6.3 Micromachining of Optoelectronic Devices 169

6.4 Focused ion beam micromachining for IC diagnostics 176

6.4.1 Background 176

6.4.2 Imaging the circuit 178

6.4.3 Surface charging and its reduction 179

6.4.4 Experimental findings 183

6.4.4.1 Charge neutralization 183

6.4.4.1.1 Activation of the cathode 184

6.4.4.1.2 Operation of the electron beam gun 187

6.4.4.2 Imaging an IC through the passivation 187

6.4.4.3 Milling of insulating layers 190

6.4.4.4 Voltage contrast of FIB milled passivated IC's 190

7. FOCUSED ION BEAM LITHOGRAPHY 196

7.1 Introduction 196

7.2 Background 199

7.3 Purpose of the experimental work 200

7.3.1 Preparation of the films 201

7.3.2 Etch rates and pattern transferability 201

7.4 FIB exposure 203

7.5 Some technical considerations 211

7.6 Results 212

7.7. Summary 217

7.8 Appendix 225

7.8.1 Appendix: Raster scanning for uniform dose 225

8. SPECULATIONS AND POSSIBILITIES FOR FUTURE RESEARCH 227

VITA 245

List of Tables

1.1 Some Reliable Liquid Metal Sources 3

7.1 Typical Etch Conditions 202

List of Figures

1.1 Focused ion beam column. 5

1.2 Extractor voltage versus suppressor voltage. 6

1.3 Current-voltage curves for LMIS with varied suppressor bias. 7

1.4 Energy dependence of beam spot diameter. 9

1.5 Overall system schematic. 10

2.1 Schematic of diode models for I(V) calculation. 15

2.2 Schematic of LMIS I(V) characteristic. 22

2.3 Experimental and theoretical I(V) curves. 26

2.4 Experimental I(V) curves for needle and capillary LMIS sources. 36

2.5 Geometry used for surface tension and threshold voltage calculation. 39

2.6 Apparatus used by G. I. Taylor for test of threshold voltage prediction. 42

3.1 Unwetted emitter. 61

3.2 Mechanically ground Mo emitter. 63

3.3 Ground W emitter and electrochemically roughened surface. 64

3.4 Emitter radii possible by electrochemical etching. 67

3.5 W emitter before and after electrochemical blunting. 70

3.6 Mo substrate after several heating cycles. 72

3.7 Gallium wetted Mo emitter. 73

3.8 Mo/Re emitter for gallium LMIS. 75

3.9 Ta surface after reacting with Ga. 76

3.10 Emitter before and after wetting in vacuum system. 78

3.11 Gallium added to emitter via syringe. 80

3.12 Backscattered electron image of poorly wetted emitter. 81

3.13 Gallium/Molybdenum phase diagram. 84

3.14 Emitter poisoned by Mo backsputtering from extractor. 86

3.15 Enlarged view of Figure 3.14 surface. 87

3.16 Instability in LMIS current due to operation in contaminated system. 91

3.17 Instability in LMIS current due to operation in a "cleaned" vacuum system. 92

3.18 LMIS emitter after operation in "cleaned" vacuum system. 93

3.19 De-wetting of liquid metal on contaminated emitter. 94

3.20 Scanning Auger Microscopy of contaminated emitter. 95

3.21 Contamination of gallium by carbon. 96

4.1 Some possible ion/solid interactions. 99

4.2 Projected range and longitudinal straggle for H, Be, Zn, Se, Cd, Te in GaAs. 103

5.1 SIM micrograph of Ga rich droplet evolution. 115

5.2 SEM micrographs of Ga rich droplet evolution. 116

5.3 SEM micrograph reveals varying droplet composition. 120

5.4 Effect of ion beam defocusing. 121

5.5 Scanning Auger analysis of Figure 5.6 areas. 122

5.6 Degree of focus is correlated with droplet size. 125

5.7 Threshold dose for droplet formation versus incident beam energy. 126

5.8 Early stages of film formation at low temperature. 128

5.9 Possible material motion without ion bombardment. 130

5.10 Film formation; beam blanked between micrographs. 131

5.11 Series continues as sample warms slowly. 132

5.12 Droplet formation from non-uniformly thick film. 133

5.13 Film formation and droplet motion. 134

5.14 Droplet freezing under ion bombardment. 136

5.15 Droplet freezing and sputtering continued. 137

5.16 Further evidence of "defocusing effect" on droplet size. 140

6.1 Focused ion beam micromachining: IC microsurgery. 157

6.2 Incident beam angle and ejection angle dependence of sputtered flux. 158

6.3 "Picture frame" effect. 165

6.4 Single line scans across diode laser edge. 167

6.5 FIB milling damage. 170

6.6 FIB micromachining of diode lasers: MC^2 172

6.7 Ten-stripe MC^2 diode laser. 173

6.8 Surface-emitting laser viewed from the top (output end). 175

6.9 Secondary electron emission coefficient dependence on energy. 182

6.10 Cathode activation for electron beam gun used for charge neutralization. 185

6.11 Operation of electron gun used for charge neutralization. 186

6.12 Secondary electron images of chip isolated from ground. 188

6.13 Secondary electron and ion images over passivation layer. 192

6.14 Voltage contrast effect over milled Al run. 193

6.15 Influence of passivation on surface charging. Effect on VCSEM. 194

7.1 Illustration of positive and negative resists. 198

7.2 Test of pattern transferability through non-implanted bilayer. 204

7.3 Auger spectroscopy depth profiles of gallium in E. B. silicon and in SOG. 207

7.4 Experimental arrangement for FIB lithography. 208

7.5 Demonstration of uniform dose implantation. 209

7.6 Series of fixed dose lines. 210

7.7 Results of dry etching the implanted bilayer. 213

7.8 Resultant lines viewed at high incidence angle. 214

7.9 Variation of linewidth with dose. 215

7.10 Bilayer process of Kato et al. 216

7.11 Non-gaussian aspect of the beam is demonstrated. 218

7.12 Resist sensitivity reveals stage vibrations. 219

7.13 Kuwano's work is repeated. 220

7.14 Continued etching causes the lines to disintegrate. 221

7.15 Sputtering through top layer acts as positive resist. 223

ABSTRACT

A THEORETICAL AND EXPERIMENTAL STUDY OF LIQUID METAL ION SOURCES AND THEIR APPLICATION TO FOCUSED ION BEAM TECHNOLOGY

Joseph Puretz, Ph.D.

Oregon Graduate Center, 1988

Supervising Professor: Jon H. Orloff

A key parameter of liquid metal ion source (LMIS) operation is the current-voltage (I(V)) relationship. Some issues surrounding this relationship, which is complicated by severe space-charge near the emitter, are examined for a LMIS. A simple technique is introduced which relies on the principle of momentum conservation within a simple diode structure and enables the solution of space charge problems without resorting to the Poisson equation. As an illustration of this approach, the result of Stern-Gossling-Fowler is easily derived. This method is then applied to the problem of modeling the I(V) characteristic of a LMIS. A simple and physically intuitive criterion is derived which demonstrates that the ratio of the viscous drag force on the emitter to the force of the ion beam impinging on the collector determines whether the ion current is dominated by the flow of liquid metal or by the space charge in the beam. This explains, for the first time, how these two factors are related. Another result is that, contrary to currently accepted thinking, it is not the

flow impedance per se which influences the ion current but the product of the film thickness and the flow impedance.

Since the advent of LMIS, the understanding of their fundamental properties and their application to focused ion beam (FIB) technology have followed parallel developments. One of the goals of the research presented in this dissertation has been to expand the applications of the liquid metal ion source. The gallium LMIS in particular has been found to be the most suitable ion source for many applications. Yet despite its apparent simplicity, the opportunity exists for producing ion emitters which operate poorly. The major difficulties encountered during their fabrication, testing and operation are due primarily to contamination by oxygen, carbon bearing gases and backsputtering of material to the source, particularly from the extraction electrode. The application of this source to FIB lithography and micromachining has been examined. Particularly exciting is the FIB micromachining of semiconductor lasers which has resulted in the fabrication of novel devices, including the first diode lasers fabricated by focused ion beam micromachining.

1. INTRODUCTION

High brightness ion sources have been studied since Müller's earliest work in field emission and field ionization[1,2] in which neutral gas atoms were ionized in the vicinity of the apex of a field emitter. The first use of field ionization of gases to produce focused ion beams came with the work of Levi-Setti's group at the University of Chicago[3,4], and that of Orloff and Swanson at the Oregon Graduate Center[5-7]. These experiments demonstrated that ion beams of H_2 and Ar could be focused into sub-half micron diameter spots providing target current densities of the order of a milliamp per square centimeter.

The interest in liquid metals for use as ion sources (LMIS) probably has its origins in studies by Krohn[8] and Perel et al[9]. of ion engine thrusters for space propulsion and later due to the work of Mahoney et al[10]. who experimented with liquid metal alkali ion sources such as cesium. Liquid metals were first employed by Krohn[11] and Krohn and Ringo[12,13] to form focused beams of cesium, gallium and mercury using a capillary type LMIS. These researchers measured the virtual source size and energy spread in a gallium beam.

Since that time, research into the properties of many metals, alloys and substrates for their use as liquid metal or alloy ion sources (LMIS or LAIS) has been conducted by several groups around the world. A wide variety of ions has thus become

available. A partial list is given in Table 1.1.

Though the beams formed by these sources may differ in their composition of monomers, polymers, charged clusters, and charged and neutral droplets[14-19], the various LMIS and LAIS share some interesting properties. This is due primarily to the fact that the ions are formed by a field emission process i.e. by field evaporation and/or field ionization. The electric fields required are extremely large; of order 1 volt / Å and are generally the largest electric fields produced deliberately and controllably by science.

The utility of the liquid metal ion source stems from its ability to produce ions which can be formed into focusable beams with high current density at the target. This arises from several remarkable and interrelated physical characteristics; the angular intensity (and its relative, the brightness), virtual source size, and the energy spread at the source. A detailed exposition of these important source parameters will not be attempted as they have been dealt with extensively in the literature over a period of several years. See, for example, Swanson[20]. They are only described here briefly.

The angular intensity is defined as the current per unit solid angle or

$$I' = \frac{dI}{d\Omega}$$

The virtual or Gaussian source size is defined as the size of the apparent emission site as seen by the optical column downstream of the LMIS and appears to be relatively insensitive to total extracted current[21]. On the other hand, the energy spread of the beam increases rapidly with the extracted current and is responsible for the chromatic contribution to the spot size through the chromatic aberration coefficient of the optical column. The virtual source diameter, the chromatically limited spot diameter,

Table 1.1

Pure Element/Substrate	Ion Species
Ga/W	Ga^+
In/W	In^+
Sn/W	Sn^{++}, Sn^+
Bi/NiCr	Bi^{++}, Bi^+
Au/W	Au^{++}, Au^+
Al/C	Al^+

Alloy/Substrate	
Pd_2As/W	As^{++}, As^+
$Pd_{50}As_{36}B_{14}$/W	As^{++}, As^+, B^+
$Be_{40}Au_{60}$/W	Be^{++}, Be+
$Si_{20}Au_{80}$/W	Si^{++}, Si+

and the angular intensity determine the current density which can be focused into a small spot. (see Section 2.4)

While the fundamental physical properties continue to be elucidated, the research into the properties of ion optical focusing columns and the technological applications of the LMIS and LAIS expand as well. Some of the issues surrounding the properties and applications of LMIS have been discussed, for example, by Mair and Mulvey[22].

The ion column used for much of the work reported in this dissertation is shown schematically in Figure 1.1. It consists of a three-element asymmetric einzel lens and an octupole sitigmator/deflector. The LMIS itself is supported within a structure called a suppressor electrode. The suppressor can be biased either positively or negatively either to increase or decrease the extraction voltage required to produce a given extracted current. By varying the suppression voltage it is possible to maintain a constant extracted current while varying the extraction voltage. This is illustrated in Figure 1.2. Likewise, it is possible to vary the extracted current while maintaining a constant extraction voltage. The focusing properties of the lens depend primarily on the ratio of beam voltage to extraction voltage and for the most part are independent of the suppressor voltage. The emitter/suppressor acts as a weak lens having negligible aberrations compared with the aberrations of the main focusing lens. [23] This is a convenient feature because it is possible to adjust a slowly drifting current to its original value without altering the lens focus. It is conceivable to use closed loop feedback to maintain the emission current by this means but this has not been done.

As shown in Figure 1.3 different values of the suppressor voltage do not affect the slope of the LMIS emission current (see Chapter 2 for a discussion of dI/dV) but serve to change the required extraction voltage thus altering I'[24]. This alters the

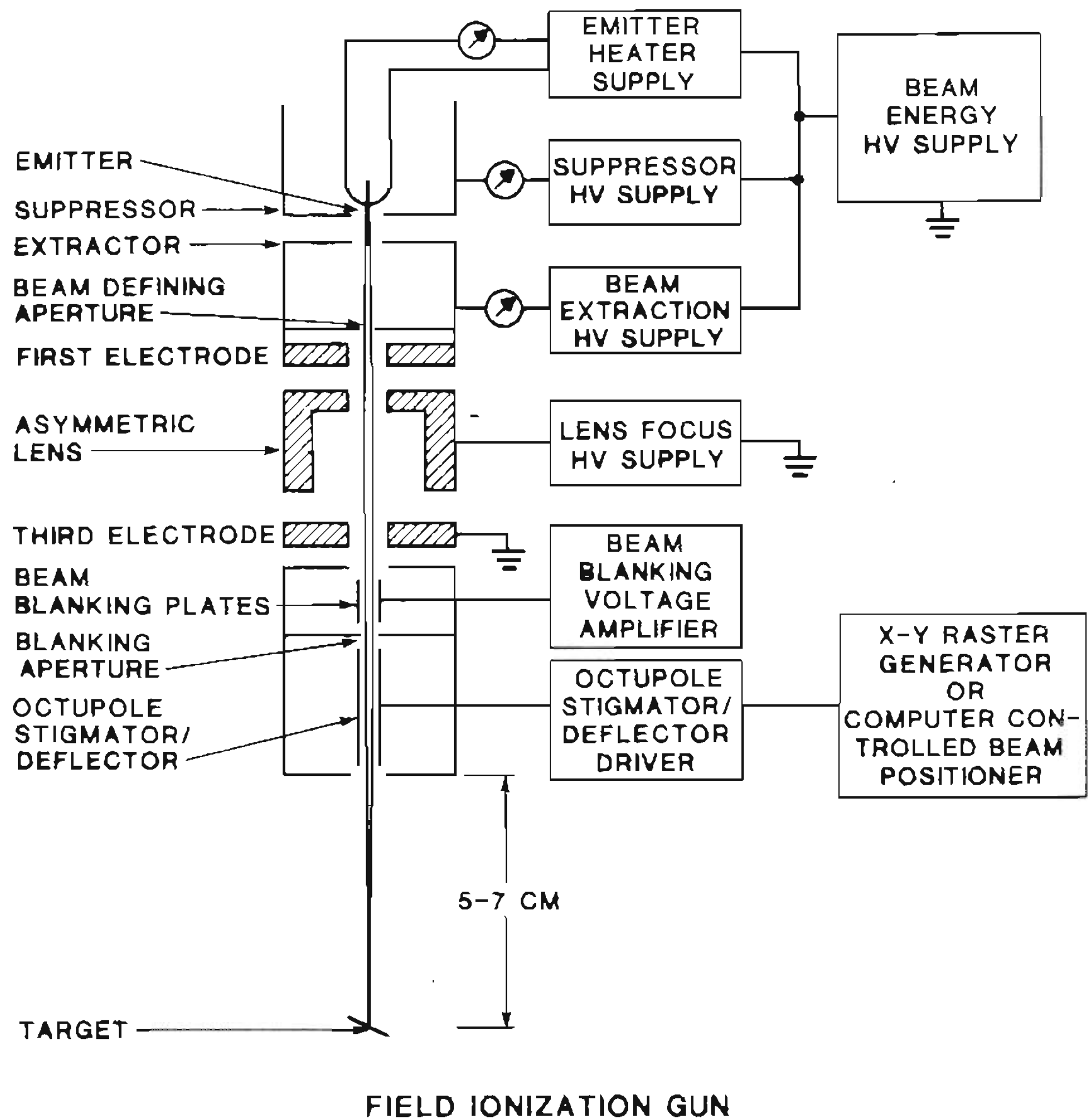

Figure 1.1 Three element asymmetric einzel lens gun with an octupole stigmator and deflector. This single lens gun employs liquid metal ion sources which can be focused and deflected over a target under computer control or with a standard raster generator.

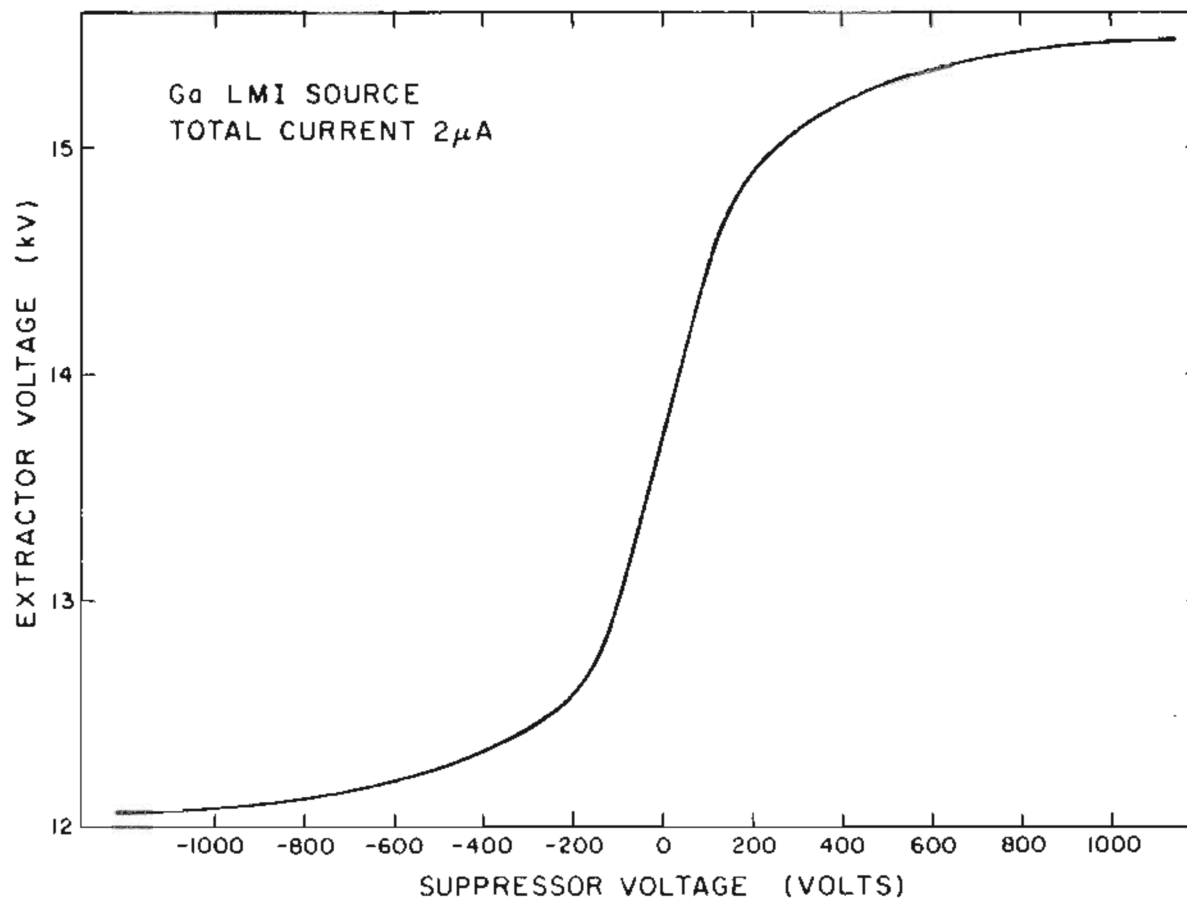

Figure 1.2 To provide a given extracted current (2 μA here), the extraction voltage and suppressor voltage vary as indicated.

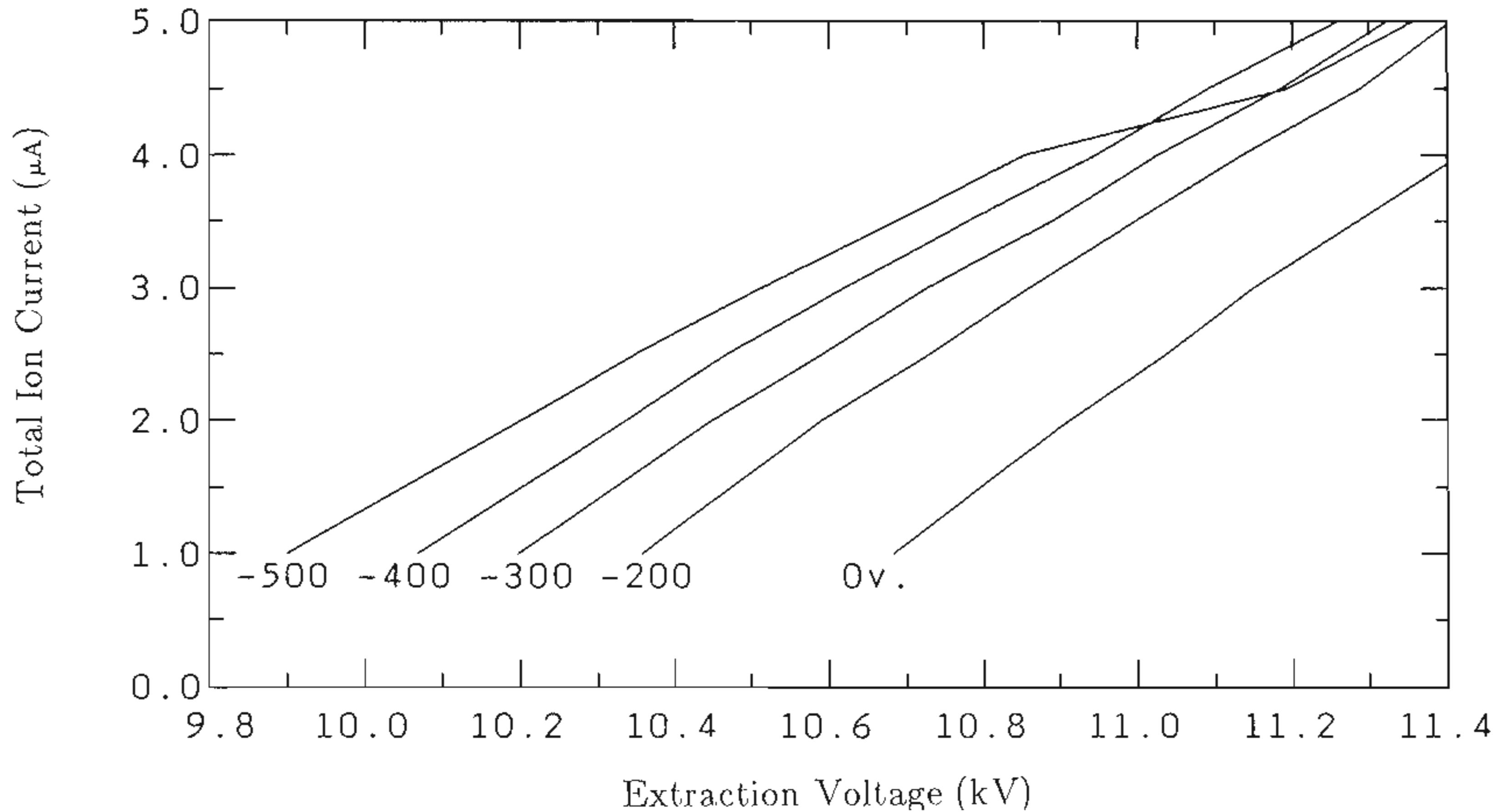

Figure 1.3 Varying the suppressor voltage does not alter the dI/dV for a given LMIS emitter. In this case, the extraction voltage required to provide a desired extracted current must be adjusted.

beam current via: $I_b = J'\pi\alpha^2$ with α the acceptance angle of the lens, and the current density, J, in the spot[23]. The change in slope indicated for a suppressor voltage of -500 volts is possibly due to a change in the I(V) characteristic itself. Figure 1.4 shows the focused spot diameter as a function of beam energy at a working distance of 75 mm. and a beam current of 0.3 nA.

The research reported in this dissertation encompasses both scientific and technological aspects of liquid metal ion sources and their applications. Figure 1.5 shows a schematic diagram of the system used for many of the experiments reported here. We note that secondary ion mass spectrometry (SIMS) with LMIS has also been demonstrated during the course of the research into LMIS applications. In particular, the transmission of the OGC SIMS system has been measured as a function of mass and energy of the incoming ions. This work is not described here however, as it is specific to the OGC SIMS system and does not have general utility.

Throughout this dissertation, we have chosen not to dwell on details which are readily available in the literature or appear in handbooks. Derivations of well known expressions are also not presented if they can be found elsewhere. We merely cite the relevant references.

Chapter 2 presents a discussion of the I(V) characteristic of liquid metal ion sources and develops a novel approach to understanding the two factors which control the current: space charge in the beam and the flow of liquid metal to the emitting region. This approach affords some physical insight not available previously. A brief discussion of energy broadening is also given and a relationship is obtained which relates the physical parameters by simple dimensional arguments. Chapter 3 presents a discussion of real Ga liquid metal ion sources and considers contamination issues

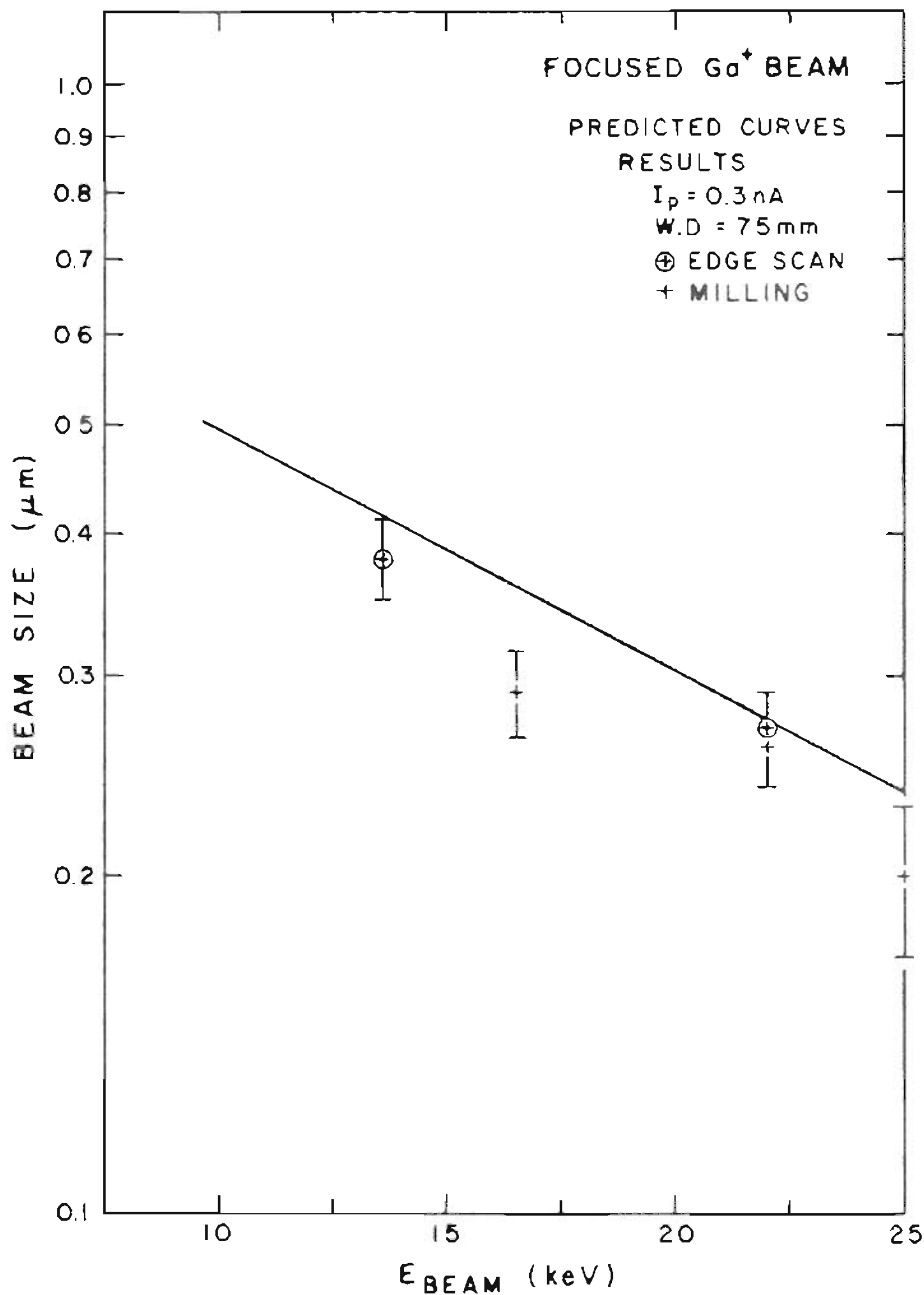

Figure 1.4 The beam diameter or "spot size" is a function of energy. Edge scan denotes a technique often used to measure electron beam spot diameter. This consists of scanning the beam across a knife-edge and measuring the rise time of the current density profile in a transmission or "reflection" i.e. secondary electron capture mode. The milled scan lines were made across thin (< 1000 Å) gold films on silicon substrates.

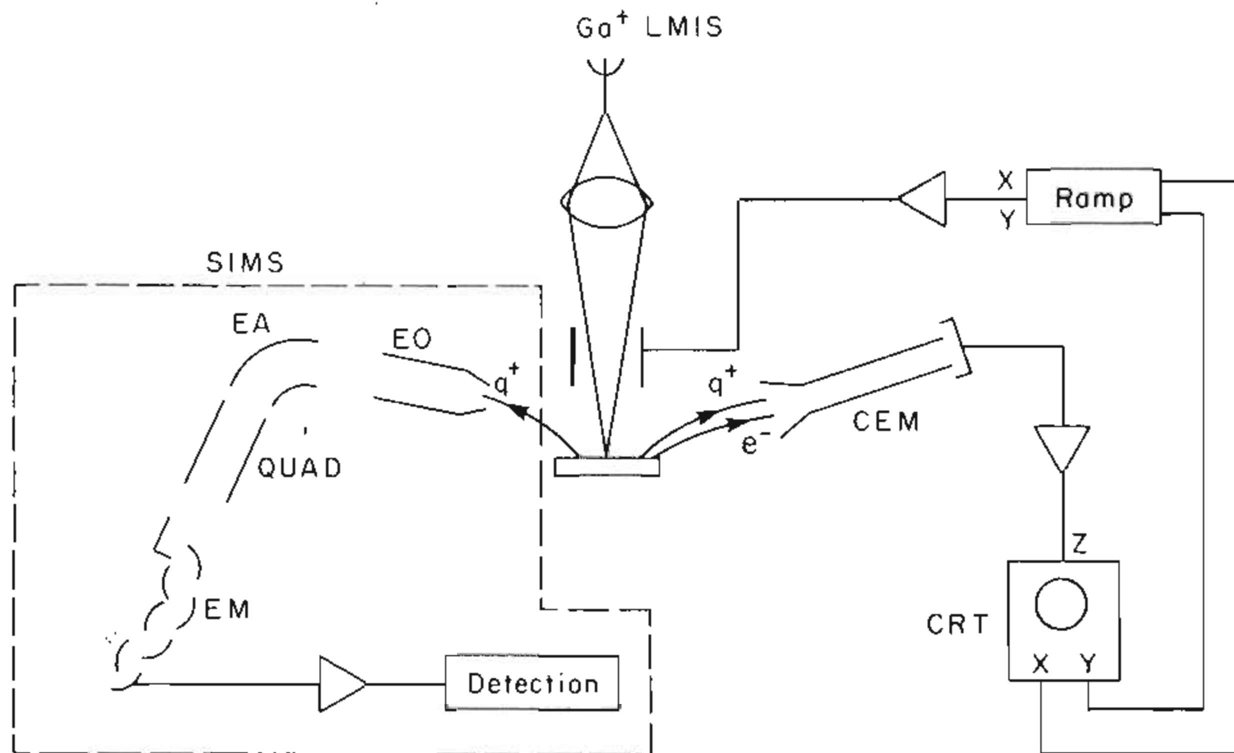

Figure 1.5 Overall system schematic. Detection of secondary electrons and positive and negative secondary ions enables operation as a scanning ion microscope. The SIMS system is also illustrated. The X, Y ramps synchronously drive the ion gun deflection plates and the CRT deflection. The signal is detected by a channel electron multiplier (CEM), amplified and modulates the CRT intensity.

which affect their successful fabrication, including their testing and operation in a focused ion beam column. As a preface to the applications examined in this dissertation, Chapter 4 presents a capsule review of some of the basic phenomena involved in ion bombardment of solids in general. These phenomena are common to ion bombardment of solid targets, whether by a focused or unfocused ion flux. In Chapter 5, we examine some of the observations of surface topography induced under ion bombardment and present the first systematic study of droplet formation on gallium arsenide and aluminum gallium arsenide under gallium focused ion beam bombardment. Chapter 6 examines the novel and successful application of FIB technology to micromachining of optoelectronic devices and integrated circuits and Chapter 7 concludes with an example of focused ion beam lithography.

2. SOME THEORETICAL CONSIDERATIONS FOR LIQUID METAL ION SOURCES

2.1 Introduction

The following analysis takes a novel approach in deriving the functional form of some of the characteristics of liquid metal ion sources (LMIS). It is based on fundamental physical considerations, and allows some general conclusions to be drawn. The current-voltage characteristic is derived from first principles in a manner which demonstrates that it is applicable for arbitrary space charge and liquid flow impedance. Some aspects of energy broadening in the ion beam are discussed as well. No effort has been made to provide a microscopic theory of LMIS operation as has been done, for example, in a recent series of papers[25-28]. Rather, the purpose is to provide an alternate point of view to the derivation of LMIS I(V) curves and other properties by employing fundamental physical principles. The detailed micro-physics surrounding their operation and the mechanisms of ion emission are outside the scope of the model. In fact, it is clear that these considerations are not directly relevant for establishing the I(V) characteristic which depends primarily on the diode geometry, properties of the liquid such as viscosity, density and surface tension, the wettability of the liquid-substrate system and on macroscopic qualities of the capillary or needle

substrate. The influence of these properties has been discussed in a recent paper by Bell and Swanson[24].

Previous analyses and derivations of I(V) curves for LMIS have considered the electrical and mechanical forces acting on the liquid body during steady state ion emission or at the onset of ion emission. For example, Mair[29] treats the capillary LMIS which provides an ion current commonly considered to be space charge limited. The possibility that the flow may influence I(V) is disregarded for such emitters. His treatment will be described in another section of the present discussion. On the other hand, Wagner[30] considers the needle type LMIS and develops a simple hydrodynamic model of the I(V) characteristic where liquid flow apparently controls the current. The model relies essentially on mass conservation, laminar fluid flow and the estimate of a voltage dependent pressure gradient to obtain I(V). It predicts a minimum emission radius of 130 Å, while observations of operating LMIS in a high voltage SEM[31] reveal radii of 10 to 20 Å. A plausible and exciting feature of that model is the prediction that the energy spread may be influenced by the flow impedance of the source. This would provide the means for increasing the current density in the focused ion beam spot. (see Section 2.4) This suggestion has also been made by Mair[32]. Unfortunately, experiments have since demonstrated (and these workers have acknowledged) that flow impedance has essentially no influence on the energy spread. Such experiments have been done using gallium[33,34] and gold ion beams[35]. The transient effects which occur at the threshold for ion emission have also been investigated. Thompson and Prewett[36] show that viscous dominated flow along the shank of needle type LMIS and not inertia is responsible for limiting the liquid redistribution in the Taylor cone during the transient emission onset period.

2.2 Principle behind the model

The present analysis considers the forces acting on the ion current emitter as well as on the current collector and differs in this respect from other studies. It will be seen that this approach may have applications beyond the present problem.

From the conservation of total momentum, i.e. the momentum of the electromagnetic field plus the mechanical momentum as expressed in electrodynamics one can write for the ith component of momentum:

$$\frac{d}{dt}\,(P_{mech}+P_{field})_i = \int\int_S \sum_{j=1}^{3} T_{ij} n_j da \qquad (2.0.0)$$

where S is the boundary surface of the volume V, and T_{ij} is the Maxwell stress tensor defined as

$$T_{ij}=\epsilon_0(E_iE_j-\frac{1}{2}E_iE_j\delta_{ij})-\frac{1}{\mu_0}(B_iB_j-\frac{1}{2}B_iB_j\delta_{ij})$$

and $\sum T_{ij}$ is the component of the momentum flow per unit area across S and into V. $i,j = 1,2,3$

For steady state ion emission we have:

$$\frac{d}{dt}\,(P_{field})=0$$

Furthermore we assume that the magnetic field due to the current is negligible. The electromagnetic stress tensor then reduces to the electrostatic stress tensor, the first term in the expression for T_{ij}.

Consider the case of a planar diode with plate A the ion emitter, and plate B the ion current collector. (see Figure 2.1a) Performing the operations indicated in equation (2.0.0) on plate A, plate B, and plates A and B together yields the simple relation:

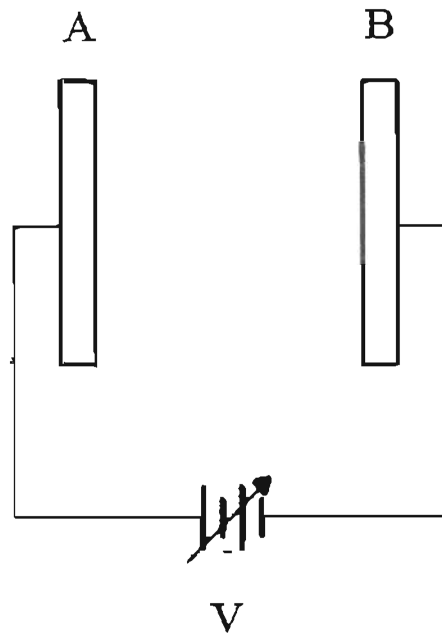

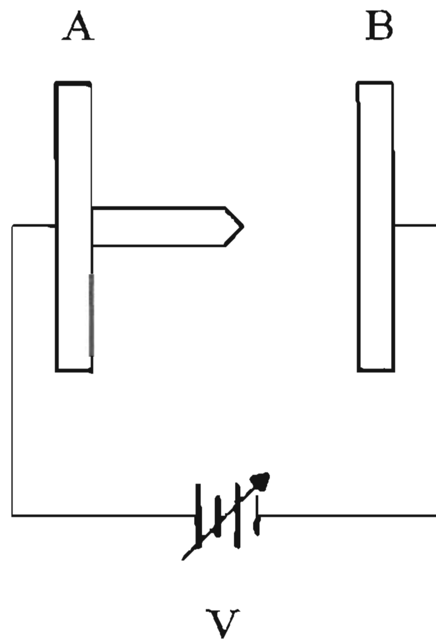

Figure 2.1 Upper: Simple planar diode model used to obtain the basic equation (2.0.1) in text. Plate A provides the ion current. Plate B receives the ion current. Lower: LMIS emitter adapted to the planar diode model.

$$-\frac{\epsilon_0}{2}E_B^2A_B + I(\frac{2mV}{q})^{\frac{1}{2}} + \frac{\epsilon_0}{2}E_A^2A_A = 0 \qquad (2.0.1)$$

with I the beam current, m the ion mass, and V the potential difference between the plates. Equation (2.0.1) can be seen to represent equation (2.0.0) in a more recognizable form if we consider the emitter and collector and the included "empty space" with its charge and current density distributions as a closed system. We see then that the total force on the system must equal zero since there are no external forces. Therefore, equation (2.0.1) is the equation of motion of the system. In mechanical terms, the situation can be regarded as follows. The force on plate A is equal to the Maxwell stress on A times its area. The force on plate B is given by the vector sum of the Maxwell stress times the area of plate B and the rate of change of momentum due to the impinging ion current.

Three points concerning equation (2.0.1) should be noted:

i. This equation expresses the law of momentum conservation for our system and is entirely general i.e if all the electromechanical forces on the plates are included, then equation (2.0.1) must be correct. It expresses the physically intuitive idea that the mass flow between emitter and collector is driven by the difference in Maxwell forces between them. This is true whether the mass is in the form of charged or uncharged atoms, droplets or clusters. Any interaction between particles, e.g. the quasi-continuous space charge responsible for spacial beam spreading or the stochastic Coulomb forces thought responsible for the beam energy spread, merely "readjusts" the relative magnitude of the terms comprising equation (2.0.1) so that it always remains true. This provides the basis for the analysis.

Note that in the present treatment the ions are not given an initial

velocity and multiply charged particles are not considered at this point. Only a singly charged monomer ion beam is considered. The generalization to non-zero emission velocity is easily made and does not alter the essential features of the model or its conclusions.

ii. Reasoning as above shows that equation (2.0.1) is unaffected by the degree of space charge in the diode, which manifests itself only through the fields E_b and E_a. If there is no space charge, E_b and E_a are simply the Laplace fields. If there is a space charge, E_b and E_a include the retarding field due to the ions i.e. these are the net fields which act on the collector and emitter after the space charge has been established.

iii. The use of this equation circumvents the requirement of beginning with the Poisson equation to investigate space charge problems. This surprising conclusion will be discussed briefly in Appendix 2a.

In fact, equation (2.0.1) can be applied in a simple manner to derive the Child-Langmuir Law for a space charge limited current in a planar diode (see Appendix B1). This result, although interesting in its own right, is not directly relevant to the present problem. All field emission processes require extremely high electric fields at the emission site and not zero field as required by the classical Child-Langmuir formulation for space charge limited electron emission. For the LMIS, field evaporation and postionization electric fields are in the range 1 to 3 volts / Å. Fortunately, equation (2.0.1) can also be used to obtain the result of Stern et al, who considered the problem of space charge in a planar diode[37]. Their analysis results in an expression relating the electric field in the presence of space charge to the electric field at the same

surface in the absence of space charge. This result, originally derived via the Poisson equation, is derived beginning with equation (2.0.1) and is given in Appendix 2c.

As shown by Mair[29], when one considers the Stern, et al. equation in the limit of small space charge, the resulting expression can also be used for the case of very large space charge since it differs from the exact expression i.e. the Child-Langmuir law by only 15%. This approximation serves as the point of departure for his derivation of the I(V) characteristic for a capillary type LMIS.

Since equation (2.0.1) implicitly contains the results of Stern et al (and hence those of Mair), it should be possible to derive the I(V) characteristic directly from this equation. This is done in the following section.

2.3 Model

The LMIS is not well represented as an ion emitting planar anode, so we make the following observations. If the LMI emitter is attached to plate A, as depicted in Figure 2.1b, the force on the plate can be considered to consist of the sum of the force F_a on the non emitting region, and the force F_E on the emitter substrate or needle. The decomposition of forces on plate A can then be written,

$$F_A = F_a + F_E \tag{3.0.1}$$

The second term contains part of the total viscous traction force or drag force over the emitter needle which is given by,

$$F_v = F_E - F_T \tag{3.0.2}$$

with F_E the electrostatic force and F_T the surface tension force. These forces are obtained by integrating the respective stresses over a surface containing the fluid

where the first term is the applied Maxwell force on the liquid anode but excluding

surface in the absence of space charge. This result, originally derived via the Poisson equation, is derived beginning with equation (2.0.1) and is given in Appendix 2c.

As shown by Mair[29], when one considers the Stern, et al. equation in the limit of small space charge, the resulting expression can also be used for the case of very large space charge since it differs from the exact expression i.e. the Child-Langmuir law by only 15%. This approximation serves as the point of departure for his derivation of the I(V) characteristic for a capillary type LMIS.

Since equation (2.0.1) implicitly contains the results of Stern et al (and hence those of Mair), it should be possible to derive the I(V) characteristic directly from this equation. This is done in the following section.

2.3 Model

The LMIS is not well represented as an ion emitting planar anode, so we make the following observations. If the LMI emitter is attached to plate A, as depicted in Figure 2.1b, the force on the plate can be considered to consist of the sum of the force F_a on the non emitting region, and the force F_E on the emitter substrate or needle. The decomposition of forces on plate A can then be written,

$$F_A = F_a + F_E \tag{3.0.1}$$

The second term contains part of the total viscous traction force or drag force over the emitter needle which is given by,

$$F_v = F_E - F_T \tag{3.0.2}$$

with F_E the electrostatic force and F_T the surface tension force. These forces are obtained by integrating the respective stresses over a surface containing the fluid

volume of interest. Due to the cylindrical symmetry of the diode system, the longitudinal component is understood.

When there is no emission (hence, no steady state fluid motion), $F_v = 0$, implying that the total electrostatic force and the total force due to surface tension are equal and opposite. This itself does not necessarily mean that the respective stresses are in equilibrium at all points on the surface of the shape existing at that voltage. Stress balance is a local equilibrium condition while force balance is a global relation. The connection between them comes from the observation that if there was an imbalance in the local stress equilibrium at any point there would be a net motion. Since there is no motion of the existing shape this implies that local equilibrium is satisfied. Notice that this shape is not necessarily the Taylor cone shape although the Taylor cone shape must also satisfy it. Definition (3.0.2) merely expresses the fact that if the only forces acting are due to surface tension and the electric field, then these forces must be in equilibrium or there will be fluid motion. If there is steady state fluid motion, there results a viscous drag given by definition (3.0.2). The fact that, strictly speaking, the Taylor cone can exist stably only when there is no ion emission, is also " built into " the definition. This has been expressed somewhat differently by Thompson and Prewett[36] and others who have stressed that the Taylor cone solution satisfies the static solution only. Whether the LMIS is of the high or low flow impedance variety, there is always a viscous drag on the substrate. The extent to which this influences I(V) will be discussed in Section 2.3.2. During ion emission one can write,

$$F_E = F_n + \frac{\epsilon_0}{2} E_e^2 A_e \qquad (3.0.3)$$

where the first term is the applied Maxwell force on the liquid anode but excluding

the ion emission area A_e, and the second term is the Maxwell force on the emission area itself.

Now we define:

$$\Gamma(g) \equiv 1 - \frac{(F_a + F_n)}{\frac{\epsilon_0}{2} E_B^2 A_B} \tag{3.0.4}$$

where " g " signifies symbolically the physically fixed emitter-collector geometry as well as the voltage variable shape of the liquid anode and $0 < \Gamma \leq 1$. While in operation, this shape is now widely accepted to consist essentially of a jet-like protrusion affixed to an underlying Taylor cone. The geometry dependence of the LMIS is implicit in Γ, since it is a measure of the contribution to the total force on plate A which comes from the large non ion emitting area, A_a, and the force due to the electrostatic stress on the needle surface, both relative to the Maxwell force on plate B. It is clear that changing emitter parameters such as cone angle, apex radius, emitter length or the apex distance to the plate could change the relative magnitude of the terms comprising it. Furthermore, the magnitude of Γ will depend on the degree of space charge reduction of the force F_n. That there is such a reduction in the electric field is evident from the work of Kingham and Swanson who find that the Laplace field at the apex of the jet-like protrusions can reach $8V/\text{Å}$ although the Poisson field is closer to $1.5V/\text{Å}$ for Ga, for example[26].

Now we notice that regardless of the field at the emitter, E_e, the field at plate B is approximately uniform and can be written:

$$E_B = \frac{\alpha V}{d}$$

where V is the potential difference between the plates as before, d is the distance

between them, and $\alpha = \alpha(r,\theta)$ is a constant for a given geometry. Also α has its maximum value at the plate B for $\theta = 0$ where the field strength is greatest. Furthermore, α must $\rightarrow 1$ for all points (r,θ) on the plate far from the emitter.

With the substitution of equations (3.0.1) and (3.0.3), definition (3.0.4) and the last relation into equation (2.0.1) one obtains for the current:

$$I = \frac{\epsilon_0}{2}\left(\frac{\Gamma(g)\alpha^2 V^2 A_B}{d^2} - E_e^2 A_e\right)\left(\frac{q}{2mV}\right)^{\frac{1}{2}} \tag{3.0.5}$$

where the emission area A_e is allowed to depend on current or voltage.

Experimentally, it is observed that the onset and extinction of ion emission usually exhibits hysteresis, represented schematically in Figure 2.2. As the voltage is increased from zero, we approach V_{on} , which is the threshold voltage for ion emission. The current jumps discontinuously from $I = 0$ to $I = I(V_{on})$. Further current increase proceeds along the solid line. On the other hand, the current decrease from a point for which $V > V_{on}$ follows the dotted line to the voltage $V_m = V_{off} + \delta$ where the current jumps discontinuously from $I_m \equiv I(V + \delta)$ to $I(V_m) = 0$, where δ is some small positive voltage. The value of δ is related to the stability of the liquid near V_m and will not be discussed here.

At I_m , we obtain from equation (3.0.5) the relationship

$$E_e^2(V_m) = \frac{\Gamma_m \alpha^2 V_m^2 A_B}{d^2 A_e(V_m)} - 2\frac{I_m}{\epsilon_0}\left(\frac{2mV_m}{q}\right)^{\frac{1}{2}}\frac{1}{A_e(V_m)} \tag{3.0.6}$$

where $A_e(V_m)$ is the area of the emission site at the voltage $V = V_m$. Following the argument of Kingham and Swanson[26], which makes plausible a nearly uniform field evaporation rate at the emission site, we assume that the electric field at the emission site remains constant with increasing current. Then substituting equation

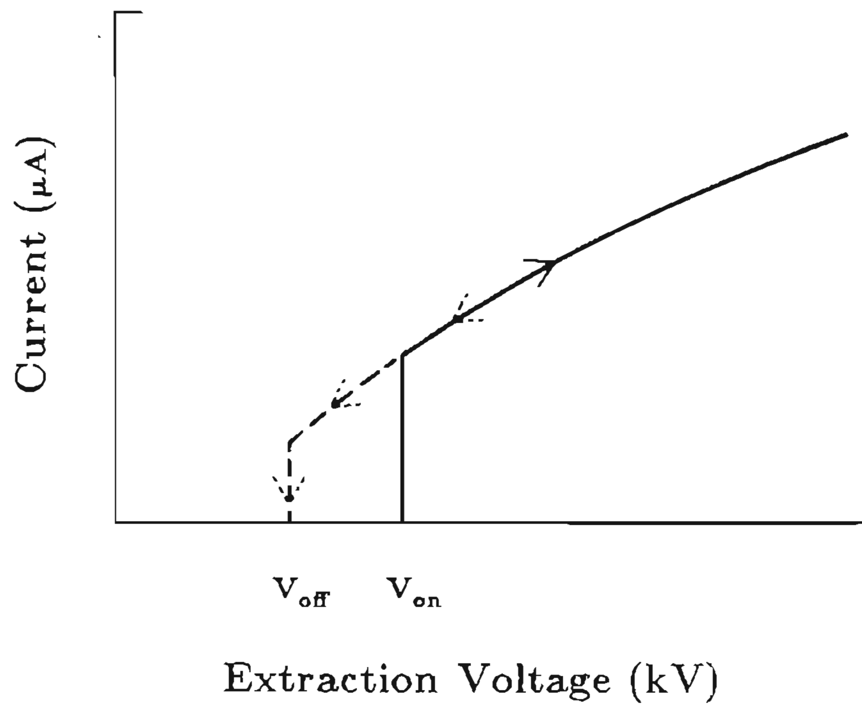

Figure 2.2 Schematic of the I(V) characteristic of a LMIS. Note the hysteresis of the threshold for emission onset and extinction.

(3.0.6) into equation (3.0.5) one obtains the following expression for I(V).

$$I = \eta V^{-\frac{1}{2}} \left(\frac{\Gamma}{\Gamma_m} V^2 - V_m^2 \frac{A_e(V)}{A_e(V_m)} \right) + \frac{I_m A_e(V)}{A_e(V_m)} \left(\frac{V_m}{V} \right)^{\frac{1}{2}} \tag{3.0.7}$$

with η defined as:

$$\eta = \left(\frac{q}{2m} \right)^{\frac{1}{2}} \frac{\epsilon_0}{2d^2} \alpha^2 A_B \Gamma_m \tag{3.0.8}$$

The analysis presented here considers the forces on plate A to which the emitter and liquid metal film are "attached", and on plate B which receives the ion current. We see therefore, that equation (3.0.7) applies for arbitrary space charge and flow impedance, the fact that Γ may be a function of voltage notwithstanding . To understand this, it is sufficient to realize that the forces acting on the viscous liquid film are transmitted by the viscous shear stress to the substrate and hence to plate A. The viscosity influences I(V) to a greater or lesser degree for a given emitter and produces energy losses in the fluid. Any analysis based on the flow of energy in a system including dissipation is generally quite difficult. The model presented here however, relies only on the balance of forces and therefore is not affected by energy losses occurring in the liquid during steady state ion emission. It will be recalled that many physical systems can be analyzed either in terms of their energy content and flow or via their interaction forces; the two approaches being complimentary. This is particularly clear in Newtonian mechanics when frictional forces are present. Newton's equation, $F_{net} = ma$, applies whether the motion is supplied with energy or allowed to decay via the losses; yet the flow of energy through the system is different for each case. Therefore, one concludes that the I(V) characteristic is given by equation (3.0.7) whether viscosity (and hence, flow impedance) or space charge limits the ion current. We will return to this point in Section 2.3.2.

Equation (3) can now be compared with an expression derived by Mair[29] for so-called low flow impedance capillary ion sources. Following Mair, we now allow the minimum current to be zero and not I_m as defined in the present analysis i.e., $I_m=0$. This occurs at $V = V_m \equiv V_{off}$, the extinction potential[29,36] and is a simple way of handling the discontinuity at V_m. In any case, this difference should have only a small effect on the I(V) characteristic except perhaps near V_m. In his treatment, the effect of changes in emission area on current is negligible at small currents. Therefore, according to Mair we may substitute:

$$\frac{A_e(V)}{A_e(V_m)} = 1$$

in equation (3.0.7). Furthermore, we may let $\Gamma = 1$. As will be shown in the next section, this assumption is consistent with the low flow impedance ion source presently being considered. With these substitutions, equation (3.0.7) becomes:

$$I = \eta V^{-\frac{1}{2}} \left[V^2 - V_{off}^2\right] \tag{3.0.9}$$

with η defined by (D3). The equation for I(V) derived by Mair is:

$$I = 3\pi(\frac{2q}{m})^{\frac{1}{2}} RT\cos\phi V_0^{-\frac{1}{2}} \left\{(\frac{V_0}{V_{0x}} - 1) + \frac{1}{2}(\frac{V_0}{V_{0x}} - 1)^2\right\} \tag{3.0.10}$$

with the extinction voltage defined:

$$V_{0x} = \left(\frac{2\kappa RT\cos\phi}{\epsilon_0}\right)^{\frac{1}{2}} \tag{3.0.11}$$

but this may be written more simply as:

$$I = \frac{3\pi}{2}(\frac{2q}{m})^{\frac{1}{2}} RT\cos\phi V_0^{-\frac{1}{2}} \left[\frac{V_0^2}{V_{0x}^2} - 1\right] \tag{3.0.12}$$

and can be written in our notation:

$$I = \eta_M V^{-\frac{1}{2}} \left(V^2 - V_{off}^2 \right) \tag{3.0.13}$$

where η_M is defined as:

$$\eta_M \equiv \frac{3\pi}{2} \left(\frac{q}{2m} \right)^{\frac{1}{2}} \frac{\epsilon_0}{\kappa} \tag{3.0.14}$$

and the constant κ arises through his use of Taylor's slender body approximation[38].

We note that this has precisely the form of equation (3.0.9) (with $I_m = 0$) derived here via different considerations. As shown by several authors[29,39,40] curves of the form given by equation (3.0.9) fit the experimental data quite well. (see Figure 2.3)

2.3.1 Space Charge versus Flow Impedance

A question of continuing interest and occasional controversy is whether the space charge established in the diode or the flow impedance of the source limits the ion current. We hope that the approach taken in this thesis can provide an answer to this question which as yet appears unresolved. This is evidenced by a recent review paper from which we quote[41]:

> One might reason that there is instability and the tip radius should decrease without limit; since the higher the field, the sharper the tip, and the sharper the tip the higher the field. However, the sharper the tip the higher the emission, and eventually space charge is thought to limit the current. An alternate explanation is that the hydrodynamics of liquid-metal flow down the needle limits the current and determines the I-V characteristics of the source. The fact that the emission is strongly depen-

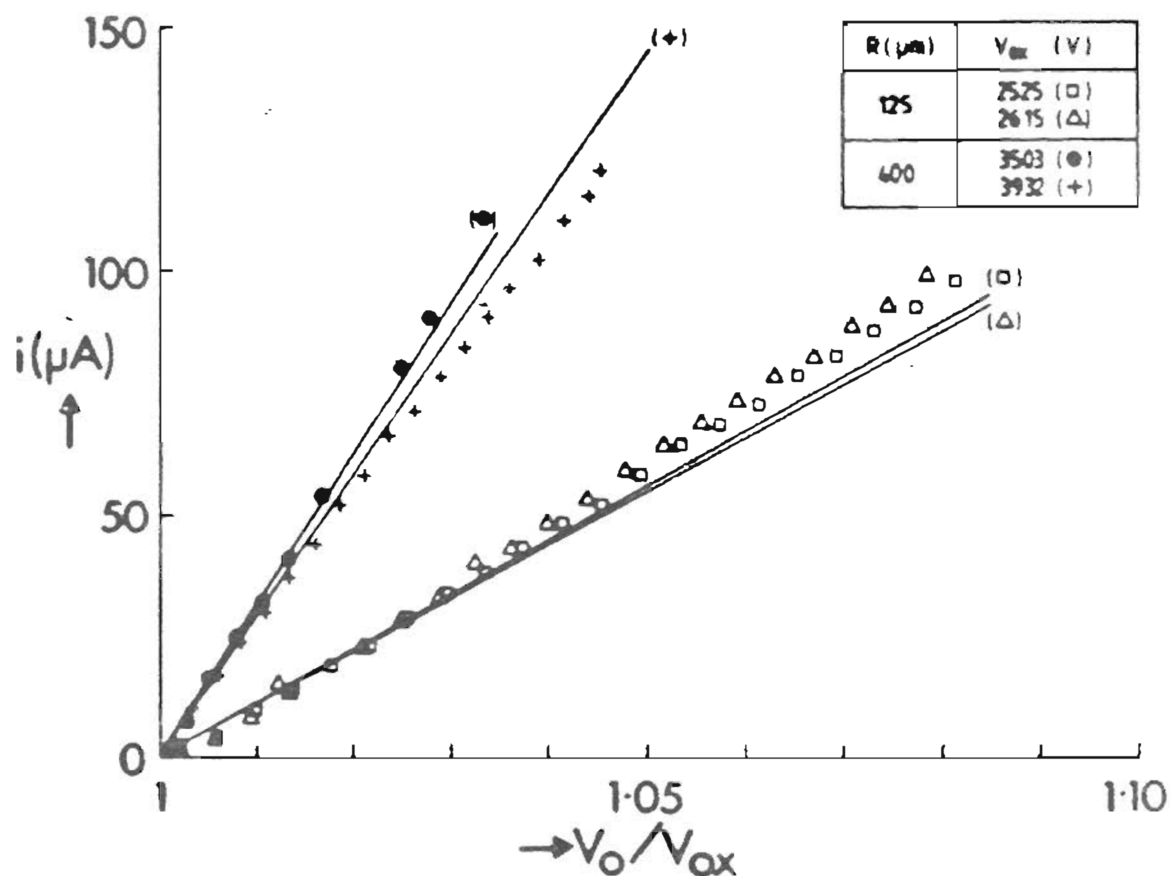

Figure 2.3 Comparison of experimental data with theoretically derived expression for I(V) of the form of equation (3.0.9) derived here. The figure is obtained from Mair[29]

dent on the needle radius and on whether the needle is smooth or has grooves argues for this explanation over the space charge. Whichever reason is correct, the configuration appears to be stable over time, and a number of liquid metal sources can operate for 100 hours or more.

It will be demonstrated in this section that both factors contribute to the control of the current and that the meaning of the question itself deserves some comment. As noted before, capillary ion sources are said to be space charge limited since the liquid flow is apparently unrestricted; hence they are considered to have very low flow impedance. On the other hand, the coated needle type LMIS, especially when the needle is smooth, is said to have high flow impedance. Typically, the flow impedance is considered low if dI/dV is steep and high if dI/dV is shallow. This will be discussed in the concluding section.

Having discussed the terminology, we now attempt to answer the question. Essentially we wish to determine whether the emission current is limited by the supply of material i.e. by the availability of the liquid to be ionized or by the space charge in the beam. A brief look at the analogous situation in a thermionic diode may serve to clarify the issue. To answer the question as to whether a thermionic emitter is operating in the space charge limited regime or in the temperature, i.e. supply, limited regime one simply has to increase the temperature or the extraction voltage. If increasing the filament temperature has no effect, the space charge is certainly limiting the current. On the other hand, if the filament temperature affects the current, then the diode is operating in the temperature limited regime. Since there are two distinct operating regimes, with parameters which can be varied independently, the above question is meaningful. For the LMIS on the other hand, the two

"regimes", if we can call them that, are not necessarily independent. For example, it has been observed empirically that increasing the temperature increases the current. A temperature increase serves to reduce the viscosity, thereby lowering the "flow impedance" of the liquid film. There appears to be little evidence, if any, that there exists an operating regime where the temperature fails to affect the ion current (but this should be an area for future study). This is independent of the initial flow impedance, i.e. both so-called low and high flow impedance sources exhibit this behavior although, as emphasized in the following discussion, the effect will be small if the flow impedance is small. Furthermore, increasing the extraction voltage always results in an increase in current. Apparently this occurs at all current levels for emitters with both shallow and steep dI/dV curves, at least in the range approximately $\leq 0.5\mu A$ to $100\mu A$. Therefore, one may conclude that both flow impedance and space charge simultaneously influence the current. The extent to which one or the other dominates will be explored in the following discussion where it will be shown how both factors are related.

2.3.1.1 Perveance

Some insight into the relative influence of the space charge and flow impedance can be gained if one considers the perveance, defined (with $I_m = 0$) as:

$$P \equiv \frac{I}{V^{\frac{3}{2}}} = \eta \left(\frac{\Gamma}{\Gamma_m} - \frac{V_m^2}{V^2} \frac{A_e(V)}{A_e(V_{off})} \right) \tag{3.1.1}$$

a quantity which can be used to characterize the degree of space charge in the diode. Qualitatively, the larger the perveance, the larger the space charge. From the previous discussion and definition (3.1.1) we see that at a given voltage, the space charge

influence depends on the value of Γ. It follows from the concept of flow impedance that the greater the impedance, the greater the applied force (i.e. the Maxwell force) necessary to produce a given mass flow rate. From (3.0.2), we see that for a given surface tension force, a greater applied force produces a larger viscous traction force. Definition (3.0.4), and equation (3.0.3) indicate that this results in a smaller Γ which, in turn, implies a smaller perveance, resulting in less space charge in the diode. This illustrates directly that the greater the influence of flow impedance, the smaller the influence of space charge and conversely. In a limited sense, the force F_a is arbitrary, since it depends on the area of the plate A not occupied by the emitter. Therefore, we temporarily let $F_a = 0$ to simplify the interpretation. This will have no effect on functional dependencies or on the predictions of the model. For the case $\Gamma = 1$ considered earlier, we have from equation (3.0.4) $F_n = 0$ which, from equations (3.0.2) and (3.0.3) implies a small viscous traction force. This is consistent with the notion that an emitter with a small flow impedance will support an ion current which is limited by space charge. On the other hand, Γ small implies a large F_n which from equations (3.0.2) and (3.0.3) means that F_v is large. Therefore, when dI/dV is large, space charge exerts a large influence while for dI/dV sufficiently small, it is plausible that the flow impedance is the dominant factor. Of course, for all values of dI/dV, both factors will contribute. We will examine the flow issues in the following section.

2.3.2 Hydrodynamics and fluid flow

We now examine the flow issues more explicitly by considering the needle LMIS. The wetted emitter shank may be modeled as a thin liquid film flowing over the surface of a cylinder of radius R. The surface of the thin film is at coordinate $r = aR$

and has a thickness t. The volume flow rate is calculated by assuming that laminar flow exists and that the flow is fully developed.

The two fundamental equations for laminar flow of a Newtonian fluid are:

$$\frac{1}{r}\frac{d}{dr}(r\tau_{rz}) = \frac{dP}{dz} \tag{3.2.1a}$$

and

$$\tau_{rz} \equiv -\mu\frac{dv_z}{dr} \tag{3.2.1b}$$

where $\frac{dP}{dz}$ is the pressure gradient along the flow direction, taken as the positive z-axis. The shear stress in the fluid, τ_{rz}, is equal to the product of viscosity, μ, and the velocity gradient across the flow and represents the rate at which the momentum of fluid travelling along the z-axis is transferred from "layer to layer" along the r direction. Solving equation (3.2.1a) for τ_{rz} gives immediately :

$$\tau_{rz} = \frac{dP}{dz}\frac{r}{2} + C_1 \tag{3.2.2a}$$

Two boundary conditions which often occur in fluid flow problems relate the velocities and shear stresses at interfaces. One generally requires that the tangential component of velocity is zero at a solid surface (the normal component is obviously zero) and the shear stress at a free surface is zero. At the fluid surface we have $\tau_{rz} = 0$ at $r = aR$ and obtain:

$$\tau_{rz} = \frac{1}{2}\frac{dP}{dz}\left(r - \frac{(aR)^2}{r}\right) \tag{3.2.2b}$$

To obtain the velocity distribution in the film, substitute equation (3.2.1b) into equation (3.2.1a) and integrate. Now since $v_z(r{=}R) = 0$, we obtain:

$$v_z = -\frac{R^2}{4\mu}\frac{dP}{dz}\left[1 - (\frac{r}{R})^2 + 2a^2 \ln\frac{r}{R}\right] \quad (3.2.3)$$

where $a \equiv 1 + \frac{t}{R}$.

To calculate the volume flow rate, we integrate over the velocity distribution i.e.

$$Q = \int_0^{2\pi} \int_R^{aR} v_z r dr d\theta \quad (3.2.4a)$$

Now since:

$$\int x \ln x dx = \frac{x^2}{2}\ln x - \frac{x^2}{4}$$

we obtain after combining terms:

$$\frac{Q}{H} = -\frac{1}{2}(a^2 - 1)^2 - \frac{1}{4}(a^4 - 1) + a^4 \ln a$$

where $H \equiv -\frac{\pi R^4}{2\mu}\frac{dP}{dz}$. The logarithm may be expanded:

$$\ln(1 + \epsilon) = \epsilon - \frac{1}{2}\epsilon^2 + \frac{1}{3}\epsilon^3 - \frac{1}{4}\epsilon^4 + \ldots$$

and after substituting $a = 1 + \epsilon$, with $\epsilon \equiv \frac{t}{R}$, the first non-zero term occurs for third order in t. One finally obtains:

$$Q = \frac{2\pi}{3\mu} t^3 R \frac{\Delta P}{L} \quad (3.2.4b)$$

where for steady, uniform flow, we have written $\frac{dP}{dz} = -\frac{\Delta P}{L}$. The flow impedance, Z, may be defined by:

$$Z \equiv \frac{\Delta P}{Q} = \frac{3\mu L}{2\pi t^3 R} \quad (3.2.5)$$

by direct analogy to electrical resistance. The viscous drag force can be calculated by integrating the surface stress over the wetted area and evaluating at $r = R$.

$$F_v = 2\pi r L \tau_{rz} \tag{3.2.6a}$$

This gives:

$$F_v = (2\pi RLt + \pi Lt^2)\frac{dP}{dz} \tag{3.2.6b}$$

which may be written in terms of the ion current by incorporating the conservation of mass relation $I\frac{m}{q} = \rho Q$, with ρ the fluid density. Substituting this into equation (3.2.4b) for Q yields:

$$F_v = \frac{3\mu LmI}{t^2 q\rho} \tag{3.2.6c}$$

where only the term of first order in t has been retained.

Having made the previous analysis, we return to the issue of space charge versus flow impedance control of I(V). Equation (2.0.1) may be recast in a somewhat different form:

$$I = H(V,F_T,F_a)\left[\left(\frac{2mV}{q}\right)^{\frac{1}{2}} + \frac{2\pi Rtm}{q\rho}Z\right]^{-1} \tag{3.2.7}$$

where equation (3.0.2) and equation (3.2.6c) have been substituted into equation (2.0.1) and

$$H(V,F_T,F_a) \equiv \left[\frac{\epsilon_0 \alpha^2 V^2 A_B}{2d^2} - F_a - F_T\right] \tag{3.2.8}$$

The second bracket in equation (3.2.7) contains a flow dependent term and a voltage dependent term. This explicitly expresses the physical continuity of the space charge and flow "regimes". One may now obtain a quantitative estimate of their influence. For a flow dominated ion current from a needle LMIS the flow impedance must satisfy:

$$Z >> \frac{\rho}{\pi R t}\left(\frac{qV}{2m}\right)^{\frac{1}{2}} \qquad (3.2.9a)$$

Despite the common use of the terms "flow impedance" in the LMIS literature, the flow impedance is not a directly measurable quantity. Therefore, we express equation (3.2.9a) in terms of the viscosity, which may be altered by heating or cooling the liquid. The relation required for a flow dominated current then becomes:

$$\mu >> \frac{2\rho t^2}{3L}\left(\frac{qV}{2m}\right)^{\frac{1}{2}} \qquad (3.2.9b)$$

For a Ga needle LMIS, taking: $\mu = 0.002 N{-}s/m^2$ at $T = 300$ °K, $\rho = 6.1 g/cm^3$, $L = 2.0mm$, $R_D = 127\mu m$, a typical extraction voltage $V = 8000$ volts, and allowing the film thickness to vary from $t = 500\text{Å}$ to $t = 1\mu m$, one finds that the R.H.S. ranges from approximately 4.0 x 10^{-3} to 0.2 N-s/ m^2. One sees that such a variation in film thickness can shift the control of the current from flow to space charge dominance. An important assumption of this analysis has been that the film thickness t remains constant i.e. it is independent of the current (or voltage). This will be discussed in the concluding section. In this case, equation (3.2.7) can be expressed:

$$I_{flow} = \frac{q\rho}{2\pi Rtm}\frac{1}{Z}\left[1 - \left(\frac{2mV}{q}\right)^{\frac{1}{2}}\frac{q\rho}{2\pi Rtm}\frac{1}{Z}\right] H(V,F_T,F_a) \qquad (3.2.10a)$$

For a space charge dominated current, the inequality obviously points in the other direction. In this case, the current can be expressed:

$$I_{sc} = \left(\frac{q}{2mV}\right)^{\frac{1}{2}}\left[1 - \frac{2\pi Rtm}{q\rho}\left(\frac{q}{2mV}\right)^{\frac{1}{2}} Z\right] H(V,F_T,F_a) \qquad (3.2.10b)$$

We see from equation (3.2.10a), if we ignore the possible dependence of film thickness

on current and recall that $H \propto V^2$, that I_{flow} essentially follows a V^2 dependence while equation (3.2.10b) is virtually independent of supply and has a $V^{\frac{3}{2}}$ dependence, a universal characteristic of space charge limited currents.

Although equations (13) apply strictly only to the flow model presented here i.e. laminar flow of a thin film over a cylinder, equation (3.2.7) may be written more generally:

$$I = H(V,F_T,F_a) \left(\left(\frac{2mV}{q}\right)^{\frac{1}{2}} + \frac{m}{q\rho} G_j \sum Z_i \right)^{-1} \tag{3.2.11}$$

where G_j characterizes the geometry of the emitter and film and has dimensions [length^2]. $\sum Z_i$ is the sum of the flow impedances of the emitter, including the shank, conical section and apex and $Z_i = \frac{\Delta P_i}{Q}$. (The flow impedance of any type of emitter may be "partitioned" in this manner since the impedances add in series). Furthermore we note that, contrary to the commonly accepted view, it is *not the flow impedance itself* which influences I(V). Rather it is the product of a film thickness and flow impedance which is relevant i.e. "tZ". Mathematically, it is possible to alter "Z" without changing "t". For example, the viscosity, μ, may be changed by heating or cooling the liquid but whether this implies that "t" can remain physically fixed for a given current is not known. It is likely that a complete electro-hydrodynamic treatment must be developed before this question can be answered. In any case, for a given current, "tZ" is proportional to the viscous drag on the substrate and the foregoing analysis allows the following general physical interpretations:

1. For the current to be flow dominated, the viscous drag force per unit current must be greater than the momentum per unit charge brought to

the extractor. Equivalently, we may say that the viscous drag force on the needle substrate must be greater than the force of the impinging ion current on the extractor. If not, the current is space charge dominated. Of course, in some cases neither influence may be said to be dominant as both may have similar relative "strengths". This is particularly true of the needle type LMIS as was illustrated above.

2. This reasoning is independent of the details of any given model of liquid flow.

Employing the Hagen-Poiseuille law for a capillary LMIS, one obtains $Z = \frac{8\mu L}{\pi R_c^4}$ for the impedance. The previous analysis may then be used to determine the condition for a flow dominated ion current for the capillary LMIS giving:

$$Z >> \frac{\rho}{\pi R_c^2}\left(\frac{2qV}{m}\right)^{\frac{1}{2}} \tag{3.2.12a}$$

or in terms of the viscosity, μ:

$$\mu >> \frac{\rho R_c^2}{8L}\left(\frac{2qV}{m}\right)^{\frac{1}{2}} \tag{3.2.12b}$$

Taking typical values for a capillary LMIS and using cesium as an example, from Mair and Mulvey[22]: $L = 5$ mm, $\mu = 0.63 \times 10^{-3}\mathrm{Ns/m^2}$, $\rho = 1.84\mathrm{g/cm^3}$, $R_c = 125\mu\mathrm{m}$, and $V = 2600$ volts shows that the R.H.S. of equation (3.2.12b) is nearly 5 orders of magnitude greater than μ. According to this criterion, the capillary LMIS is strongly space charge limited, as expected. This also explains the data shown in Figure 2.4[22] which shows that large changes in Z have virtually no effect on dI/dV for a capillary LMIS. It may be of interest to obtain the radius of a capillary which gives the same flow impedance as for a thin film flowing over a cylindrical

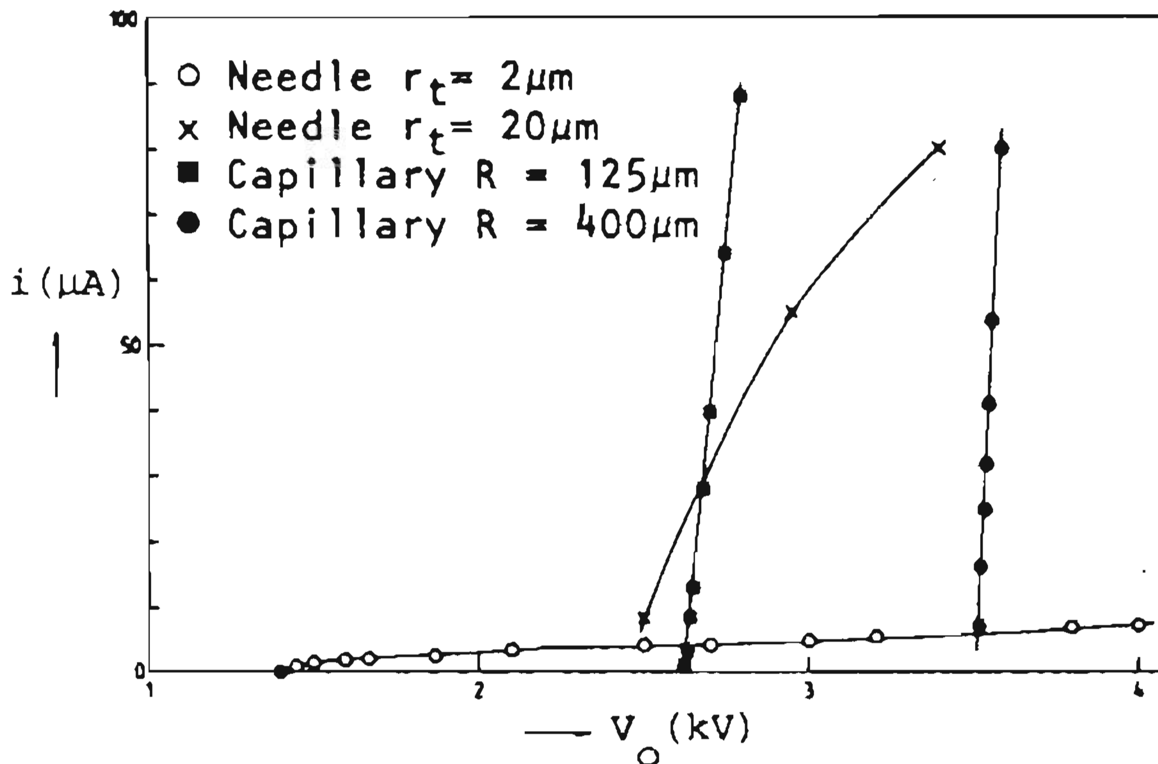

Figure 2.4 Behavior predicted by equation (3.2.12) in text that large changes in flow impedance (Z) will produce very small changes in dI/dV for a capillary type LMIS. Data is for a cesium. The needle substrates are nickel. This figure is obtained from Mair and Mulvey [22]

needle. Equating the Hagen-Poiseuille law for the capillary and (3.2.5) derived above for the needle LMIS we obtain:

$$R_c \approx 1.5t^{\frac{3}{4}} R_n^{\frac{1}{4}}$$

Substitution of $R_n = 0.005$ inches $= 127\mu m$ and $t = 500\text{Å}$ one finds that the R_c equals $0.5\mu m$. For $t = 1\ \mu m$, we obtain $R_c = 5\mu m$. This shows that perhaps only for capillary LMIS with radii smaller than $5.0\mu m$ will the current be flow limited. Any practical capillary LMIS probably has a radius much larger than this. This suggests that it may be possible to take advantage of some aspects of the capillary LMIS while maintaining a flow controlled current. For example, if such a small capillary LMIS can be fabricated, one might achieve the high degree of stable operation and reproducibility claimed for this type of ion source. "Aging" effects such as variations in film thickness and surface roughness during operation associated with the needle type LMIS could thus be avoided. The latter effects can produce marked changes in I(V) and angular intensity for a given extracted current. A relatively smaller liquid surface area would be accessible to backsputtered material thus avoiding additional instability.

2.3.3 Threshold Voltage

We now examine the condition at the threshold for ion emission. A complete theory of the threshold voltage for ion emission or extinction (V_{off} or V_{on}) must consider the approach to threshold i.e. as $I - I_{on}$ or $I - 0$ respectively. As V_{th} is approached, the parameters adjust themselves accordingly. A more complete understanding of LMIS operation requires a discussion of the approach to equilibrium from both directions. We do not attempt to discuss this here as this involves issues of the

stability of the electrically stressed liquid surface near the discontinuity. Unfortunately, such interesting and important questions lie outside the scope of the model. Precisely at the emission threshold, the current changes discontinuously from $I = 0$ to some finite value and discontinuously to zero as the emission is turned off. However, we see from the analysis that exactly at $I = 0$ equation (3.2.7) predicts:

$$V_{th} = \left(\frac{2d^2}{\alpha^2 \epsilon_0 A_B} (F_a + F_T) \right)^{\frac{1}{2}} \tag{3.3.1}$$

The surface tension force over the needle surface can now be calculated with the aid of Figure 2.5. We are interested in the longitudinal component of this force over the emitter. We assume that when there is no emission, the liquid film wets the substrate which is in the shape of a cylindrical needle topped by a conical section whose surface intersects a sphere at its tangents as illustrated in the figure. The radius of curvature of the needle apex is, by definition, the radius of the sphere. The total force is the sum of that on the conical portion and that over the spherical section. The surface tension stress is given generally as:

$$T = \gamma \left(\frac{1}{r_1} + \frac{1}{r_2} \right) \tag{3.3.2}$$

where r_1 and r_2 are the principle radii of curvature of the surface. The total force is obtained by integrating the surface tension over the surface and γ is the coefficient of surface tension. For the conical section this becomes:

$$F_z^{cone} = \int_{l_1}^{l_2} 2\pi\gamma \sin\beta \cos\beta \, dl$$

and we obtain

$$F_a^{cone} = 2\pi\gamma\cos\beta\left(\frac{D}{2} - r_0\cos\beta\right) \tag{3.3.3}$$

The longitudinal component of the surface tension force over the spherical section

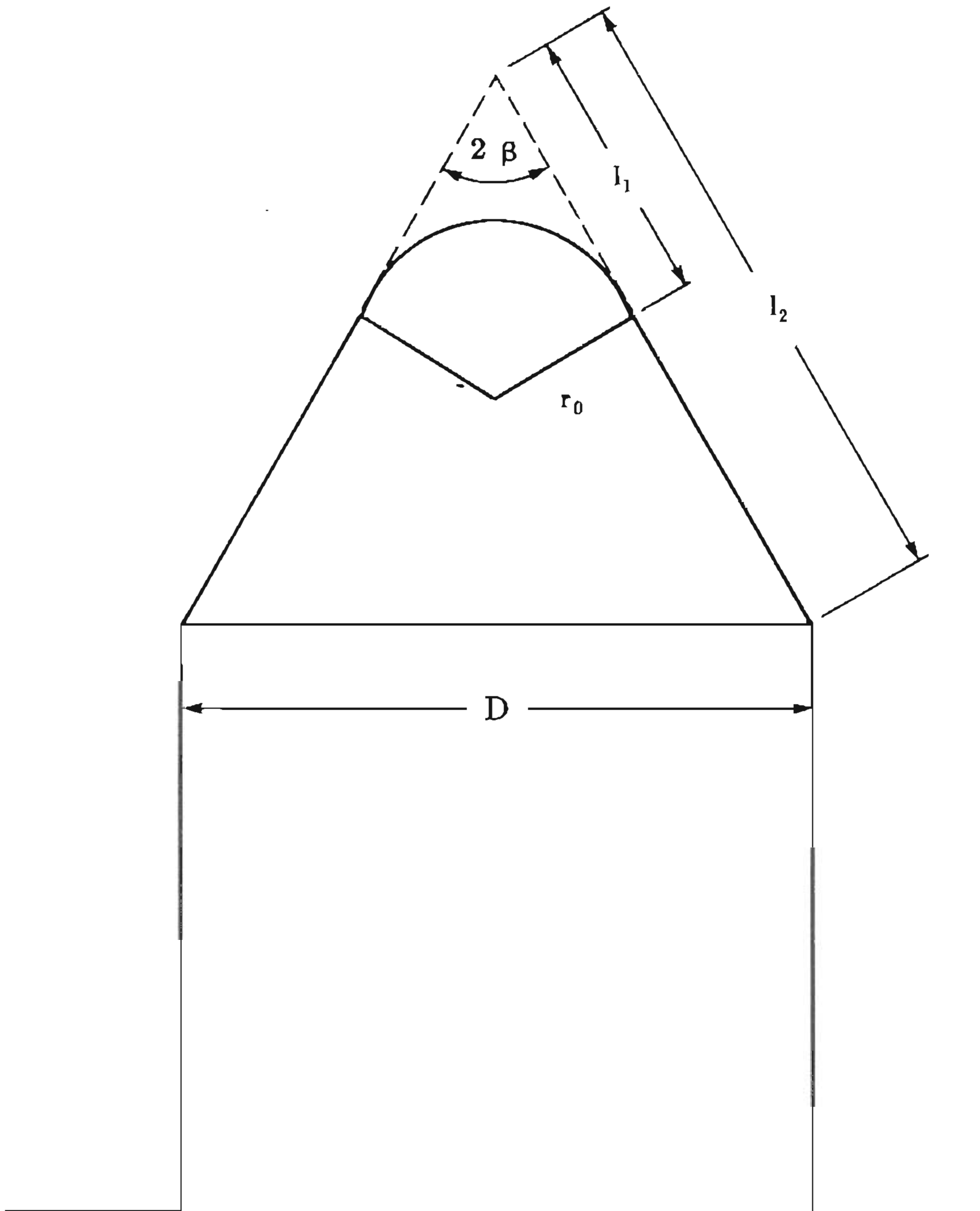

Figure 2.5 The surface tension force is calculated to obtain the threshold voltage derived in text. See Section 2.3.3.

alone is:

$$F_z^{sphere} = \int_0^{90-\beta} 4\pi\gamma r_0 \sin\phi \cos\phi \, d\phi$$

This results in:

$$F_z^{sphere} = 2\pi\gamma r_0 \cos^2\beta \qquad (3.3.4)$$

Therefore, the total longitudinal component of the surface tension force is:

$$F_z^{(1)} = F_z^{cone} + F_z^{sphere}$$

and we obtain:

$$F_z^{(1)} = D\pi\gamma\cos\beta \qquad (3.3.5a)$$

Making the same calculation for the full cone without a spherical cap (i.e. over l_2) yields also:

$$F_z^{(2)} = D\pi\gamma\cos\beta \qquad (3.3.5b)$$

Therefore, from the standpoint of equation (3.3.1), this suggests that the full cone and the partial cone capped by a spherical section are unstable shapes with respect to each other because they yield the identical threshold voltage:

$$V_{th} = \left(\frac{2d^2}{\alpha^2\epsilon_0 A_B}(F_a + D\pi\gamma\cos\beta)\right)^{\frac{1}{2}} \qquad (3.3.6)$$

(We have assumed that F_a and α change very little between the two shapes) We see immediately that there is no r_0 dependence on V_{th}. This may not be a realistic prediction for the needle type LMIS since Bell and Swanson[24] have observed that only for 49 ° cone angles there is essentially no dependence on r_0. Thus, one may speculate that for a needle LMIS, the liquid shape never approaches the shape described here i.e. the liquid never passes through the intermediate spherical shape illustrated in the figure before ion emission. On the other hand, the derivation may be more appropriate for the capillary and truncated cone type LMIS where a large liquid volume is free

and not constrained by the needle substrate. While this derivation does not carefully deal with the instability near threshold, it is at least consistent with the following observation of Mair and Thoms[42].

> With our capillary, as the voltage is raised, the liquid surface rises to a point where it forms an almost spherical section that merges with the sides of the truncated-cone-shaped upper part of the capillary; it is at this voltage that it becomes unstable and grows into a cone.

At OGC, we have also observed similar behavior for the solid truncated needle LMIS.

In our notation, we may re-write Taylor's expression for the threshold voltage[38] which was applied by him to the system illustrated in Figure 2.6

$$V_{th} = \left[\frac{4\pi d^2 \gamma D \cos\beta}{L^2} \left(\ln(\frac{4L}{d}) - 1.5 \right) \right]^{\frac{1}{2}} \tag{3.3.7}$$

and note the similarity to equation (3.3.6) derived here. One notable difference is the absence in our expression of the L^2 factor in the denominator. It is likely that both α and F_a in equation (3.3.6) depend on the distance of the needle apex to the collector plate but it is not possible to extract this dependence from the present model. Recalling that α gives some measure of the electric field strength at the collector, a large L would correspond to a large α. Without a detailed calculation, it is not possible to determine whether α and L are proportional.

2.3.4 Emission Area

If the emission area increases linearly with current, as suggested by Gomer's analysis[43] and the numerical analysis of Kingham and Swanson[26], one can write:

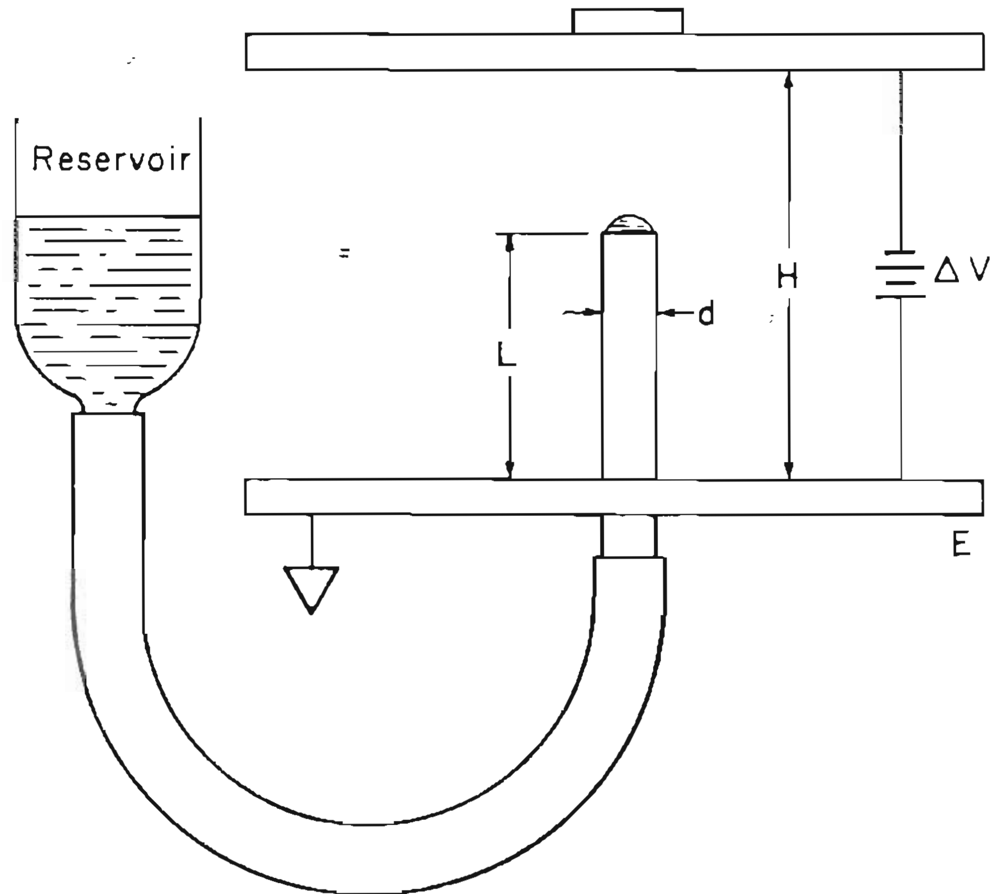

Figure 2.6 Apparatus used by G. I. Taylor to experimentally verify his predictions of the threshold voltage (equation (3.3.7)). The liquid level and fluid pressure could be adjusted by raising and lowering the reservoir.

$$\frac{A_e(V)}{A_e(V_{min})} = a(I - I_m) + 1$$

Equation (3) can then be written:

$$I = \frac{\eta V^{-\frac{1}{2}} \left(\frac{\Gamma}{\Gamma_m} V^2 - V_m^2 (1 - aI_m) \right) + \left(\frac{V_m}{V} \right)^{\frac{1}{2}} I_m (1 - aI_m)}{1 + aV^{-\frac{1}{2}} (\eta V_m^2 - I_m V_m^{\frac{1}{2}})} \tag{3.4.1}$$

From equation (3.0.6) and definition (3.0.8), one obtains the following expression for the emission area required by momentum conservation.

$$A_e(V) = \frac{2}{\epsilon_0 E_e^2} \left(\frac{2m}{q} \right)^{\frac{1}{2}} \left(\eta \frac{\Gamma}{\Gamma_m} V^2 - IV^{\frac{1}{2}} \right) \tag{3.4.2}$$

In order to calculate this, we require a value for η. Equation (3.4.1) could be fit to experimental I(V) data and an estimate for a can be obtained from Kingham and Swanson's paper[28] for a few metals. However, there still remains the ratio $\frac{\Gamma}{\Gamma_m}$ which unfortunately cannot be obtained directly from I(V) data alone. Interestingly, if we assume $\Gamma = 1$ is correct for a capillary LMIS as in the previous example from Mair and use equation (3.0.14) with $\kappa = 4$, the emission radius determined by (3.4.2) is extremely large. In fact, one finds that r_e lies in the range 0.3 to 0.5 μm, at least two orders of magnitude larger than expected. On the other hand, if one uses the data of Thompson and Prewett (still with $\frac{\Gamma}{\Gamma_m} = 1$)[38] for a flow dominated gallium needle LMIS, one finds emission radii in the range of hundreds of angstroms. This is still at least an order of magnitude larger than expected. However, we are probably not justified in our assumption that $\Gamma = 1$ since as pointed out before F_n may be quite large for a flow dominated LMIS i.e. Γ may be small. This would tend to

decrease r_e. A hundred fold decrease would be required if expression (3.4.2) is to yield a resonable emission area for the needle LMIS. For the capillary LMIS, a reduction of four orders of magnitude in Γ would be required. This seems unreasonable and at present an explanation can not be offered. A common trend appears to indicate that for capillary LMIS, the emission area as calculated by (3.4.2) is always much larger than that of the needle type LMIS. While there have been no experimental observations of the emission area for capillary LMIS, the predictions of (3.4.2) nonetheless are not in agreement with the concensus of opinion at this time and more analysis is needed to determine whether the model is more limited than was originally thought.

2.3.5 Discussion and Comments relating to I(V)

The numerical estimates following equations (3.2.9a) rely on the assumption that the film thickness, t, is independent of the current or voltage. However, it has been observed by Benassayag et al[31]. employing the 3 MeV HVTEM at Toulouse, France that as the current is increased, the flow enhancement arises from an increasing film thickness and a nearly constant film velocity at the surface. It should be noted that the relationships derived from equation (3.2.7) are independent of this assumption. Only the numerical estimates will be altered. For example, in equation (3.2.9) taking a film thickness $t = 1700\text{Å}$ shifts the control of the ion current from the nearly equal space charge and flow influences to one where space charge is more likely limiting the current.

In a practical needle LMIS, the film thickness is usually also a function of emitter length since a large reservoir of liquid metal is attached to the supply end of the needle by surface tension forces. Obviously, the film thickness is macroscopically

large near this end, perhaps of order 1 mm, and decreases dramatically towards the apex. Therefore, it is likely that needle LMIS which are otherwise identical will differ in their I(V) characteristic depending on the volume of metal in the reservoir and the needle length through the dependence on film thickness. From personal experience with many needle LMIS, it has frequently been observed that the identical needle substrate will give differing I(V) curves depending on the reservoir volume, giving a relatively shallow dI/dV if the needle has been wetted without additional metal being added to the reservoir. It is also frequently observed that warming an emitter briefly changes the I(V) even after the emitter has cooled to its initial temperature. This probably results from a redistribution of film on the substrate. These examples illustrate that changes in film thickness can alter the I(V) curve. This is commonly observed as the reservoir becomes depleted and the emitter gradually exhibits shallower dI/dV curves.

These considerations bring us back to the question of the flow and space charge influence on the current. Returning to equations (13), it may appear odd that these expressions are independent of the current and depend only on the potential difference, for any current. This occurs because both the viscous drag force and force due to the ion impact on the collector are directly proportional to the current, which drops out in a ratio of the two.

2.4 Energy Broadening in Particle Beams

Over the years there has been a great deal of theoretical and experimental interest in the spread of the energy distribution of charged particle beams. The so-called Boersch effect[44] has been studied experimentally and theoretically for many

years. Analytical expressions have been obtained for the energy broadening, ΔE, Monte Carlo simulations have also been performed to obtain the current, mass and charge dependence of the energy broadening[45,46]. Two regions of particular interest are the emission area in the vicinity of point source emitters and the crossover region in optical focusing columns. The analytical treatments typically require different physical assumptions; the region around a point emitter consists of diverging particle trajectories and has been considered to be collision free since the particles have essentially no chance of crossing paths[47]. In the vicinity of the crossover, many ray crossings are likely. A different dependence of ΔE on current is claimed for these two regions. In any case, stochastic Coulomb interactions are thought to be responsible for the broadening[33,45,48-51]. Recently, attention has been focused on the practical need to produce high resolution ion beams from liquid metal ion sources (LMIS) and liquid alloy ion sources (LAIS). Surface analysis by SIMS[52,53], ion imaging[54], lithography[55-58], implantation of dopants in semiconductors[59], and the creation of optical structures by focused ion beam micromachining has been demonstrated. (see Chapter 6)[60,61]

In all applications of focused ion (and electron) beams, the performance, in many respects, rests on the ultimate current density and resolution or "spot size". In a focusing optical column the spot diameter is given by:

$$d^2 = M^2 \left[\delta^2 + \left(\frac{C_s \alpha_o^3}{2} \right)^2 + \left(C_c \alpha_o \frac{\Delta E}{E} \right)^2 \right] \tag{4.0.1}$$

where δ is the virtual source size, C_s and C_c are the spherical and chromatic aberration coefficients, M the lens magnification and E is the beam energy. We note, in passing, that A. V. Crewe has called into question the validity of combining the indi-

vidual contributions in quadrature as above[62]. The virtual source size has been found to be only slightly dependent on the ion mass and emitted current[21] but ΔE depends strongly on the current. Even though the total extracted current may be kept low, the spot diameter is usually limited by the chromatic contribution. For a focusing column using a LMIS, Swanson has shown[20] that the current density in the focused spot can be written:

$$J = 4\left(\frac{V}{MC_c}\right)^2 \frac{I'}{\Delta E^2}$$

where C_c and M are the chromatic aberration coefficient referred to the object side of the lens and the magnification, respectively. Thus, we see the importance of understanding the origin of the energy broadening for both fundamental and practical reasons.

2.4.1 Dimensional Analysis and Energy Broadening Expressions

We now present a simple analysis of energy broadening expressions which is independent of the specific requirements of particular models. This enables us to explore the relationship amongst the various physical parameters typically appearing in such models.

If we assume that the energy spread due to coulomb interactions is a function of a length l, potential V, beam current I, particle mass m and the charge q, then $\Delta E = f(l, V, I, m, q)$ can be written as the product of powers of the above parameters as follows:

$$\Delta E = C l^{\alpha} V^{\beta} I^{\delta} m^{\epsilon} q^{\iota} k^{\gamma} \tag{4.1.1}$$

with C a constant and $k = \frac{1}{4\pi\epsilon_0}$ where ϵ_0 is the permittivity of free space.

In order to express all quantities in dimensions of mass , length, and time, the following relations are used:

$$F = Eq = kq^2l^{-2} \tag{4.1.2a}$$

and

$$V = El \tag{4.1.2b}$$

where F has dimensions of force and E has dimensions of electric field. Finally, to express the charge q, in terms of time t, we use an energy relationship

$$ml^2t^{-2} = kq^2l^{-1} \tag{4.1.2c}$$

We then obtain:

$$V = m^{\frac{1}{2}}l^{\frac{1}{2}}k^{\frac{1}{2}}t^{-1} \qquad I = m^{\frac{1}{2}}l^{\frac{3}{2}}k^{-\frac{1}{2}}t^{-2} \qquad q = m^{\frac{1}{2}}l^{\frac{3}{2}}k^{-\frac{1}{2}}t^{-1}$$

Substituting these relations into equation (2.0.1) results in the following algebraic equations:

$$\frac{\beta}{2} + \frac{\delta}{2} + \frac{\iota}{2} + \epsilon = 1 \tag{4.1.3a}$$

$$\alpha + \frac{\beta}{2} + 3\frac{\delta}{2} + 3\frac{\iota}{2} = 2 \tag{4.1.3b}$$

$$\beta + 2\delta + \iota = 2 \tag{4.1.3c}$$

$$\frac{\beta}{2} - \frac{\delta}{2} - \frac{\iota}{2} + \gamma = 0 \tag{4.1.3d}$$

From (2a) and (2c), we find $\epsilon = \frac{\delta}{2}$ which means that one must always obtain the functional dependence

$$\Delta E = C' \left(Im^{\frac{1}{2}} \right)^{\delta}$$

regardless of the dependence on the other parameters.

It is interesting to note that in the LMIS literature, plots of (ΔE) versus $Im^{\frac{1}{2}}$ on a log-log scale are frequently observed. The statement is sometimes made that a particular theoretical model is supported by the goodness of fit of the experimental and theoretical plots. We have just seen however, that all theoretical models must fall on such a line with slope δ. Therefore, such a plot really indicates the validity of the experimental data and does not support a particular model. Unfortunately, the experimental points have sufficient scatter that a unique value for δ cannot be found.

Solving for the other exponents, one finds that the energy spread can be written:

$$(\Delta E)_{MKS} = Ck^{\gamma}l^{2\epsilon-\gamma}V^{1-\epsilon-\gamma}(Im^{\frac{1}{2}})^{2\epsilon}q^{1-3\epsilon+\gamma} \tag{4.1.4a}$$

The exponents ϵ and γ can take any values. This can also be written in a more convenient form:

$$(\Delta E)_{CGS} = Cl^{2\epsilon}V^{1-\epsilon}(Im^{\frac{1}{2}})^{2\epsilon}q^{1-3\epsilon}\left(\frac{q}{lV}\right)^{\gamma} \tag{4.1.4b}$$

where for CGS units, $k = 1$ and the dimensionless quantity $\left(\frac{q}{lV}\right)^{\gamma}$ has been factored out. It is clear that only two parameters are required to determine the functional dependence of ΔE.

A recent paper presents a model of energy broadening based on Poisson emission of ions or electrons from a spherical emitter and employs classical statistical arguments to derive the functional form of the the energy spread[51]. The expression obtained has the general form (in the authors' notation)

$$<\Delta E> = \left(I^2m\right)^{\alpha}V_0^{h(\alpha)}G(\alpha) \tag{4.1.5}$$

where $h(\alpha)$ is a function of α and $G(\alpha)$ is a product of geometrical factors. The statement is made that varying α results in a " rather interesting unification of energy broadening theories ". Actually, this occurs only after varying both α and $G(\alpha)$ appropriately (Recall from equation (24) that two parameters can be varied independently). However, such a unification is only apparent and varying α does not represent physical field - geometrical effects as claimed. The nature of expression (4.1.5) is identical to that of equation (24) which correctly " predicts " the functional dependence of all conceivable energy spread models of a form given by equation (4.1.1). This is true merely because it is required for dimensional consistency regardless of the physical assumptions of a particular model. While a physical model may be used to determine the values of ϵ and γ (and thereby, the functional dependence on the other parameters), there is no unifying physical principle involved in establishing equation (24). Finally, equation (24) is useful for checking the dimensions of theoretical energy spread expressions, since working directly with MKS or CGS units can often be confusing and is error prone, especially when fractional exponents are encountered.

2.5 Summary and Conclusions

Some theoretical aspects of liquid metal ion sources have been explored. A model of the I(V) characteristic for the LMIS has been developed based on conservation of momentum in a closed system containing the emitter, collector and the transported current. This provides a physically intuitive approach which, for the first time, unifies the treatment of the space charge and flow dominated operation of the LMIS. The model thus clarifies some aspects of the relationship between flow

impedance and space charge control of the ion current. For example, contrary to the commonly accepted view, it is not the flow impedance per se which influences I(V) as is frequently stated in the literature. Rather, it is the product of a film thickness and the flow impedance which controls I(V), notwithstanding the fact that the flow impedance itself is a function of film thickness. This distinction may not be of practical importance when comparing the capillary and needle type LMIS, for example. However, for comparison of needle type LMIS it may be useful to note the distinction. Regardless of its practical significance, we see that the correct view has not been noted previously.

The point of view expressed in this analysis is that it is the difference in the Maxwell stress between emitter and collector which provides the driving force for the current. This is an alternative to the generally accepted (and correct) statement that the current is driven by the difference between the electric and surface tension stresses at the emitter. The present approach avoids the requirement of treating the space charge and the liquid metal flow as separate problems and enables us to see where the limitations in the standard treatments come from. Any I(V) model for space charge dominated currents, i.e. those entirely neglecting liquid flow, is concerned only with the transport of charge from the emission area to the collector. The necessity of supplying fluid to the emission area is irrelevant. In contrast, any model of flow controlled currents is concerned only with the supply of material to the emission area. Once it is reaches that point, the liquid is assumed to become ionized and further requirements of transport to the collector are ignored. On the other hand, the analysis presented in this thesis considers the entire problem of the flow of matter to the emission area and then to the collector. Furthermore, utilizing the present perspective it has been possible to obtain a general criterion for establishing the space

charge or flow dominance for a LMIS emitter. This novel relationship compares the viscous drag over the needle with the force of the ion current against the extraction electrode.

Finally, the fundamental nature of the model allows simple derivations of the Child-Langmuir Law and the Stern-Gossling-Fowler result which, surprisingly, do not directly utilize the Poisson equation as do standard treatments of space charge problems.

Some simple dimensional arguments have been used to examine energy broadening expressions. The physically relevant parameters were expressed in the form of a power law which shows that the functional dependence $\Delta E = C' \left(I m^{\frac{1}{2}} \right)^{\delta}$ is required. A general expression for ΔE was obtained which is useful for checking the dimensions of energy spread models of charged particle beams.

The foregoing analysis indicates that it is useful to perform a dimensional analysis on any quantity of physical interest to separate the truly physical dependencies of a given model from those which are merely required for dimensional consistency.

2.6 Appendices

2.6.1 Appendix 2a: Poisson Equation

Conventionally, one begins the examination of space charge problems with the Poisson equation:

$$\nabla^2 V = -\frac{\rho}{\epsilon_0} \tag{A1}$$

where V is the potential in space and ρ is the charge density. The analysis presented in this paper, on the other hand, begins with equation (2.0.1). From a mechanical point of view this equation is easy to understand but the relation to the Poisson equation is not obvious. These two approaches must certainly be related and are examined here briefly.

The motivation for the present approach comes from Jackson's treatment of the conservation of momentum for a system of charged particles and electromagnetic fields[63] (although written there in CGS units) and his statement that:

> (Equation 0) can therefore be used to calculate the forces acting on material objects in electromagnetic fields by enclosing the objects with a boundary surface S and adding up the total electromagnetic force according to the right-hand side of (equation 0).

As shown by Jackson, the Maxwell stress tensor T_{ij} and equation (2.0.0) arise naturally after substituting the Poisson equation into the expression for the mechanical momentum. This eliminates the charge density and results directly in the expression for the stress tensor. Finally, writing the conservation of momentum for the system gives equation (2.0.0). Writing equation (0) for the closed system of parallel

plane diode and the current within it yields equation (2.0.1). As pointed out in the present analysis, this equation has a simple physical interpretation.

We see then that the Poisson equation is implicitly contained in equation (2.0.0) and one should not be entirely surprised that the approach taken here leads to relations usually obtained via the Poisson equation. It is perhaps somewhat more surprising that this has not been previously exploited.

For the sake of comparison, we now give the standard derivation of the Child-Langmuir relation. The new method is applied to this relation in Appendix 2b. In one dimension we may write:

$$\frac{d^2V}{dx^2} = -\frac{\rho}{\epsilon_0}$$

Assuming an electron with zero initial velocity we have:

$$v(x) = \left(\frac{2eV(x)}{m}\right)^{\frac{1}{2}}$$

Since $J = \rho v(x)$ and eliminating ρ from the Poisson equation, we have:

$$\frac{d^2V}{dx^2} = \frac{J}{\epsilon_0}\left(\frac{m}{2eV}\right)^{\frac{1}{2}}$$

Multiplying both sides by $2\frac{dV}{dx}$ and integrating gives:

$$\left(\frac{dV}{dx}\right)^2 = 4\frac{J}{\epsilon_0}V^{\frac{1}{2}}\left(\frac{m}{2e}\right)^{\frac{1}{2}} + C_1$$

Now if we assume that the field is zero at the cathode, as in the classical treatment, then $C_1 = 0$. Therefore, we can write:

$$V^{-\frac{1}{4}}dV = 2\left(\frac{J}{\epsilon_0}\right)^{\frac{1}{2}}\left(\frac{m}{2e}\right)^{\frac{1}{4}}dx + C_2$$

Integrating once more and noting that $V = 0$ at $x = 0$ implies $C_2 = 0$ gives finally:

$$V = (\frac{3d}{2})^{\frac{4}{3}} (\frac{J}{\epsilon_0})^{\frac{2}{3}} (\frac{m}{2e})^{\frac{1}{3}}$$

which can be rewritten in its standard form given in Appendix 2b as equation B1.3.

2.6.2 Appendix 2b: Child-Langmuir Law

Writing equation (2.0.1) for the parallel plate diode, and dividing by the common plate area, we obtain:

$$\frac{\epsilon_0}{2}E_A^2 + J_0\left(\frac{2mV}{e}\right)^{\frac{1}{2}} - \frac{\epsilon_0}{2}E_B^2 = 0 \tag{B1.1}$$

where J_0 is the current density.

The Child-Langmuir law for a space charge limited current, for the case in which there is no initial particle velocity, is easily derived from equation A1. Employing the classical argument that for a completely space charge limited current the field at the emitter must be equal to zero gives:

$$J_0\left(\frac{2mV}{e}\right)^{\frac{1}{2}} = \frac{\epsilon_0}{2}E_B^2 \tag{B1.2}$$

Substituting $E = -\frac{\partial V}{\partial x}$ into equation (B1.2) and integrating directly yields the Child-Langmuir equation:

$$J_0 = 4\frac{\epsilon_0}{9}\left(2\frac{e}{m}\right)^{\frac{1}{2}}\frac{V^{\frac{3}{2}}}{d^2} \tag{B1.3}$$

Comparison with the standard derivation shows that beginning with equation (2.0.1) rather than the Poisson equation saves one integration step. Additionally, it affords a more physically intuitive " feel " since it directly involves forces and not charge densities.

An important point regarding the present derivation of the I(V) curves for LMIS should be noted. An algebraic solution of equation (2.0.1) has been employed i.e. it has not been integrated in a manner analogous to that above. However, this will not

result in qualitative differences from the " exact " solution. The functional form will clearly be the same. Quantitatively, the constant η would be different, but η may be regarded as an experimental parameter. In this sense, equation (3.0.7) may be considered exact.

Although equation (2.0.1) has been written for plane parallel electrodes, the essential principle used in establishing it holds for any geometry. To the extent that the forces exerted on the electrodes can be evaluated, equation (2.0.1) should result in useful expressions.

2.6.3 Appendix 2c: Result of Stern, Gossling, Fowler[37]

We begin again with equation (2.0.1):

$$\left(\frac{\epsilon_0}{2}E_0^2 + 2J_0\left(\frac{m}{2e}\right)^{\frac{1}{2}}V^{\frac{1}{2}}\right)^{\frac{1}{2}} = \left(\frac{\epsilon_0}{2}\right)^{\frac{1}{2}}\frac{\partial V}{\partial x} \tag{B2.1}$$

Once this equation is written, the development is identical to that beginning with the Poisson equation.

$$\int dx = \left(\frac{\epsilon_0}{2}\right)^{\frac{1}{2}}\int\left(b + AV^{\frac{1}{2}}\right)^{-\frac{1}{2}}dV$$

where $b \equiv \frac{\epsilon_0}{2}E_0^2$ and $A \equiv 2J_0\left(\frac{m}{2e}\right)^{\frac{1}{2}}$

Now substituting:

$$y \equiv b + AV^{\frac{1}{2}}: \quad dy \equiv \frac{1}{2}AV^{-\frac{1}{2}}dV: \quad dV = \frac{2}{A^2}(y - b)dy$$

yields:

$$x = \left(\frac{\epsilon_0}{2}\right)^{\frac{1}{2}}\int y^{-\frac{1}{2}}(y - b)dy = \frac{2}{A^2}\left(\frac{2}{3}y^{\frac{3}{2}} - 2by^{\frac{1}{2}} + C\right)$$

Employing the boundary conditions:

$$x = 0\,,\, V = 0$$
$$x = d\,,\, V = V_0$$

gives for the constant $C = \frac{4}{3}b^{\frac{3}{2}}$ and

$$d = \frac{2^{\frac{1}{2}}\epsilon_0^{\frac{1}{2}}b^{\frac{3}{2}}}{A^2}\left[\frac{1}{2}\left(1+\frac{AV_0^{\frac{1}{2}}}{b}\right)^{\frac{3}{2}} - \frac{3}{2}\left(1+\frac{AV_0^{\frac{1}{2}}}{b}\right)^{\frac{1}{2}} + 1\right]$$

If we define γ as :

$$\gamma = \frac{AV_0^{\frac{1}{2}}}{3b}$$

we finally obtain:

$$\frac{E_0}{F_0} = \frac{8}{27\gamma^2}\left[1 + \left(1+3\gamma\right)^{\frac{1}{2}}\left(3\frac{\gamma}{2} - 1\right)\right]$$

where

$$\gamma^2 \equiv \frac{16J_0^2\left(\frac{m}{2e}\right)V_0}{9\epsilon_0^2E_0^4}$$

and $F_0 \equiv \dfrac{V}{d}$ is the field at plate A with no space charge present and E_0 is the space charge field.

3. THE GALLIUM LIQUID METAL ION SOURCE

3.1 Introduction

The heart of any LMIS FIB system is, of course, the ion source itself. The LMIS is typically found in one of three basic configurations; the needle, the capillary, and the needle in the capillary forms, the latter being essentially a needle protruding from a capillary filled with the liquid metal. For operation in an optical column, the most widely used variety is probably the needle type LMIS. This consists essentially of a needle substrate, spot welded to a loop of wire which is supported on a base. Figure 3.1 shows a LMIS wetted with gallium. The substrate needle is molybdenum which is spot welded to a tungsten filament loop. The orientation of the needle is along the optical axis of the optical column and is coated with a metal or alloy which must be heated by some means. This is usually done by direct ohmic heating of the supporting wire loop but electron beam heating has also been used[64]. Undoubtedly, the simplest such source is that fabricated for gallium. It is relatively easy to fabricate and if operated in good vacuum and kept uncontaminated, can provide stable beams with a lifetime limited only by the volume of metal in the reservoir and the total current extracted. Several hundred hours of operation have been routinely obtained from such sources fabricated at OGC.

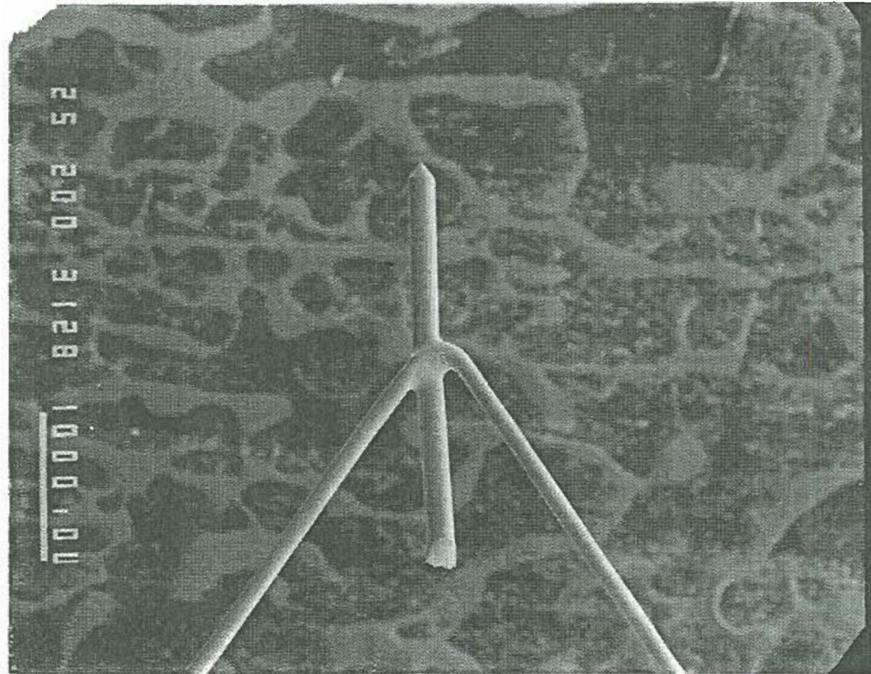

Figure 3.1 SEM micrograph of molybdenum LMIS spot welded to W filament loop at low magnification.

3.2 Fabrication of the LMIS

Most of the experience at OGC in FIB applications has been gained with the needle type gallium LMIS. There are two techniques employed to fabricate the substrate needles for these types of sources; mechanical grinding and electrochemical etching. The mechanical grinding technique for W substrates generally results in more reproducible needle forms than etching. The substrate usually employed for gallium LMIS is tungsten but some experiments were performed to examine other materials for gallium LMIS and are described in this chapter. Figure 3.2 shows a mechanically ground Mo emitter. This technique was developed at FEI, Inc. presently located at the Oregon Graduate Center Science Park and at OGC precisely because it was appreciated that the needle geometry could play a significant role in the angular intensity and the current-voltage characteristic of the LMIS. This has been elaborated in study of the influence of the emitter geometry made recently by Bell and Swanson[24]. Nevertheless, the electrochemically etched variety is still often fabricated and gives satisfactory performance. Recent interest in LMIS STM requires emitters with much smaller tip radii ($1 \mu m$ or smaller) than necessary for the standard needle LMIS and have also been fabricated by electrochemical etching. Furthermore, the mechanically ground LMIS emitters are often " blunted back " electrochemically to produce a somewhat larger radius tip than is possible by grinding.

3.2.1 Cleaning the tungsten wire substrate

A polycrystalline tungsten wire 0.005 - 0.007 inches in diameter is electrochemically cleaned in NaOH to remove lubricants which fill the grooves created when the wire is drawn through dies during its manufacture. Figure 3.3a shows a mechanically

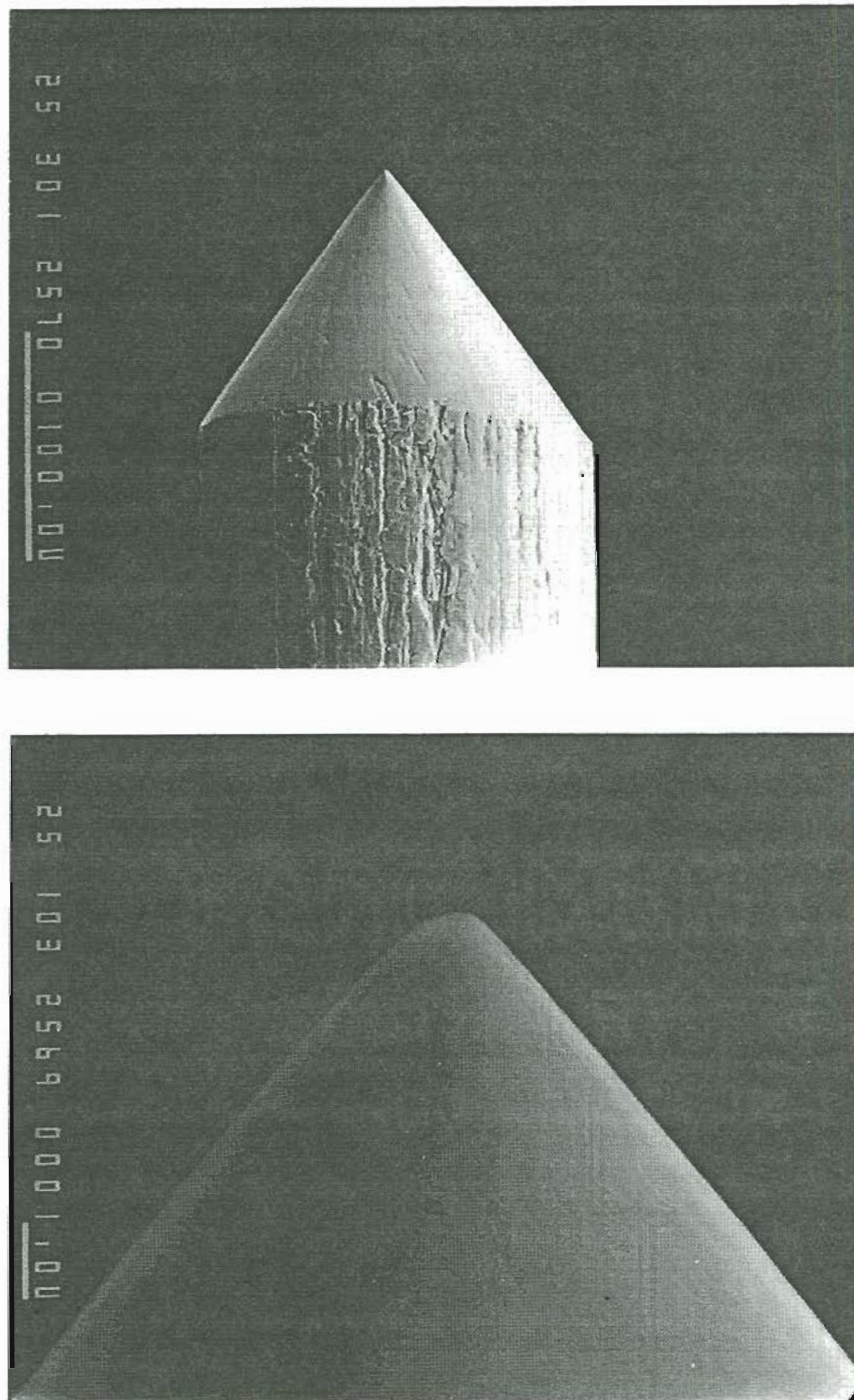

Figure 3.2 (a) SEM micrograph of mechanically ground Mo emitter (b) Higher magnification view of conical section. Tip radius $r_t = 1\ \mu m$

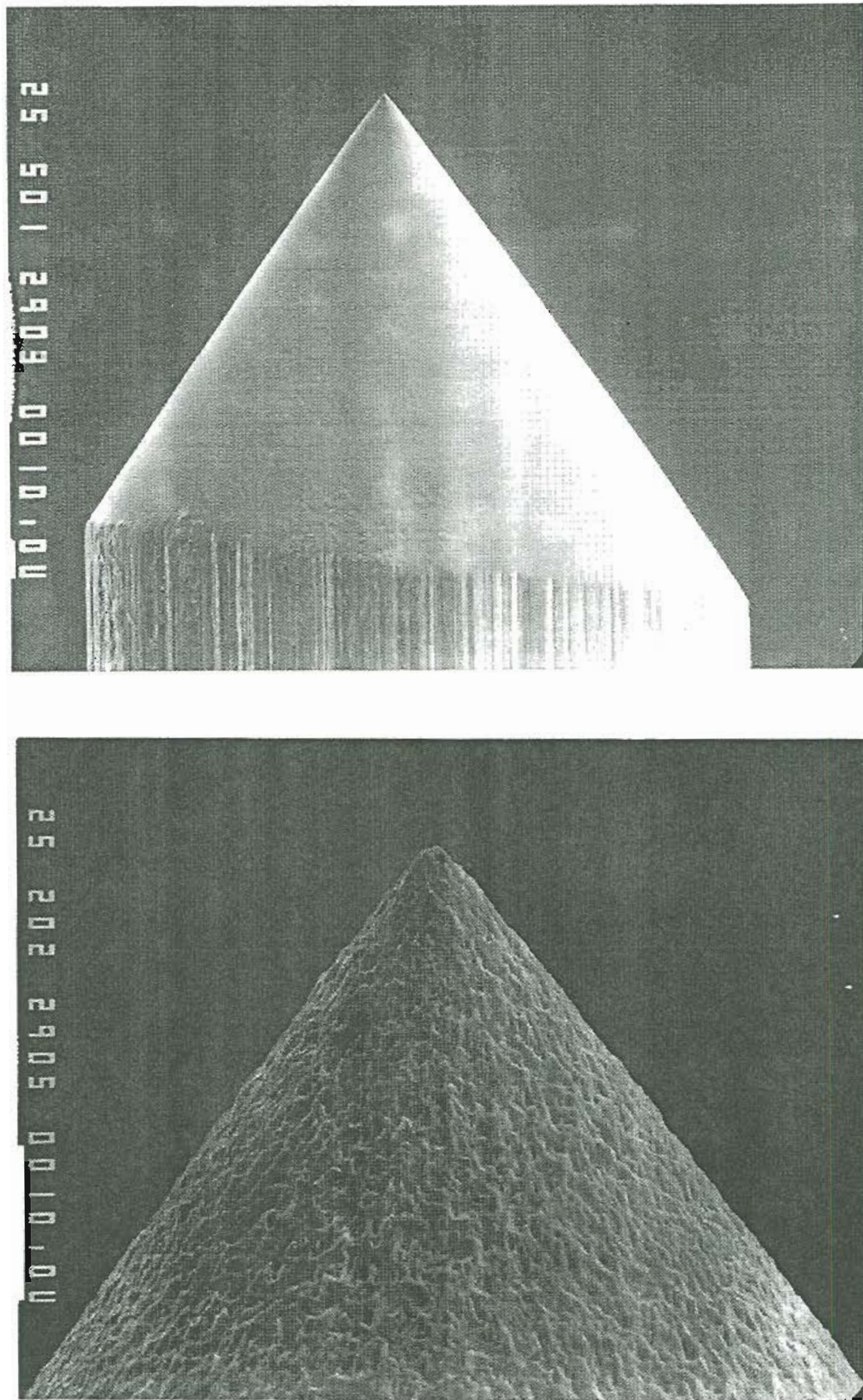

Figure 3.3 (a) Upper: SEM micrograph of mechanically ground W emitter (b) Lower: Conical surface roughened electrochemically.

ground W emitter with a smooth cone. The grooves are visible along the emitter shank below. This grooving is a fortunate "accident" which, through capillary action, assists the liquid flow during operation of the source. Therefore, the cleaning is a crucial step which is sometimes inadvertently omitted because the substrate may appear visibly clean in an optical microscope. This frequently results in emitters which run for a short while (10 hours or less) and then inexplicably exhibit problems. When emitters follow this behaviour, contamination of the grooves should be suspected. To clean them, the gallium is first removed chemically by immersing the entire emitter in NaOH or briefly in HF. The HF does not attack W appreciably but the ceramic or glass (Macor) emitter base is quickly attacked by it. Of course, the gallium may also be removed by evaporation in the vacuum system which has the additional benefit of increasing the surface roughness (see Section 3.2.2). With all the gallium removed, the entire length of wire, including the loop, is immersed in the NaOH and low voltage pulses (5 volts a.c. of half-second duration or so) are applied via a momentary switch (usually a telegraph key) between the wire and another electrode immersed in the liquid. It is convenient to use tungsten for this electrode also. Particles of the lubricant are ejected from the grooves and fall through the liquid.

3.2.2 Etching the tungsten wire

The etching of the W wire into an emitter end form is done in a 2N NaOH solution and can produce forms which are either "paraboloidal" or "cusp" shaped. Three techniques are often used. They are generally known as the A.C. intermittent polishing technique, the A.C. self-termination technique and the D.C. drop off technique.

The one described here has been developed during the course of this thesis research and differs slightly from others.

Tungsten wire which has been mechanically cut with specially hardened tungsten cutting pliers sometimes cracks near the cut end. If the split end is not removed the etching process tends to propagate the crack along the wire length resulting in a forklike wire unsuitable for use as a LMIS. To remove the cracked portion, a D.C. etching procedure is used. This is also somewhat different than the standard technique. A short section of the cracked wire is immersed in the NaOH solution to a depth less than the crack length itself. With positive polarity on the emitter wire, a voltage of 35 - 40 volts D.C. is applied. It is not necessary to pulse the voltage for the procedure, as the cutting of the wire terminates the process. The liquid meniscus is repelled and results in "cut" ends which are essentially flat or somewhat rounded. The shorter the immersed portion, the less violent is the process resulting in a more symmetrical cut off shape.

The power supply is then switched to A.C. and a technique which may be called a modified A.C. self-termination process is used. In the standard technique, the wire is etched at 7 volts A.C. or so and the wetting surface moves down the wire as the conical portion of the tip is being formed. The etching stops at the liquid surface and the resulting shape depends on how much of the wire is immersed in the liquid. Etching longer lengths of wire produces sharper tips with smaller cone angles.

The modification consists simply of physically moving the liquid level up and down with the voltage applied. This results in a variety of controllable shapes and tip radii (see Figure 3.4). Additionally, it is routinely possible, although it requires care, to control the cone angle. This can be achieved if a stable vibration free support and manipulator is available. The liquid containing vessel is merely moved up

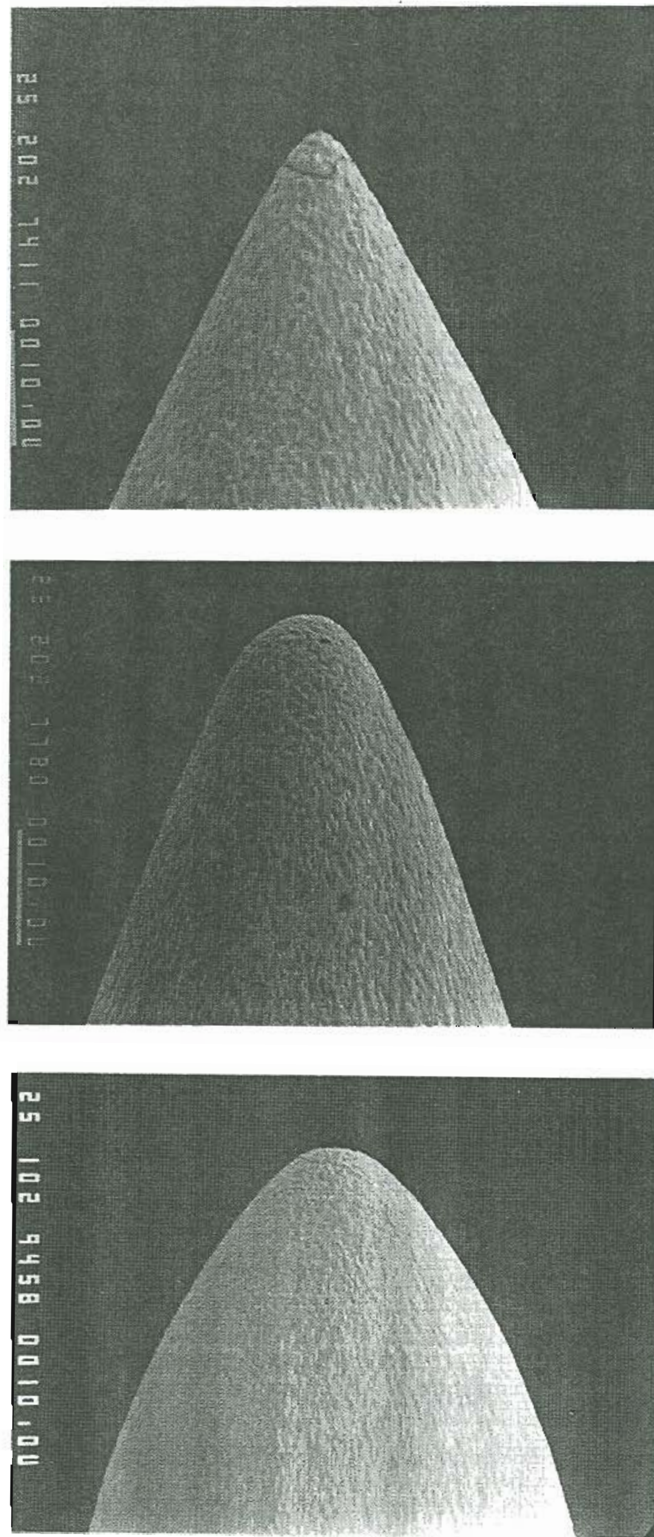

Figure 3.4 SEM micrograph of three electrochemically etched and roughened W substrates. Note the large range of tip radii and cone angle possible. Upper: $r_t = 2.3$ μm Middle: $r_t = 5$ μm Lower $r_t = 25$ μm.

to immerse any portion of the wire. Then with the voltage applied the liquid vessel is simultaneously lowered. In this manner, essentially any cone angle may be achieved. It is possible to restrict the etching to only the final 3 or 4 mils of wire. Unfortunately, it seems that the tip radius and cone angle can not be varied independently e.g. large cone angle and small tip radius are unattainable and conversely. This appears to be independent of the particular technique employed.

To ensure adequate liquid metal flow along the etched tapered conical form, it's surface must be roughened. This is an essential aspect of emitter fabrication. Only the "conical" portion of the needle is immersed in the NaOH and low voltage (less than 1 volt a.c.) is applied for 10 seconds or so. The voltage may be pulsed so the degree of roughening with time may be observed but this is not essential. The degree of surface roughening depends on the concentration of the NaOH which has been taken as 2N for the above descriptions. For 1N NaOH, almost no roughening occurs.

3.2.2.1 " Blunting back " the emitter

When emitters are produced either by grinding or etching which are too sharp their apex radius must be enlarged. This so-called " blunting back " procedure can only be done by etching. The method developed during this research is slightly different than more standard methods and consists essentially of the cut off process described in Section 2.2 followed by a re-etching and roughening of the cut-off apex. An important distinction lies in the fact that the usual cut-off procedure begins with a piece of wire while the blunting process begins with a formed emitter in which a considerable investment in time and effort has been made. Therefore, great care is required. As in the method of Section 2.2, the D.C. voltage is 35 - 40 volts, with the

emitter positive. However, the voltage is turned on *before* the liquid level is raised. As the emitter touches the liquid surface the liquid is repelled and produces the blunting. Figures 3.5 show the same emitter before and after the procedure.

3.2.3 Substrates other than tungsten

As the wetting of gallium with the substrate is key to its stable performance, several other materials were examined for their suitability. Based on the fact that some chemical reactivity would enhance wetting, molybdenum, a 50-50 at.% molybdenum/rhenium alloy and tantalum were examined. With one exception, only qualitative observations were made.

3.2.3.1 Molybdenum

A ground and polished Mo wire was used. No electrochemical cleaning, etching or roughening was done. (In any case, NaOH is not the most suitable for this purpose since a dark brown "slimy" film forms on the emitter. The film is easily removed but is a small nuisance.) The emitter was flashed quickly to white heat. After approximately one minute at a pressure $P \simeq 2 \times 10^{-7}$ torr, it was found that gallium will still wet the Mo. This is in contrast to Ga/W wetting described later which requires the emitter to be hot when immersed into the liquid. After waiting longer than this at this pressure however, the Mo would no longer wet. This is a consistent and reproducible result.

If a Mo emitter with gallium on it is heated to a dull red color (estimated to be 700 - 800 °C) in an interesting reaction results. Under a low power microscope (30X) the surface takes on a " matte " finish and self-roughening is evident. With a gallium

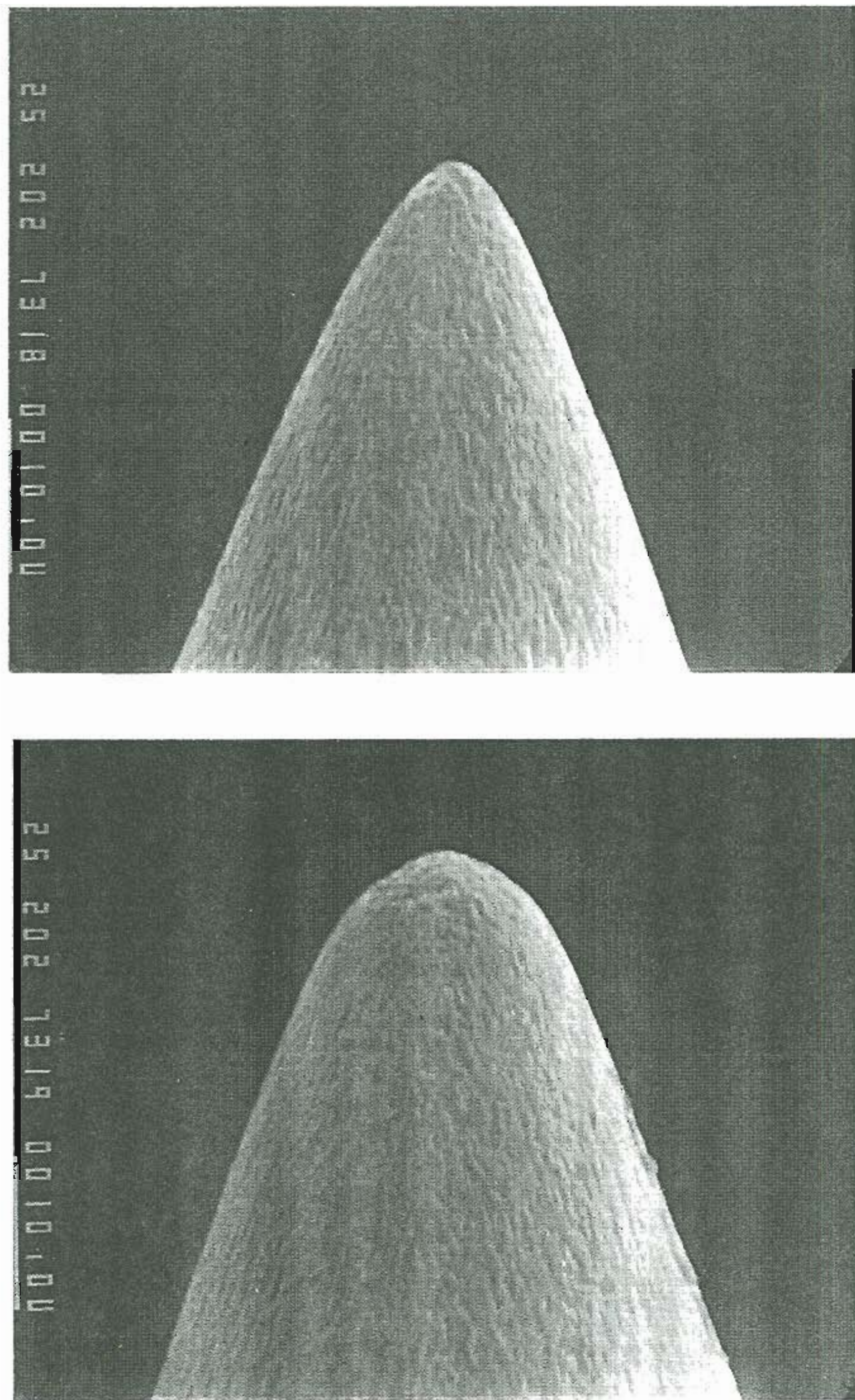

Figure 3.5 SEM micrograph of etched and roughened W emitter before (upper) and after (lower) electrochemical blunting.

film on the wire, after an initial wetting, there is a temperature, T_L, at which the gallium is *absorbed into* the wire. This occurs either by moving into pores created during the wetting or by creating new pores (or both). This is remarkable to observe and can easily be mistaken as evaporation the first time it is seen. The emitter surface appears dry as all the liquid has soaked in. At T_L, the emitter will soak up additional gallium in a spongelike manner if it is immersed into the liquid. At a higher temperature, T_H, the gallium moves back to the surface leaving it shiny as if freshly wetted. This process seems to be reversible initially although with continued cycling between T_L and T_H the temperature at which this occurs becomes higher as more Mo disolves into the Ga. The initial temperatures T_L and T_H were estimated by assuming the emissivity of Mo and W are similar and measuring T with an optical pyrometer. We then find $T_L = 600°C$ and $T_H = 875°C$. Loading an emitter with gallium at T_L and cycling between T_L and T_H caused the spot weld to fail and resulted in the swollen emitter depicted in Figure 3.6.

Without heating, the Ga/Mo emitter ran stably in the test chamber for 10 minute periods and occasionally for as long as 20 minutes. It required heating to restart it. In the ion gun, the emitter (see Figure 3.7) ran stably but turned off frequently without heating. With a small heating current of $\sim 3/4$ ampere, the emitter ran very stably for several hours with no noticeable drift. In the long run, Mo wil probably not be suitable as a substrate for gallium LMIS due to its high reactivity. Nevertheless, its wetting properties are quite remarkable.

3.2.3.2 Molybdenum/Rhenium alloy

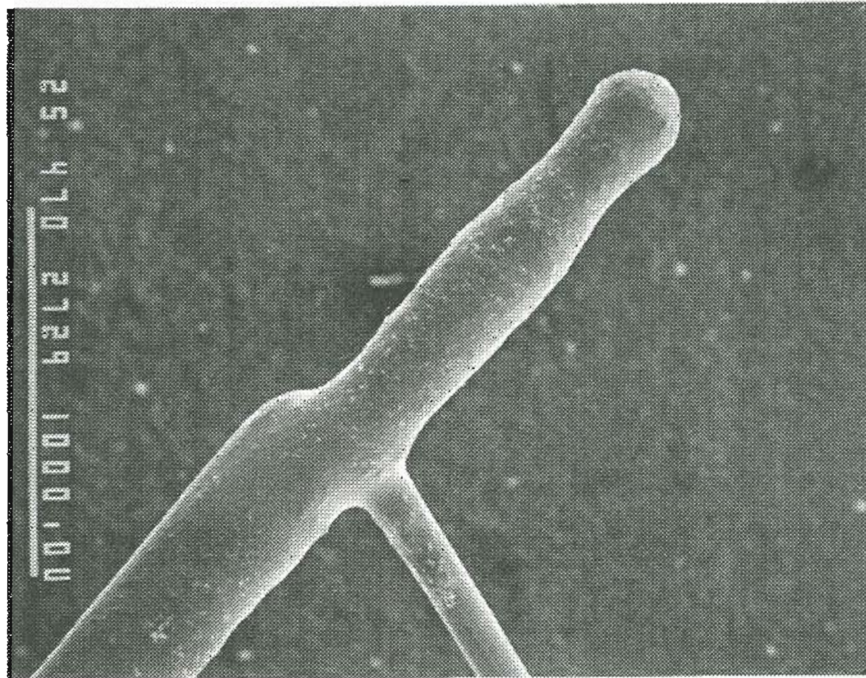

Figure 3.6 SEM micrograph of Mo emitter after several cycles between T_L and T_H. The spot weld failed immediately after heating to T_L and " quenching " by suddenly reducing the heating current. Note that the original wire diameter was the same as for the W loop but has swelled by a factor of 2.5 for the Mo.

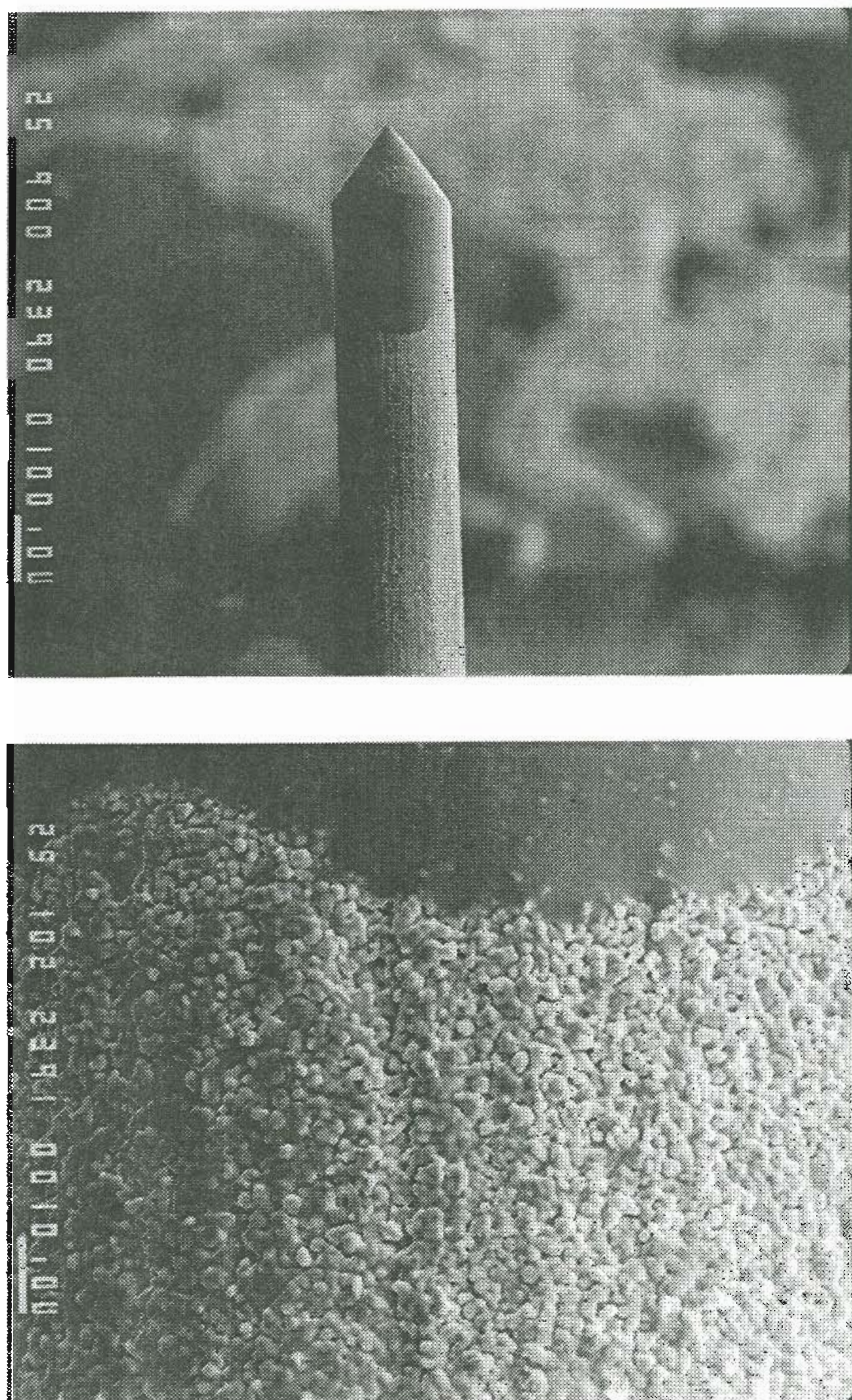

Figure 3.7 (a) Upper: SEM micrograph of molybdenum emitter wetted with gallium. Only part of the shank is wetted. (b) Lower: The interface between the gallium and the shank below it give some indication of film thickness since the liquid just begins to cover the Mo grains. Estimated thickness is 1 μm. The granular appearance resulted from the prior heating of the emitter with gallium on it.

A Mo/Re wire was spot welded to a W filament loop and an emitter fabricated by mechanical grinding. This alloy was also found to be too reactive. Figure 3.8 shows the emitter condition after evaporating gallium at high temperature.

3.2.3.3 Tantalum

The same experiments were repeated and very similar effects were observed. The degree of reactivity appears qualitatively similar to Mo. (see Figure 3.9).

3.3 Wetting and testing the emitter

After fabrication, the W emitter is rinsed in hot water to remove NaOH and finally rinsed with deionized distilled water and then acetone or ethanol. After drying with dry nitrogen or compressed air, the emitter is placed in a sample introduction chamber which is first rough pumped mechanically to 20 millitorr. A gate valve which isolates the introduction chamber from the wetting/testing chamber is opened and both sections are pumped out by a turbomolecular pump to a pressure P $\sim 3 \times 10^{-7}$ torr. The emitter is then transferred to the wetting/testing vacuum chamber which contains a vessel of the liquid metal. The gallium vessel can move vertically via a linear motion feedthrough. The chamber is fitted with a glass viewport and low power binocular microscope (1X - 30X) through which the wetting and testing process can be observed.

3.4 Source Contamination

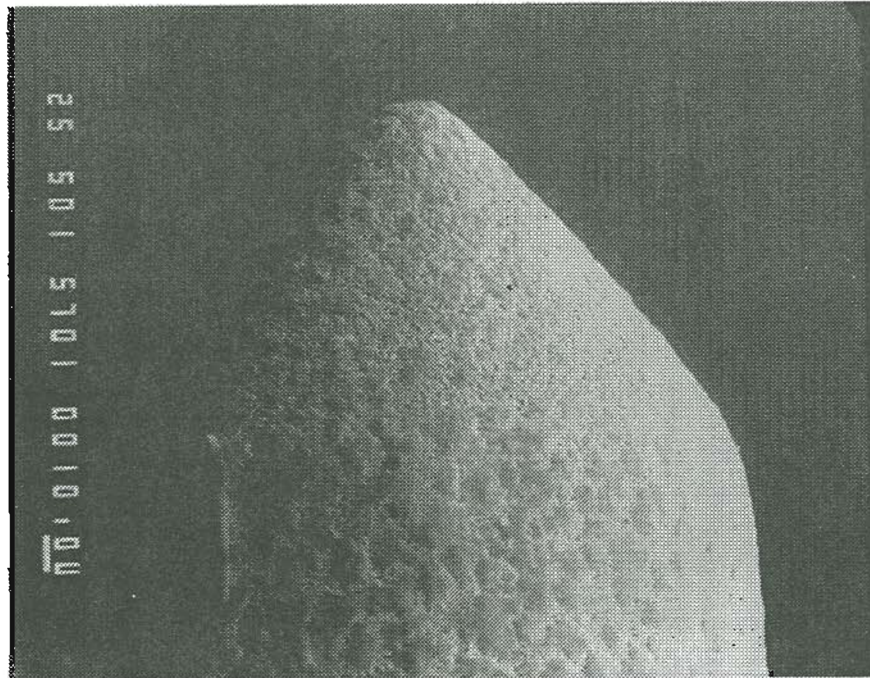

Figure 3.8 SEM micrograph of Mo/Re emitter for gallium LMIS. The gallium was evaporated at elevated temperature (flashed to white heat). It is likely that Mo has disolved into the gallium and forms a residue after evaporation. Note that the residue has migrated to the W loop.

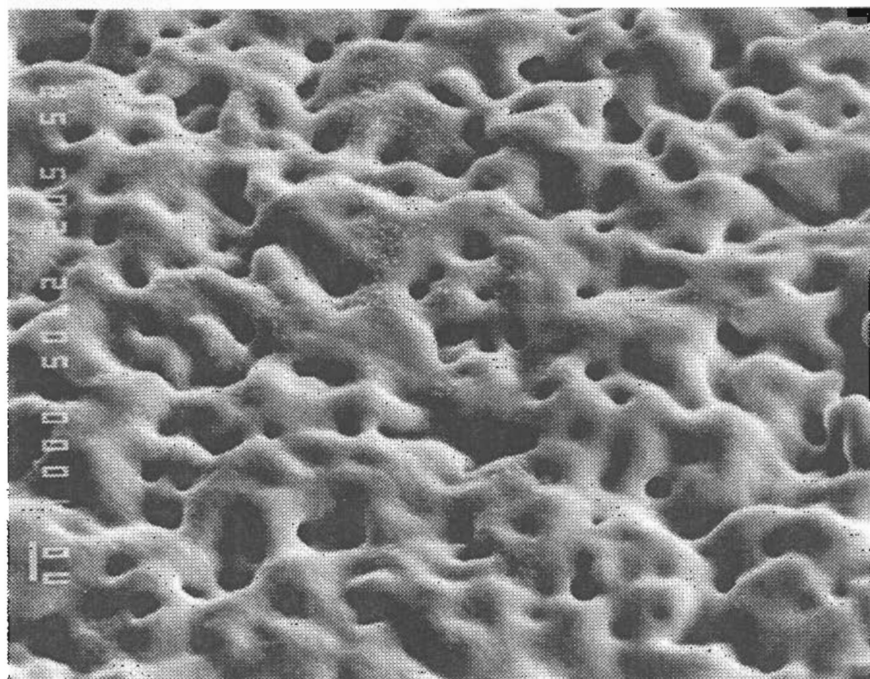

Figure 3.9 SEM micrograph of tantalum surface after reaction with gallium at high temperature (flashed to white heat).

We have seen that the physical concept and embodiment of the LMIS as a practical ion source is extremely simple. The Ga needle ion source may be the simplest and most convenient LMIS to employ for micromachining (FIBM), secondary ion mass spectroscopy (SIMS), and scanning ion microscopy (SIM). Despite its simplicity, the utility of the LMIS may be severely restricted by the presence of contaminants arising either during wetting, testing or during its operation.

3.4.1 Contamination during wetting and testing

Many metals and alloys must be heated to their melting point both for wetting the substrate needle and during operation of the source. Gallium is an easily supercooled liquid and as such often remains liquid at room temperature (approximately 20 °C) although its melting point is near 29 °C. The gallium source does not usually require heating during operation but it is sometimes found that after exposure to air some heating of the substrate is necessary in order to " start " the source. (see Section 5.2.2) It is sometimes observed that several cubic centimeters of liquid gallium can freeze spontaneously upon agitation of a gallium containing vessel so that some means for heating it in vacuo is desirable. In the wetting chamber, the tungsten needle is flashed quickly to white heat and immediately immersed into the liquid metal. The heating vaporizes residual contamination, if any remains after the electrochemical cleaning and etching steps. The needle is withdrawn and warmed to a dull red which causes the adhering gallium to flow along the needle grooves. It is then reinserted into the metal pool. This may be repeated several times until a satisfactory coating is obtained (see Figure 3.10). After satisfactory wetting, the emitter may be removed from the vacuum system and a small amount of gallium applied to the reser-

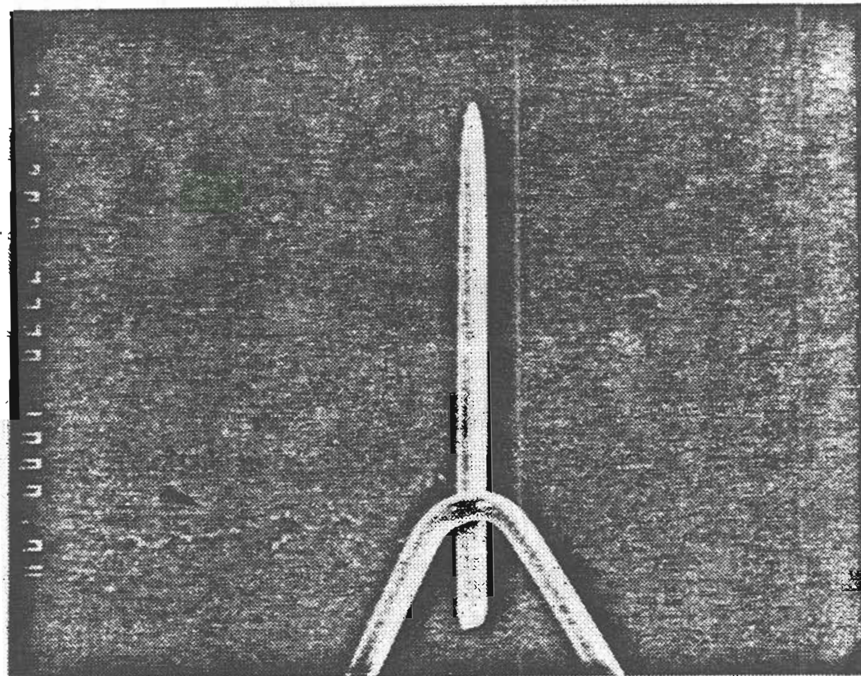

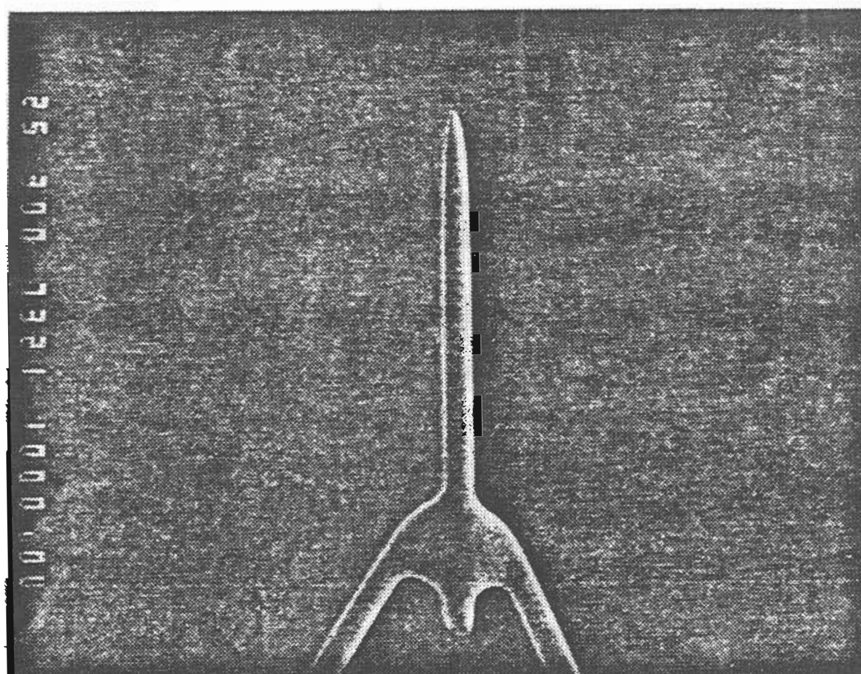

Figure 3.10 (a) Upper: SEM micrograph of tungsten emitter before wetting. Same as Figure 3.5. (b) Lower: Tungsten emitter after wetting. Gallium adheres to the needle and a small reservoir has formed in the vicinity of the spot weld. This is as much gallium as this type of emitter can hold by dipping into the liquid metal reservoir. More may be added by syringe. The W wire diameter is 0.005 inches.

voir via a syringe. Occasionally, the additional gallium thus applied in atmosphere will not wet properly (see Figure 3.11). One remedy is to heat the emitter in vacuum until the wetting is satisfactory. One drawback is that sufficient gallium will evaporate to coat the vacuum chamber viewport. The importance of the high temperature flashing cannot be overstated. In fact, complete wetting of the needle is never achieved without heating in this manner. A clean but cold tungsten needle will allow only a few minute droplets of gallium to adhere. These wet poorly but adhere because of the large ratio of surface tension force to weight.

It has been assumed above that the liquid gallium in the reservoir itself is free of contamination. Gross surface contaminants may be removed by agitating the vessel. This causes debris to move to the surface where it can be removed by skimming the surface with a clean stainless steel scalpel or similar tool. If this is not done, it is quite possible to coat the needle with the contaminants themselves. The presence of such contaminants on the liquid surface often produces regions which adhere to the needle as it is being withdrawn from the liquid pool (see Figure 3.12). This produces LMIS emitters which may act erratically, emitting ions off axis or from multiple points. Fortunately, it is relatively easy to observe this behaviour during testing. When ion current is extracted during testing, secondary electron bombardment back to the wetted needle results from the ion bombardment of the collection electrode. The contaminants are often non-conducting and the charging by the electrons is responsible for the "arcing" observed during the testing of emitters which have become contaminated in this manner. In the usual case, the extraction electrode is the surface of the gallium reservoir and if the surface "scum" is not too severe, the ion bombardment during testing is sufficient to clean the surface by sputtering. The contaminated emitter is again immersed into the now cleaned (at least cleaner than

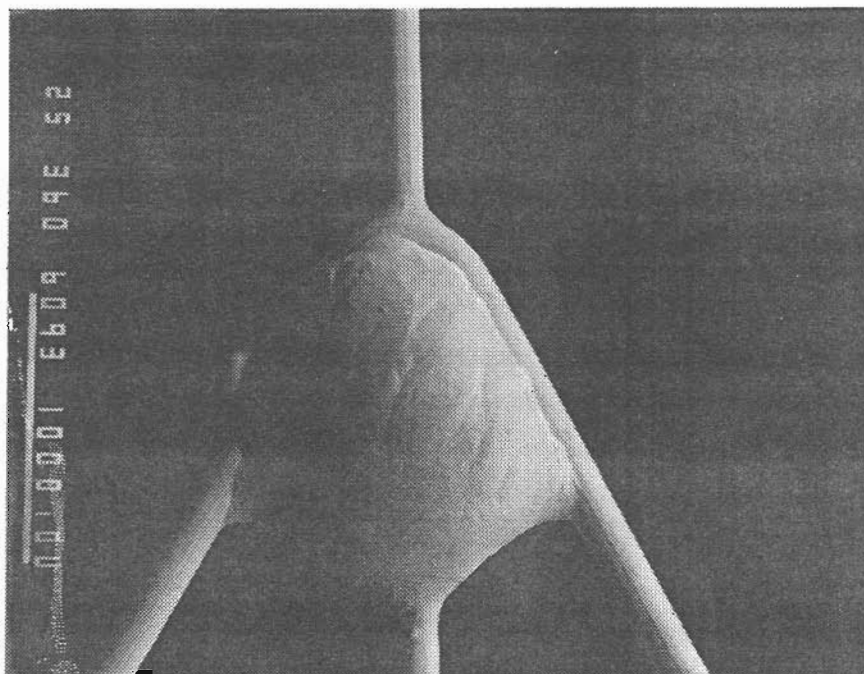

Figure 3.11 After wetting an emitter properly in vacuum it was removed from the vacuum system and gallium was added in atmosphere via syringe. Note that this has resulted in a poorly wetted emitter which would not be expected to run stably for long. Emitters such as this are returned to the vacuum system and heated to dull red. This often results in satisfactory performance.

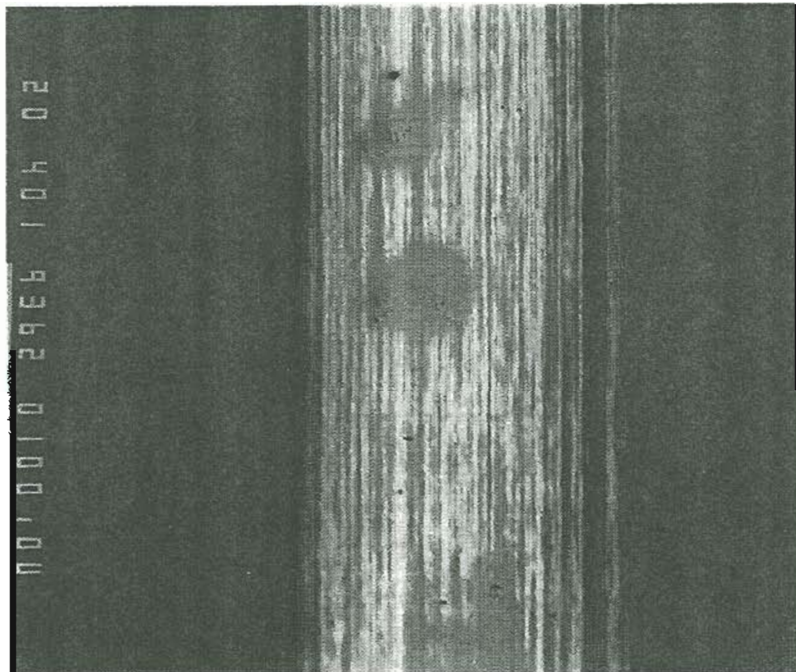

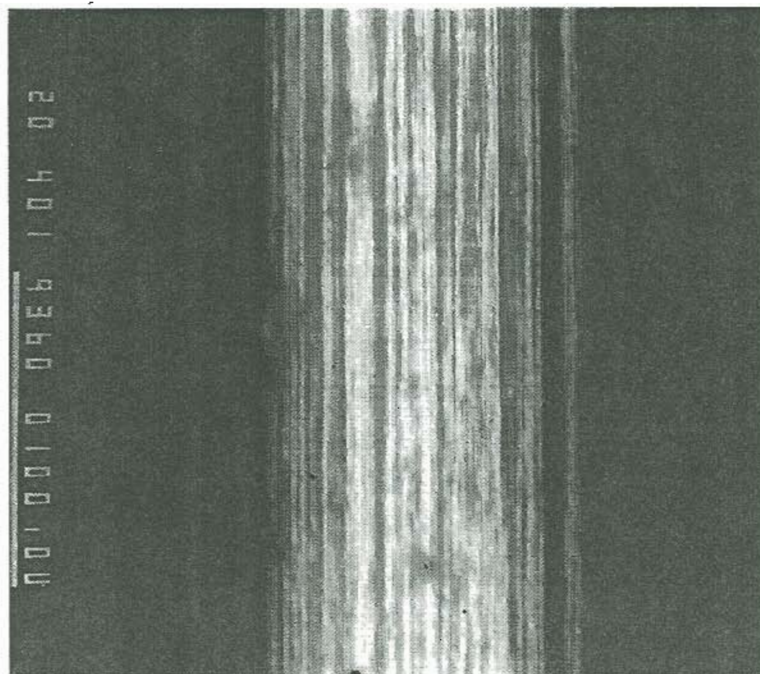

Figure 3.12 Backscattered electron SEM micrograph of poorly wetted emitter shank. Note the exposed grooves. Gallium adheres to the contamination picked up during the wetting procedure. This emitter ran erratically due to poor liquid supply.

before) gallium pool and some of the surface debris on the emitter floats away. Some agitation or transverse motion of the emitter may be necessary to move it away from the new debris. The emitter is withdrawn again and current extracted from the source allowing further sputter cleaning of the surface. The process is repeated until a clean emitter and gallium surface are achieved by this "dilution" cleanup of the gallium reservoir. The chamber pressure does not appear to be crucial for successful wetting, although it is usually maintained in the low 10^{-7} torr by the turbomolecular pump. On the other hand, during testing of the ion emission in the same chamber it is necessary to keep the pressure as low as possible. More importantly though, the composition of the vacuum environment must be kept free of hydrocarbons as emphasized in Section 3.2.4.

3.4.2 Contamination during operation

Experience within the Surface Physics and Electron Optics group at OGC indicates that contamination of the liquid metal surface will have a marked effect on its lifetime and stability usually via its wettability. In liquid alloy ion sources (LAIS) developed at OGC it was found that the purity of the bulk material is an important factor due to the possibility of segregation of bulk impurities to the surface and subsequent de-wetting of the liquid. The surface cleanliness plays a critical role in the ability to produce long lived, stable ion sources[65].

The use of LMIS in poor vacuum $\sim 10^{-5}$ torr or higher can be tolerated in those experiments where long lifetime and long term stability is not critical. For example, Ga and other LMIS have been used at such pressures in a diffusion pumped system by Barofsky at OGC for SIMS of organic molecules. The lifetime was usually

limited to only a few hours, however[66]. A simple calculation shows that the quantity of source material could not be depleted in such a short time, yet the ion source was no longer operable. Most likely, this is directly related to the formation of surface carbon films although the LMIS lifetime is affected by surface contamination in general. For most FIB applications, the short term stability and long term drift are of critical importance since the magnitude of the beam current affects the throughput in FIB processes and motion of the emission site is magnified by the optical column. This source motion thereby produces image motion and uncertainty in the beam placement.

3.4.2.1 Contamination due to backsputtering

Depending on the ion gun and optical column structure it is possible for backsputtered neutral atoms from electrodes downstream of the emitter to contaminate the gallium at the source. This is most likely to occur when the ions bombard the extraction electrode. For example, at a total extracted current, I_t, of $\sim 4\mu A$ the angular divergence of a gallium LMIS reaches $\sim 14°$ half angle[50]. Therefore, any extraction geometry which subtends an angle smaller than this will be struck by the beam. Sputtered atoms which have a direct line of sight path to the emitter will contaminate the gallium.

The material used to construct the electrodes and apertures of the ion columns used at OGC is molybdenum. A look at the Ga/Mo phase diagram (see Figure 3.13) shows that a small amount of sputtered Mo can raise the melting point of gallium sufficiently to cause the metal to freeze. If the source can operate at all the emission will probably be erratic due to obstruction of liquid metal flow by frozen regions.

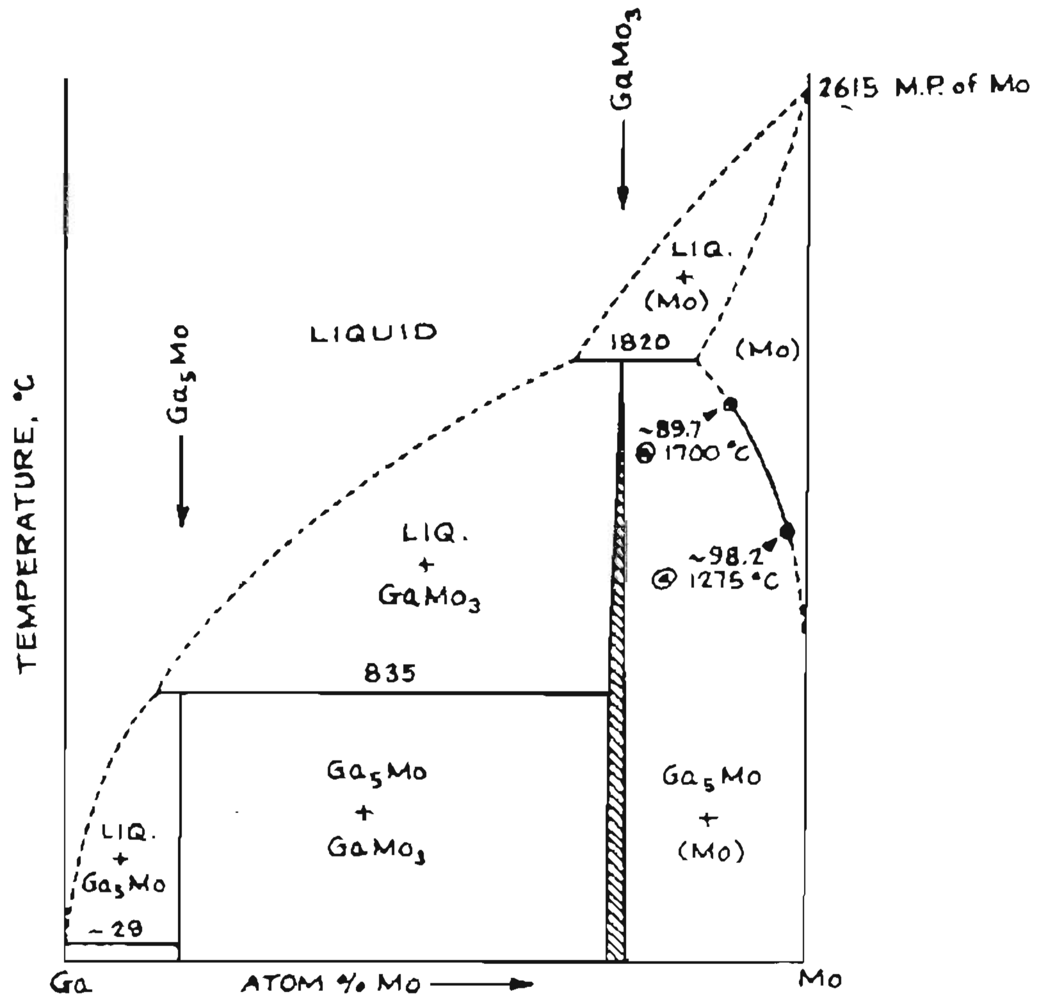

(Schematic only; not to scale)

A previously reported Ga_4Mo phase is thought to be identical to the Ga_5Mo phase identified in this study. No evidence was found to support the existence of a compound Ga_2Mo reported in earlier literature.

JLCM, 30 (1973), p. 205

Figure 3.13 Gallium/Molybdenum phase diagram. It is evident that a small quantity of backsputtered Mo will raise the melting point.

Figures 3.14 and 3.15 show how such an emitter looks after backsputtering of Mo from the extractor electrode of the ion gun. The Mo formed hexagonal platelets on the W surface and were identified by x-ray elemental analysis.

3.4.2.2 Effect of oxygen

Although heating the gallium LMIS during operation is not usually necessary, it is frequently observed that if the gun chamber is brought up to atmospheric pressure (to inspect or change the beam defining aperture, for example) and pumped back down, the source may not start even with the maximum extraction voltage applied. If it does "turn on", it usually runs erratically. This is probably due to the oxidation of the gallium surface to Ga_2O and Ga_2O_3. Operating temperatures of 600 - 700 °C have been shown to result in stable Ga^+ LMIS emission. It is thought that this results in the thermal evaporation of the Ga_2O which has a vapor pressure of 760 torr at 600 °C. For Ga_2O_3 the vapor pressure is very low ($< 10^{-10}$ torr) at this temperature but the following reaction may occur in the presence of gallium metal beginning at 500 °C[67].

$$Ga_2O_3 + 4Ga \rightarrow 3Ga_2O$$

The conversion to the higher vapor pressure oxide in this manner enables its removal and produces a clean surface.

3.4.2.3 Effect of chlorine

For FIB micromachining (Capter 6) of $Al_xGa_{1-x}As$ semiconductor lasers it is desirable to use chlorine gas to enhance the etch rate[68,69] and to reduce droplet formation[69] (see Chapter 5). However, it has been found that chlorine gas

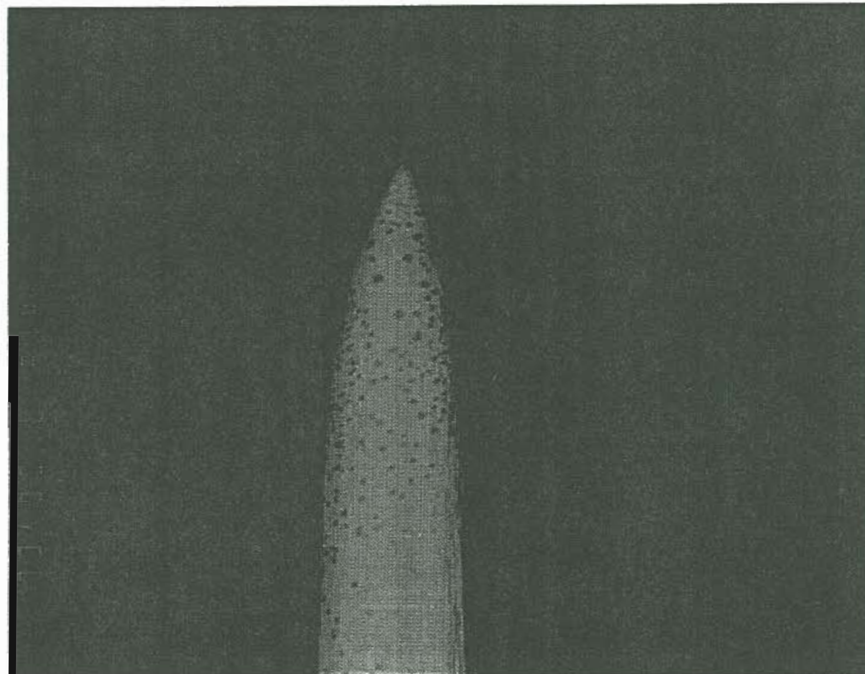

Figure 3.14 Backscattered electron SEM micrograph reveals " poisoning " by Mo. The Mo was most likely sputtered back to the emitter from the extractor electrode. The Mo spots result after the gallium is evaporated from the needle by heating.

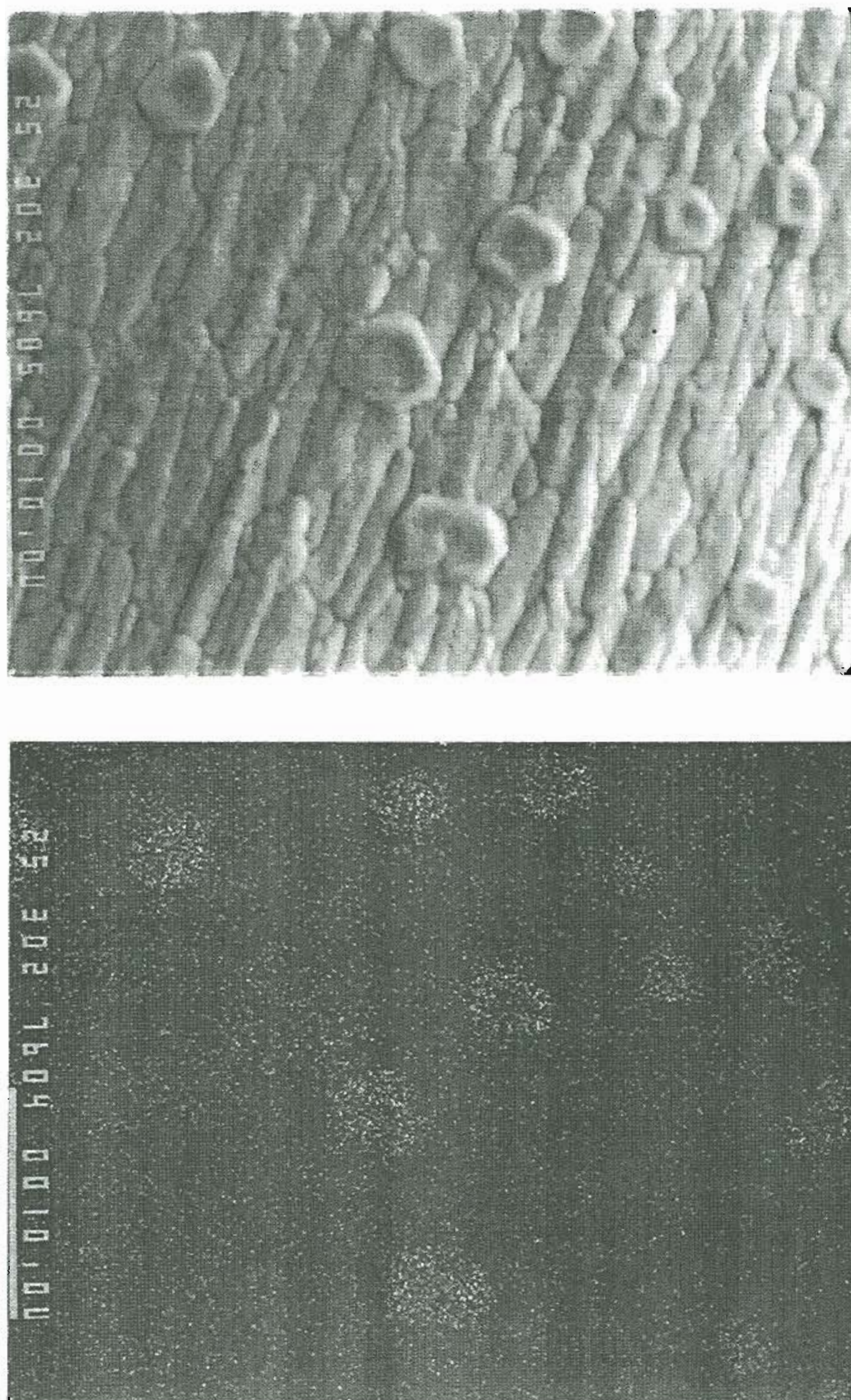

Figure 3.15 (a) Upper: Enlarged view of Figure so14 surface. (b) Lower: X-ray elemental map indicates that the platelet like structures are Mo crystals.

contamination affected the stability of the gallium LMIS[68]. This is probably due to the production of $GaCl_2$ and $GaCl_3$. At 600 °C the source ran stably probably due to the evaporation of the chlorides whose boiling points are 535 °C and 200 °C respectively[70]. It is likely that gas enhanced FIB etching in chlorine containing gases will reveal similar effects if the ion source is not separated from the reaction chamber by an appropriate differential pumping aperture.

3.4.2.4 Effect of carbon bearing gases

The source stability and lifetime can be affected dramatically by the presence of carbon containing gases and simultaneous electron bombardment of the emitter. Hyrdocarbons adsorb on the surface of the liquid metal. Secondary electrons which are produced when the ion beam strikes an extractor or collector electrode are accelerated back toward the emitter by the strong electric field. The hydrocarbons are "cracked" by the electrons, leaving a pure carbon sack-like film surrounding the metal. Since the electrons experience a potential difference equivalent to the ion extraction voltage of several kilovolts, the energies involved are similar, within a factor of three or so, to those used in the SEM. Likewise, the carbon deposition commonly experienced in diffusion pumped SEM columns and that described here are also similar. This is not a tolerable situation for an LMIS operating in an optical column, not only from the standpoint of the necessity for frequent replacement of the source due to short emitter life but also due to the associated long term instability and drift of the beam current before the emitter fails entirely.

These issues have been examined by Sudraud et al[71]. who found that a large fraction of secondary electrons produced by the ion beam which strike an electrode

several centimeters from the LMIS return to the source. In the presence of hydrocarbon materials at partial pressures $< 10^{-7}$ torr, the stability of the LMIS is greatly affected. The authors used an acetone and an air leak at 3 x 10^{-6} torr to provide the contaminants. They also observed a significant increase in the low frequency noise current in the presence of secondary electrons. When the secondaries were suppressed by positively biasing a collector electrode, the noise power spectrum was reduced almost uniformly by a factor of 2.2 over the range 0.125 Hz to 50 Hz. For the air leak experiment, they found that even with a pressure 3 times higher than for the acetone, the noise power was 4 times smaller even with the secondary electrons not suppressed[71].

3.5 An example of LMIS source contamination

We now describe the contamination of a vacuum system by heavy hydrocarbons and the effects it had on the operation of a gallium LMIS. It should be noted however, that even the presence of methane can effect the operation of a gallium LMIS source i.e. the deleterious effects can be observed for contamination much less severe than that described here.

The system in which two gallium LMIS had operated had been previously baked while containing some volatile organic materials. Solvent cleaning and subsequent baking of the system did not eliminate all the contaminants. This resulted in an environment of unknown composition although it clearly contained hydrocarbons. The LMIS was not in the vacuum chamber while it was being baked. During its operation the total pressure remained in the range 1 x 10^{-7} to 5 x 10^{-7} torr which is generally regarded as a sufficiently low pressure in which to operate a gallium LMIS.

Nevertheless, these sources operated for only a few hours before they failed.

As indicated in Figures 3.16 and 3.17, the emitters quickly became unstable in this environment. SEM micrographs reveal a severe contamination problem (see Figures 3.18 and 3.19) resulting in an almost complete de-wetting of the gallium. A hard sack-like film coats the emitter. After cracking the film with tweezers the appearance was as shown in Figure 3.18. A SAM analysis was done which revealed a variety of contaminants, most notably carbon (see Figure 3.20). Depth profiling Auger analysis of the sack-like film in Figure 3.21 shows that a carbon layer 250 - 750 Å thick had formed on the gallium (see Figure 3.21). We may conclude from this example that although the total pressure of the system is acceptable, it is at least as important (and in this case, more so) to be aware that the composition of the vacuum environment plays a key role in determining the stability of the LMIS particularly with the simultaneous presence of hydrocarbons and secondary electron bombardment of the emitter.

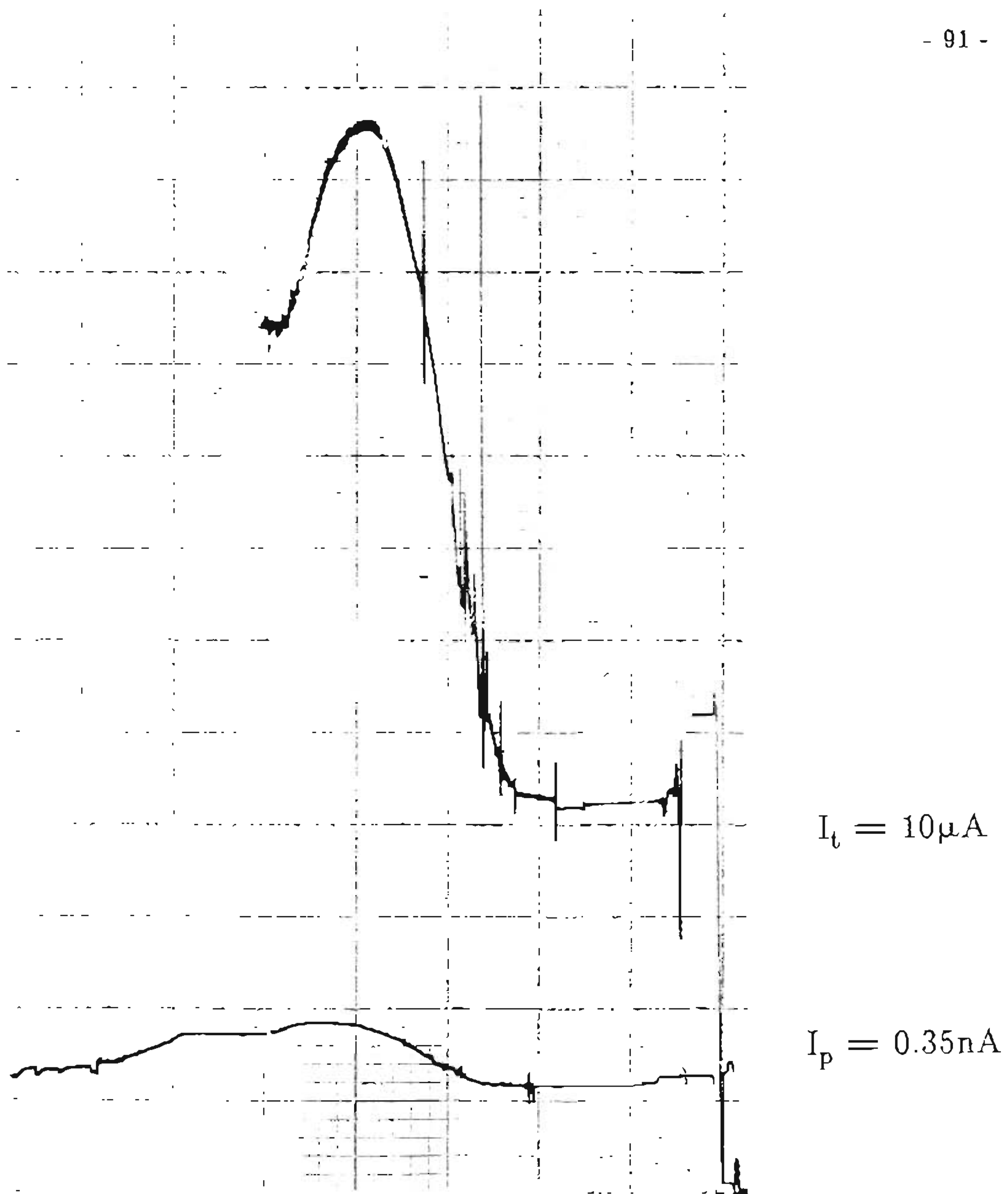

Figure 3.16 First emitter operated in the contaminated but "cleaned" vacuum system at a pressure of $\simeq 3 \times 10^{-7}$ torr. Upper trace: Extracted current $I_t \simeq 10\mu m$. Lower trace: Beam current $I_b \simeq 0.35nA$. Erratic operation became evident within 45 minutes.

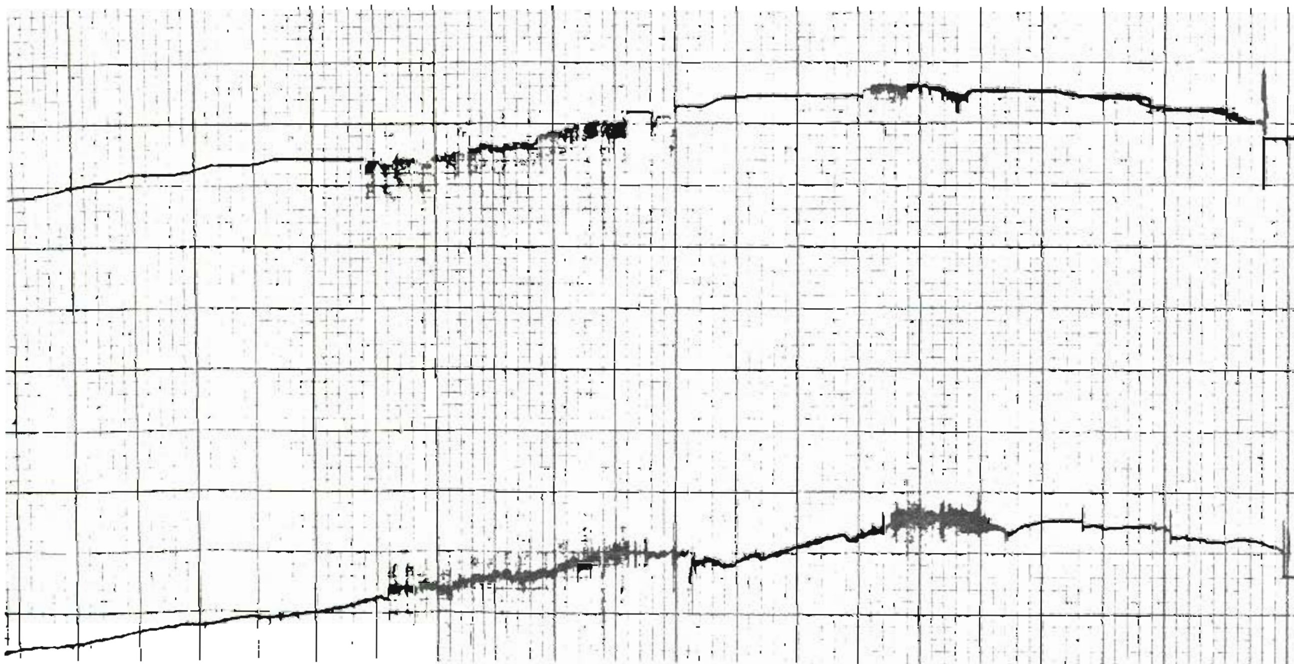

Figure 3.17 Second emitter operated in "cleaned" vacuum system. Upper trace: $I_b \simeq 0.3\mu m$. Lower trace: Total extracted current $= 5.8\mu A$. Erratic behavior after 2 hours.

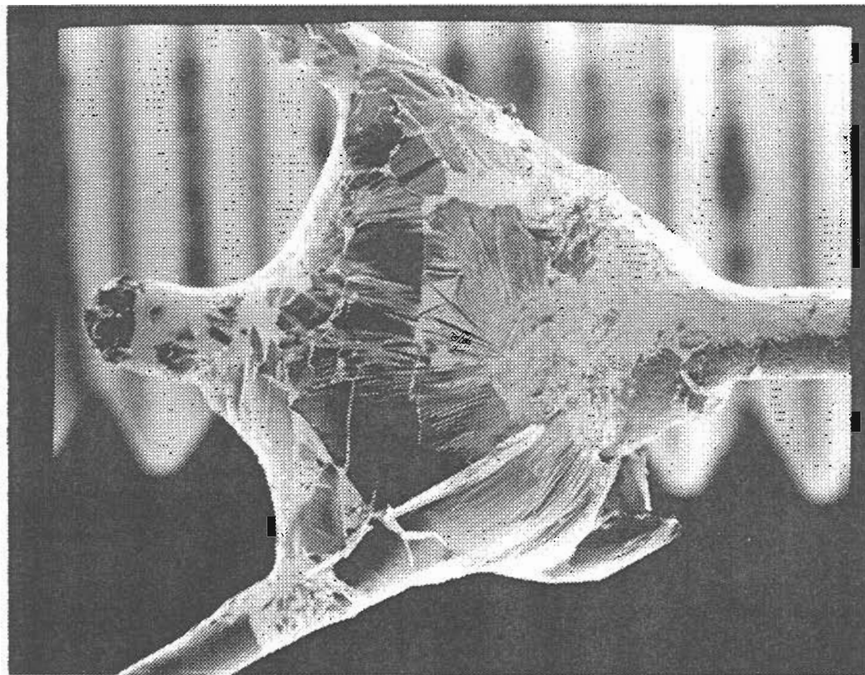

Figure 3.18 SEM micrograph of emitter operated in contaminated but "cleaned" vacuum system. The shell-like fragments are almost pure carbon.

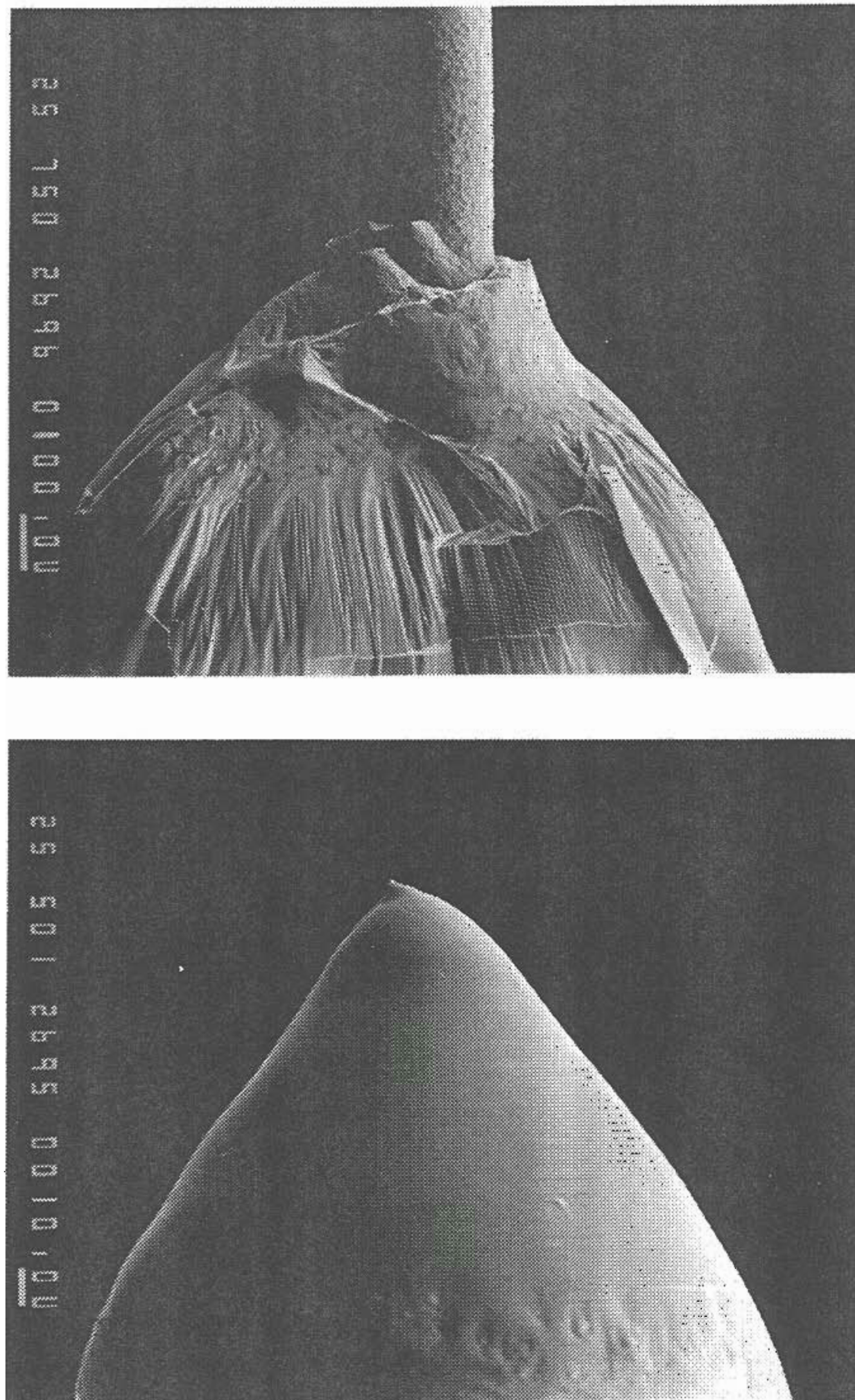

Figure 3.19 (a) Upper: SEM micrograph of emitter in contaminated but "cleaned" vacuum system. Note the complete de-wetting of the gallium film. (b) Lower: Same emitter as above. Note small off-axis frozen Taylor cone.

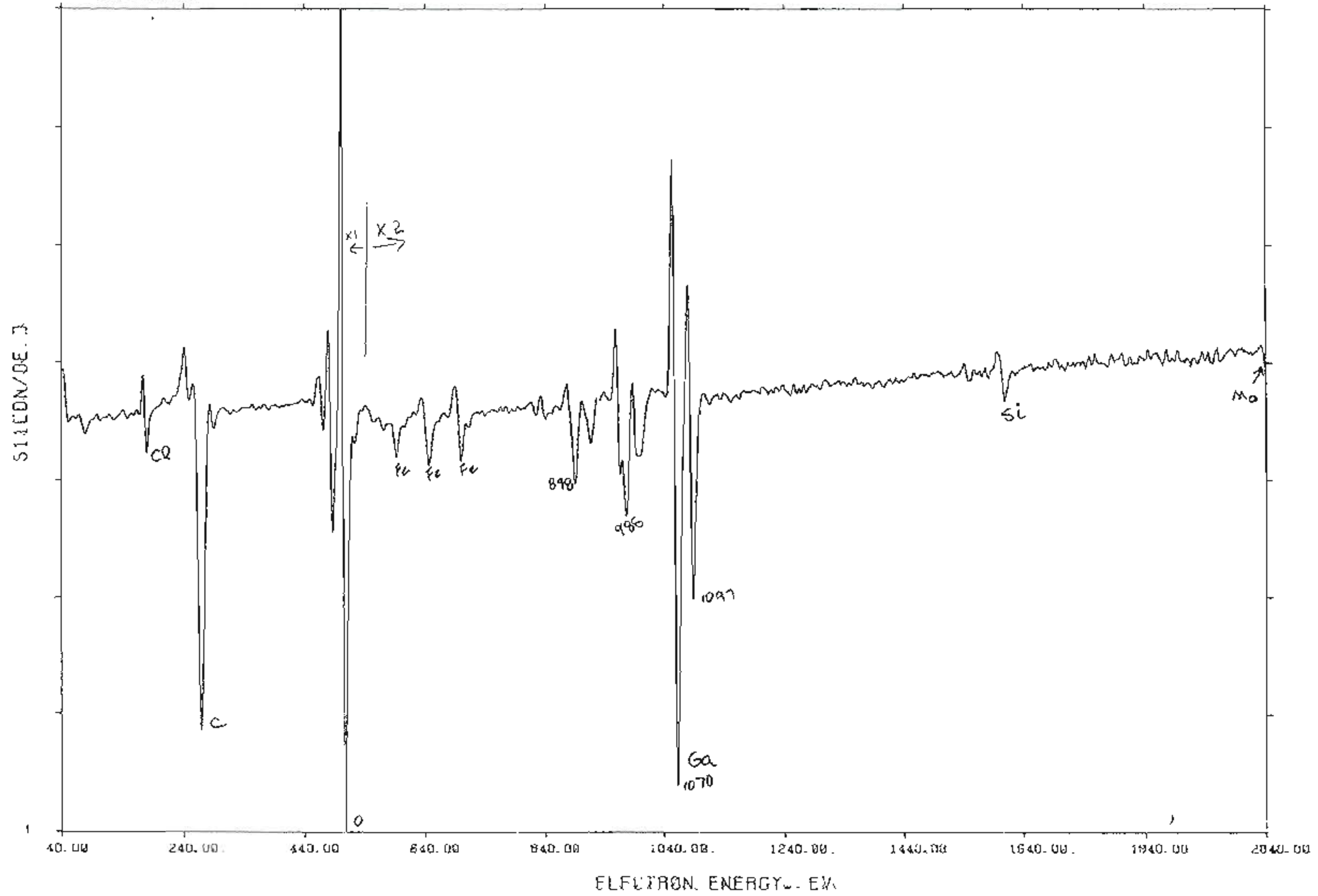

Figure 3.20 SAM analysis of emitter contaminated with Cl, Fe, Si, Mo and C. Both emitters produced essentially identical spectra.

Figure 3.21 (a) Upper: Depth profiling with Ar beam sputtering and Auger analysis. Same surface visible in Figure so18. (b) Lower: Same area after Ar sputtering indicates motion of carbon " islands " which float on the gallium. Film thickness = 250 Å - 750 Å.

4. OVERVIEW OF ION / SOLID INTERACTIONS

A particle beam, of almost any incident energy, impinging on a target can produce a variety of effects which may be utilized for technological and scientific purposes. Positive, negative and neutral particle bombardment have been used to induce ground state and excited state, neutral particle sputtering, and electron, ion and photon emission. These in turn may be responsible for chemical surface effects and radiation damage to the substrate. Detection of the ejected particles provides the basis for spectroscopy for surface analysis and imaging for microscopy. Some brief descriptions of the phenomenon will be given since they are responsible, in one way or another, for the effects on which the focused ion beam applications presented in this thesis are based.

4.1 The various phenomena in general

Ion penetration into a solid results in a series of collisions with the lattice or target atoms (nuclear or elastic scattering) and with the atomic electrons (inelastic scattering). These two energy loss processes are usually considered independent[72]. Elastic collisions may result in backscattering of the incident ions, in sputtering or ejection of target atoms and, at relatively higher energies, formation and emission of

nuclear reaction products. Inelastic collisions produce characteristic x-ray emission, ionization and atomic excitation. These account for the processes occurring inside and outside of the target as a direct consequence of the primary ion bombardment and are indicated schematically in Figure 4.1. There are also processes which occur within several Angstroms of the target involving interactions amongst the secondary or emitted particles themselves. In particular, some models of secondary atom ionization (the basis for SIMS) require such interactions. Several models have been proposed but the phenomena involved are complex enough that many models may be said to agree with particular experiments. Finally, it should be noted that the distinction between the "inside" and "outside" of a target surface is not always clear at the solid/vacuum interface itself. For example, emission of excited atoms is thought to occur during passage within a layer several Angstroms from the surface.

4.2 The specific effects of ion bombardment

Ion penetration into a solid target produces surface and bulk modifications which can be broadly categorized by one or more of the following processes; implantation, radiation damage, sputtering, and atomic mixing. The nuclear collisions result in defect production and displacement of target atoms from their lattice sites causing physical damage in the target. For the typical energies encountered in FIB ion bombardment of solids (5 - 30 keV) there is sufficient incoming energy to dislodge hundreds of lattice atoms or more since the displacement energy lies in the range 5 - 20 eV depending on the material. For GaAs, the displacement energy is subject to speculation but 10 eV is a typical estimate[73]. As the incident ion collides with the lattice its trajectory changes randomly and produces damage within a volume termed

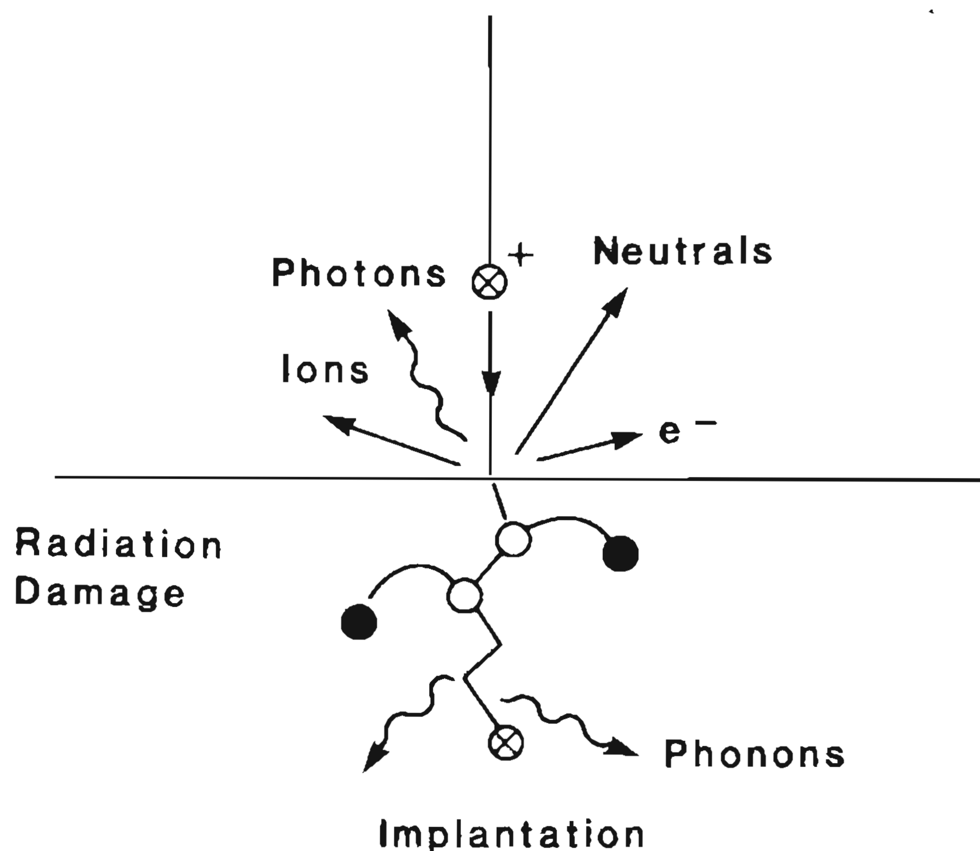

Figure 4.1 Schematic diagram illustrates some possible ion/solid interactions. Detection of the various outgoing particles is the basis for spectroscopy and imaging. Of course, the physics of any interaction depends on target and beam parameters e.g. incident energy and angle, target and ion mass and possible chemical reactions. These directly affect the particle yields.

the collision cascade volume. This terminology is frequently employed in discussions of sputtering theories. In addition to the resulting material damage, one or more target atoms may be ejected per incident ion. This is known as sputtering and the ratio of the average number of outgoing particles to the average number of incoming particles is called the sputter yield, S. It appears that the term sputtering is becoming associated with the material erosion as well as with the ejected particles. Accurate absolute measurements are difficult to make due mostly to the errors involved in measuring the quantity of material removed. There are also difficulties when there is a significant amount of the beam species retained by the target. Continued bombardment results in alteration of the surface topography. This is discussed in Chapter 5. After sufficient ion dose, the surface erosion becomes significant and one commonly speaks of ion milling or machining. This technique finds important technological applications in the semiconductor industry, for example, where sputtering is employed in various dry etching schemes and also in thin film deposition. Sputtering is the basic phenomenon underlying the FIB micromachining reported in Chapter 6.

Recently, ion bombardment of thin films deposited on a target substrate has been utilized in a technique appropriately called ion beam mixing[74]. The bombardment induces recoil implantation in the film and atomic mixing within the collision cascades at the interface which transports the film atoms into the underlying substrate. Because this mechanism is collisional and temperature independent this phenomenon is already being exploited to produce materials which are not limited by the constraints of thermodynamic equilibrium (unlike chemical mixing). Interestingly, some collisionally mixed systems can be unmixed at elevated temperatures, Au-Ge being an example. Ion beam mixing does not yet appear to have been used with focused ion beams.

4.2.1 Energy loss and ion stopping

The total energy loss of the ion beam as it penetrates the target can be written as the sum of two independent terms:

$$\frac{dE}{dx} = \left(\frac{dE}{dx}\right)_n + \left(\frac{dE}{dx}\right)_e$$

i.e. the sum of the nuclear and electronic contributions. In practical applications, only approximations are used for the energy losses because the exact forms for these distributions are quite complicated and depend not only on the incident ion energy but also on the projectile-solid combination[75,76]. There is no comprehensive theory which covers all the possible combinations. For each combination, there exists a "crossover" energy where the contributions are equal and above which the electronic energy losses dominate. A discussion of this subject appears in many books dealing with the subject of ion implantation, for example. For the range of energies which concern us in this work, the electron energy loss is nearly proportional to $E^{\frac{1}{2}}$. This is true for energies less than about 1MeV. As the ion slows down, the nuclear energy loss dominates and is usually described by the so-called LSS theory after its authors Lindhard, Scharff and Schiott[76] who described the situation using a Thomas-Fermi electrostatic interaction potential.

4.2.2 Penetration depth and straggle

The nuclear and electronic energy losses can be used to calculate the penetration depth or ion range of an ion with energy E_0 with the following expression:

$$R = \int_0^{E_0} \frac{dE}{\left(\frac{dE}{dx}\right)_n + \left(\frac{dE}{dx}\right)_e}$$

The appropriate stopping cross-section, can then be defined $S(E) \equiv \frac{1}{N}\frac{dE}{dx}$ where N is the number density of target atoms. As mentioned previously, the ion path through the target was assumed to consist of a succession of binary collisions with its associated energy loss depending on the particle velocity. This results in a nearly Gaussian statistical distribution in the total path length. However, because the path deviates at every collision, it is frequently more important to know what the component of the total path length is along the direction normal to the surface and how much of a longitudinal and lateral spread there is in the ion trajectories. These qualities are termed the projected range, R_p, and the parallel and perpendicular or transverse straggle, ΔR_p and ΔR_l, respectively and are of great practical importance in all ion bombardment associated technologies; particularly in the area of ion implantation. Figure 4.2 shows the projected range and straggle of H , Be, Zn, Se, Cd and Te in GaAs. This data will be used in Chapter 5. The LSS theory[76] has been shown to model the experimental R_p particularly well[77,78] in cases where nuclear stopping dominates. The agreement between theory and experiment is not quite so good where electronic losses dominate. The electronic stopping should result in a smooth slowing down of the incident particle and the cross-sections should likewise vary smoothly. However, experimentally the magnitude of the electronic stopping cross-sections oscillates with the incident particle and target atomic number. Range parameters based on the LSS theory have been tabulated for various beam-target combinations[79,80]. With the range distributions in hand, one can obtain the peak concentration using:

$$N_p \sim \frac{N_s}{2.4\Delta R_p}$$

where N_p is the peak concentration and N_s is the implanted dose in ions per cm^2

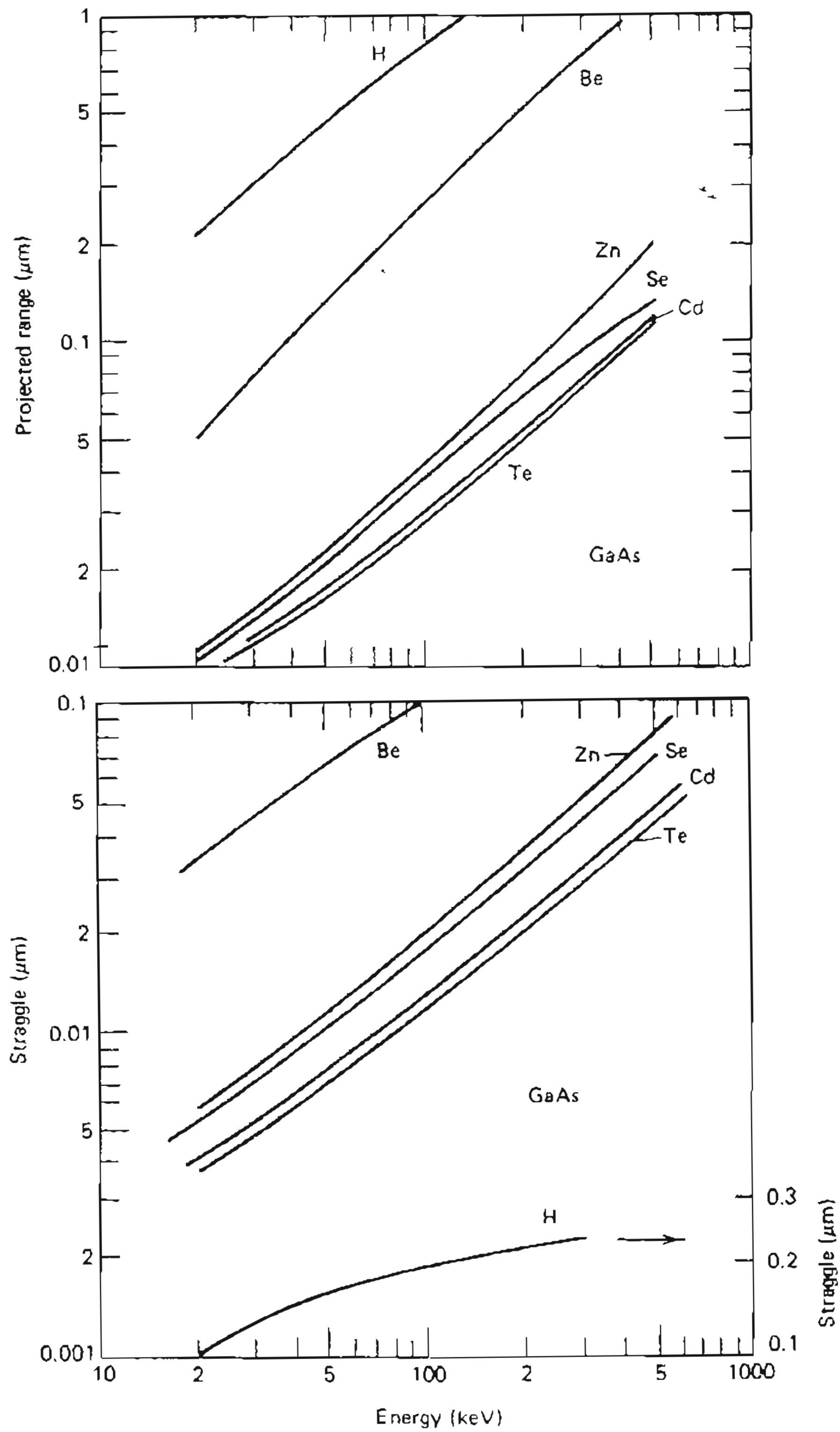

Figure 4.2 Projected range (upper) and longitudinal straggle (lower) for H, Be, Zn, Se, Cd, Te in GaAs.

(from VLSI Fabrication Principles by Sorab K. Ghandhi, John Wiley & Sons, 1983)

with the depth distribution given by:

$$N(z) = N_p \, e^{-\frac{(z - R_p)}{(\Delta R_p)^2}}$$

4.2.3 Incident ion channeling

As mentioned previously, the foregoing discussion has been limited to ion penetration of amorphous targets. As early as 1912, Johannes Stark predicted that for ions incident along low index crystal directions, there would be a significantly enhanced penetration of bombarding ions. When the ions are incident nearly parallel to an open crystallographic direction or "channel", they can oscillate between the atomic rows and become focused towards the center of the channel. These ions "see" the atomic structure and lose energy primarily due to electronic collisions. If the incident angle is too far off the channeling direction however, the ions can make more oblique collisions and become dechannelled via nuclear scattering. This angle is defined as the critical angle for channeling and is given below. These ions continue to make random impacts with atomic nuclei and do not "see" the crystal structure. They behave nearly as they would if they were travelling in an amorphous target. This is a well-known phenomenon in ion implantation where it is the usual practice to tilt the target a few degrees to provide this pseudo-amorphous environment. The penetration range and straggle statistics can then be obtained from the equations presented earlier. The critical angle for channeling as obtained by the LSS theory is given by:

$$\Psi_c \sim \left[\frac{a}{d} \left(\frac{2 Z_t Z_p e^2}{E d} \right)^{\frac{1}{2}} \right]^{\frac{1}{2}}$$

with Z_t, Z_p, the atomic numbers of the target and projectile particle, e the electron charge, d the distance between atoms along the axis, a the Thomas-Fermi screening distance, and E the incident particle energy. This is the angle which a substrate must be tilted in order to avoid a non-random implant distribution. For many materials Ψ_c lies between 3 ° and 8 °.

4.2.4 Radiation damage

A heavy ion of several keV incident energy can deposit enough energy to displace many target atoms from their lattice sites. This can result from the primary ion collisions and also from ion collisions between target atoms which have themselves been given enough energy to displace additional atoms. This produces a displacement or collision cascade which causes a damage profile of large volume. In fact, the peak and range in depth of the maximum energy deposition can be quite different than the depth at which the ions are most likely to be implanted. As a consequence, most of the damage may not be in the region of the peak in the implantation depth. Rather, a homogeneous region in the near surface can be created which may be on the order of the ion range. Furthermore, the situation is different for light and heavy ions. This is due directly to the differences in the energy loss process and the fact that the ion ranges can be very different. This means simply that for a given energy, a heavier particle will deposit more energy per path length than a lighter particle and the displacement damage will be proportionately closer to the surface. This so-called " cascade mixing " has a direct effect on the depth resolution of SIMS depth profiles. In order to have an estimate of the displacement damage distribution, it is necessary to know the magnitude of the energy deposition per path length and the collision cas-

cade volume. Tabulations of collision cascade parameters are available in the literature[81] and the number of collisions per incident ion is given by:

$$N_d(E) = \frac{0.42\nu(E)}{E_d}$$

where $\nu(E)$ is the deposited nuclear energy distribution. However, this expression is based on simple collisional models[82-84]. and the displacements and energy distributions may often be very inaccurate as revealed by channeling measurements and transmission electron microscopy. This is due to the fact that the above predictions are based on a linear collision cascade theory whereas cooperative processes may exist which require distinctly non-linear energy transfer to explain them. This leads directly to the concept of non-linear thermal and displacement spikes. This is discussed in Section 5.6.4 in the context of the ion bombardment of GaAs.

These phenomena are explained somewhat differently by different researchers and there is still some debate over which systems exhibit "spiking". Some very informative articles which deal with many of the phenomena described above as they relate to material modification under ion bombardment can be found in a book edited by Auciello and Kelly[85].

5. SURFACE TOPOGRAPHY INDUCED BY FOCUSED ION BEAM BOMBARDMENT OF GaAs AND AlGaAs

5.1 Background

Among the many effects of ion irradiation of solid materials is the development of surface topography. Topography changes occur at different doses for different materials and depend also on the bombarding ion species and energy[86]. It is possible to define some broad categories of bombardment induced topography and much work has been done over many years to identify ion / material " systems " in order to identify the various phenomena. However, the task is exceedingly difficult and is complicated by the number of diverse materials of scientific and technological interest for which some type of ion bombardment processing is employed. For example, homogeneous and heterogeneous materials, chemically pure materials with randomly oriented crystallites, multicomponent materials in the form of alloys, compounds, and layered materials of varying composition can exhibit an enormous range of surface morphology for a given dose of a particular incident ion. The changes may be negligible and barely visible or quite striking, revealing faceting and the formation of cones[87], pyramidal structures, grain relief[88], blisters[89,90], furrows, grooves, ridges,

pits, steps, whiskers[91] and droplets, as reported here. Understandably, the mechanism of the formation of many such features is not completely known but undoubtedly depends on complex and interacting factors including ion bombardment enhanced surface diffusion[92,93], preferential sputtering of multicomponent materials[94] and various aspects of radiation damage in solids in general.

In crystalline materials, it is well known that defects generated close to the surface may interact and intersect the surface producing well defined topographical features. The symmetry of the crystal also plays a role in the development of regular surface structures which may be distinguished from the often irregular features requiring impurities and appearing on amorphous substrates. It has been suggested[95] that beneath the ion bombarded crystalline surface an array of dislocations may form due to the agglomeration of point defects and de-channel incident ions. The energy loss would thereby increase in the near surface and create a spatially periodic sputter yield resulting in regular surface features. This type of radiation damage induced topography depends on the average migration speed of defects and if the sputtering is too rapid the dislocations have no time to form and the topography does not develop. On the other hand, a periodic variation in surface stress resulting from the dislocation array has been invoked to suggest a periodic variation in sputter yield which in turn enables surface undulations to form[96]. Even in amorphous materials, however, regular surface undulations can develop under ion bombardment. There is another class of topography development which appears not to depend on beam induced defects at all but rather requires the presence of irregularities in the target before the ion bombardment. All materials seem to be susceptible to this sort of topography development which includes features related to the angular dependence of the sputter yield and which may depend strongly on included impurities, crystal defects and the initial

surface morphology.

A complicating factor in understanding topography evolution is due to the alteration in the surface composition of multicomponent materials by preferential sputtering. During a transient period, this non-stoichiometric sputtering depletes the components with the higher sputter yield relative to the lower yielding components. After steady state conditions are achieved the non-stoichiometric sputtering ceases and the sputtered flux represents the bulk target stoichiometry although the surface composition will be different from the bulk. Generally, the surface will be enriched in the component which has the lower sputter yield.

The mechanism of preferential sputtering depends strongly on mass differences between the components, and their surface binding energy. This information is not readily available from sputtering yield experiments since the sputtering yield depends strongly on phenomenological considerations e.g. the incident energy, mass ratio of the target and bombarding ion and beam incident angle.

According to Kelly[97], the mass dependence arises primarily from so-called recoil sputtering i.e. target atoms struck directly by the beam, whereas chemical binding effects play a role in cascade sputtering, thermal sputtering, and surface segregation. In cascade sputtering, the bonding dependence arises directly from the sputtering yield dependence:

$$S_c \propto \frac{1}{U}$$

where U is a surface binding energy. U has variously been identified with the heat of sublimation, the heat of vaporization or some other characteristic binding energy. For thermal sputtering, the sputtering yield is given by:

$$S_{th} \propto T_{sp}^{\frac{3}{2}} M^{-\frac{1}{2}} U^{-2} e^{-\frac{U}{kT}}$$

with M the atomic weight and T_{sp} the thermal spike temperature. Kelly also shows that bonding considerations are more successful than mass differences in explaining preferential sputtering. Although cascade sputtering is thought to account for most sputtering, it does not explain all the compositional changes observed experimentally. Surface segregation combined with sputtering may provide a better explanation.

Ion beam mixing, in which up to 50 substrate atoms may be mixed per incident ion, has been modeled by Schwartz and Helms[98]. While many of the basic issues still remain to be understood, it is thought that collisional mixing within the collision cascade and enhanced diffusional mixing due to the presence of induced defects are responsible.

To summarize briefly, the ion bombardment of multicomponent targets results in a modification of the near surface composition which may be due to a variety of causes; segregation, which tends to produce spatial variations, cascade mixing and diffusion which randomize the variations, recoil implantation, which transports lighter species into the target, thermal sputtering and possibly additional effects.

5.2 Introduction to the present work

The present study is an examination of the formation of droplets during Ga^+ focused ion beam micromachining of GaAs based materials. This appears to be related to sputter cone formation during ion bombardment, which is probably the most commonly observed and best understood of these phenomena. Consequently, we will discuss some aspects of sputter cone production in the concluding sections[99].

Despite the intense interest in semiconductors there have been relatively few studies of topography changes under broad area i.e. unfocused ion bombardment to

date. Most such studies have dealt with elemental metal targets or metal alloys[100]. Some recent investigations have been made of surface morphology changes in GaAs, Si, and InP after bombardment with argon, cesium, and oxygen ions at various energies and target temperatures[86,101-103]. However, studies of topography changes by LMIS FIB bombardment of semiconductors are rare.

An interesting form of topographic modification involves the formation of liquid or liquid-like droplets. The work reported here describes this aspect of Ga^+ ion bombardment during the focused ion beam micromachining (FIBM) of semi-insulating GaAs and AlGaAs semiconductor lasers of varying composition and structure. There have been no previously reported systematic studies of such droplet production in GaAs and GaAs based materials although it evident that they have been observed by other researchers[69,104]. We have also observed the development of surface topography in the FIB micromachining of InP based diode lasers but a systematic study has not been made and their composition has not been examined. Moreover, it is probably not correct to describe them as droplets since their shape is irregular and there is no evidence of a liquid phase. Experiments related to but different from those reported here have been made by Ishitani et al[105]. and Moore et al[106]. who have reported on the bombardment of silicon by Ga^+ ions which resulted in the condensation of gallium at the surface. Rudenauer et al[107]. have used In^+ ion bombardment of silicon to examine the droplet content of an indium LMIS beam itself which was operated at relatively high extracted currents (25 μA). However, they incorrectly cite the work of Ishitani et al. as supporting the conclusion that droplets were carried by the beam. It is clear that Ishitani et al. were describing droplet condensation due to ions in a beam with a negligible droplet component while Rudenauer et al. were considering the beam droplet component itself. Other forms of topography

modifications has been observed for Cs^+ bombarded GaAs[102].

5.3 Experimental

A Macor substrate was used to thermally isolate the specimen from its support. A small Al plate was screwed in place and a square of (100) oriented semi-insulating GaAs ~ 2 mm. x 2 mm. was cleaved from a larger wafer and attached to the Macor surface with Ag paint. Surface debris was removed from the GaAs wafer by sonication in ethanol in an ultrasonic bath for several minutes. The sample was then rinsed in deionized water and air dried. No further cleaning treatment of the GaAs surface was employed. An iron-constantin thermocouple was attached directly to the Al plate close to the GaAs sample and the thermoelectric e.m.f. measured with a battery operated digital voltmeter. Via a silver braid, the sample was in thermal contact with a sealed copper box through which liquid nitrogen could flow. The temperature of the sample could be varied and maintained by adjusting the flow of liquid through the copper box. However, the feedthrough into the vacuum chamber was not thermally insulated and the sample could not be cooled to LN_2 temperature (77 ° K) due to large thermal conduction losses at the feedthrough. The pressure in the vacuum chamber was in the range 1 - 2 x 10^{-7} torr while the experiments were conducted but the partial pressure of gases in the chamber was not monitored. Since the ion beam column was equipped with a beam blanker, scanning ion micrographs were obtained during the experiments. Video tape recordings of the SIM images were also obtained for some of the experiments so the droplet formation and motion could be reviewed. The beam was raster scanned over the GaAs wafer substrate for a given time. In this manner, both the ion dose and current density could be accurately con-

trolled. The dose, $D = \frac{J\,t}{q}$, with J the average current density, q the ion charge and t the exposure time.

A preliminary experiment was performed to test the ability of the ion beam to form droplets at room temperature. Outside the chamber, a film of Ga was spread directly on the GaAs wafer with a clean glass microscope slide producing a non-uniformly thick three dimensional Ga liquid film. The sample was then placed into the vacuum chamber and evacuated. As expected, without the ion bombardment (beam off between SIM imaging) and the sample at room temperature, there was no droplet formation and no motion of the film in general. Under Ga bombardment, the film motion was quite dramatic. Large regions of the film split into islands which moved under the beam. The islands did not form into round droplets however, but appeared smooth and were irregularly shaped. Presumably, this is related to the wettability of the large Ga islands with the GaAs surface. On the other hand, droplets produced under ion bombardment of a GaAs substrate, without a liquid Ga film first applied, were nearly hemispherical. Interestingly, the removal of adsorbed surface contaminants by the sputter cleaning of the substrate during the first moments of ion irradiation results in poorer wetting with the liquid. This generally indicates a higher energy surface. On the contrary, the "dirtier" and perhaps somewhat oxidized GaAs and liquid Ga surfaces wet each other more readily. This interesting behavior has been observed in the wetting of W emitter substrates with Ga i.e. the oxidized gallium "skin" wets the tungsten more easily than the clean gallium[108]. The contact angle with the surface varies amongst droplets and does not appear to be related to their size. It is often greater than 90 degrees as viewed in SEM micrographs. Figures 5.2 show two such droplets, the larger one approximately $3\mu m$ in diameter formed

without any gallium first applied i.e. solely under ion bombardment. As will be shown, film development is necessary before droplet formation can begin at low temperatures. This simple experiment shows that the ion beam is capable of producing smaller structures from a pre-formed Ga film and can provide the driving force for droplet formation once a film has developed under ion bombardment.

5.4 Results and Observations

Photographic evidence of droplet production and motion in various stages of their lifetime is presented in the figures. Both scanning electron micrographs (SEM) and scanning ion micrographs (SIM) were obtained. The SIM images were obtained in situ during the ion bombardment in the secondary electron imaging mode (SEI). Secondary ion images (SII) were also obtained but are not presented here due to the small secondary ion signal and consequent poor quality micrographs. Figures 5.1a and 5.1b (SIM) depict the evolution of particle sizes during room temperature ($\sim$20°C) Ga^+ bombardment of GaAs at 25 keV beam energy. The figures suggest a bimodal particle size distribution of nearly uniform larger particles and a more or less uniform distribution of smaller particles. As seen in these two micrographs, there is no apparent correlation between droplet sizes at different times. For example, while particles 1 and 2 of Figure 5.1a are nearly the same size, particle 1 continues to grow while particle 2 diminishes as shown in Figure 5.1b. This figure reveals some other general features of droplet evolution. Particles 3 and 4 of Figure 5.1a appear to touch enabling the formation of a larger droplet by coalescence. Yet, as shown in Figure 5.1b, what appears to be the same particle(s) (now labeled $3'$) has lost approximately 95% of its volume while particle 5 has lost less than 75% of its volume. Par-

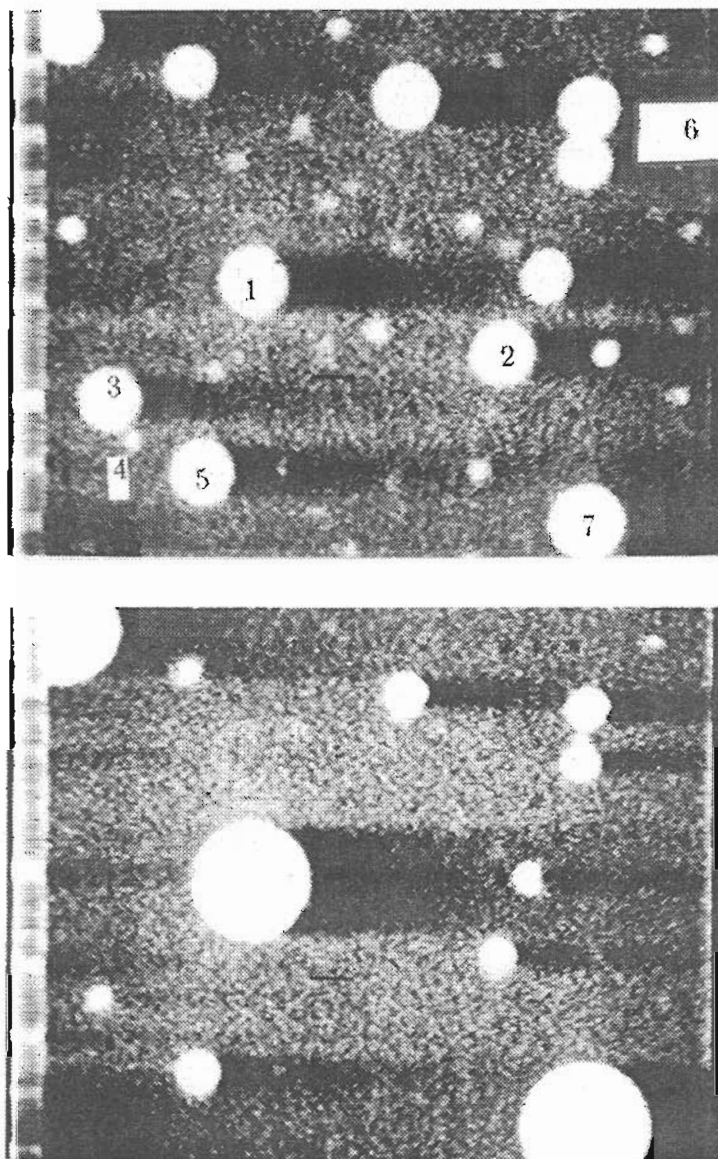

Figure 5.1 SIM images depict the non-uniform growth of particles at 25 keV. Note that it is not possible to predict which particles will increase or decrease in size. Upper: Particles 1, 2, 5 are nearly the same diameter.

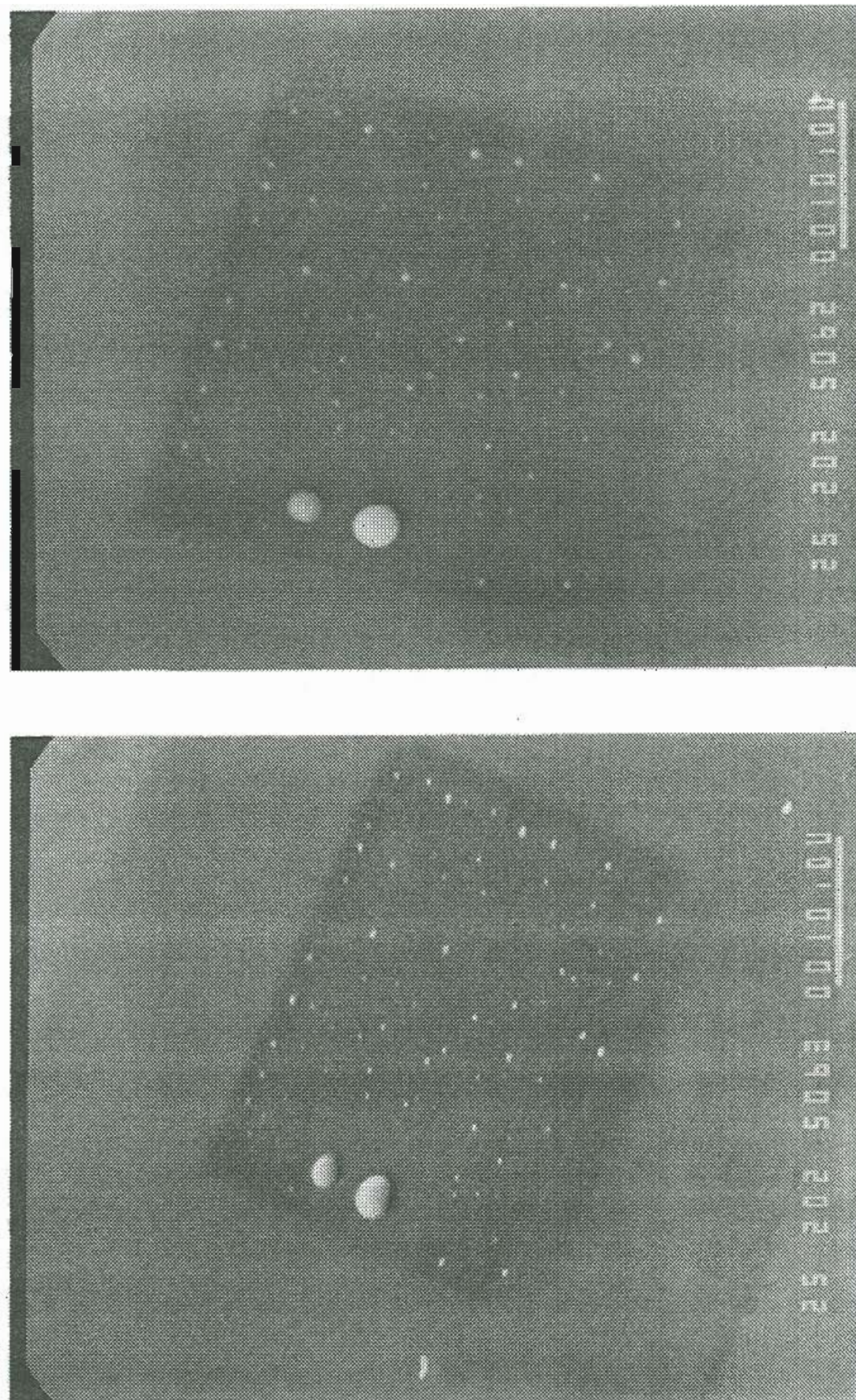

Figure 5.2 SEM micrographs of droplets formed after Ga^{+} ion bombardment. Large droplet is $\simeq 3\mu m$ in diameter. Several interesting features are evident. The particle size distribution is approximately bi-modal i.e. almost uniform smaller particles with few (2) larger particles. Droplets are essentially hemispherical and rise above the surface. The contact angle of the larger particle appears > 90 °. The sample was tilted $\simeq 40°$ in the lower micrograph.

ticles 6 also appear to touch, however Figure 5.1b indicates that they diminish together and never combine. There are other examples in subsequent figures and numerous examples from micrographs not represented in the figures which illustrate this general behavior. On the other hand, droplet coalescence has been observed in other micrographs and in video tape records. These indicate that during ion bombardment a nebulous liquid-like material often moves between well formed droplets. This is barely visible in particles 6 of Figure 5.1b but this phenomenon is quite visible in some of the video recordings. There is no apparent relationship between the direction of motion of this material and the size of the droplet from which it emanates i.e. the material may move away from or toward a larger or smaller droplet to feed or starve it. The life cycle of these droplets is difficult to predict since it is determined by the simultaneous effects of direct transport of metal in the beam, sputtering of the droplets and the surrounding target at variable rates as droplets form, transport of material between droplets due to redeposition and surface diffusion and the direct motion and coalescence of droplets. Observations reveal that there is no critical particle size which ensures that a given particle will survive. This is in contrast to the film formation mechanisms in vapor phase condensation and in low energy (~ 100eV) ion bombardment enhanced film formation[109] which require that only those particles larger than some critical size will survive while smaller ones evaporate. Therefore, it does not appear possible to predict, by observation alone, whether a given particle will be sputtered away by the ion beam or grow by the accretion of unformed material and coalescence of nearby drops.

We note that the droplet formation discussed here most likely occurs relatively late in a process which begins with film formation. The evidence for this is presented in a discussion of the micrographs.

5.5.1 Micrographs

The total volume sputtered and the ion dose between micrographs are easily calculated. The total droplet volume, and the change in droplet volume can be calculated assuming a nearly hemispherical shape. Figures 5.2 for example, show that this may be a valid assumption, particularly for the larger droplets, ($3\mu m$ in the figure) thus giving an estimate of the droplet volume. Returning to Figures 5.1a and 5.1b, the ratio, $R = \frac{\text{droplet mass}}{\text{mass input}}$ can be calculated. There may be a large error in calculating the volume of small particles due to the r^3 dependence but their contribution to the total volume is small. Therefore, their contribution to the total error will be small. Figure 5.1a gives a droplet volume of 57 μm^3 and a mass input of 1.2 x 10^{-10} grams from the ion beam. The density of liquid gallium is $\sim$ 6 g/cm^3. Scanning Auger Microscopy (SAM) reveals that droplets are typically 86.4 at. % Ga and 13.6 at. % As. For simplicity then, we assume that 86.4% of the droplet volume is due to gallium. Considering this assumption and the error involved in calculating droplet volume from the micrographs, we must be satisfied with a semi-quantitative estimate. Finally, we find that $R = 2.4$ for Figure 5.1a while Figure 5.1b gives a droplet volume of 93 μm^3, a mass input of 2.3 x 10^{-10} grams and the value $R = 2.1$. These numerical estimates indicate that not all the gallium present in the droplets comes from the beam. At least half the gallium is released from the GaAs substrate itself probably due to a preferential loss of arsenic. The mechanism for this is not known at present. Preferential sputtering due to mass differences can hardly be responsible since the masses are barely different but, as discussed in the Background section, other mechanisms may be available. In contrast, Ishitani et al[105]. reported on gallium condensation after Ga^+ LMIS bombardment of silicon. Obviously, in that

case, all the gallium present as liquid came directly from the beam. A direct calculation was not made and would have been difficult since the liquid gallium shape was not well defined and the thickness unknown. Retention of gallium within the silicon matrix was justifiably assumed negligible due to its small solubility in silicon (0.1%)[106]. The experiments of Ishitani et al. were repeated at OGC and yielded similar results. Figures 5.3a and 5.3b are SEM micrographs revealing another phenomenon which is sometimes present. It appears that segregation of material within the droplets has occurred. This is manifested as the bright material at the droplet center surrounded by darker material within several of the droplets. Notably, this is visible only for the smaller particles and is particularly clear for particles 3 - 8. It may be that all the droplets in the figure have such a "cap" material but it is only observable where the surface concentration is high enough. Unfortunately, it has not been possible to analyze their composition but the increased secondary electron signal suggests a different composition. Another example is given in Figure 5.4b where a very bright particle can be seen at the upper left of the micrograph. Occasionally, bright particles are visible amongst a field of "normal" darker particles. It is reasonable to speculate that this must be due to a composition difference which produces a different secondary electron yield since the topographic contrast should be nominally the same. Figure 5.3b is the SEM counterpart of the SIM image 5.1b. As indicated in Figures 5.5, SAM has been utilized to reveal three distinct surface compositions within bombarded areas, with the signal intensities adjusted for the elemental sensitivities for gallium and arsenic. The corresponding analyzed regions are indicated in Figure 5.6 with the following results given for Ga/As in at. %:

Pt. 1. Ga rich droplets 86.4/13.6

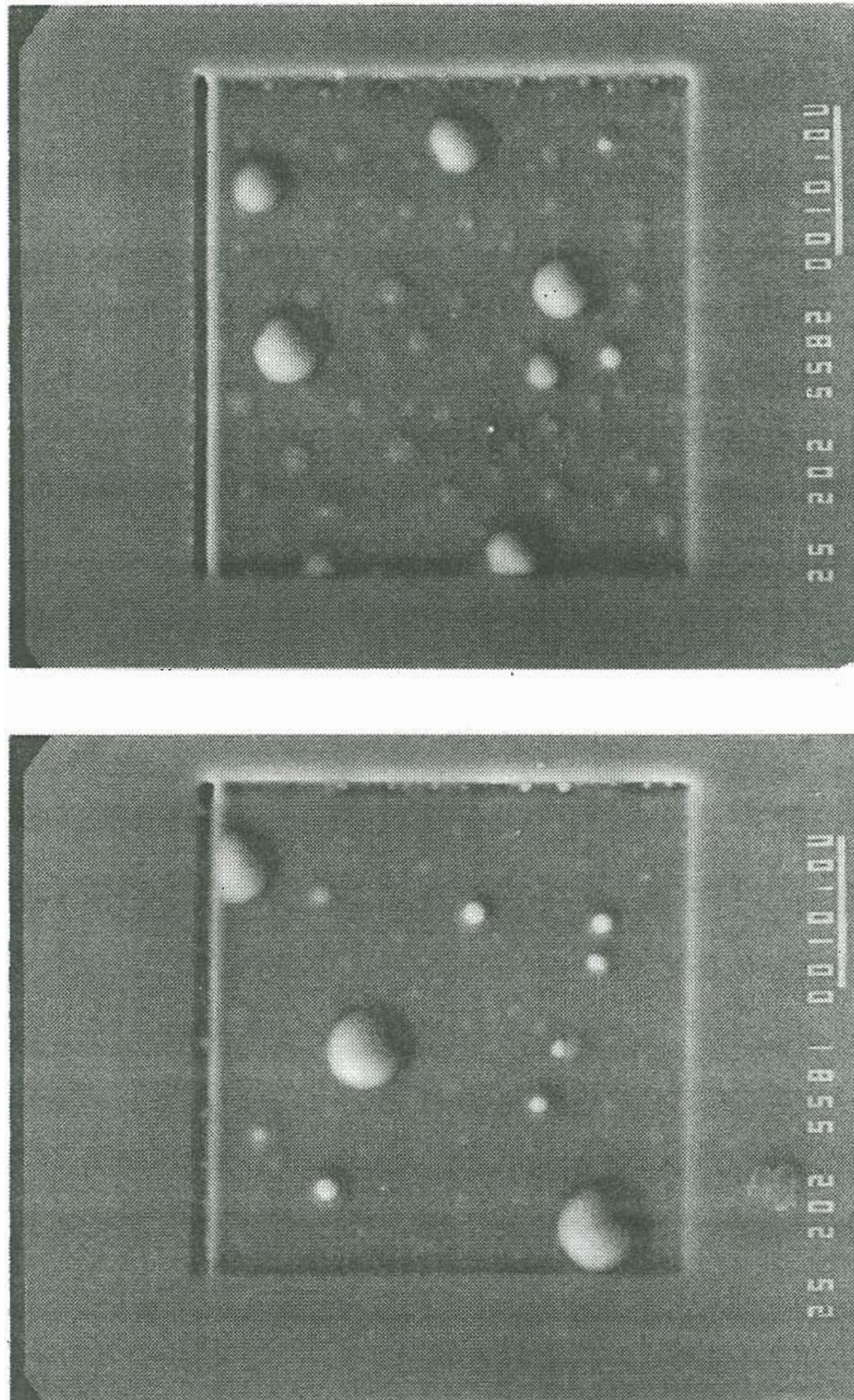

Figure 5.3 SEM micrographs reveal evidence of segregation within the small particles. Note the bright areas within their centers.

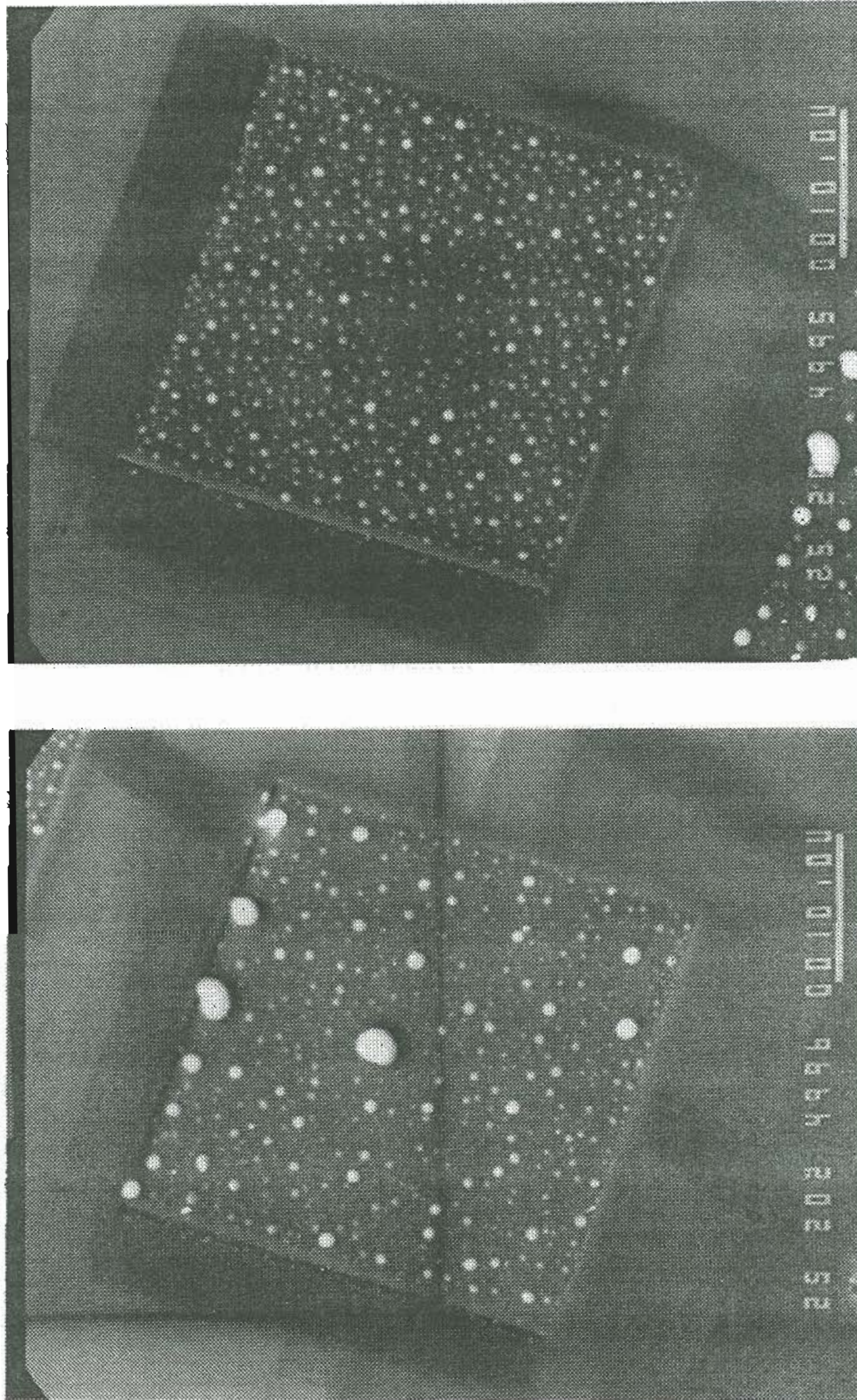

Figure 5.4 The bright particles in the upper left suggest a different average composition from the other droplets. Ion bombardment with the beam somewhat defocused produces larger droplets (lower) than with the focused beam (upper). The dose is approximately 2×10^{16} ions / cm^2 for both.

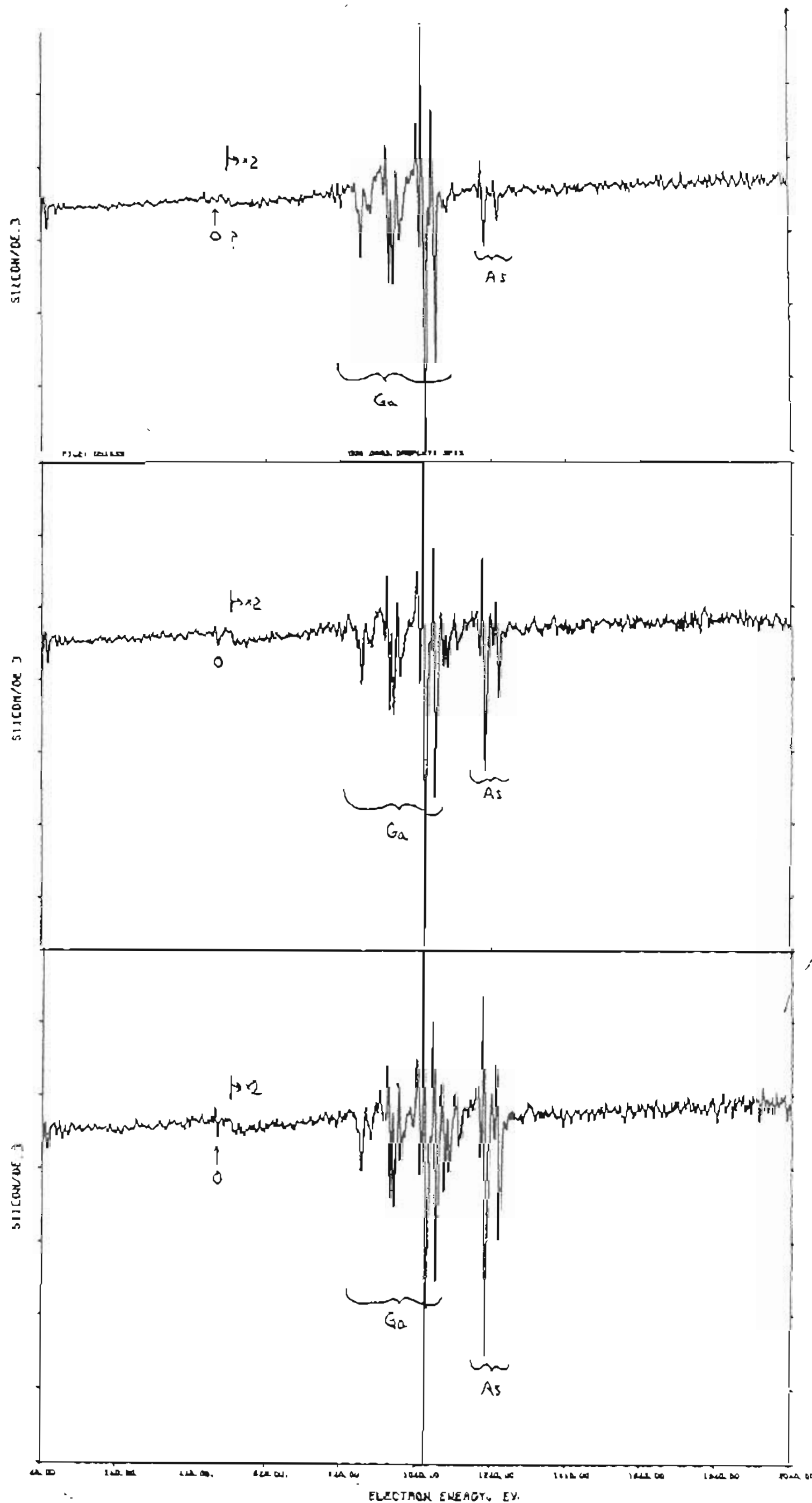

Figure 5.5 Scanning Auger spectra correspoding to points 1, 2, 3 in Figure 5.6. Upper (1); Middle (2); Lower (3)

Pt. 2. Slightly Ga rich " milky " film 54.3/45.7

Pt. 3. "Smooth" floor within the bombarded region between drops and milky film 52.1/47.9

Pt. 4. Outside the high dose region the general surface of the GaAs wafer is As rich 40.8/59.2

Areas far from the Ga^+ bombarded areas represent the virgin wafer of approximately 50/50 stoichiometry.

Material similar to that of Pt. 2 is visible in several micrographs and is the same substance seen moving between the droplets observed in the video tape records. The relative depletion of gallium in the Pt. 4 area points to a dose dependence of the surface concentration. The dose is unknown for this area but is probably less than 10^{13} ions / cm^2 due to brief ion exposure while moving the sample and focusing the beam.

5.5.1.1 Effect of substrate temperature

A series of experiments was performed under the experimental conditions described earlier in order to determine the substrate temperature dependence of the droplet formation and motion. The following are descriptions of SIM micrographs taken in the SEI mode.

5.5.1.2 Threshold dose

We define the threshold dose D_{th} as the dose acquired by the sample immediately before the onset of droplet formation. This was determined in situ by observing

the CRT monitor. There is some uncertainty in this since it relies on determining the general condition of the bombarded surface. To obtain the relative dose for different conditions, one must decide that the observation has been made at the same relative point in the evolution of the droplets. This requires that the viewing conditions are the same and calls for a subjective decision. Therefore, it was decided to choose as the definition of D_{th} the point at which any deviation in the surface topography could be observed. It was always found that the droplet formation itself was imminent within a second or so of this time so the absolute error will be small. Figure 5.7 shows that D_{th} is a decreasing function of energy. This data is for room temperature FIB bombardment.

5.5.1.3 Micrographs A Note: Micrographs appearing six per page are consecutive across a row and return to first column.

The series of micrographs in Figure 5.8 show that the first stage of drop formation at a substrate temperature T = - 51 °C for 20 keV Ga^+ bombardment begins with film formation (a). The total ion dose is 6.9 x 10^{16} ions/cm^2, corresponding to roughly 70 monolayers, if the film were uniform. The film is distinctly nonuniform however, and it appears that droplets form at boundaries between regions of differing film thickness. The ion dose is already approximately 2.4 times greater than required for room temperature (~20°C) droplet production but the formation process has barely begun. Figure 5.8b probably corresponds more closely to the point which would be defined as the beginning of droplet formation under room temperature bombardment. This dose is 2.6 times the experimentally determined threshold dose at room temperature for the same bombardment conditions. Only 34 seconds has elapsed between Figures 5.8a and 5.8b. Approximately 2 minutes 40 seconds has

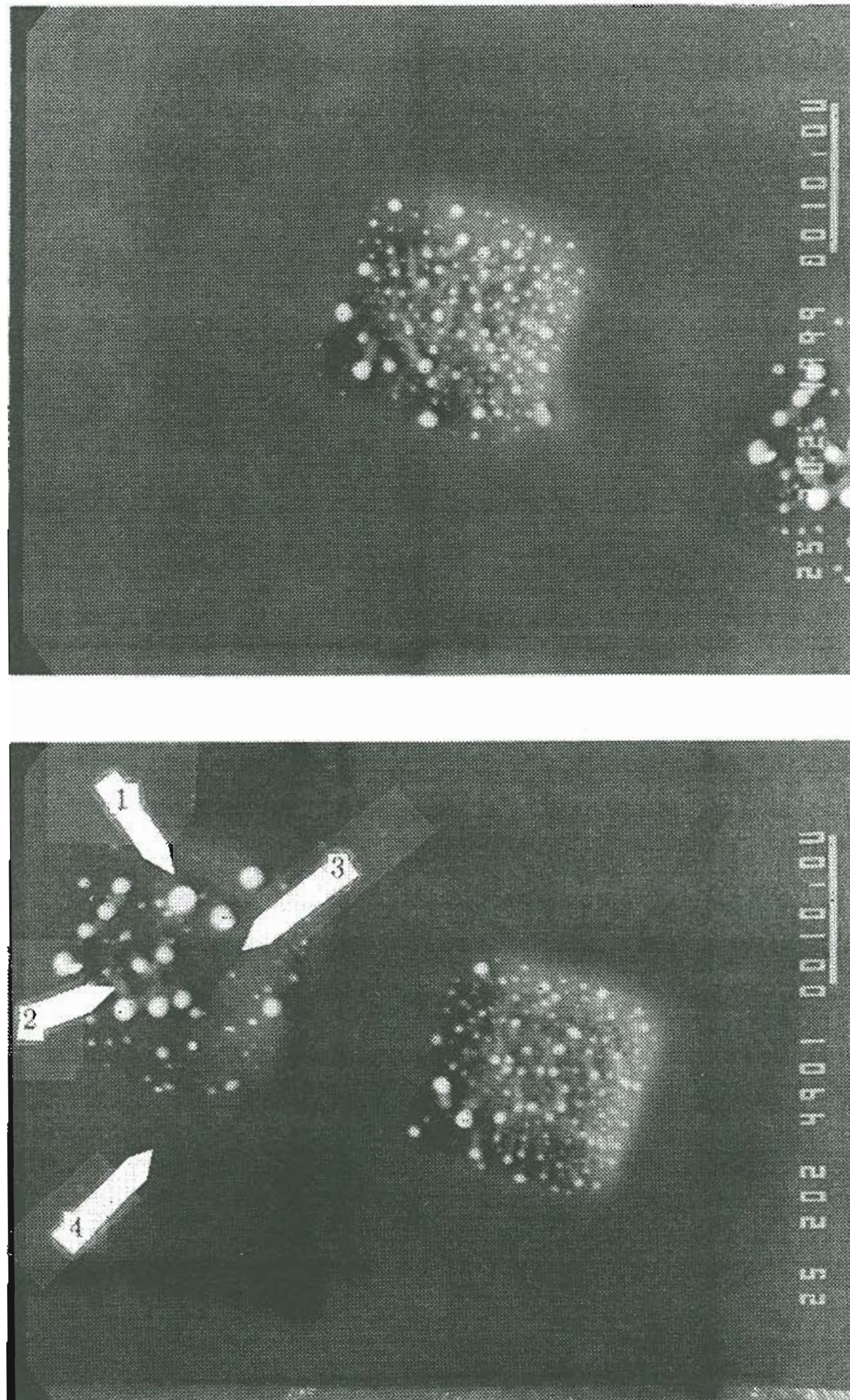

Figure 5.6 Points 1, 2, 3, and 4 identify the different Auger analyzed areas. The FIB exposed areas show that the degree of ion beam focus is correlated with the resulting droplet size.

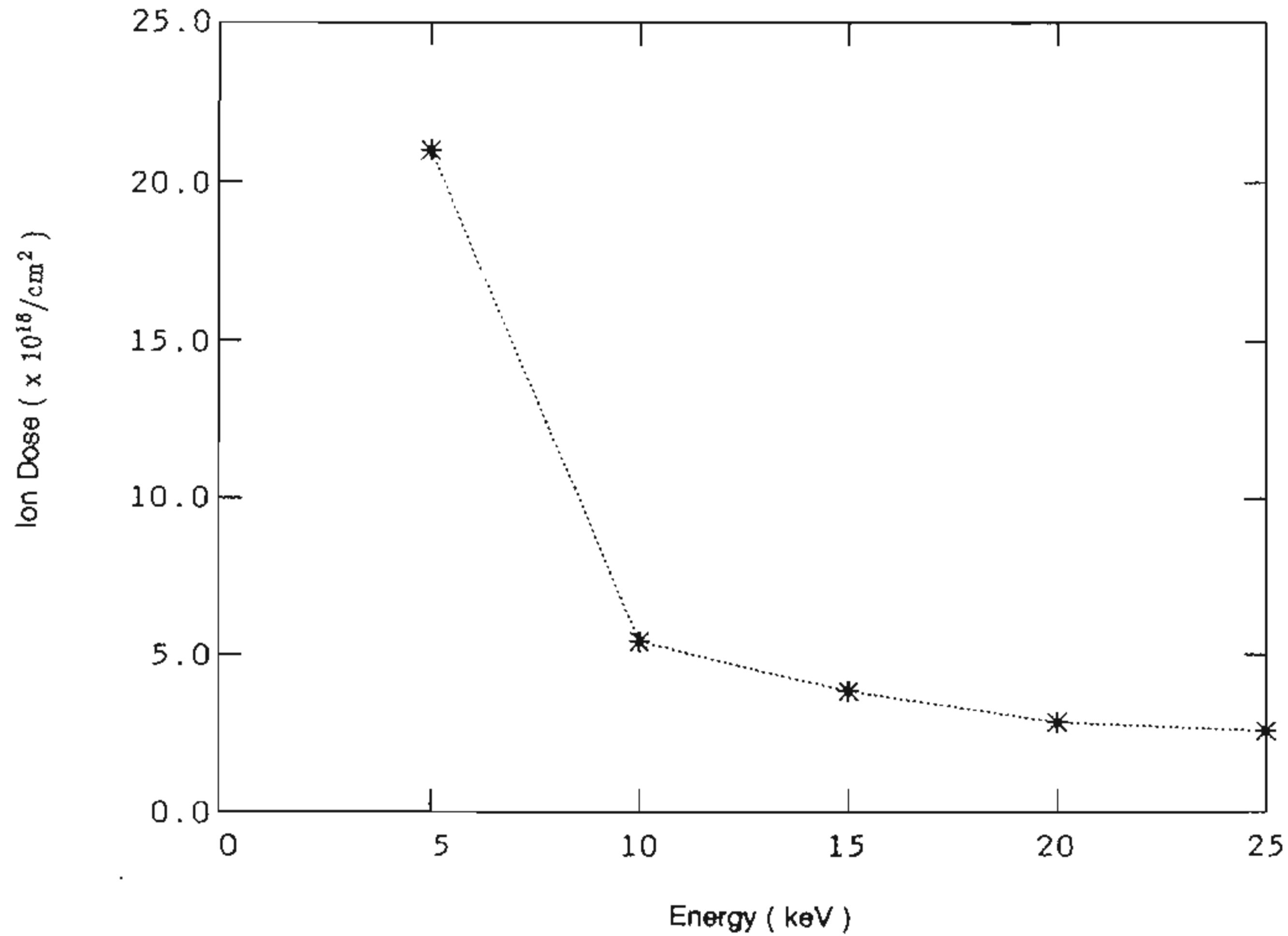

Figure 5.7 Threshold dose dependence on ion bombardment energy at room temperature.

elapsed between 5.8a and 5.8f showing that rapid growth and mobility is observable during ion bombardment.

The next experiment was done to determine if there is any motion without ion bombardment. This might occur at the lowest temperatures if the time needed to reach a minimum energy equilibrium was long i.e. the liquid is very "sluggish". Figures 5.9a-f are SIM micrographs taken with the ion beam blanked and the target allowed to warm. The temperature was allowed to increase from T = - 38 °C to T = -20°C in 14 minutes by turning off the liquid nitrogen flow. The only ion bombardment of the target is during the photographic exposures which lasted for 1 to 2 seconds. Micrographs (a) through (c) reveal that there is indeed material motion. Particle(s) 1 are identified with a circle in the upper center of the micrographs. Between (a) and (c), it is clear that the small particle to the left of the larger one is gradually moving towards the larger particle. By (c), the small particle has been partially incorporated into the larger one and by d has been entirely absorbed. This is rather remarkable as it demonstrates the movement of a particle roughly 0.7 μm in diameter over a comparable distance with an average speed of nearly 13 Å per second. A possible explanation is that the motion occurs only during the brief photographic exposure. Some charging is evident from these micrographs also. For example, the entire image is moving towards the top of the frame between a and f. With the beam blanked for 5-15 seconds, the image returns to its original position as the surface potential relaxes with a characteristic time constant. In so doing, the incident beam is deflected, causing image motion. As this affects the entire image however, it is difficult to see why a given particle should move while others remain stationary if charging were responsible. It is probably also safe to assume that the entire surface is at equipotential and therefore there should be no relative motion due to charging.

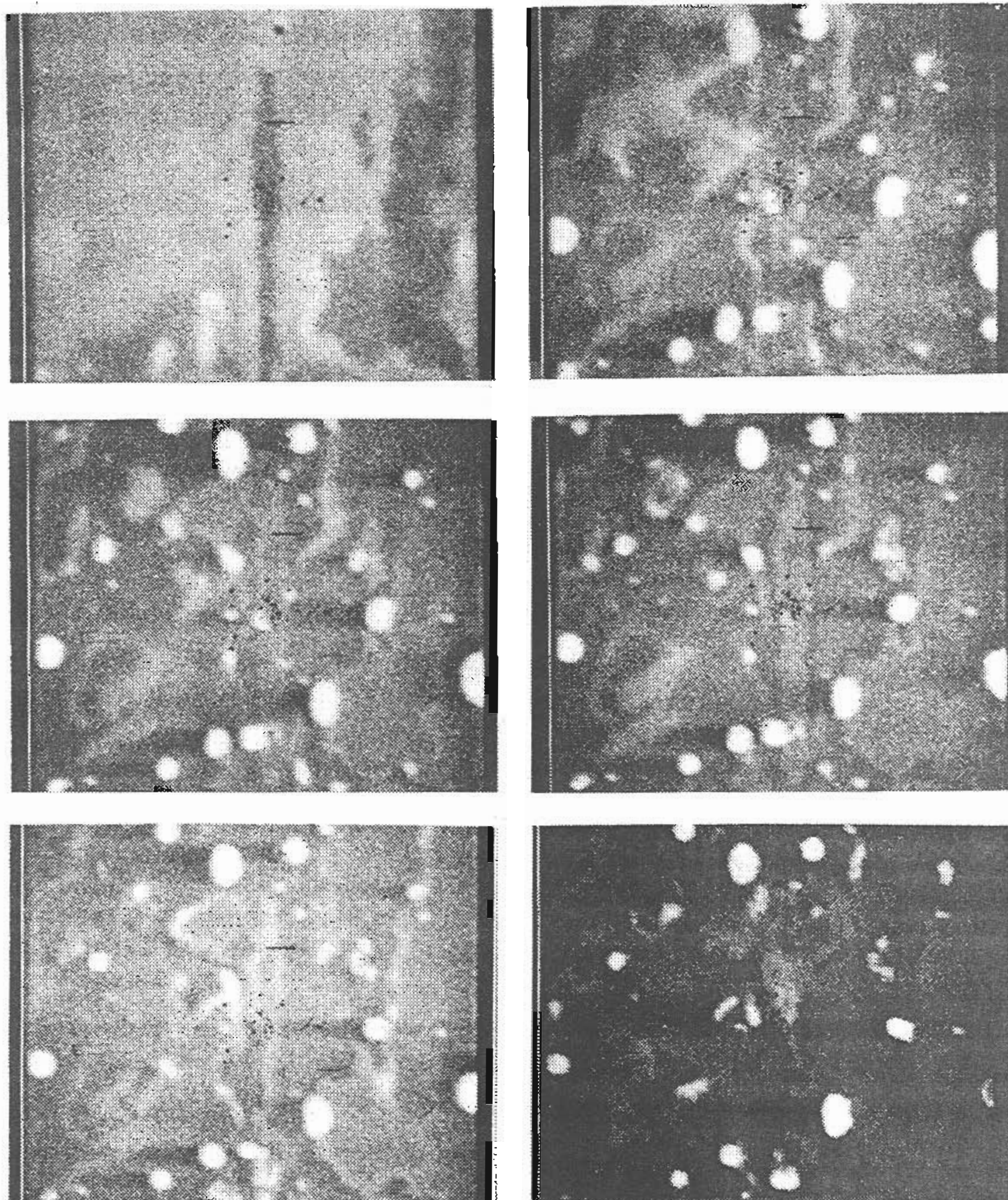

Figure 5.8 SEM micrographs of the first stages of droplet formation (at low temperatures). At a substrate temperature T = - 51 °C, droplet formation begins with a nonuniform film.

Instead, it may be that we are observing an irregularly shaped " particle " of high viscosity material in the process of reshaping itself as the temperature increases.

5.5.1.4 Micrographs B

These SIM images show the film formation beginning at a dose of 7.4 x 10^{16} ions/cm^2 with substrate temperature T = - 56 °C. The beam energy is 20 keV. In Figure 5.10, between (a) and (f) the beam was blanked and no motion is evident. During micrographs 5.11a-f the sample was allowed to warm from T = - 56 °C to T = - 44 °C. There is no noticeable motion of the film until (e) at $T = -38°C$. In Figure 5.12, micrographs (a)-(f) are very interesting in that they show droplets being formed directly from the film. The non-uniform film near the boundaries between thicker (brighter) and thinner regions defines the sites from which droplets grow. Other qualitative information can be obtained from these micrographs.

5.5.1.5 Micrographs C

Figures 5.13(a)-(d) show the droplet formation from a film for a beam of energy 20 keV at a temperature $T = -62°C$. Between 5.13(e) and 5.13(d), the temperature remains constant at $T = -62°C$, during ion bombardment. There is considerable ion beam induced mobility of relatively large features (several microns and smaller) during bombardment. Figures 5.13(a)-(f) apparently show that the film is three dimensional (i.e. many monolayers thick) with several non-wetting regions. Again the non-uniformity of the film is evident and the droplets form at boundaries. With increasing ion dose, the film thickness increases as evidenced by the build up of material around the non-wetting regions. Further bombardment results in the

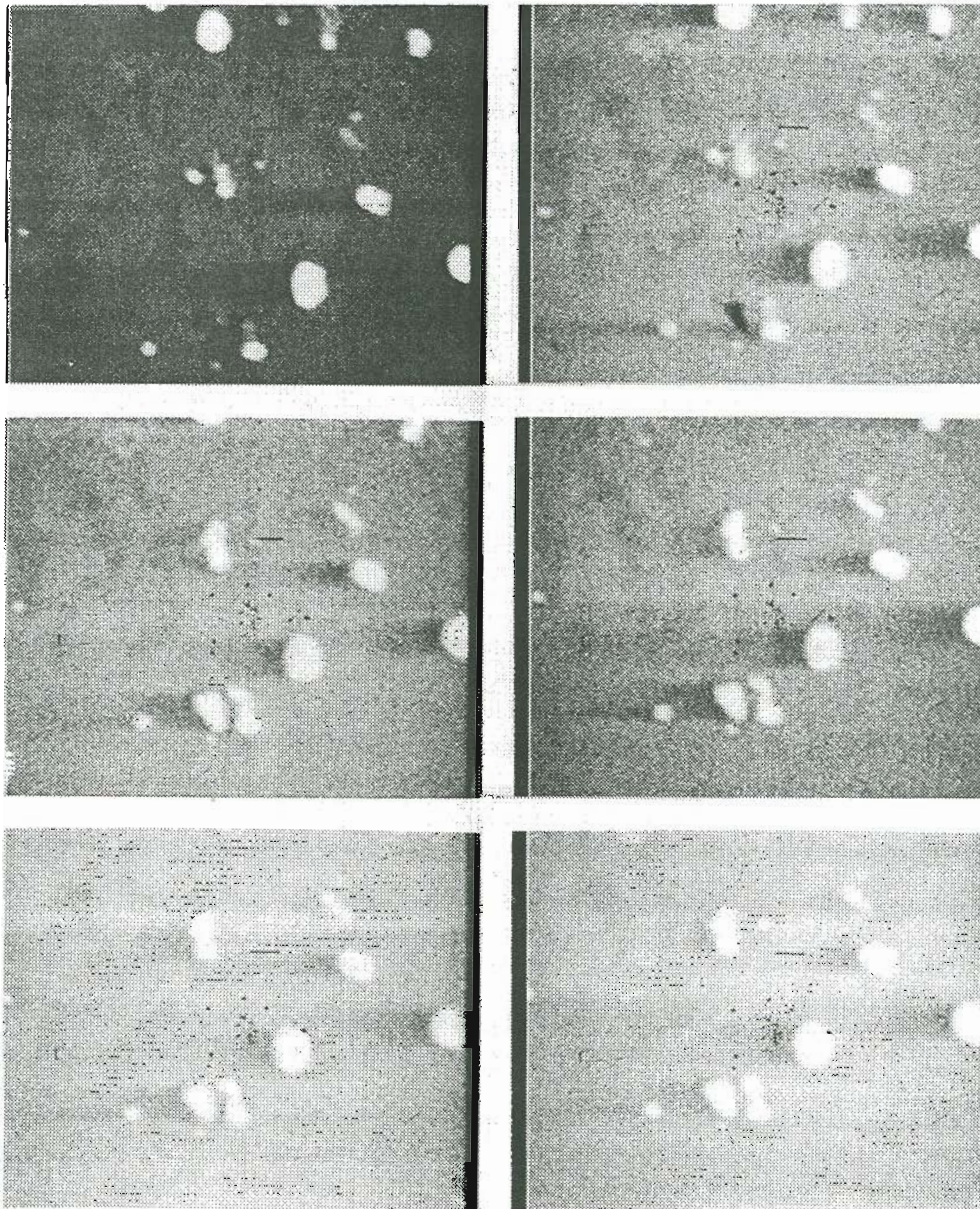

Figure 5.9 SIM micrograph depicts possible material motion in the absence of ion bombardment. The substrate temperature was allowed to increase from T = - 38 °C to T = - 20 °C in 14 minutes.

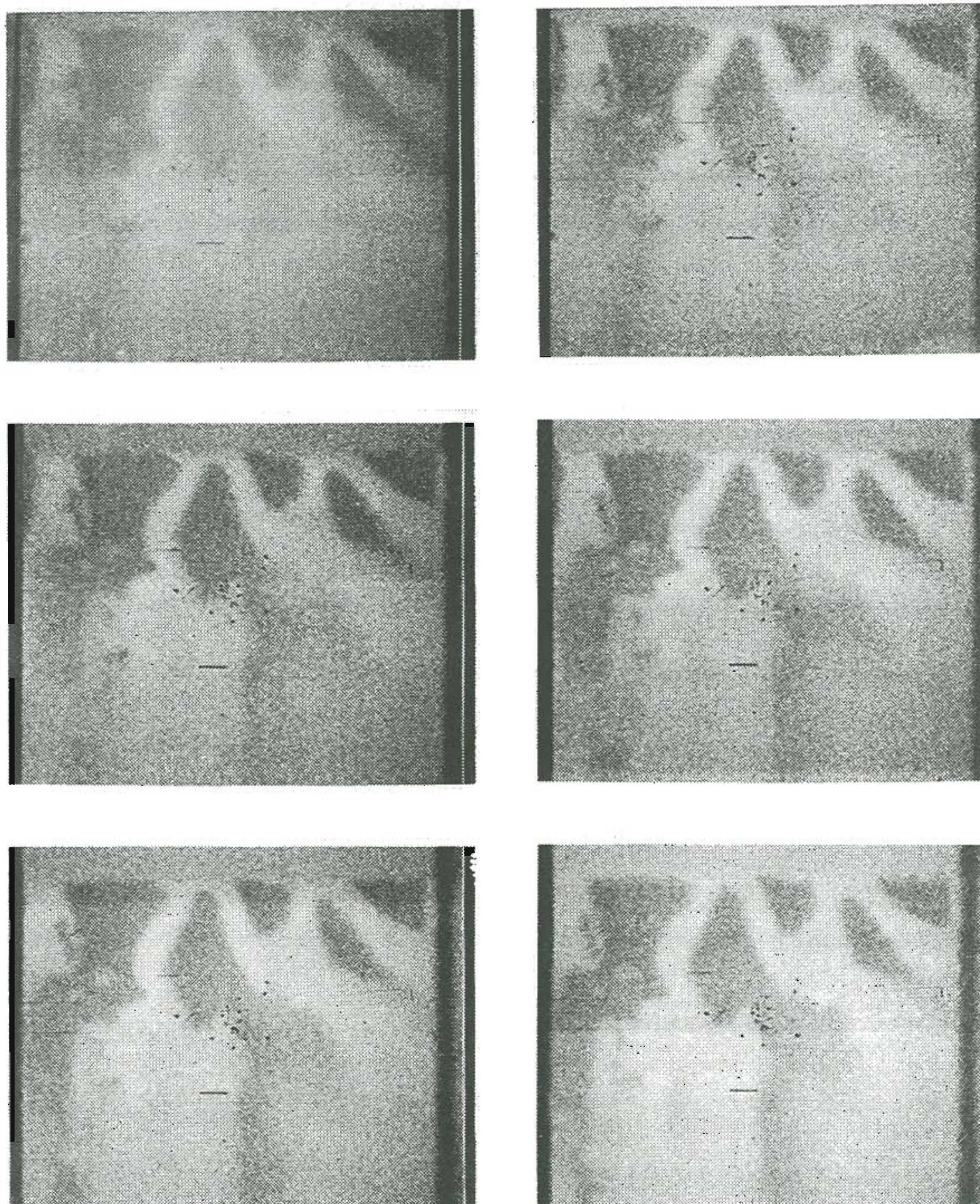

Figure 5.10 SIM micrographs show the earliest stage of film formation beginning at a dose of 7.4 x 10^{16} ions/cm^2 with the substrate at T = - 56 °C. No motion is evident with the ion beam blanked (a)-(f).

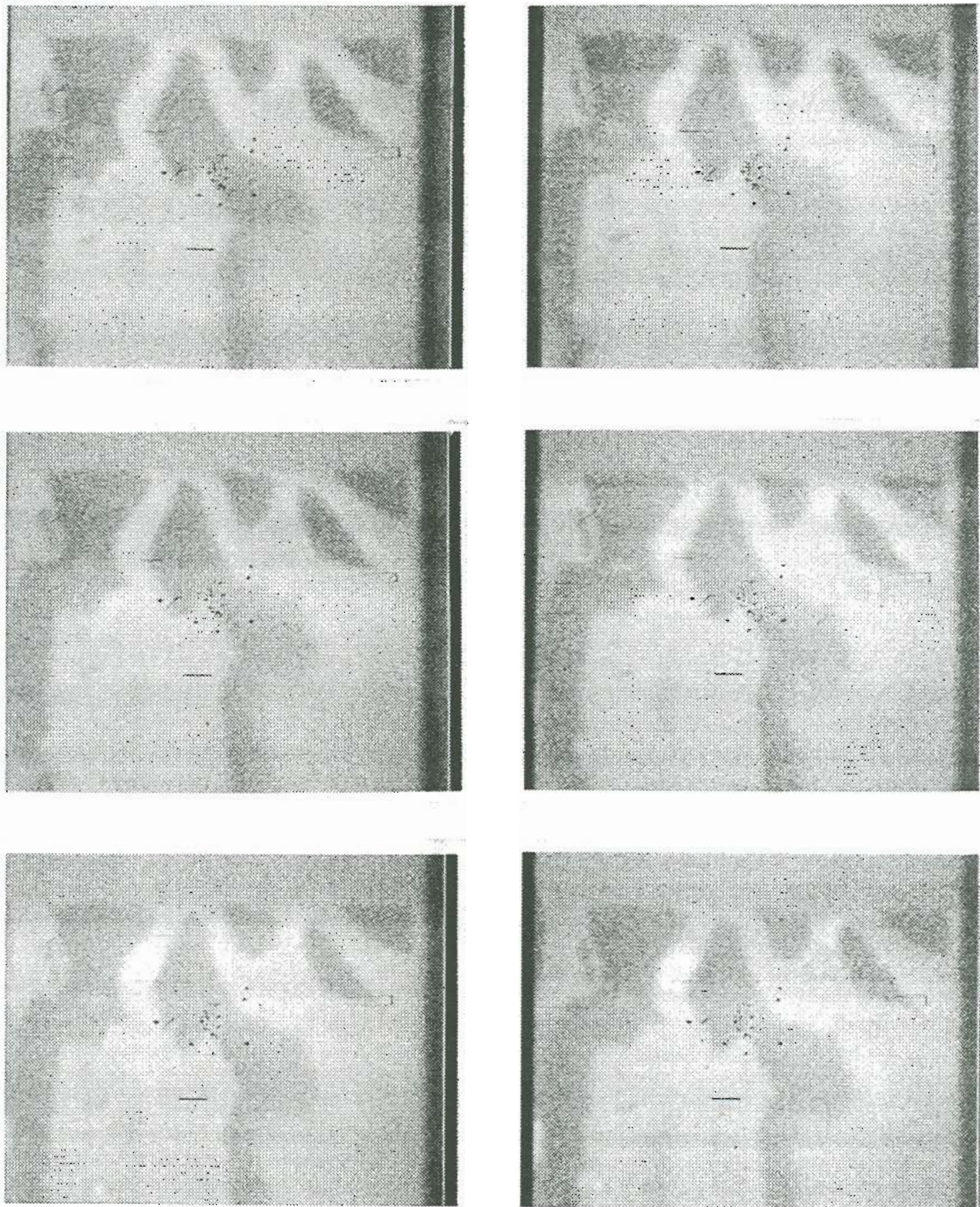

Figure 5.11 Previous series continued. The sample is allowed to warm from T = - 56 °C to T = - 38 °C where some slight film motion is evident at (f).

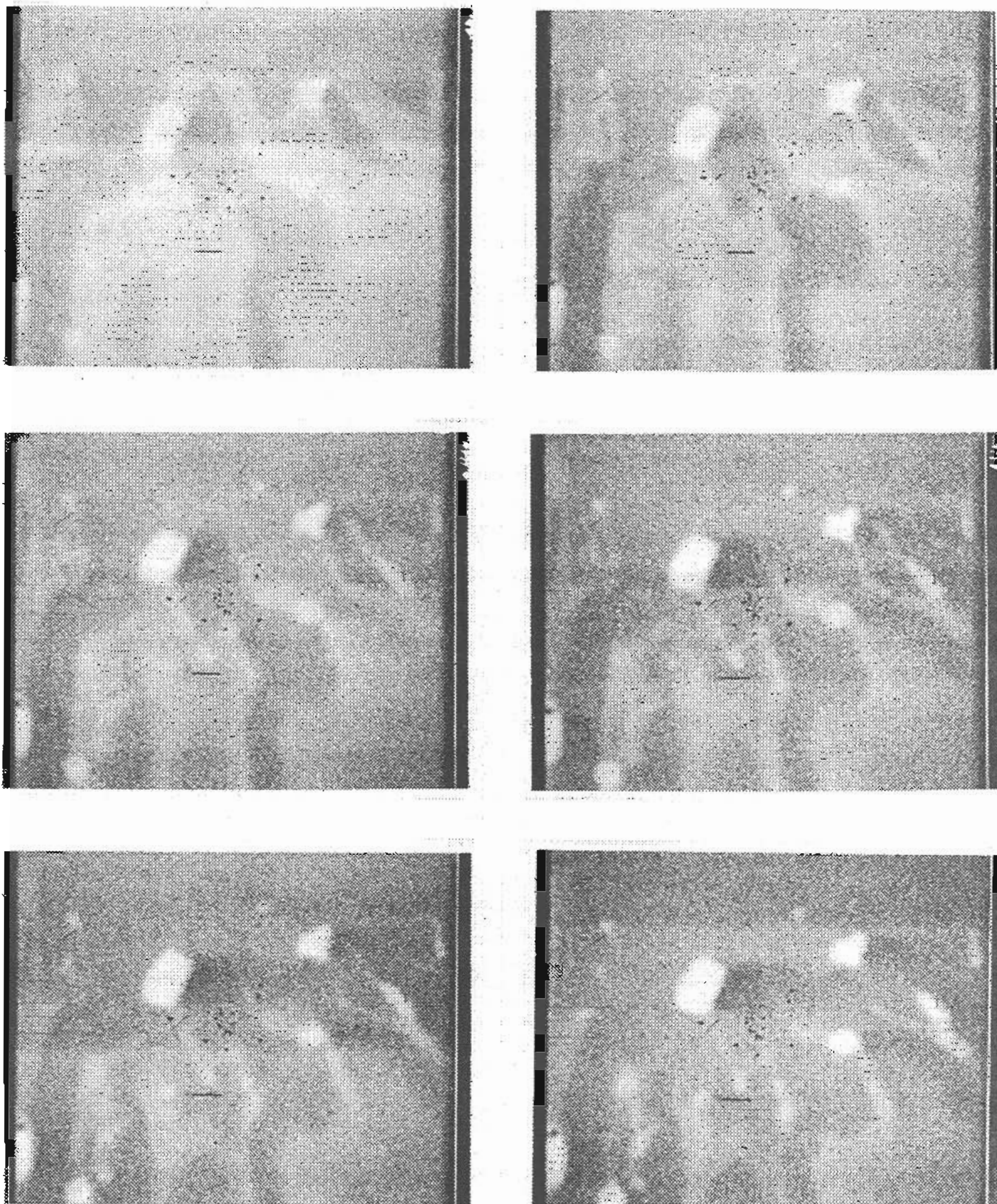

Figure 5.12 SIM micrographs (a)-(f) clearly indicate that the droplets form at the boundaries of non-uniformly thick film.

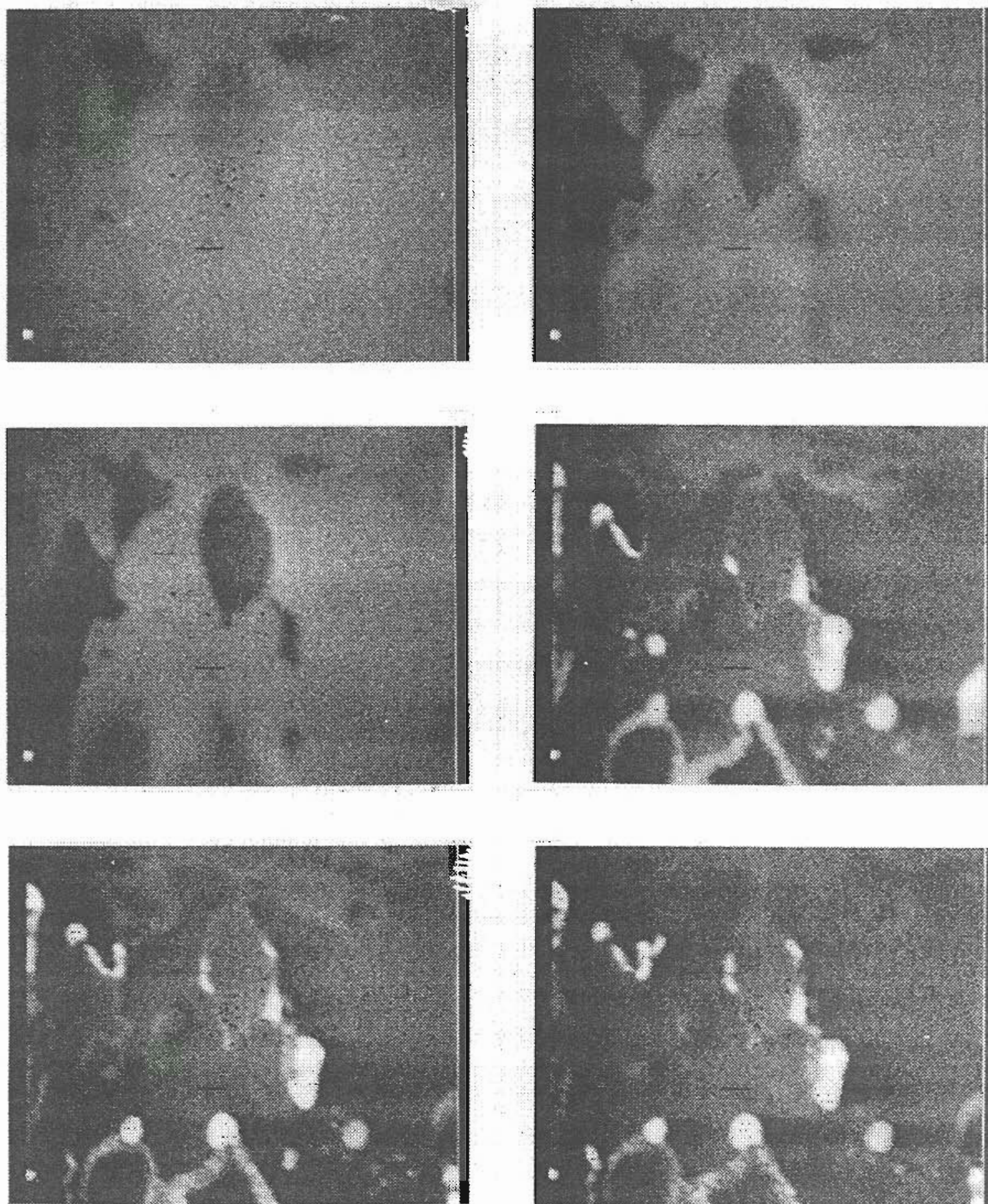

Figure 5.13 SIM micrographs depict film formation and subsequent droplet formation at T = - 62 °C at 20 keV. Ion beam induced motion of large features (several microns) is evident.

"condensing" and thickening film breaking up into smaller particles. The triangular region at the bottom center of 5.13 illustrates this.

5.5.1.6 Micrographs D

Figure 5.14 depicts several of the features already discussed including droplet coalescence. During series (a)-(f), the substrate temperature decreased from T = + 26 °C to T = - 46 °C during ion exposure. At (f), the first indication of droplet freezing is evident and is conspicuous by 5.14(f) through 5.15(a)-(c). Since the beam and droplet have azimuthal symmetry one would expect the droplet to be sputtered uniformly when viewed from this direction. This is not the case, however. The shape assumed by the droplet probably depends on the angular dependence of the sputtering yield and the ability of atoms to move about at thes temperatures. Notice that by 5.15(f) the droplet is round once again, apparently at the beginning of another such cycle. and the temperature dependent bombardment induced atom mobility.

5.5 Discussion

The mechanisms involved in the droplet formation discussed here are complex. As we are dealing with a two or three component substrate (GaAs or $Ga_{1-x}Al_xAs$ with layers where x may have different values) the FIB Ga^+ bombardment will undoubtedly produce a variety of complications caused by preferential sputtering, collisional mixing, and enhanced bulk and surface diffusion. Of course, even a single component substrate may be considered as a two component substrate once the Ga^+ bombardment occurs. It is plausible that we can gain some understanding of the present phenomenon by considering the related processes occurring in low energy ion

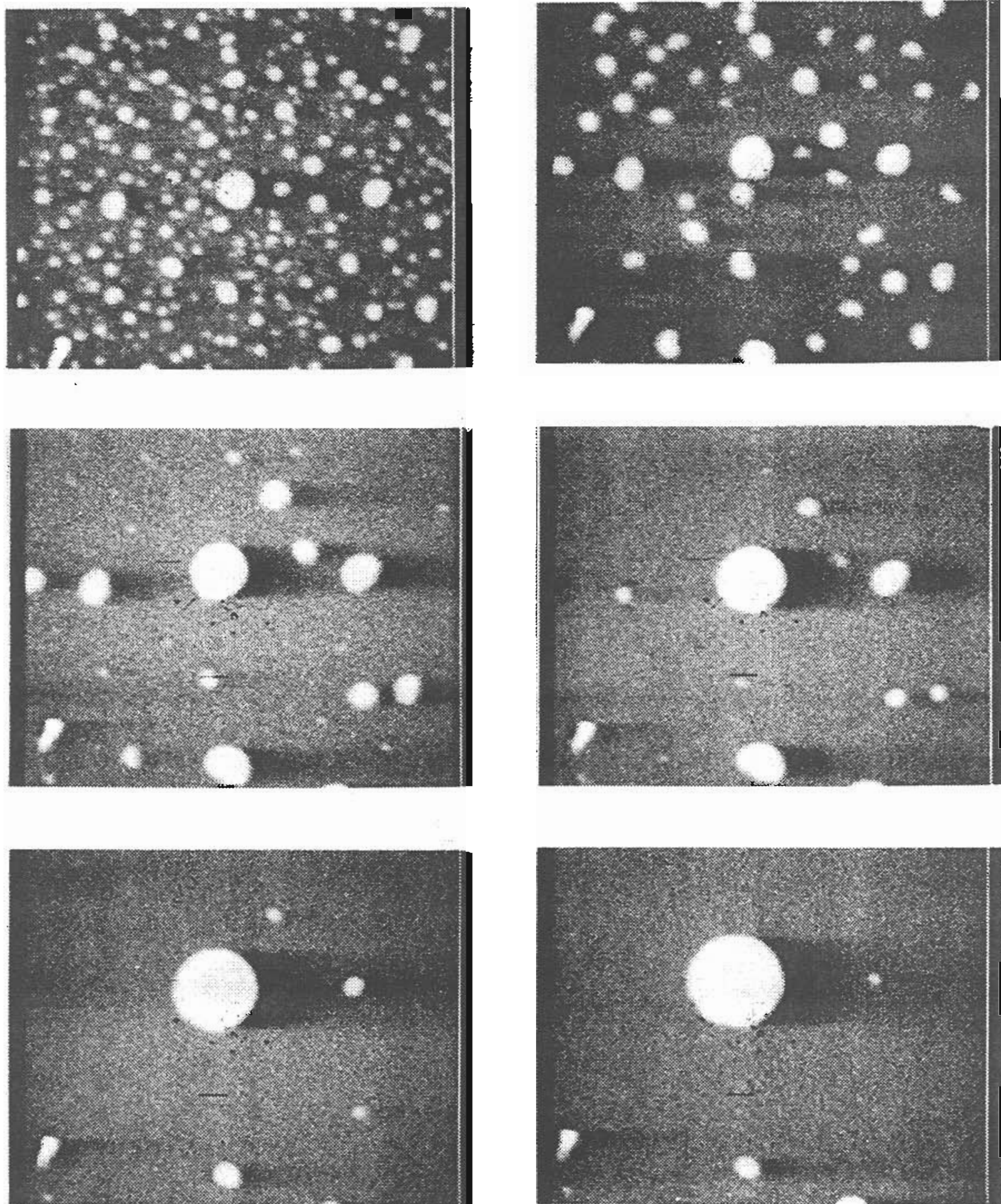

Figure 5.14 SIM micrographs indicate first evidence of droplet freezingbeginning at -46 °C during ion exposure.

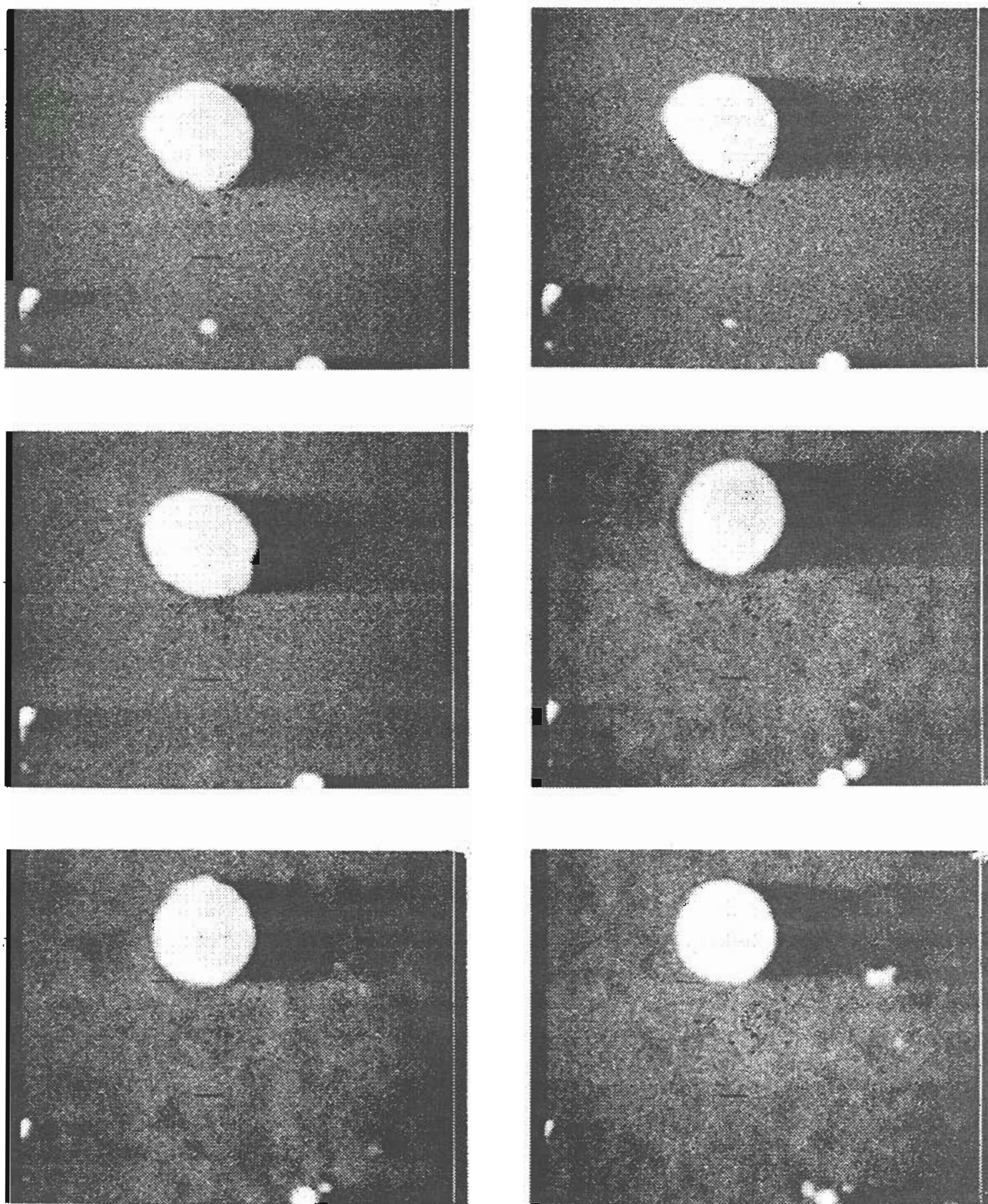

Figure 5.15 Previous series continues. Note that the frozen droplet appears round in (f).

bombardment during vapor phase film deposition[109]. Further understanding may come from examining the issues involved in sputter cone deposition; particularly the enhancement of surface diffusion by ion bombardment[93].

Unfortunately, the analogies should probably not be carried too far. The FIB energies and current densities are many times larger than those employed in broad beam techniques which use beams with energies in the range < 100 eV to a few 100 eV. Therefore, further complications in understanding the present observations are due to the simultaneous implantation and sputtering as well as the possibility of non-linear collision cascades occurring within the FIB bombarded substrates.

In the following, no attempt is made to provide a thorough understanding of the mechanisms involved in the motion and morphology of the droplet-like structures. However, some possibilities are suggested. This is only a preliminary study which nevertheless represents the first time the origin of the droplets arising during FIB Ga^+ ion bombardment of GaAs and AlGaAs has been examined.

5.6.1 Ion Source Current Effects

There appear to be several different phenomenon involved in the formation of droplets at an ion bombarded surface and in order to sort them out, one must know how much of the droplet mass should be attributed to the beam directly and how much results from the beam/target interaction itself. A possible complicating factor which arises in examining the droplet formation on surfaces is intrinsic to the use of the LMIS itself. Ishitani et al[105]. and Moore and Prewett[108] realized this and operated the source at low currents. During operation of the ion source, droplet emission may accompany ion emission at a rate which depends on the the total extracted

ion current. There can also be a significant ionized cluster component which may carry a large fraction of the total mass in the beam. These aspects must be considered in order to eliminate the possibility that the droplets were carried by the beam directly and to calculate the mass brought to the target by assuming a singly charged beam. The experiments reported here were done with total extracted currents of approximately $2 - 3\mu A$. It is well known that at such currents, the neutral and droplet content of the beam is very small and the charged component contains more than 99.99% singly charged ions[18,19,30,110,111]. Therefore, we conclude that

i. none of the observed droplets is present in the beam itself and

ii. all the mass in the beam is carried by singly charged ions

5.6.2 Droplet size

Another interesting feature of the droplet formation is the correlation between the median droplet size and the ion beam spot size. This is clear from the series of micrographs which show an increase in the droplet size as the beam is defocused. Figures 5.16a, 5.16b, 5.6a and 5.6b together depict a succession of exposures. The dose is the same for each but the beam is progressively defocused resulting in larger droplets. The defocusing causes some expected rounding or softening of the sputtered crater edges. The beam energy was 20 keV. The most dramatic evidence of this correlation is depicted in Figure 5.16c. Two squares were partially overlapped and exposed, each to the same dose of 6.4×10^{16} ions/cm^2 at 25 keV and $T = \simeq 20^{\circ}C$. The defocused beam produced the square to the left of the figure and resulted in a solitary droplet while the focused beam resulted in numerous small droplets. For the

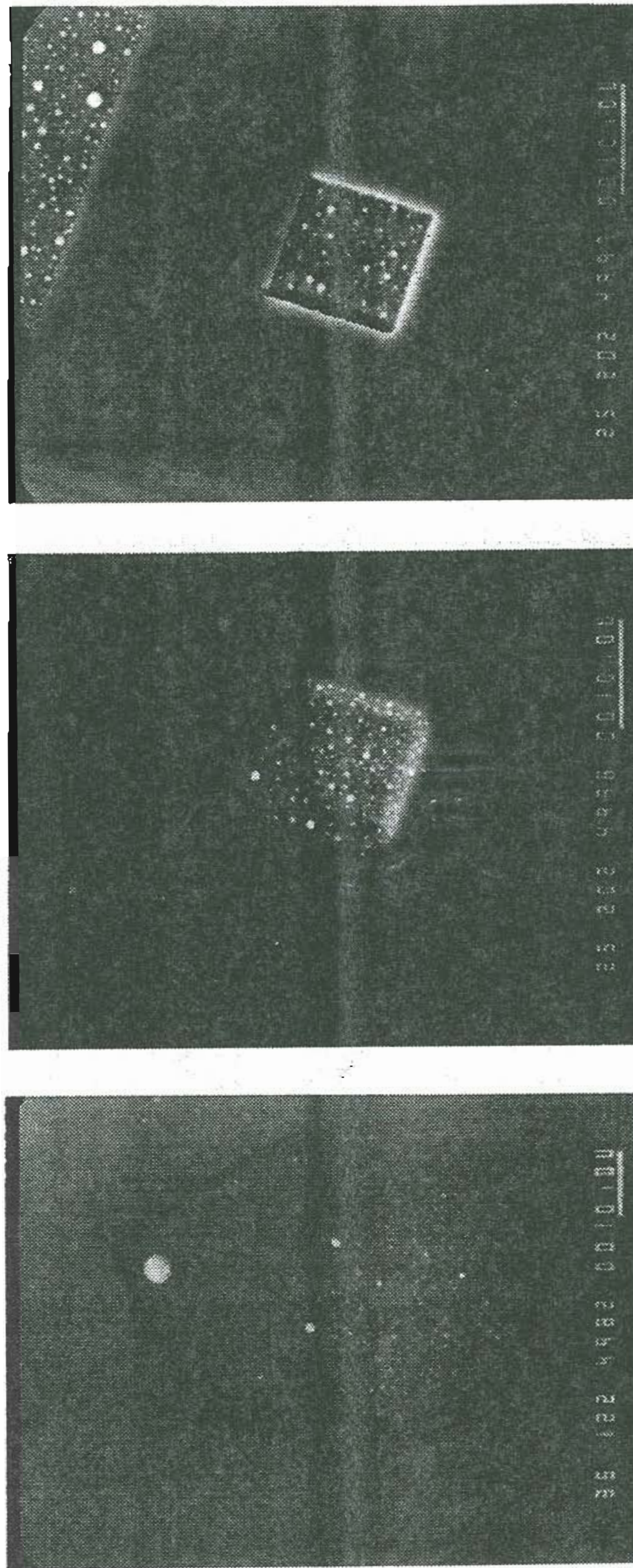

Figure 5.16 SEM micrographs depict the effect of defocusing the beam. Both squares in the lower micrograph were exposed to the same dose but result in dramatically different droplet size distribution.

solitary droplet, and assuming it is hemispherical as before, one finds that R = 1.9. Thus, we see once again that nearly half the droplet mass comes from the GaAs target.

5.6.3 Droplet Motion

The most obvious characteristic of the droplets is that they can move about the surface. Some of the film and droplet motion may be the result of the direct momentum transfer from the ion beam to the surface film itself. A simple calculation shows that at 20 keV bombarding energy, a stationary gallium droplet (in free space) of $1\mu m$ radius can recoil at $1\mu m/sec$. This suggests that the beam momentum alone may be sufficient to move micron sized particles along the surface. However, the uniformity of the bombardment tends to rule out the possibility of momentum transfer in a particular direction along the surface. Nevertheless, despite the uniform ion bombardment, the photographic evidence indicates obvious non-uniform film growth in the earliest observable stages. Therefore, it seems possible that a uniform bombardment of the target may induce motion as material of non-uniform shape and thickness recoils against the beam momentum i.e. there is a large enough component of momentum in the plane of the wafer surface. A less likely possibility is that there is a charge induced component of the motion resulting from the non-uniform surface potential between liquid droplets of various sizes and an eroding and changing semi-insulating substrate. These areas may experience electrical stresses until the physical surface is at equipotential but this is likely to occur many orders of magnitude faster than the time interval during which there is observed motion.

5.6.4 Beam Heating Effects

Heating of GaAs in vacuum can result in the loss of As resulting in Ga condensation at the surface[112]. Thus, beam heating of the substrate during ion bombardment may appear to be a contributing factor to the droplet formation. However, simple calculations of beam heating and experimental work by various researchers indicate that for the incident beam power available, the rise in substrate temperature is small. Despite the large power density of the beam, ($\sim 10^4$ watts / cm^2), the power per spot is still quite small ($\sim 5\mu W$). The temperature increase of a bombarded substrate can be obtained via several related analyses, the results of which are given below. The analysis of M. Lax has been used[113, 114] for laser beam absorbtion in a solid. This analysis is appropriate here since it treats the case where the beam diameter is much larger than the beam penetration depth. For the LMIS FIB used here, the ratio of beam diameter to the projected range is roughly 50 and the results may be directly applied giving:

$$T = \frac{P}{2\pi\kappa} < \frac{1}{r} > \tag{1}$$

where for a Gaussian beam $< \frac{1}{r} > = \sqrt{\pi}\frac{1}{\omega}$ and ω is the beam waist. The classic text by Carslaw and Jaeger[115] considers the problem of the steady state temperature rise in a semi-infinite plate due to the power dissipation from a small spot and obtains:

$$T = \frac{8P}{3\pi^2 r_s \kappa} \tag{2}$$

Finally, a recent review article[41] provides a simple expression under similar conditions:

$$T = \frac{JVr_s^2}{2\kappa\rho} \tag{3}$$

for $\rho \geq r_s$ with ρ a radial coordinate centered at the origin of the incident beam spot. J is the current density and V the beam voltage. For the foregoing equations, P_b is the incident power, r_s the spot radius and κ the thermal conductivity of the target. For GaAs, $\kappa \sim 0.5W / cm-{}^\circ K$. These expressions indicate that for the typical beam conditions of these experiments, and depending on the particular assumptions used, the temperature rise will lie in the range ~0.07 to ~0.2 °K. This is certainly not large enough to induce thermal effects in the substrate. Experimental work by other researchers also support this conclusion. Furthermore, there was no measurable temperature rise during ion bombardment for the present experiments although the thermocouple could easily detect changes less than 1 °C. Since temperatures of 650°C are required to produce Ga droplets on the surface of bulk GaAs in vacuum by heating alone[112] it appears unlikely that beam heating due to ion beam bombardment plays a role in the droplet formation. The possibility that there is a "local" thermal effect must also be considered. It is conceivable that there is a local volatility of arsenic due to its high vapor pressure. According to Kelly[116] in some situations, an enhancement of the sputter yield, S , is observed which may have a thermal origin. These so-called thermal spikes may be divided into "prompt thermal" and "slow thermal" processes and have been invoked to explain sputter yield data which do not fit the collisional or "Sigmund" type sputtering[83]. Within the spike volume, temperatures in the range 3600 - 10600 °K have been reported for various substrates[116]. These temperatures are obtained by fitting a Maxwellian distribution to experimentally measured energy distributions. For GaAs, it was found[117] that for substrate temperatures less than 250 °C, the measured energy distribution was of the form

predicted by the collision cascade theory of Sigmund[84].

$$\frac{dN_{coll}}{dE} \sim \frac{E}{(E + E_b)^3} \tag{4}$$

with $\frac{dN}{dE}$, the differential flux of sputtered particles of energy E and E_b, the surface binding energy. Only at higher target temperatures was it found necessary to explain the low energy tail of the distribution by assuming it was Maxwellian i.e.

$$\frac{dN_{sp}}{dE} \sim E\exp(-\frac{E}{kT_{sp}}) \tag{5}$$

with T_{sp}, the spike temperature. For example, at $T_{target} = 310°C$, the temperature in the spike was found to be $T_{sp} = 5920°K$ and it was concluded that room temperature bombardment of GaAs does not involve spike processes. Therefore, according to the foregoing analysis, one would not expect a beam induced temperature rise to be associated with the ion bombardment of GaAs under our experimental conditions; either due directly to the incident beam power or locally within thermal spikes.

Recently, Ar^+ ion beam induced temperature rises have been inferred from the results of cone formation experiments[118,119]. The purpose of the experiments was to re-examine the influence of impurity seeding on cone formation. In one of the experiments, an Ar^+ ion beam was used with $r_s = 100$ μm, $J = 100$ μA / cm^2 at $V_b =$ 3 kV to bombard polycrystalline Mo films. Substituting into equation (3) and taking $\rho = r$ with $\kappa_{Mo} = 1.4$ W / cm$-$°K we obtain $T = 1 \times 10^{-3}$°K (!!), once again finding that the temperature rise should be negligible. Note that within the spot, this amounts to only 0.3 W / cm^2 i.e. $\simeq 10^5$ times smaller than the power density of the LMIS FIB. Despite this observation, the morphology of cones formed within the sputtered crater indicated to the authors that the smaller cones near the bottom of the crater were heated to the melting point of Mo or higher i.e. > 2622 °C by the ion

impact itself. In another experiment[120], the melting at the tips of Cr needles grown on an electron field emission cathode operating in $Cr(CO)_6$ vapor was observed. The ion bombardment conditions were nearly the same as in the cone formation experiment and the authors concluded that

> "the thermal effect of Ar^+ ions in the energy range of a few keV is much stronger than expected."

To reiterate, although simple models suggest that thermal effects are negligible, recent experimental evidence indicates that they may be significant. Therfore, we see that the thermal effects of ion bombardment are difficult to evaluate and one may speculate that thermal effects exist under FIB bombardment, *notwithstanding the calculations and general concensus.* Therefore, we suggest that this issue should not be considered settled until additional data become available. One point, however, is very clear. Whatever role beam heating may play in the initial stages of droplet formation, the fact that the droplets remain liquid and are mobile proves that there is sufficient heating of the droplets themselves despite the cold substrate temperatures. This must certainly be due to the limited thermal conduction path from the droplet to its surroundings. Although no calculations have been done, it would be very unlikely that they would predict that there was insufficient heating to keep the droplet material liquid. In view of the experimental evidence, a better model would be sought to explain it. The obvious conclusion from the observations is that beam heating is sufficient to keep the droplet substance above its melting point even if it may not be sufficient to raise the temperature of the substrate itself.

5.6.5 A simple model of droplet formation onset (is too simple)

Perhaps the simplest approach to understanding the onset for droplet formation is to assume that the gallium ions are implanted to their projected range, R_p, while the surface is simultaneously eroded by sputtering. This approach has been used to calculate the secondary ion signal enhancement during oxygen exposure of silicon[121] and by Ishitani et al[105] to explain the condensation of gallium in Ga^+ bombarded silicon. We assume that when the sputtered surface erodes to the depth of the projected range, including the straggle in the range, it reveals the highly concentrated gallium region. The distribution of implanted ions is given by the range statistics of the well known LSS theory[122] with the ion concentration normally distributed

$$C(z') = \frac{0.4}{\Delta R_p} \exp\left[-\frac{(z' - R_p)^2}{2\Delta R_p^2}\right] \Delta\Phi \tag{7}$$

where ΔR_p is the spread in the ion projected range and $\Delta\Phi$ is the primary ion currrent flux

$$\Delta\Phi = \frac{J_p \, \Delta t}{q} \tag{8}$$

J_p is the average current density in the scanned area, and Δt the exposure time. If we assume that the surface erodes at uniform velocity V_s, then we can substitute $z = z' - V_s t$ into equation (7) and integrate yielding:

$$C(z,t) = \frac{J_p}{2qV_s}\left[\mathrm{erf}\left(\frac{z - R_p + tV_s}{\sqrt{2}\Delta R_p}\right) - \mathrm{erf}\left(\frac{z - R_p}{\sqrt{2}\Delta R_p}\right)\right] \tag{9}$$

where

$$\mathrm{erf}\left(\frac{x}{\sqrt{2}}\right) \equiv \left(\frac{2}{\pi}\right)^{\frac{1}{2}} \int_0^x \exp\left(-\frac{t^2}{2}\right) dt \tag{10}$$

Therefore, the moving surface has a concentration:

$$C(t) = \frac{N_0 \rho}{2SM} \left[\operatorname{erf}\left(\frac{tV_s - R_p}{\sqrt{2}\Delta R_p} \right) + \operatorname{erf}\left(\frac{R_p}{\sqrt{2}\Delta R_p} \right) \right] \tag{11}$$

where the coefficient has been rewritten with N_0, Avogadro's number, ρ the density of the target material, M its molecular weight and S the sputtering yield.

Taking $S = 6$ at 20 keV, we obtain for the velocity of surface recession, $V_s = 4.4\text{Å} / \text{sec}$ for bombardment at 20 keV and $J \sim 150\mu A / cm^2$. This value for the sputter yield has been determined experimentally by measuring the volume of sputtered craters, assuming a uniform sputtering rate, and agrees with published and unpublished data[108, 123, 124]. At this rate, the time, t_s, required to reach the gallium enriched regions of the implanted ions should be given approximately by:

$$t_s \sim \frac{R_p + \Delta R_p}{V_s} \tag{12}$$

The values of R_p and ΔR_p for Ga^+ bombardment of GaAs have been obtained by interpolation between those for Zn and Se bombardment of GaAs (see Chapter 4)

Subtitution into equation (12), gives $t_s \sim 38$ seconds. This corresponds to a dose of 6×10^{15} ions $/cm^2$ which is only 21% of the experimentally measured threshold dose. In other words, the experimental threshold dose is nearly 5 times larger than that predicted by the simple model. We see that this model cannot correctly explain the onset of the droplet formation. This is not entirely surprising as the model ignores many important possible material/beam interactions e.g. solubility, diffusional mixing and chemical segregation. On the other hand, it should be noted that for Ga^+ bombardment of Si[105] the predicted critical dose lies within a factor of two of the experimental value and the model seems to give reasonable agreement.

5.7. Sputter cone topography

We briefly mention some aspects of cone production since there appear to be some similarities to the droplet formation and other ion bombardment induced topography. The first sputter cones were probably produced by V. A. Gunterschultze and W. Tollmein[125] Observation of cones were subsequently made by many workers in related fields and some theories of cone formation were formulated. Although the mechanism for nucleation of cones is not yet absolutely established it is probably the best understood aspect of ion beam induced surface topography. Nevertheless some of the issues are not yet settled. While it had long been thought that surface impurities with lower sputtering yields than the surrounding target were required for cone formation, Wehner[126] shows that the surface impurities must have a higher melting point and not merely a lower sputtering yield.

The impurity atoms are assumed to move between adsorption sites by a random walk process. As long as they can overcome the potential barrier between sites they form clusters of impurity atoms which serve to protect the underlying substrate. This activation energy, E_d, depends on the impurity / target combinaation and also has a small temperature dependence. The surface diffusion takes place within a radius given by[92,93]:

$$r_d = 2x10^6 \exp(-\frac{E_d}{2kT})$$

with r_d in Å. The impurity atom flux, mass and the distance between adsorption sites also have an influence but are much less important. As in ordinary vapor phase condensation, there is a critical cluster size below which cluster growth is not possible. If the diffusion of impurity atoms is sufficient to overcome the losses by sputtering, the cluster will grow. The diffusion radius required to enable an impurity cluster

to grow is given by:

$$r_d = \frac{r_c}{F_i^{\frac{1}{2}}}$$

where $F_i^{\frac{1}{2}}$, is the ratio of impurity atoms to incident ions. The theory predicts a critical temperature which allows the required diffusion for cone production.

$$T = 587E_d$$

with E_d in electron volts and T in ° K. The theory also predicts that the sputter yield of the impurity seed atoms need not be lower than that of the substrate for cone production to take place. This has been verified experimentally. The " protection " of the target is afforded by the diffusion of the impurity seed atoms to sustain a cluster of size $r > r_c$ as the surrounding material is sputtered away. In fact, it appears that there is a stronger requirement that the " seed " material have a higher melting point than the target. On the other hand, Whitton et al[127]. dismiss the requirement for surface impurities altogether. In their view, ion beam induced defects are responsible for nucleation sites for cone formation. Auciello[128] attributed cone formation to surface inclusions and impurities of the initial surface topography. At present there is no concensus and it appears that several phenomena are responsible and all of these possibilities may play a role. It is generally accepted, however, that impurity generated cones do not require the sputtering yield of the impurity to be lower than the surrounding material as had previously been thought. The first evidence for this comes from the sputtering of gold impurities on aluminum. It seems that virtually any substrate is a candidate for sputter cone formation with essentially any impurity providing the seed material. Explanations for sputter cone formation in the presence of impurities involve sufficiently mobile adatoms to nucleate, form clusters and grow

via surface diffusion. This requires sufficiently high temperatures which lie typically in the range 500°K to 800°K .

5.7.1 Experimental Sputter Cone Production

Experiments to deliberately produce cones , have consisted of " shining " a broad beam of ions onto a target of " seed " material at a glancing angle so that a broad beam consisting of neutral seed material and ions strikes a surface onto which the cones and prismatic or faceted structures are grown[99,119]. Some related experiments have been done on the effect of ion bombardment on the nucleation and formation of thin films which have also been performed in a similar manner[109]. Some of the observations of these experiments reveal that:

1. Stable cone populations require a continuous supply of impurity material or the cones will soon be sputtered away.
2. The substrate temperature effects the cone spacing.
3. Cone spacing and size are correlated with the ion impact rate i.e. current density.
4. " Quasi-liquid " states involving macroscopic motion of material has been observed
5. A coating material of some sort covers some cones and protects them from being sputtered. When the coating fails, the cone is more rapidly eroded.
6. Except for carbon whiskers, no cones have been formed which rise above the original substrate surface.

5.8 Conclusions

The following qualitative picture emerges from the observations of droplet for-

mation. During the initial stages, the net effect of sputtering and implantation is to produce a non-uniformly thick Ga rich film. Note that we do not attempt a description of the origin or nucleation of the film itself. For a given beam current, energy and substrate temperature, droplet formation requires a threshold dose. For a given average current density, smaller ion beam spot diameters produce smaller droplets i.e. the drop size is correlated with the beam diameter. It is interesting that this occurs since the beam is raster scanned and the average current density remains nominally the same. However, it is not possible to decide from these experiments whether it is the local current density or merely the beam diameter alone which is responsible for the correlation. On the other hand, there are droplets which are significantly smaller than the spot diameter. These may be the result of somewhat larger droplets in the process of being sputtered away (less likely) or may actually be growing from smaller nuclei (more likely) or coalescing from still smaller droplets. In the future, the change in spot size could be obtained by changing the beam defining aperture, thus leaving the beam current density the same. In any case, one must conclude that some local effect plays a role i.e. the scanning is not sufficient to " smooth " out the effects. Experiments should also be conducted to determine the effect of the scan velocity (dwell time per spot) on droplet size (perhaps significant) and on threshold dose (probably negligible).

Surface mobility of macroscopic droplets and islands consisting of both droplet and the precursor film motion occurs. Note that this can occur at low substrate temperatures (- 62 °C) where there is certainly no ambient thermal component to the motion. There is a considerable ion beam induced component to the motion, at all substrate temperatures examined, as evidenced by photographs and video records. Although the input power per spot is still small, the arguments presented here cast

some doubt on simple beam heating calculations. It is possible that the bombardment induced component is not entirely isolated from a thermal effect due to local beam heating and this should be explored further. At low temperature, the film formation is clearly seen to preceed the droplet formation. The precursor film is never seen at room temperature FIB exposures so it is plausible that at room temperature the droplet formation process may be sufficiently rapid that a film is never seen i.e. drops suddenly appear at the critical dose. Scanning Auger Microscopy (SAM) analysis of the surface after the threshold dose reveals distinct regions within the bombarded region and a different surface composition outside the high dose bombarded area. These correspond to different regions identified in SEM micrographs. Transfer of macroscopic material between formed droplets and those in the process of forming is visible in the video recordings. These probably occur as a result of momentum transfer from the incident beam.

As in sputter cone formation, there is an enhanced surface atom mobility due to the ion bombardment. This depletes certain regions of the film by supplying material to the growing droplets. The material which builds up around relatively poorly wetting areas is supplied by the surrounding film which thereby becomes thinner. The droplets themselves, while being sputtered at a rate determined by the incident angle presented to the beam, "protect" the underlying substrate. The unprotected regions undergo continued simultaneous sputtering and implantation which results in a steady state surface concentration which was determined by SAM.

In comparison with sputter cone formation, there is an endless input of "impurity" atoms brought by the beam and coming directly from the substrate. For the droplet experiments, there is sufficient mobility in the presence of the ion flux even at relatively low temperatures, while cone formation may be suppressed at temperatures

lower than several hundred ° C. As long as there is sufficient mobility the droplets are never sputtered away but at low enough temperatures droplets are observed to be sputtered. Both sputter cone formation and droplet formation are associated with liquid or " liquid-like " phases. A coating material covering some cones prevents the sputtering of the underlying surface. When it fails, perhaps due to insufficient atom mobility, the cone is rapidly eroded.

An essential difference between sputter cone formation and droplet formation results from the ease with which macroscopically large quantities of droplet material move about the surface under the ion beam. This is responsible for the growth of large droplets which may rise above the substrate surface, in contrast to sputter cones which (except for one or two special cases) "grow" by the erosion of the surrounding surface. Consistent with the micrographs and video recordings, one may expect that the direct coalescence of droplets is a primary growth mechanism. While we cannot explain the correlation of beam diameter with droplet size, the easy coalescence of smaller into larger droplets may account for the observed bimodal droplet size distribution observed in the micrographs i.e. large droplets in a field of smaller droplets. If a large droplet is produced within some "active" diameter on the surface, there will be a region around the droplet and within this diameter which is depleted of material. This will effectively isolate the surrounding smaller droplets which will be unable to coalesce, resulting in large droplets on a small droplet background. If this description is correct, there must be some relationship between this active diameter and the beam diameter but this has not been determined. Unfortunately, the expression for the diffusion radius given by Robinson and Rossnagel[93] for impurity induced sputter cone formation is not directly applicable since coalescence is not a feature of their model. Other models of droplet coalescence exist in various fields of science and technology

and perhaps these may be helpful. This and other considerations discussed above remain for future study.

6. MICROMACHINING

6.1 Introduction

Virtually every form of ion bombardment associated process has been used to etch technologically important materials, semiconductors being of particular interest. Although the application of some of these processes to microfabrication has been called micromachining, the term seems most appropriate when used to describe the technique employing liquid metal ion sources (LMIS). This involves the precise control of the motion of a submicron diameter ion beam positioned over the required work area. The FIB micromachining system employed at the Oregon Graduate Center and described in Chapter 1 has been used to remove the passivation layer of integrated circuits for subsequent voltage contrast measurements (see Section 6.2), and to produce laser output mirrors, coupled cavity diode lasers, and surface emitting lasers (see Section 6.1). These accomplishments represent the first examples of the practical application of FIB micromachining to the testing and fabrication of real devices. Other applications of FIB for integrated circuit (IC) and optoelectronic integrated circuit (OEIC) fabrication also exist outside the realm of micromachining per se e.g. implantation of dopants, lithography (see Chapter 7), and surface analysis by SIMS.

Among the various ion beam technologies presently employed to fabricate IC's and OEIC's, only FIBM offers the possibility of removing small quantities of target material without the use of photoresist, oxide or metal masking layers. FIBM applications generally can be divided into two categories:

i. those requiring the removal of material from designated regions of the target e.g. FIBM of IC passivation, cutting metal lines in IC's (see Figure 6.1) repair of defects on lithographic masks and

ii. those requiring precise control of the shape and topography of the machined feature as in the formation of optical surfaces in materials e.g. for semiconductor lasers where surface structure must be much smaller than the operating wavelength

The latter pose more difficult challenges, some of which have been addressed in this thesis research. It is clear, however, that many remain. We do not imply that shape and topography issues are negligible in mask repair, for example, where redeposition may also cause difficulties[129]. However, they are certainly more critical for the applications in the second category. While recognizing that there may be exceptions, this division is meant to be operational only.

6.1.1 Ion bombardment induced erosion and redeposition

Ion bombardment induced etching relies on the gradual erosion of target material to produce structures for microfabrication. As a result of successive ion impacts there is a statistical angular distribution of ejected or sputtered particles (see Figure 6.2), which depends on the incident beam angle, the target crystal structure and composition and also the bombarding ion species[130]. This material often lands

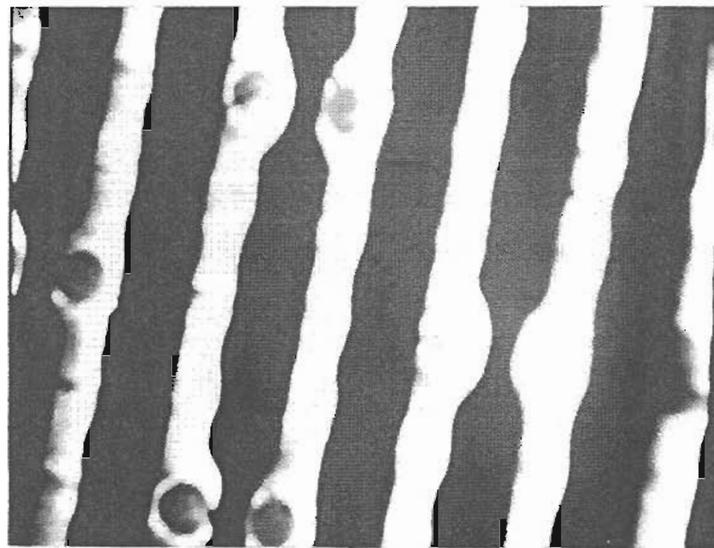

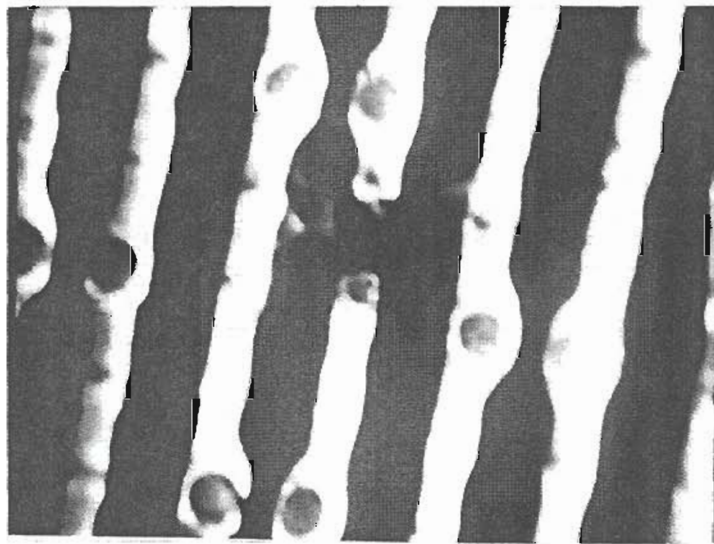

Figure 6.1 Example of IC circuit "microsurgery". A 1 μm opening ismachined in an Al conductor with a gallium FIB at 20 keV and 0.3 nA beam current. The exposure time was 9 minutes. Courtesy F.E.I., Inc.

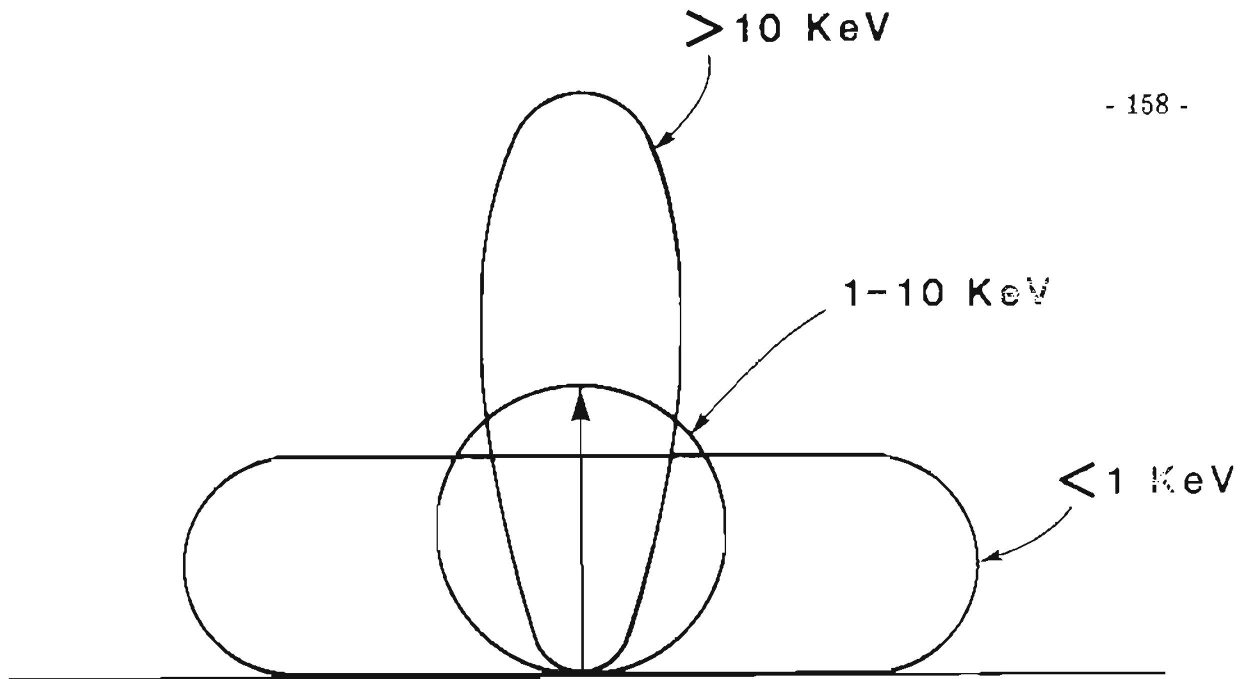

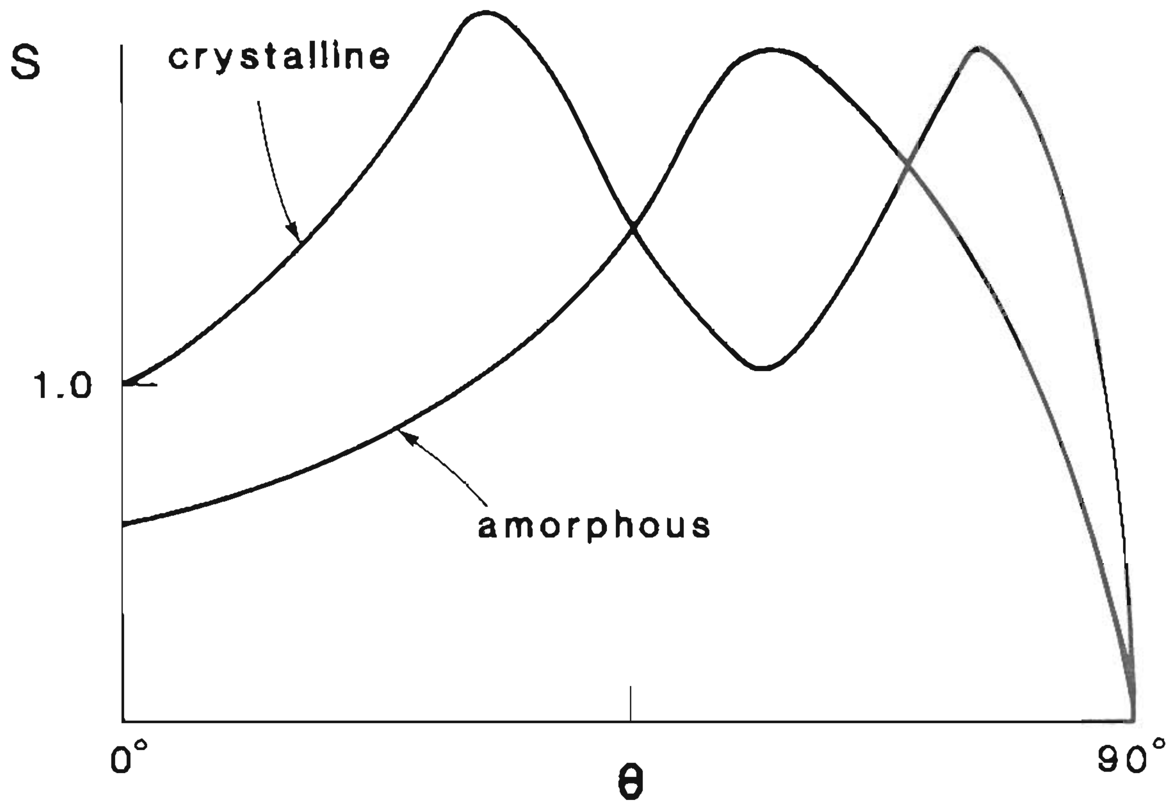

Figure 6.2 Upper: Schematic diagram of the ejection distribution for sputtered neutral atoms for normal beam incidence and an amorphous or polycrystalline target. In some models, this distribution is caused by a "refraction" effect due to interaction between momentum back to the surface and a surface potential barrier. After J. L. Vossen (ref.130). Lower: Sputter yield dependence on incident angle.

on nearby surfaces and is responsible for the phenomenon known as redeposition. It is generally appreciated that this always accompanies any sputtering process and is typically viewed as something to be avoided or minimized. For example, in photolithography for IC fabrication the redeposition of substrate materials onto masking layers causes facets to form on the mask corners and side walls. This results in more rapid etching of these surfaces due to the angular dependence of the sputter yield and diminishes edge resolution. We see then that there exists a dynamic relationship between sputtering and redeposition which determines the evolution of ion bombarded surfaces.

Models treating the evolution of surface erosion under ion bombardment in general have been devised over a period of years and continue to date. Almost all of these have been applied to the broad beam or unfocused ion beam (UFIB) case. Initially, only two dimensional structures were considered[131-134] but the effects of redeposited material were not included. More recently, the problem has been considered for three dimensional structures without including redeposition effects[135] and then again for the two dimensional case including redeposition effects[136,137]. Although the latter analyses considered the change in shape of nearby surfaces due to the redeposited material, the authors did not examine the simultaneous ion erosion of the redeposited material.

6.2 Micromachining with a focused ion beam (FIBM)

FIB micromachining relies predominantly on the sputtering process to produce structures for microfabrication. Chemically enhanced FIB micromachining, in chlorine for example, [68,69] is a more recent addition to microprocessing methods and

may be loosely classified as a form of sputtering. The chemical reaction serves to decrease the binding energy at the surface thereby increasing the effective sputter yield of the material. On the other hand, if a very stable compound is formed on the surface, the sputter yield will decrease. For example, oxides generally have lower sputter yields. There are notable differences between this and physical sputtering but chemically enhanced etching will not be discussed further and only mentioned briefly from time to time.

The practical application of FIB micromachining to restructuring materials involves somewhat different considerations than those related to broad beam methods, although the underlying physical processes are clearly similar. In contrast to the typical redeposition problems experienced with ion beam projection through masks, there is obviously no "external" mask erosion involved in FIB processing. The possible self-mask erosion in FIB lithography is described in Chapter 7. Thus it appears possible, in principle, to create smooth surfaces with vertical walls and avoid the wall tapering resulting from mask erosion in standard "unfocused" or broad ion beam arrangements. One example where this could be significant is in micromachining for SIMS depth profiling. Typically, a relatively large focused ion beam (not FIB) having a Gaussian current density distribution is raster scanned over the substrate. As expected, this produces a crater which is essentially square but with rounded walls at the top of the crater and slanted walls. A standard technique of SIMS is to electronically gate the detector so only secondary ions coming from the center of the sputtered crater are collected. Only these ions can be correlated with a precise depth but this technique reduces the available signal and diminishes the SIMS sensitivity. This could give the FIB a distinct advantage in SIMS depth profiling. In practice, however, FIB micromachining also produces slanted walls, although of much smaller

slope. Therefore gating is still required although experiments with the OGC SIMS instrument indicate that a larger central crater area can be accepted. Quantification of this effect remains for future study.

6.2.1. The basic equations of FIBM

The simplest relation for FIBM, if secondary effects are not included, can be obtained directly by the following argument. By definition, the number of particles removed per second from the target must be equal to the product of the sputter yield, and the number of incident particles per second. Therefore, the mass removed per second is given simply by

$$\dot{m}_{out} = \frac{I_p}{q} mS$$

Now $\dot{m}_{out} = \rho\dot{V}$, where ρ is the target density. For a given bombarded target area, A, we get $\dot{z}A = \dot{V}$, the volume removal rate. Remembering that $m = M/N_a$, the atomic or molecular weight divided by Avogadro's number, we obtain for the erosion depth at point x

$$z(x) = \frac{J_p MS t_d(x)}{N_a \rho q}$$

where t_d is the dwell time of the beam at x, J_p the beam current density, q the ion charge and d_s is the beam diameter. This is the basic equation of FIBM. All secondary effects such as redeposition, ion reflection, sputter yield dependence on dose and myriad other possible influences occurring in real materials have been neglected. We may also write $t_d = \dfrac{d_s}{v(x)}$ where v(x) is the beam velocity over the target and may be variable. Thus $v(x) = \dfrac{dx}{dt}$. Substitution into the basic equation gives:

$$z(x)dx = Cdt$$

with

$$C \equiv \frac{J_p M S d_s}{N_a \rho q}$$

For a desired machined crossectional profile z(x), one merely has to integrate this equation to obtain x(t) and hence the beam deflection voltage as a function of time. This has been demonstrated by Crow et al[138]. at the Oregon Graduate Center and gives good agreement considering the assumptions.

As described above, the essential difference between broad beam ion exposure of materials and FIB exposure results from the necessity for scanning the focused beam. This is the most obvious and perhaps the single most important factor contributing to the differences between FIB and UFIB material processing and provides both its advantages and disadvantages. The inherently serial FIB process is slow and may limit the throughput for some applications. On the other hand, masks are not usually necessary so the number of processing steps is reduced. Due to the systematic scanning of the beam, one can expect that the redeposition effects will be manifested somewhat differently also. Since many scans are usually necessary to supply the required dose, a given region of the target is exposed periodically. As the beam current density is large, (as large as 1 ampere / cm^2 for the FIB systems at OGC) varying the dwell time per target pixel may cause a considerable variation in the amount of material sputtered from a given site. Therefore, for a given total dose, there is a strong dependence of the milled geometry on the scan rate. This has been demonstrated by Kubena et al[139]. and by Yamaguchi et al[140]. and Yamaguchi[104] for line scans and area raster scans. A general rule of thumb is that, for a given ion dose, a higher velocity beam and more repetitions of a basic pattern will produce a

structure closer to the physically intuitive "geometric" shape than a slower beam and fewer repetitions. This is related to the fact that redeposited material accumulates in certain regions of the milled feature due to the periodic scanning of the beam. Thus, a "bias" is introduced by typical raster scanning. Attempts have been made to minimize this systematic effect by alternating the raster directions in subsequent scans[60]. It may also prove interesting to step the beam in a random fashion i.e. with uniform probability density and in this respect "simulate" the effects of broad beam milling but at much higher local current density. One would expect the redeposition to be present although manifested somewhat differently than for either FIB scanning or standard broad beam methods. This has not yet been attempted. Generally, the higher the scan rate used to mill to a desired depth, the less material is deposited per scan. This means that there is a relatively smaller change in the milled profile as it is being created and the influence of the incident beam angle dependence on the sputter yield is reduced. Therefore, all things being equal, we see that the successful fabrication of microstructures by FIBM lies in the particular scanning technique employed. This cannot be overemphasized. Scanning may employ digital or analog raster or vector means.

6.2.2 Beam scanning considerations

Linescans: If one ignores beam current fluctuations, a beam deflected linearly under analog voltage control deposits ions continuosly along its path. Across the scanned line, at any point along the line, the deposited dose is proportional to the beam current density which in our case is essentially Gaussian. For the moment, we are ignoring the non-Gaussian aspect of the beam (or halo) discussed by Ward et

al[141]. On the other hand, a beam stepped discretely under computer control can be overlapped arbitrarily according to the chosen step interval. It is conceivable then that digital scanning and analog scanning may give somewhat different results depending on the manner in which the beam is stepped.

Area raster scans: To ensure uniform exposure under aanalog controlled deflection, we must satisfy the condition $Y_T < Md_sN_l$ (see Chapter 7) with N_l the number of lines per scanned area (frame) and Y_T the size of the scanned area in the y direction. Similarly, for a discretely stepped beam, we must satisfy the above condition with $N_l = \frac{Y_T}{\delta s_y}$, and δs_y the step size interval in the y direction. As this is often equal to δs_x, the extent of the beam spot overlap on the target is the same in orthogonal directions. In contrast, analog area scans are always continuous along the x (fast) axis as in linear scans while the extent of overlap will vary along the y axis according to the above condition. Thus, the spatial distribution of dose can be different for the two scanning methods. Hence, the net effect of sputtering and redepostion may likewise be different. Whether the differences are significant will depend on the precise bombardment and target parameters.

As an example, we note that even a simple square raster may result in unpredictable shapes. Figure 6.3 shows a crater milled into GaAs with a 20 keV Ga^+ FIB. Slanted walls are produced giving the structure the appearance of a "picture frame". Both strutures received the same dose, the same number of frames was used and the beam diameters were overlapped to assure a "uniform" dose. While the overall size is nominally the same for each (they appear at different magnifications in the micrographs), the wall angle and the crater floor are different. What then is the origin of the observed differences? The beam was digitally stepped under computer

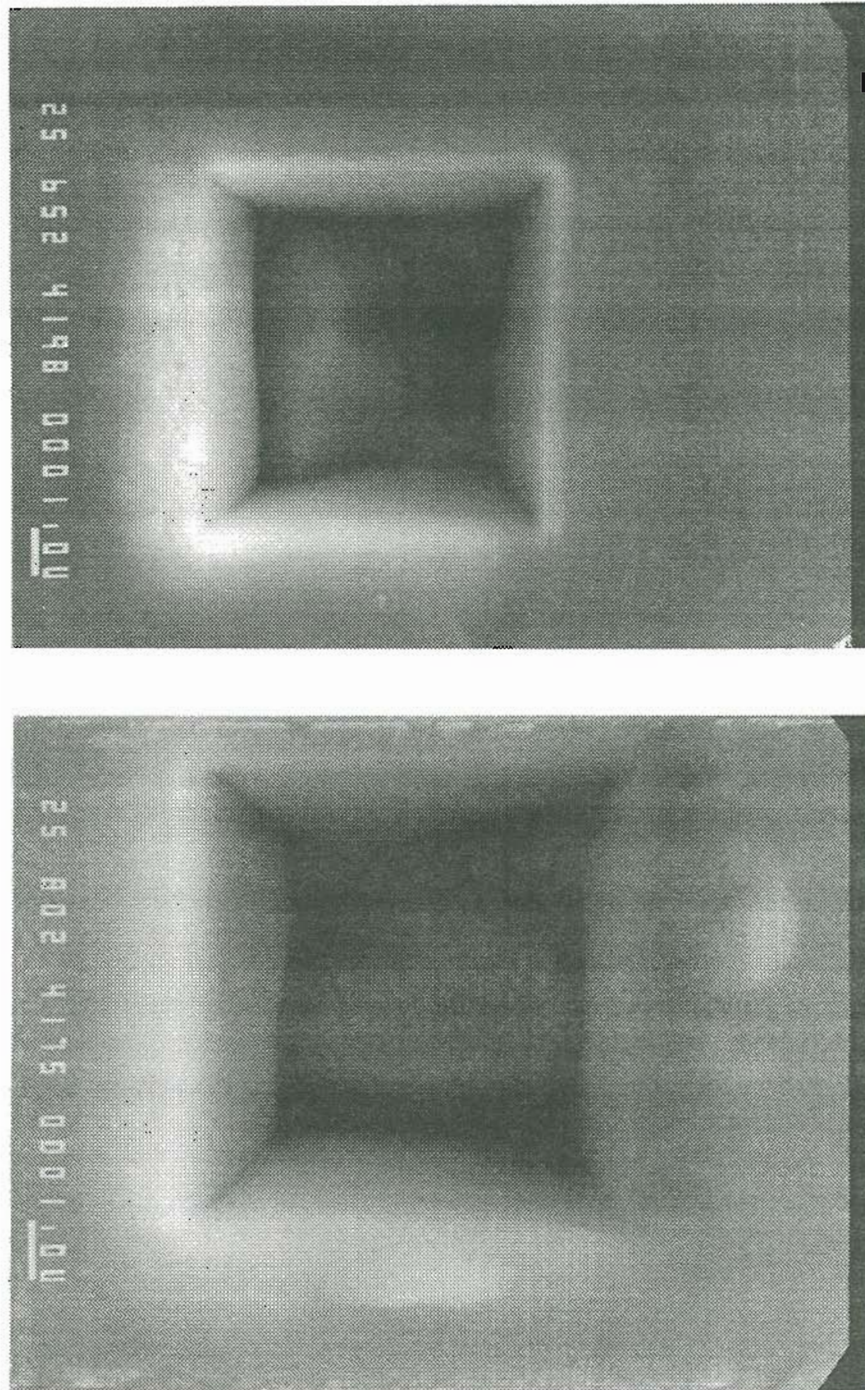

Figure 6.3 Craters milled with 20 keV gallium FIB viewed at normal incidence. The slanted walls give a "picture frame" effect. Both craters were milled "uniformly" but the beam was stepped differently for each (see text for details).

control, although differently for each. For the upper figure, the individual steps were one fourth of the beam diameter while for the lower figure, each step was one sixteenth of the beam diameter. The number of frame repetitions was the same for both and the total exposure time was the same ensuring that the dose was the same. In other words, the dwell time per step is four times longer for the upper figure. In both cases, the individual steps are smaller than a beam diameter and one might expect essentially equivalent results for such a "uniform" ion exposure. Nevertheless, the results prove otherwise. For another set of exposures, the number of steps was kept constant but the dwell time per step was varied. This time the total number of frame repetitions was adjusted so a constant total ion dose was maintained. These results (not depicted here) show that a rise in the crater floor moves progressively across the floor as the dwell time per beam step increases and the number of frame repetitions decreases (keeping the total dose constant). From the foregoing discussion, the following points are clear. A desired dose can be deposited in several ways. For a given beam current, specifying a total dose over the scanned area does not guarantee reproducible results. The number of steps per frame, the dwell time per step and the number of frame repetitions must be specified. For analog scans, one could specify the number of lines per scanned area (i.e. the ratio of horizontal to vertical frequencies), the horizontal frequency, and the number of frame repetitions must be specified. Perhaps we should not be entirely surprised that small changes in the "local" conditions can have macroscopic effects. We have already demonstrated, in Chapter 5, that defocusing the beam somewhat can alter the surface topography.

The reproducibility of high aspect ratio linescans may also be problematic. Figure 6.4 depicts multiple line scans, one beam diameter wide, across the edge of a Mitsubishi ML4102 diode laser produced at 20 keV. Several interesting features are

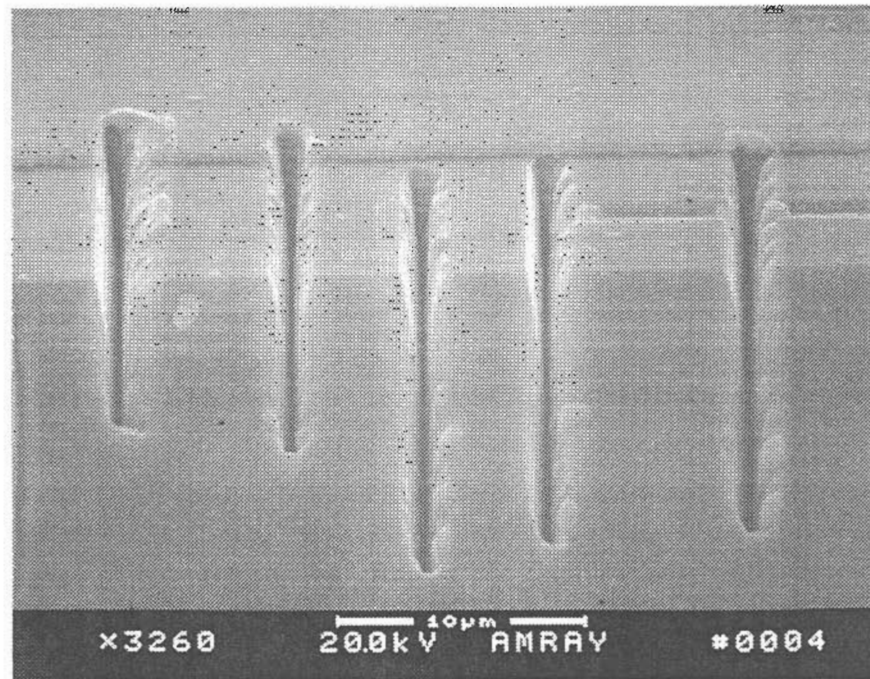

Figure 6.4 Single line scans of 20 keV gallium FIB across the end of a Mitsubishi ML4102 diode laser. Several interesting features are manifested (see text for details).

evident. The usual droplet formation in the AlGaAs is present but seems to be distributed mostly along the righthand wall with the lefthand wall being smoother. This asymmetry is even more apparent when linescans are made at 15 keV beam energy. The droplets are absent where the material composition has changed and they appear again below this altered layer where the composition is the same as that above. The typical V-shape begins at the top but then appears to straighten out at the interface of the altered composition.

In the FIB micromachining of GaAs based materials, redeposition often contributes to the formation of gallium rich droplets (see Chapter 5) which may interfere with the desired electrical or optical functioning of a device. Recent work has demonstrated the efficacy of molecular chlorine gas or excited atoms in conjunction with FIB micromachining[68, 69, 142] in increasing the effective etch rate by large factors (as high as 10 times, depending on the beam scanning speed and gas partial pressure). The formation of gallium droplets was also minimized or eliminated. This probably is a result of the creation of volatile gallium chlorides $GaCl_3$ and $GaCl_2$.

FIBM may also result in damage production. Figure 6.5 shows that the damage produced when milling GaAs at 20 keV can propagate great distances. Unfortunately, the reproduction here conceals some of the detail. observable in the original negative. Nevertheless, several tracks and lines can be seen far from the incident beam. These tracks occur both parallel and perpendicular to the target surface. The wall remaining after milling near the edge of the bulk wafer is approximately 1 μm thick. This is a preliminary result and more work must be done in the area of defect production in GaAs and AlGaAs under high dose FIB bombardment. We note, however that useful optoelectronic devices have been fabricated by FIBM (see Section 6.4) and conclude that the extent of damage depends on conditions which have not yet

been identified. This is an area requiring further study.

6.3 Micromachining of Optoelectronic Devices

The most recent application of FIB micromachining is in the area of fabrication of monolithic optoelectronic integrated circuits (OEIC). As part of the research into focused ion beam applications, Puretz et al[143]. have shown that commercial diode lasers can be modified or restructured to produce optical quality mirror surfaces for AlGaAs diode lasers. Here the most important considerations stem from the requirements for optical smoothness at the wavelength of interest and the minimization of surface damage due to defect production by the incident ions. The first requirement is related to the redeposition issue and topography development under ion bombardment. The second is related to the penetration range and straggle of the incident ions. Optically smooth surfaces with little surface damage have been produced by scanning the beam in such a manner that it impinges parallel to the desired optical surface. Thus, the damage produced by the beam is due to the lateral distribution of ions which is relatively small (40 Å or so at our beam energies).

The lasers were Mitsubishi ML-4102, V-channel-substrate inner stripe devices with a half-wavelength Al_2O_3 coating on the output mirrors. The micromachining was performed by raster scanning a 20 keV Ga^+ ion beam of 3 x 10^{-10} amperes beam current and a 0.25 μm diameter spot in a rectangular pattern along the edge of the laser. The average current density was approximately $2.1 mA/cm^2$. This demonstration resulted in the first diode lasers fabricated by focused ion beam micromachining. (see Figure 6.6b) As evidenced by the light-output versus drive current curve, the surface thus formed produced an output mirror which was of com-

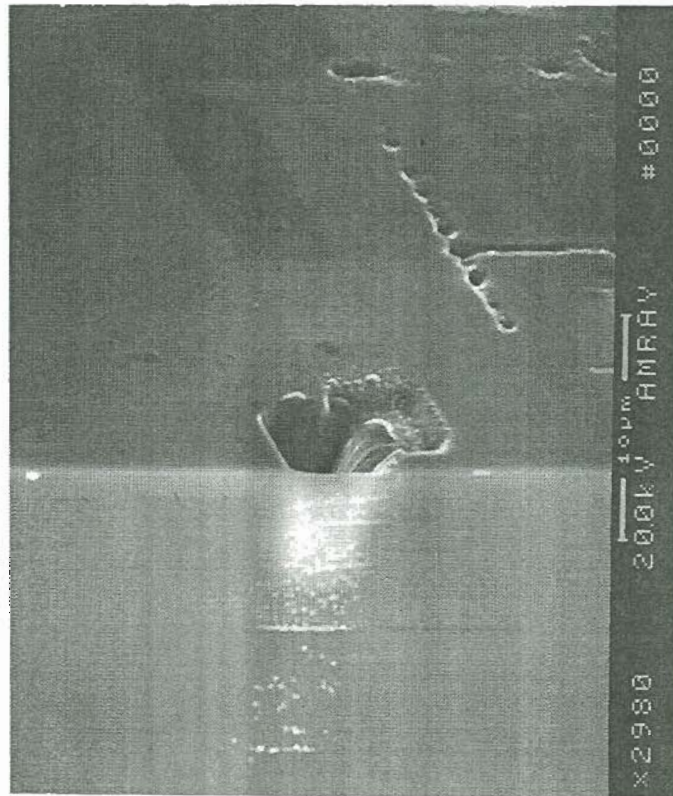

Figure 6.5 Damage produced by FIB milling of GaAs with 20 keV gallium FIB approximately 1 μm from the edge of a cleaved wall.

parable quality to the original cleaved mirror surface.

Having proven that the FIB can be used to produce sufficiently smooth surfaces for diode laser operation at approximately 0.8 μm, DeFreez et al. fabricated a different type of device; the micromachined coupled cavity diode laser or MC^2 laser[81]. (see Figure 6.6a) Prior to this, coupled-cavity diode lasers had been fabricated by chemical etching[144,145] reactive ion etching[146] and by cleaving[147]. Using FIBM, the coupling cavity is machined at normal incidence, so the greatest damage occurs directly under the beam. However, this material is sputtered as well, which moves the damaged region below the active region of the device as the machining continues. Figure 6.7 depicts another MC^2 laser fabricated from double-heterostructure material with a multiple quantum well active layer. The device begins as a 10-stripe phase locked array which is FIB machined to create the coupling etalon and electrical isolation grooves. The stripes of the array are 4 μm wide and isolated by 6 μm wide strips of proton implanted material.

Puretz et al. have also fabricated a surface emitting phase locked array of diode lasers (SEPADL) using 0.26 nA of current in a 15 keV Ga^+ beam[148]. (see Figure 6.8) Within the material, the light travels in the plane of the page and reflects off the turning mirror to exit perpendicular to the page. This device required the creation of two surfaces; a vertical surface for the laser oscillator cavity and a 45° slanted surface for the turning mirror. These were created by removing material in a series of successively smaller overlapping rectangular regions, arranged so that the subsequent ones were aligned along the same edge, thus producing a vertical surface. The slanted surface was created simultaneously by reducing the area of subsequent rastered regions while removing material to a constant depth. As noted previously, the effect of redeposition of sputtered material must be minimized in order to produce predictable

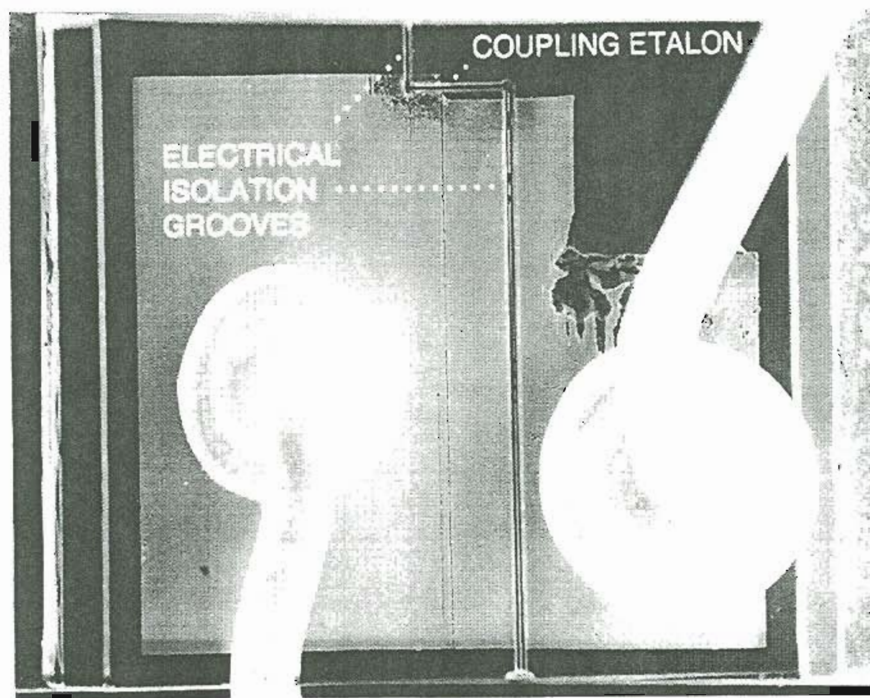

(a)

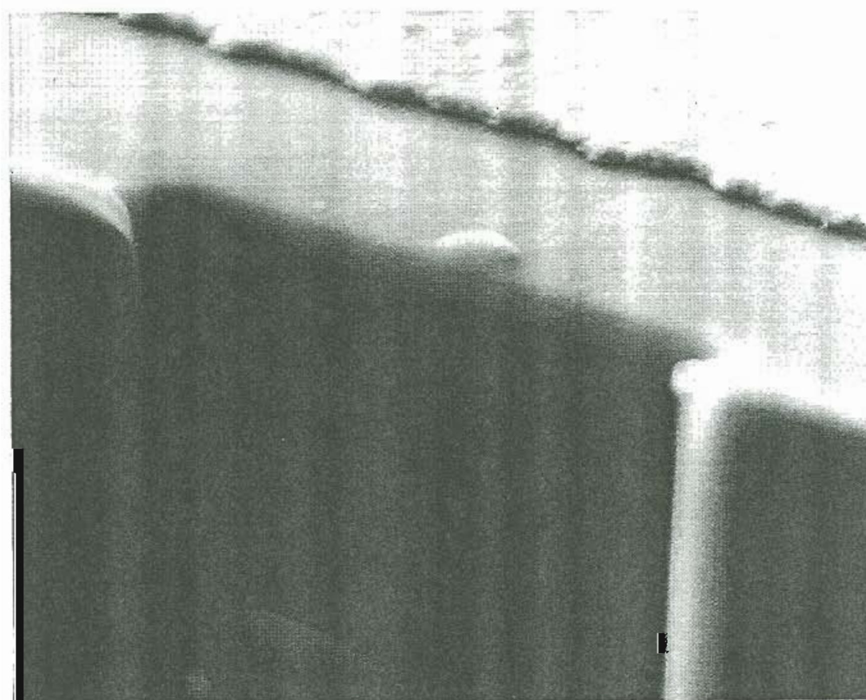

(b)

Figure 6.6 (a) Coupled cavity diode laser fabricated by FIB milling (MC^2 laser). (b) AlGaAs laser mirror facet formed by FIB milling.

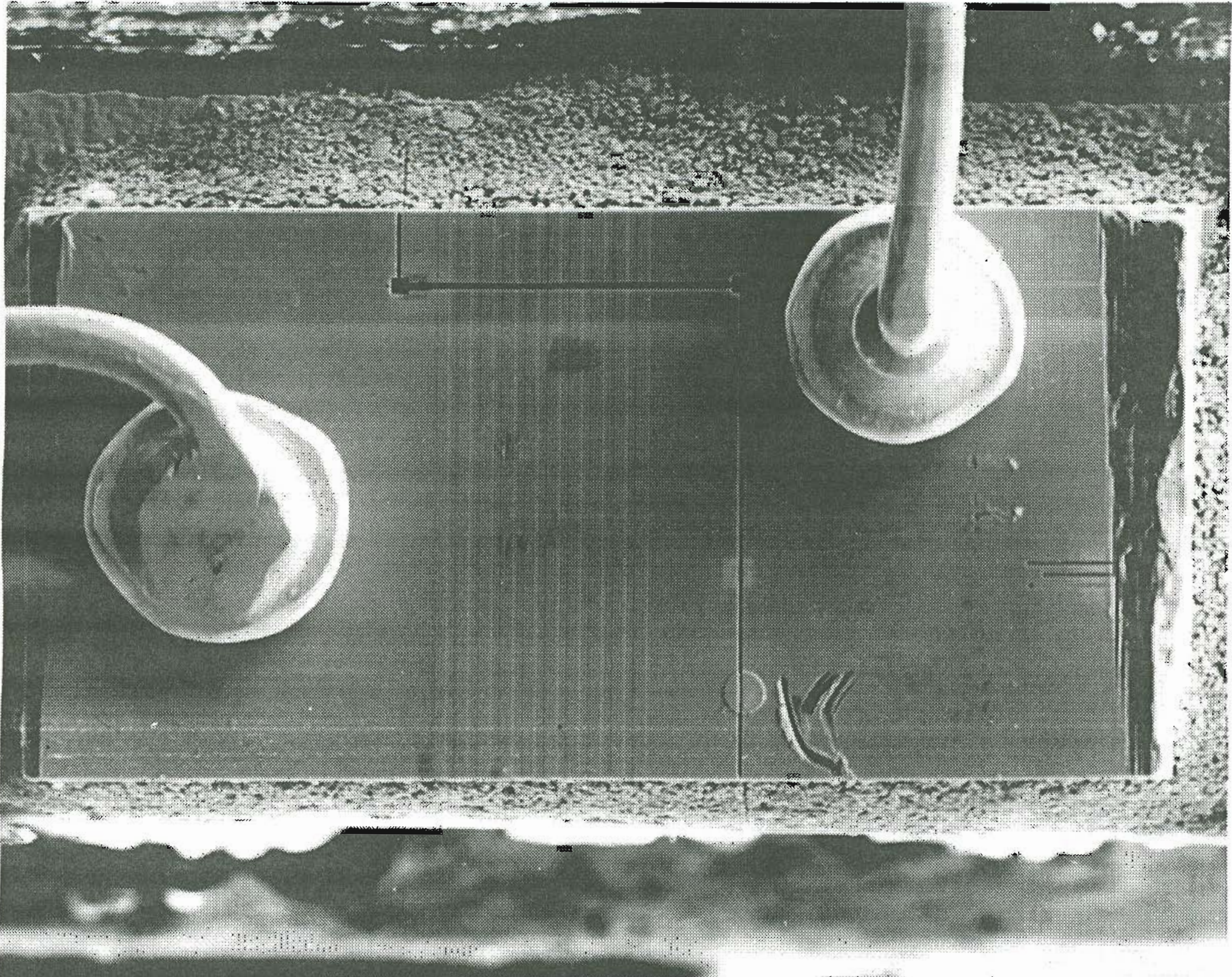

Figure 6.7 Ten-stripe MC^2 laser created by FIB milling.

structures. This was done by choosing as short a dwell time per pixel as possible with the system then employed (25 μsec). The laser array was operated in a pulsed mode with a 50 nanosecond pulse duration at a 25 kHz repetition rate. The peak optical power output was observed to be 300 mW at the limit of the current pulser used. The far-field pattern of the array observed in a direction perpendicular to the micromachined turning mirror was similar to that observed by Liau et al. for parabolic turning mirrors[149].

The procedure described above will always produce "vertical" and slanted surfaces opposing each other. However, in order to fabricate a slanted surface of given slope, the sputter etch rate must be known. This was determined by micromachining small volumes in an unused area of the device and measuring the volume removed per unit time. Since the device is composed of several layers of varying composition, the sputter rate will differ between layers and only an average sputter rate could be obtained ($\approx 0.25 \mu m^3$ / sec). One would expect that for this method of scanning the beam, the damage would be significantly greater than that reported for the work described earlier. Nevertheless, the surface damage is sufficiently small that laser quality mirrors could be fabricated.

The most direct evidence that FIBM is a practical tool for optoelectronic fabrication, at least for some types of devices, comes from recent lifetest data[150]. The results show that FIB machined AlGaAs diode lasers have survived elevated temperature lifetests in excess of 2200 hours. Since publication of these results, the lifetests have continued with stable operation in excess of 4500 hours. Therefore, we conclude that FIBM does not cause significant damage in this case and can be employed to create useful devices.

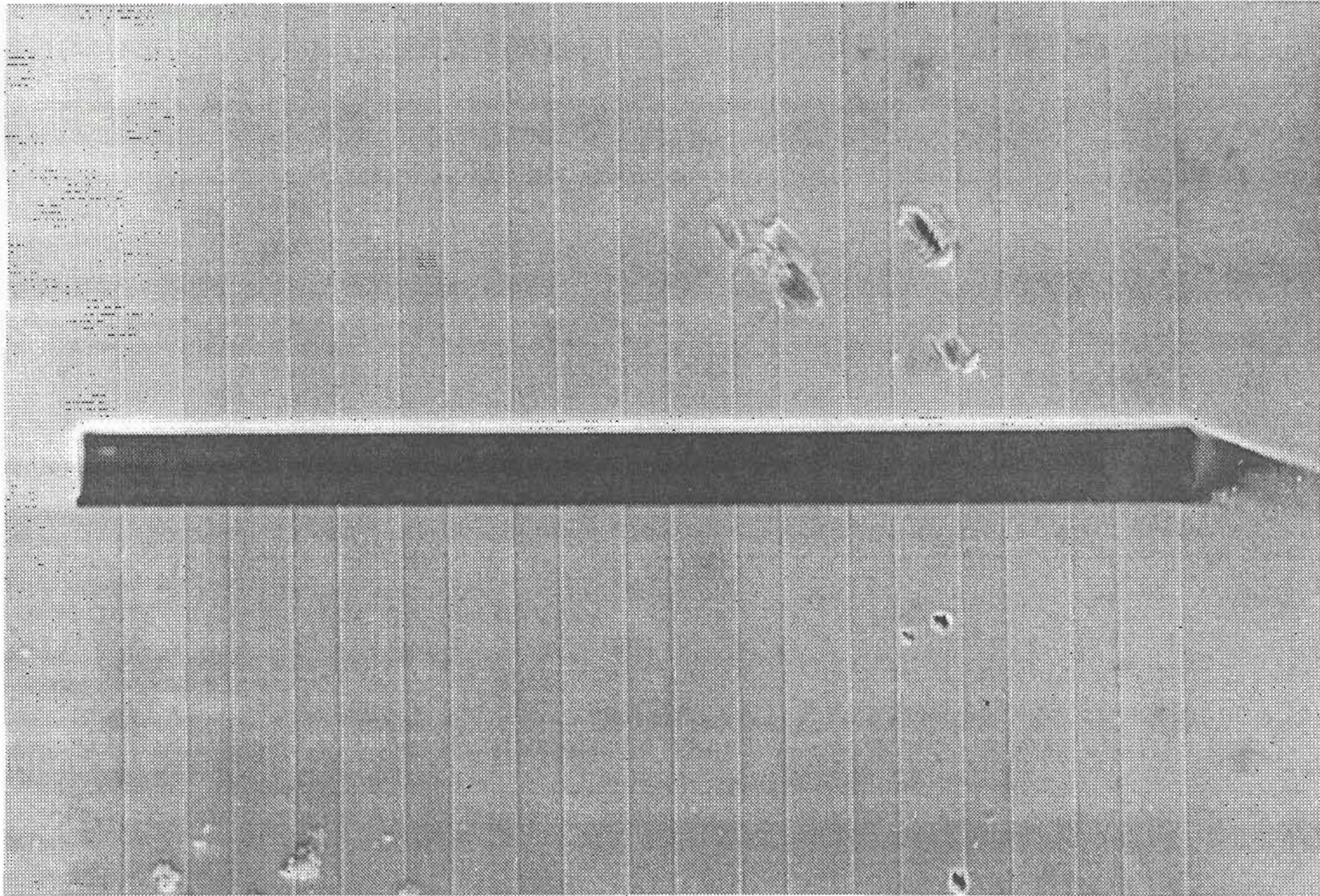

Figure 6.8 Surface emitting phase locked array of diode lasers createdby FIB milling with 15 keV Ga^+.

6.4 Focused ion beam micromachining for IC diagnostics

Among the applications of high current density focused ion beams (FIB) employing liquid metal ion sources (LMIS) is the micromachining of integrated circuits (IC's) for failure analysis. This is achieved by the removal of selected regions of the device for diagnostic testing and repair.

During the course of this thesis research, it was demonstrated for the first time that the FIB can be used to mill micron sized structures through the passivation layer of an IC. An electron beam probe may then be employed in the diacgnostic technique known as voltage contrast scanning electron microscopy (VCSEM).

6.4.1 Background

The voltage contrast technique is used to measure the electric potential of a surface emitting secondary electrons. The secondary electrons are sent through an electron energy spectrometer, and the shift in the secondary electron distribution is measured as the surface potential changes due to the applied circuit voltages. Typically, the secondary electron signal arises as a result of electron beam bombardment employed specifically for the purpose of the measurement. This measurement may be carried out in a commercial scanning electron microscope modified internally to contain the energy analyzer and is relatively straightforward if the electron or ion beam impinges on a bare conductor. However, for failure analysis testing of IC's it is usually required that voltage measurements be made on nodes which lie directly beneath the passivation layer. Typically. this is an oxide or nitride insulating layer. Electron beam probing of the circuit with the passivation in place results is several complications. Since the surface potential of the passivation is only capacitively coupled to

the metal conductor underneath, the DC voltage information of the signal is not available. The insulator charges up to some equilibrium potential which shifts the surface potential to a value independent of the voltage on the underlying conductor. Thus the voltage contrast is lost and the image definition deteriorates or is lost entirely. While it has been suggested that high energy electron beams (15 keV or so) be used to induce conductivity in the passivation, this can result in damage to charge sensitive devices and is generally incompatible with MOS technology. Additionally, there is a problem common to electron beam examination of materials in the SEM. There often exists a contamination layer due to the beam interaction with hydrocarbons adsorbed on the surface. This changes the secondary electron coefficient which further complicates the measurement. A partial solution relies on mechanical probing of the circuit. This requires either that the circuit be tested before the passivation is applied or that the passivation be removed by chemical etching which risks further damage. Since the passivation layer serves the dual function of protecting the circuit and for some devices minimizing the diffusion of more volatile constituents of the IC material, this latter option severly limits the technique. However, it is of great practical interest to measure these voltages with the circuit operating and mechanical probing distorts the measurements due to the large capacitive loading of the circuit.

A more compatible solution relies on the focused ion beam which can be used to form an image of the surface of a semiconductor device and to mill through it. If small holes are milled through selected areas of the passivation layer of an integrated circuit (IC), it is possible to make voltage contrast measurements with an electron beam on the conductors beneath the passivation layer or with the ion beam itself.

6.4.2 Imaging the circuit

The primary difficulty in milling small holes through the passivation layer of an IC appears at the outset, while attempting to image the features beneath the layer. Since the surface rapidly charges to some positive voltage, the collection of secondary electrons for imaging is often very difficult if not impossible. This is precisely the difficulty one faces in making the voltage contrast measurements themselves. As will be shown, however, it is possible to image an insulating surface under some circumstances.

The contrast mechanisms available in ordinary secondary electron microscopy (SEM) are typically due to the differences in secondary electron yield resulting from differences in materials, topography or potential differences[151]. Under electron and ion bombardment of insulators, the contrast is diminished due to the surface charging. However, if there are topographic variations it is possible to use this surface charging to advantage. Since the charging of the insulator is often non-uniform due to differences in surface conductivity between inhomogeneous regions, the contrast may be thought of as a type of induced (i.e. not directly applied to the circuit) voltage contrast which is dependent on the circuit topography and incident beam properties. It is clear though, that the passivation layer cannot be too thick or the underlying topography will be lost. For the thin insulating layers on IC's considered here, the contrast brought on by surface charging is due to the variation in insulator thickness over the underlying circuit, i.e. for a given surface charge density and dielectric constant, the surface potential is proportional to the layer thickness and the voltage present on an underlying metal run is capacitively coupled to the surface through the passivation layer. The research described here has shown that it is possible to image

the IC surface despite this insulating passivation layer. However, this can be done only during the transient surface charge up time.

6.4.3 Surface charging and its reduction

A simplified qualitative picture of transient charging of a homogeneous insulator under positive ion bombardment can be formed by considering the surface as a resistor in parallel with a capacitor. The primary beam current supplies a constant flow of charge to the surface, some of which flows through the resistor. After some time, fixed by the RC time constant, the capacitor will be fully charged and the surface potential will reach an equilibrium value limited, in principle, by the beam potential. In practice, the surface potential does not reach the beam potential because breakdown on the surface occurs or some other leakage path is found. The time constant will determine the viewing period, unless some method of discharging the surface more rapidly exists.

The surface charging of insulating or semi-insulating surfaces is of more than academic interest. Both surface imaging and surface analysis of insulators require an understanding of the charging mechanisms. However, the mechanisms are extremely complicated and have been a topic of investigation for many years. If we limit ourselves to primary and secondary currents only, the charge balance equation may be written:

$$I = I_i^+ - I_e^- + \gamma_e I_i^+ - S^+ I_i^+ + S^- I_i^+ + \delta_e I_e^-$$

where the terms on the right represent respectively a primary ion current, a primary electron current, secondary electron current due to ion impact (γ_e is the secondary electron coefficient for ions), positive secondary ion current, negative secondary ion

current (S is the secondary ion coefficient for ions), and secondary electron current due to electron impact (δ_e is the secondary electron coefficient). Rewriting this gives the deceptively simple expression:

$$I = I_i^+(1 + \gamma_e - S^+ + S^-) - I_e^-(1 + \delta_e)$$

However, the analysis and elimination of charging is more difficult than suggested by this equation. Depending on the magnitude and polarity of electric fields applied between the target and surrounding electrodes e.g. a channeltron bias, secondary ion extraction optics for SIMS, or other impressed potentials, some of these currents may be suppressed and others enhanced. In other words, each of the coefficients is a function of the external fields. The landing position of the primary beam may also be affected. There is also an electric field induced by the surface charging itself and for some geometries an induced field may exist due to space charge. In practice, the effects of both primary beam parameters and target properties will influence the degree of surface charging. For example, the incident energy affects both the secondary electron and secondary ion coefficients which may be greater than or less than unity. The beam current, current density, surface and bulk conductivities, dielectric constant and degree of homogeneity of the target material also play a role in the surface charging. In general, the degree of surface contamination strongly affects the secondary electron coefficient for ion incidence. In addition, in the scanning systems employed in our studies, the scan time per line and the raster frame rate also have to be considered[152]. This results from the non-uniform charging of the target surface under the scanning beam. In this case, the factors involved are due to the competition between charging a particular target spot due to the beam and the time constant for discharging the spot. Furthermore, the scanning beam often deposits charge in a non-uniform manner due to a Gaussian or other non-uniform current density

distribution in the spot. Obviously, all the parameters involved in surface charging of insulators cannot be contolled even if they were well understood.

Typically, most scanning microscopes presently in use, employ either electron or ion primary beams. Positive ion bombardment of an insulator results in positive charging of the surface. Electron beam bombardment of insulators can result in positive charging of the target surface since the secondary ion yield δ is usually much less than unity. Seiler[151] presents a good discussion of secondary electron coefficients under electron beam bombardment. With electron beam bombardment, there exist two values of the primary beam energy E_p where $\delta=1$. The surface potential can be stabilized at the higher value of E_p since $\frac{\partial \delta}{\partial E_p} < 1$. This is illustrated in Figure 6.9.

One method of reducing the positive charging due to the ion beam is to bombard the surface with negatively charged particles, either electrons or negative ions. From the standpoint of charge neutralization, whether the neutralizing current or current density is more important, will depend on the surface conductivity and the line scan and frame rates as discussed above. Another method utilizes the fact that the impinging metallic ions could reduce the charging by some form of induced conductivity. This method has been used successfully with Cs^+ ions in the SIMS analysis of insulating crystals[153]. In one sense, the requirements for imaging an insulating surface are less critical than those for producing an accurate SIMS spectrum, since trajectories altered by surface charging are tolerable as long as the secondary currents can be collected. For SIMS, however, the surface charging may result in a shift of the secondary ion energy to values beyond the permissible limit for the energy analyzer transmission. In one case, the secondary ion energy reached 300 eV[154].

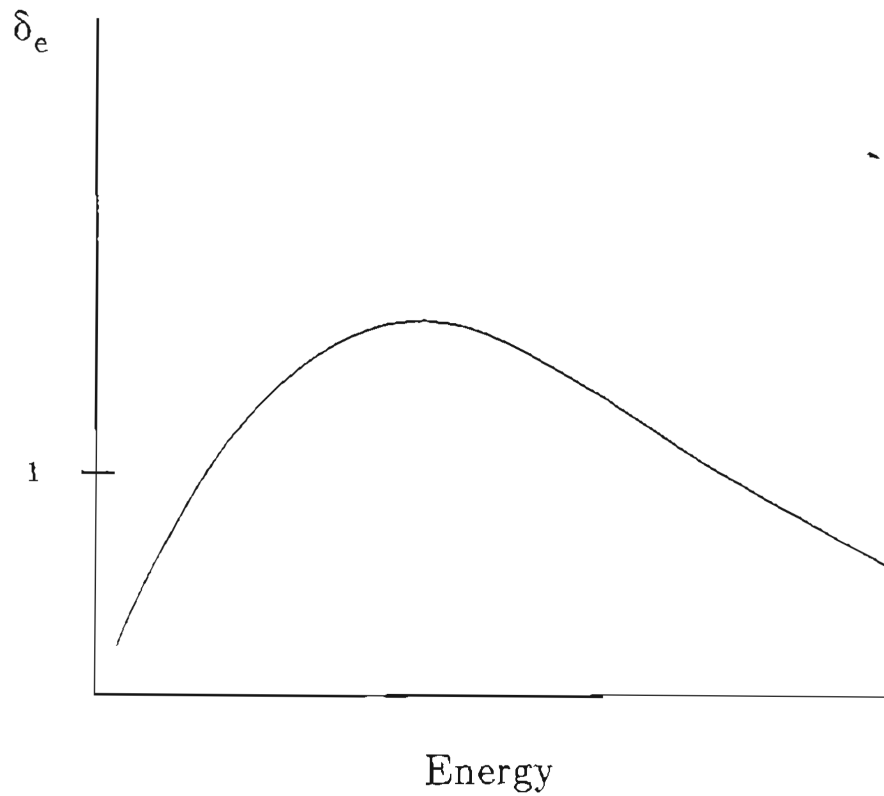

Figure 6.9 Schematic of secondary electron emission coefficient versus energy of primary electrons. The two unity crossover points are called the critical potentials. The higher energy critical potential is an important factor which determines the potential at which an insulating target will stabilize. Secondary emission coefficients can be found in ref. 151, for example.

6.4.4 Experimental findings

The scanning FIB bombardment of surfaces produces secondary electrons and secondary ions, both of which were used for imaging. However, surface charging may make it impossible to image with electrons as implied above. For very good insulators there is essentially no possibility of avoiding charging by positive ion bombardment without using an external source of negative particles. A simple W filament was sometimes employed in these experiments. This method appears to be somewhat "self-neutralizing" since it relies on the induced positive surface charge to attract the emitted electrons of the filament positioned nearby. Unfortunately, there are many difficulties involving direct heating of the target by radiation, inability to supply enough electron current, and the attraction of electrons by surfaces at greater positive potential e.g. the channeltron, making it virtually impossible to image via SEI. Chromium on glass photomasks proved particularly challenging and an auxilliary electron flood gun was employed.

6.4.4.1 Charge neutralization

Charge neutralization experiments were done using a CRT gun which was operated in an unconventional way as an electron flood gun. Its overall length was approximately 4.8 inches and it was mounted on a 6 inch flange giving a total length of $\simeq$ 7 inches from the surface of the flange to the end of the gun. The gun could not be pointed mechanically once it was mounted on the chamber but the electrical deflection was 15 millimeters or so at the large working distance to the target. Of course, the spot shape became severely distorted at large deflection angles and even at small angles was not round due to the incident angle with respect to the target. The

sample carousel and stage have been described elsewhere in this thesis. One of the sample positions held a metal plate which had been electrostatically dusted with zinc silicate which is fluorescent under electron and ion bombardment. The electron beam produced a bright green spot which was used for adjusting the flood gun. The same plate was also used for observing the position of the incident Ga^+ FIB (the apparent size and intensity of the "glowing" fluorescent region is a complicated function of physical and physiological factors which we mention only). By adjusting the deflection of both the electron and ion beams they could be made to coincide. The electron beam spot diameter was usually smaller than one millimeter depending on the operating conditions. Sometimes the front end channeltron bias was also used to move the beams. The actual experimental targets could not be aligned precisely along the same direction or at the same working distance as the fluorescent plate thus making the beam coincidence somewhat uncertain.

6.4.4.1.1 Activation of the cathode

Figure 6.10 illustrates the way in which the electron emission current was measured while the oxide cathode was activated. The following procedure was used for activating the cathode.

The 4 watt heater was operated at 8 - 10 volts. This liberated CO_2 and the pressure in the chamber rose from 2 x 10^{-7} torr to 2 x 10^{-6} torr in a rapid burst. The heater was then operated for 15 minutes at $V_H = 6.5$volts. The grid voltage was increased very slowly to $V_G = 7.8$ volts. After five minutes the emission current stabilized at 2 milliamperes.

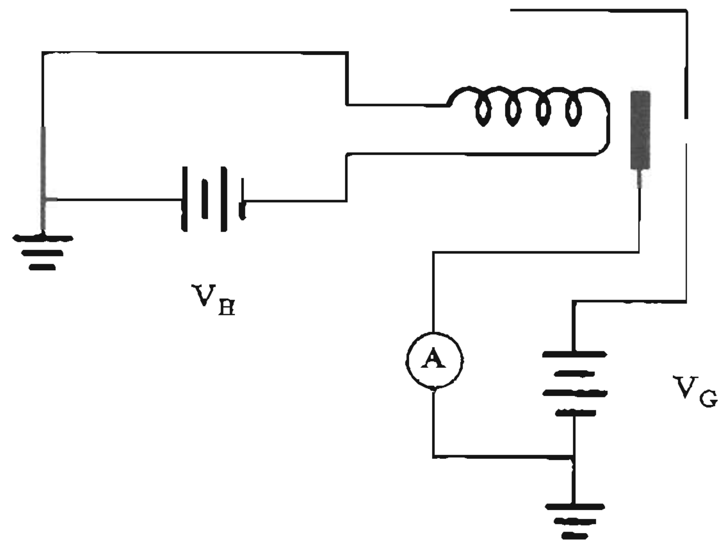

Figure 6.10 Activation of oxide cathode for electron gun used in charge neutralization experiments. V_H = 6.5 volts, V_G = 7.8 volts. This provided 2 mA of current.

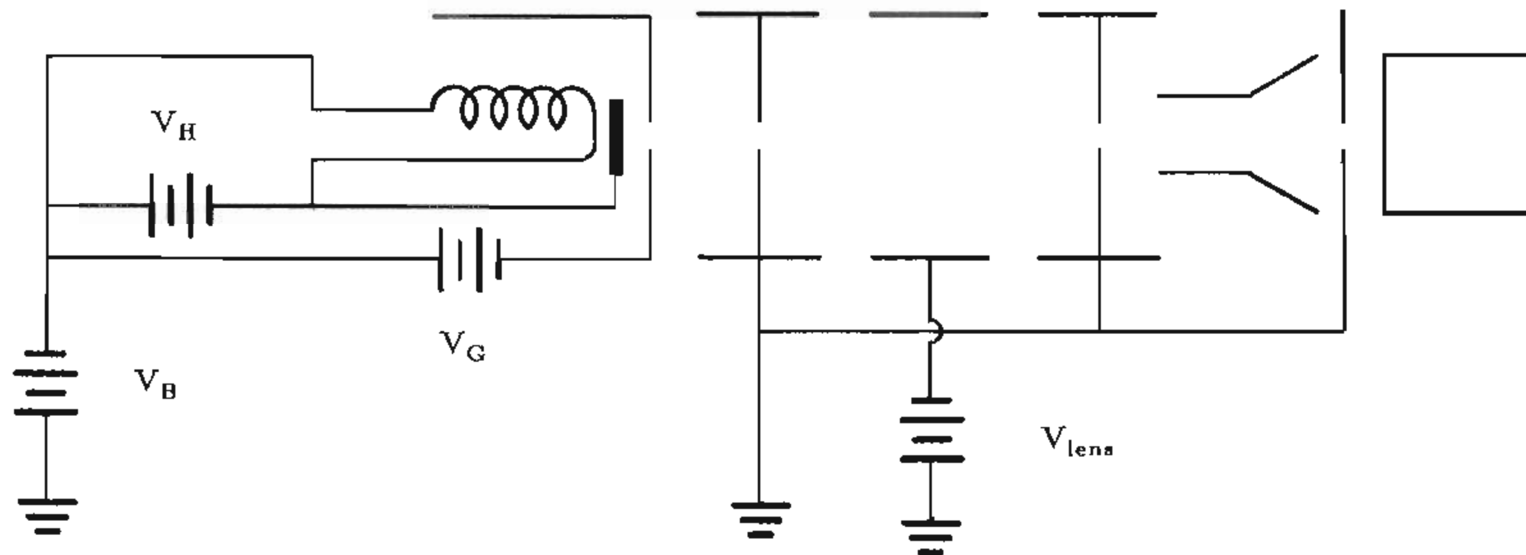

Figure 6.11 Schematic of electron gun used for low energy charge neutralization experiments. Beams in a range of energy up to 300 volts were employed.

6.4.4.1.2 Operation of the electron beam gun

Figure 6.11 shows the electrical connections for the gun while in operation. Energies in the range 0 - 300 volts were used to find the optimal operating conditions for charge neutralization. As noted above, these depend on a wide variety of factors which cannot be determined theoretically.

Preliminary experiments were performed using chromium on glass photomasks (supplied by Micrion, Inc. of Boston, Mass.) Despite some problems with 60 Hz noise due to pickup and groundloop problems, the neutralization technique clearly worked. At an electron beam energy of 170 eV and 10 - 15 keV Ga^+ ion beam energy the Cr on glass was easily visible in the SIE mode with relatively good contrast and was sufficient to observe FIB micromachined squares within the Cr strips. The best secondary electron images depended on the postition, current and focus of the beam. Unfortunately, moving the sample to a new position required re-adjustment of the current, focus, beam position and channeltron front bias. While this technique proved successful, the cathode used in the electron beam gun was not the most practical for this application. The total extracted current decreased by approximately 25% each time the vacuum chamber was vented to atmosphere and after 3 or 4 times the available beam current was insufficient to neutralize the target.

6.4.4.2 Imaging an IC through the passivation

Figures 6.12a and b show electron images obtained with a Ga^+ focused ion beam. The target is an unpackaged Large Scale Integration (LSI) multilpier chip for which the input, output and power supply pins were electrically floating. Since positive ion bombardment of the passivation layer results in a positive surface potential,

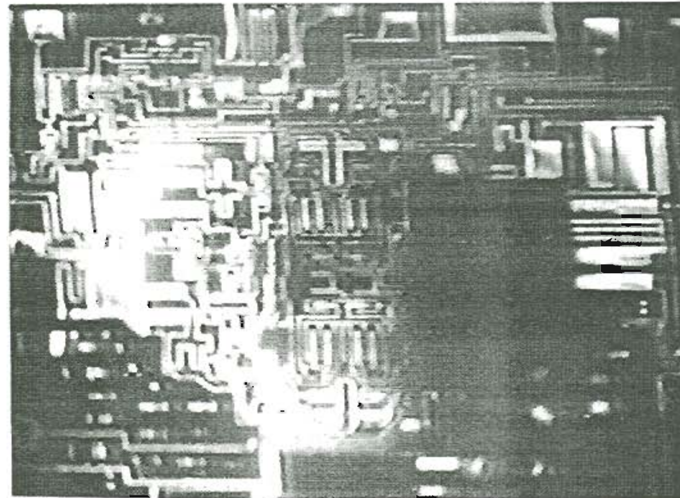

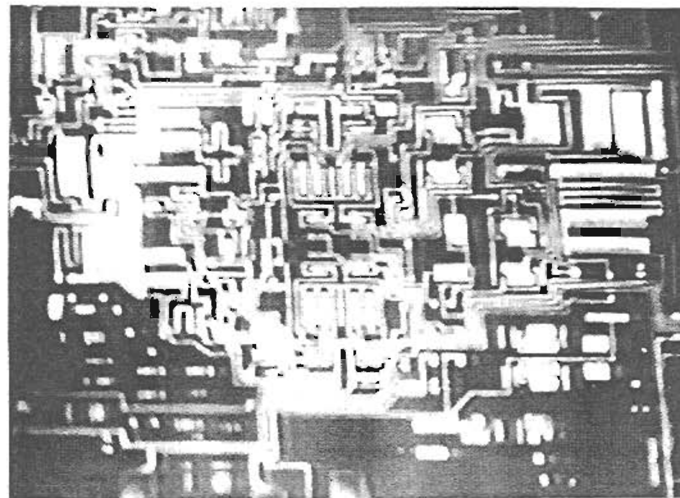

Figure 6.12 Secondary electron images of a LSI multiplier chip obtained during Ga^+ FIB bombardment. The input, output and power supply pins were floating. Imaging was possible only during a transient charge up time (see text for details).

the image is detectable only during the transient charge-up time. No auxilliary electron flood gun was used for charge neutralization in this experiment. For a primary Ga^+ ion beam current of 3 x 10^{-10} A. at $E_p = 4$ KeV and +250 volts bias on the CEM, the time constant for charging is on the order of seconds. The Figure 6.12a image lost sufficient contrast after 5 seconds to preclude seeeing the circuit detail. After 13 to 15 seconds out of the field of view of the scanning ion beam the passivation layer had discharged sufficiently so the process could be repeated. This reversible process could be repeated indefinitely. Figure 6.12b depicts a similar effect. In this case the average current density was increased by a factor of 25 by decreasing the area by a factor of 25 and the time required to achieve the same loss of image contrast was estimated to be less than one second. (This is indicated by the small dark area at the right of the center of the micrograph.) The final image was then obtained at the same magnification used to obtain Figure 6.12a.

The difficulty of imaging details with secondary electrons under ion bombardment through a passivation layer increases as the thickness of the layer increases and becomes acute when the layer exceeds 1μm. Figure 6.13 shows a secondary electron image of a portion of a dual quad NOR gate. The insulating layer thickness is estimated to be 1 μm or less. On the other hand, a 64 K dynamic RAM proved impossible to image by secondary electrons produced under ion bombardment. The passivation layer for this device consists of a layer of silicon nitride over a silicon dioxide layer with a total thickness of 1.5 μm to 2 μm. For the case of imaging by secondary ions, however, it becomes possible to see contrast after several minutes of Ga^+ bombardment even for relatively thick layers.

6.4.4.3 Milling of insulating layers

When the surface topography of the passivation layer can be imaged, it becomes possible to remove selected areas of it. Square holes were produced by raster scanning the Ga+ ion beam over the runs of a dual input, quad NOR gate. The holes took 15 seconds to produce, are 0.8 μm square, and were milled using an average current density of 50 mA/cm^2. This corresponds to a sputtering rate of 700 Å /sec. with a passivation layer thickness of 1 μm. For these cases, there appears to be no adverse effect of charging on the milled shape. Generally, one can say that the interplay of sputtering, which produces a rapidly changing shape, and charging and discharging will determine to what extent the primary beam deflection will be altered.

6.4.4.4 Voltage contrast of FIB milled passivated IC's

A simple method exists for determining when a hole has been completely milled through the passivation layer, if the underlying conductor is grounded. There is a large change in image contrast present at the moment of breakthrough due to the large yield of secondary electrons from the conducting layer. Figures 6.14a and b are SEM images of the milled region of a 3.9 μm x 3.9 μm square hole in two voltage states. With positive voltage applied to the metal run, the image is dark (a) while the bright image (b) is obtained with the run grounded. These images clearly show the voltage contrast effect. Since the penetration depth for these heavy ions is 150 Å or less at 20 KeV, the effect of bombardment will be negligible until the 1 μm thick insulation is virtually entirely sputtered through. This suggests the use of SIMS as an additional technique to monitor the milling of the passivation layer.

Figure 6.15 shows the result of a simple measurement of a resistor covered with 1 μm SiO_2 In this case, a 1 Hz, 1 volt square wave was applied to one pad of the resistor with the other pad kept grounded. The figure shows a comparison of the voltage measured with the VCSEM through the passivation layer (curve 1) with the same measurement made through the ion milled hole shown. It clearly indicates the effect of surface charging under the electron beam as the measurement is made.

Figure 6.16 shows the secondary electron energy distribution which is obtained by differentiating the output of the secondary electron energy analyzer. The measurement over the passivation layer (curve 1) is shifted 1.3 v with respect to the measurement through the hole (curve 2). The structure on the right half of each curve is an artifact of unknown origin.

Recently, more sophisticated electrical measurements have been made to measure the voltage waveform of a 256K bit dynamic RAM and employed the same technique described here[155]. The authors used a 100keV gallium FIB to mill small squares through the passivation layer over a $MoSi_2$ gate NMOSFET. They then examined the effects on the threshold voltage of the gate for both electron and FIB radiation. In this manner, they determined the dose for which V_{th} changed and established the doses which could be used without damaging the device. We do not report their results here because the critical doses depend on the passivation film materials employed, their thicknesses and the particular devices being tested i.e. the conditions would have to be "re-calibrated" for disimilar devices. The reader is referred to the original article cited above. We can conclude however, that the technique described here provides a viable method for aiding electron beam testing of integrated circuits. In fact, the method appears to be leaving the realm of laboratory

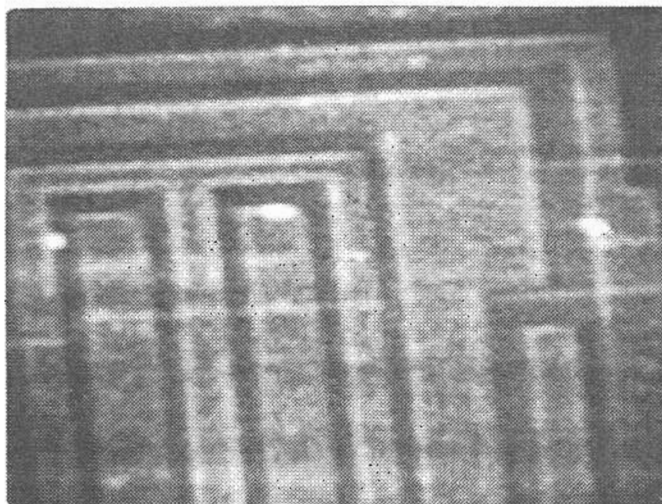

(a)

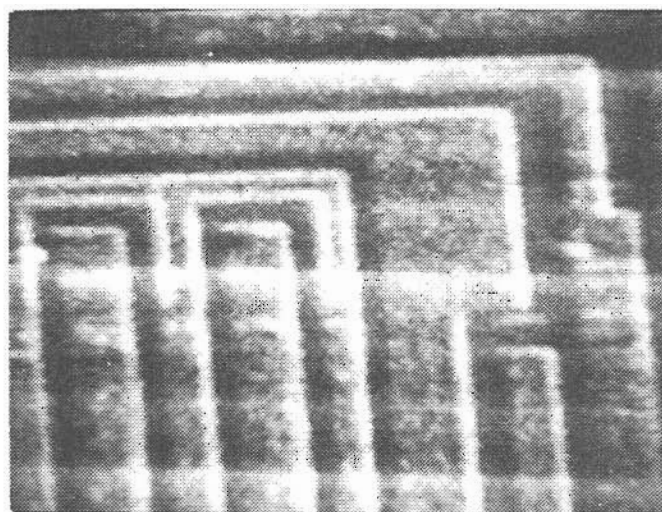

(b)

Figure 6.13 Images of a portion of a simple dual-quad NOR gate with approximately 1 μm of passivation. Upper: Secondary electron image. Lower: Secondary ion image.

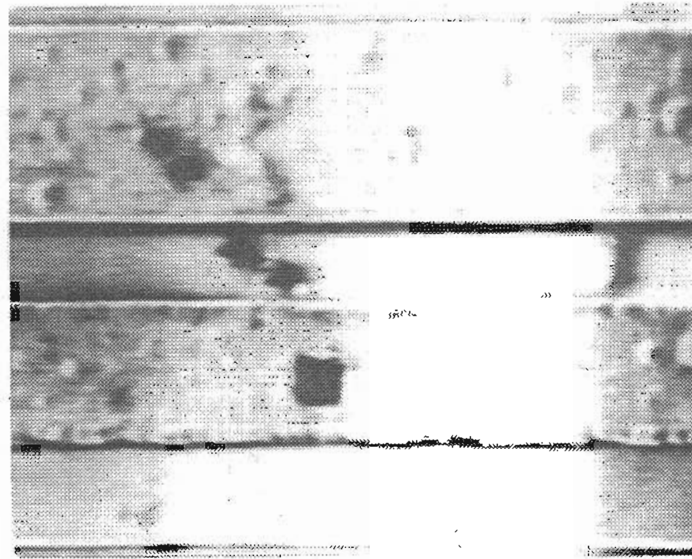

(a)

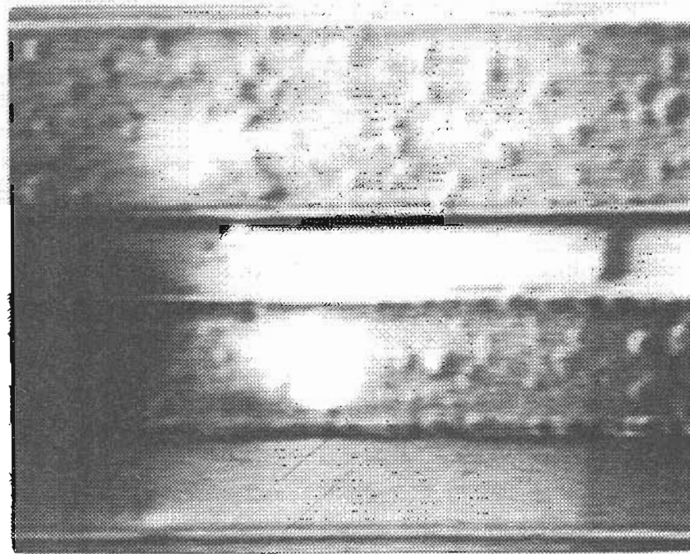

(b)

Figure 6.14 SEM images of milled region through Al run of IC in two voltage states. (a) Small positive voltage applied (dark). (b) Run is grounded (bright)

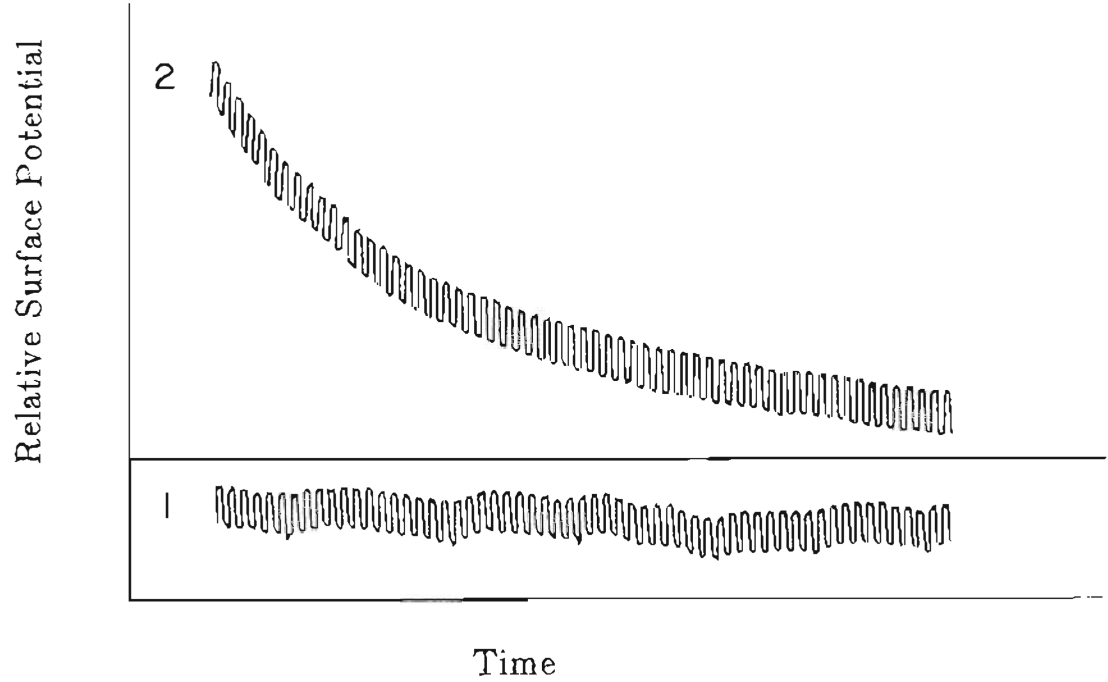

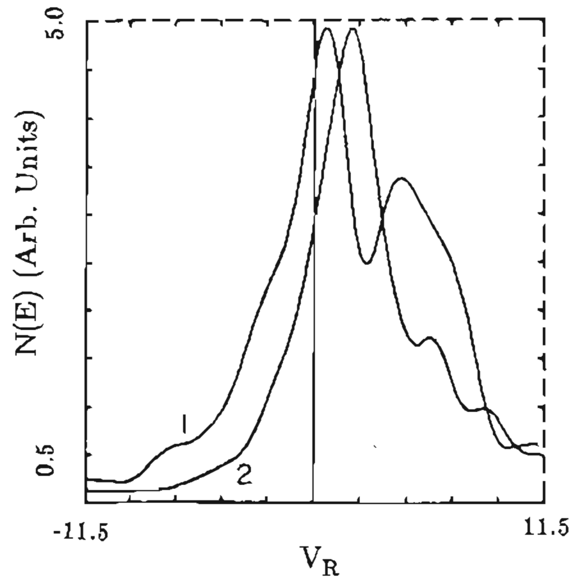

Figure 6.15 Upper: A 1 volt, 1 Hz square wave is applied across a thin film resistor. Curve 2 shows a charging effect during the VCSEM measurement. Curve 1 indicates negligible charging. Lower: Secondary electron energy distribution taken through the passivation layer (1) and milled area (2) corresponding to Upper.

curiosity and may have commercial possibilities.

7. FOCUSED ION BEAM LITHOGRAPHY

7.1 Introduction

The term lithography refers to the patterning step in the process of constructing integrated circuits and is of intense interest to the semiconductor industry. The demand for reduced pattern dimensions and increased device density requires continuing research in the areas of organic and inorganic resist chemistry, in the various exposure techniques via photons, electrons or ions and in the further development of wet chemical and dry processing methods.

Although circuit and device design advances have been made, it is clear that the advances made in lithography are directly responsible for the increase in device density per wafer and the decrease in linewidth required for constructing smaller devices. As resolution increases through the submicron regime, various lithography schemes offer their unique advantages. Currently, optical lithography dominates large scale commercial production of integrated circuits. This will probably continue into the early 1990's as advances in optical lithography continue[158].

Conventionally, thin organic films, otherwise known as resists, are spun onto wafers, baked into hardened films and then exposed through masks by photons or by electrons. The resist is then developed leaving a relief pattern on the wafer. This

pattern must now withstand, i.e. resist, further processing steps perhaps involving etching, growing material, doping of the substrate, depositing material and then removal of the resist. Resists are said to be either positive or negative as illustrated in Figure 7.1. Both wet chemical etching and dry etching techniques are currently being used to process or develop resists.

Research on the patterning of resists by ion beams in particular has been ongoing for several years, the object being to achieve narrower linewidths i.e. higher resolution and a greater density of devices per wafer. Ion beam lithography is a relatively new technique which offers certain advantages over optical lithography. Electron beam lithography is also being investigated but it suffers from certain disadvantages e.g. proximity effects, backscattering and lower resist sensitivity.

Generally, resist sensitivity for ion beam lithography is much greater than for electrons or photons. This results from the short penetration depth for such massive particles and hence the large energy deposition density. The resist is called upon to play dual roles. It must be sensitive to the incident radiation and yet be controllably resistant to further etching steps. However, due to the small ion range, the distribution of ions in the resist is not sufficient to prevent the resist from being consumed during subsequent processing. Therefore, multi-layer schemes are necessary. Most of the recent work in ion beam lithography has been in the area of unfocused beams i.e. by projecting broad ion beams through masks to expose resists. The work reported here, on the other hand, is one of the comparatively few examples of FIB or scanning ion beam lithography. This may also be called direct write or maskless lithography. The present work describes two bi-layer systems for FIB lithography.

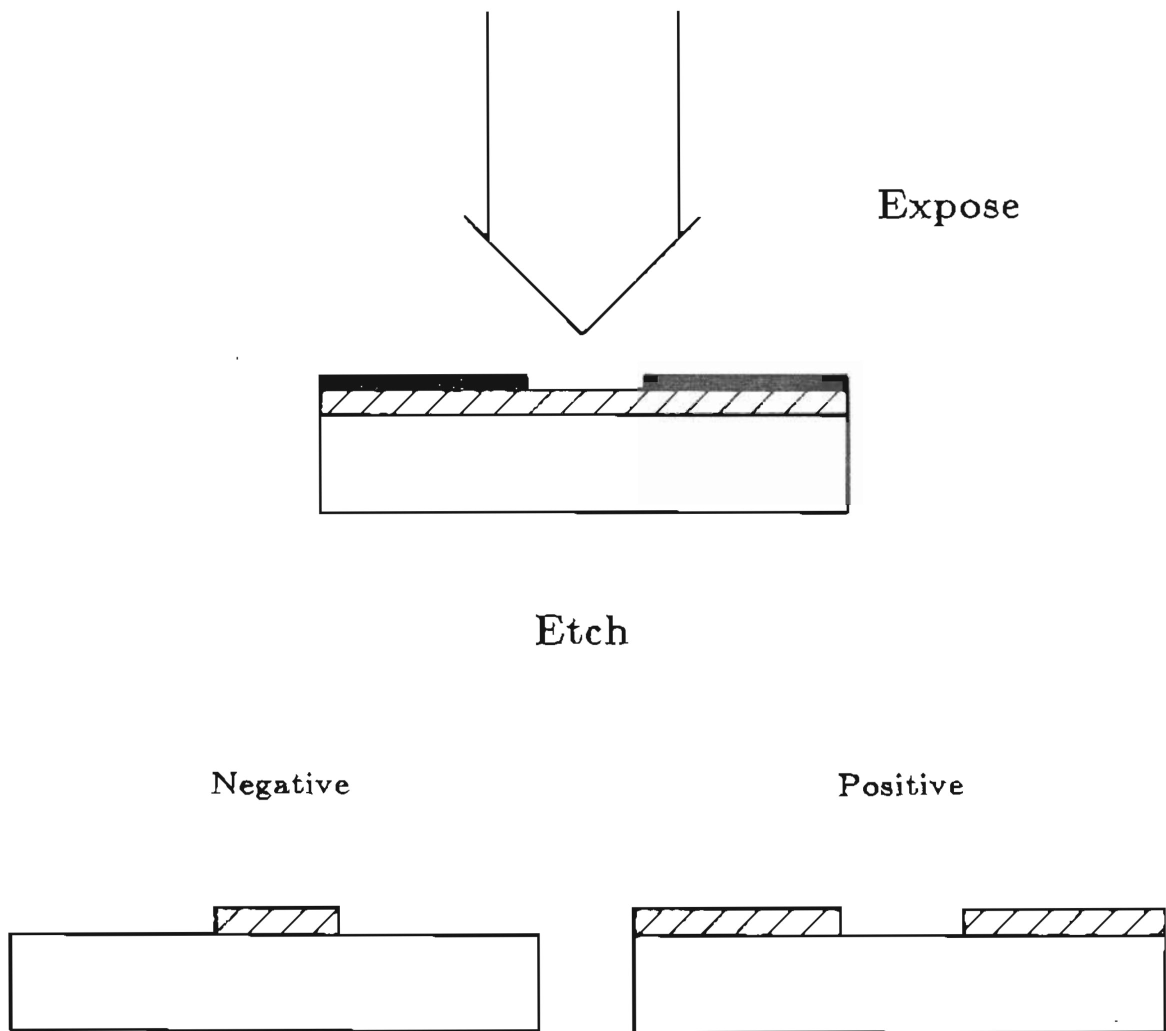

Figure 7.1 This figure illustrates the difference between positive and negative resists. The experiment described results in a negative "self-mask". Exposure of a negative resist causes "hardening" to subsequent etching. A positive resist is consumed in the exposed areas.

7.2 Background

Metals[157-159], insulators[160] silicon[161-164], and organic polymers (photoresist)[55], have been implanted in order to decrease wet chemical and dry plasma etch rates. Typically, the ion doses used have been in the range 10^{15} to 10^{18} ions/cm^2.

Kuwano[55] found that a single layer of photoresist implanted with Ga ions to a dose of 10^{16} / cm^2 could provide a differential etch rate compared with to the unimplanted resist. The implanted region acted as a negative resist and yielded 1μm lines with a height of 0.5μm but was limited by a significant linewidth variation along the patterned line. This work was repeated with FIB implanted photoresist (see Results section). Other ions and organic polymers have also been used producing similar results[159,165]. These other techniques suffered from similar drawbacks such as significant line width variation, sensitivity of line width to the plasma development and the requirement for high dose implants.

The organic polymeric material known as polyimide is commonly used in the electronics industry as a coating material because it withstands high temperatures (350 °C) and attack by many inorgainic chemicals. Hiraoka[166] used stencil masks to define a broad area proton beam whne exposing an organometallic compound on polyimide. The protons induced polymerization of the organometallic compound which then had a greater etch resistance than the polyimide, thereby producing a so-called negative resist. He also demonstrated that a 150Å Bi film on PMMA could be directly patterned by a proton beam and used as a positive resist for subsequent patterning of the PMMA. The required dose, however, was sensitive to the Bi film thickness. In this manner, Hiraoka demonstrated fine features with high aspect ratios. Kato et al[58] have demonstrated that a Ga FIB could be used to form a positive resist

mask for VLSI submicron processing by sputtering through a 1000Å gold layer on an organic polymer. After exposure, the mask is removed and the pattern developed by wet chemical or dry etching. The chemistry of ion beam resist exposure is discussed by Komuro, et al[167].

7.3 Purpose of the experimental work

In this work, the FIB system was used to expose either spin-on-glass (SOG) or electron beam deposited silicon (E.B.Si) as the top layer of a bi-layer system, the bottom layer being HUNT206 photoresist (HPR206) in both cases. These two layers were formed on top of a silicon wafer. Exposure patterns written into the top layer were then developed into the photoresist under suitable plasma and reactive ion etching (RIE) conditions. It was found that there is a differential etch resistance which can be utilized in both bi-level systems to produce smooth, vertical walled structures of constant line width having a rectangular profile and typical dimensions of 2 μm high and 0.4 μm wide. Even larger aspect ratios are possible and this will be described in the concluding section.

Different regions of the wafer were exposed by implanting Ga at 16 keV. A ramp generator was triggered manually to produce the line and raster scans. By manually moving a precision stage with a resolution of 1 μm selected areas of the wafer could be positioned under the beam. After implantation, the wafer was diced so almost every die contained a single pattern. Both implanted and non-implanted individual films as well as bi-layers were plasma processed to establish the differences among them.

7.3.1 Preparation of the films

The spin coating technique has long been employed in microelectronics and accepted as the best available method to obtain thin, uniform, adherent films. A polymer solution is applied to the substrate which is then rotated at high speed (between 1000 and 8000 rpm or so) until the solvent has evaporated. In this study, HPR206 films 2 μm thick were prepared by spinning the liquid onto 3 inch diameter silicon wafers, heating in air at 220 ° C for 30 minutes. This is done to ensure thermal stability of the film. Some of the wafers were oxidized to 1 μm, and patterned optically to yield cavities with widths from 1 to 100 μm. These wafers were used for testing the ability of HPR 206 to " planarize " i.e. smoothly coat, the surface of a patterned surface, resulting in a flat surface. This is an important aspect of wafer processing. The flat surface enables a uniform resist thickness to be produced. If the resist thickness varies, the linewidth of patterns developed in the resist will vary. This is a potential problem with all current forms of microlithography.

The SOG solution was applied to the silicon wafer by pipette. After spinning, the siloxane films were cured at 200 ° C, yielding a 1250 Å thick film. Other HPR206 coated wafers were subsequently coated with a 900 Å thick film of silicon deposited by electron beam evaporation of high purity silicon.

7.3.2 Etch rates and pattern transferability

The etch rates of the individual and non-implanted films of HPR206, SOG, and E.B. Si were determined separately under the conditions indicated in Table 7.1. The implanted and non-implanted SOG layer was processed in CHF_3 / O_2 and RIE O_2 to

Table 7.1

Typical Etch Conditions					
FILM	PRESSURE (mtorr)	GAS 1	GAS 2	R.F. POWER (watts/cm^2)	MODE
SOG	50	CHF_3	O_2	0.20	PLASMA
HPR206	7.0	O_2	-	0.32	RIE
E.B.Si	8.0	SF_6	Ar	0.08	RIE

compare their etch rate resistance. In CHF_3 / O_2 plasma, the etch rates of non-implanted and implanted SOG were substantially different. On the other hand, in RIE O_2 the etch rates of the implanted and nonimplanted SOG were similar but were small compared to the etch rate of the non-implanted HPR206 layer. In the RIE O_2 process, the ratio of etch rates of the non-implanted HPR206 to the SOG was 100:1. This shows that the top layer (SOG) could be implanted with Ga and act as a mask during the CHF_3 / O_2 processing. This mask could then be maintained during the subsequent RIE O_2 etch and result in a (Ga mask) protected structure as the HPR206 was etched away. Next, the SOG/HPR206 and E.B. Si/HPR206 bi-layer combinations were fabricated in order to test the ability of the plasma and RIE processes to transfer a pattern. The films were not gallium implanted but were exposed optically using a standard trilevel process[168]. The top photoresist, 4000 Å thick, was exposed through an optical mask in a contact printer and then developed. This pattern was transferred into the SOG and then into the HPR using RIE in O_2. This description may be clarified by examining the process illustrated in Figure 7.2. These findings form the basis of this bi-layer process.

7.4 FIB exposure

Having established the etch rates for the individual implanted and non-implanted films the next step was to implant the SOG/HPR206 and E. B. Si under the following conditions: The FIB system provided 0.2 nA of Ga^+ ion current in a 0.4 μm at a beam energy of 16 keV. The probe current was collected in a Faraday cup and measured with a Keithley 602A electrometer before each exposure. Because the ratio Ga^{++} / Ga^+ is $\leq 0.01\%$[169], there is no need for filtering the beam. The

Optical Mask

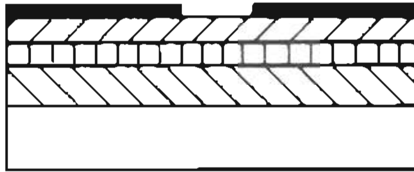

Resist
SOG (Siloxane)
HPR206

Resist patterned optically

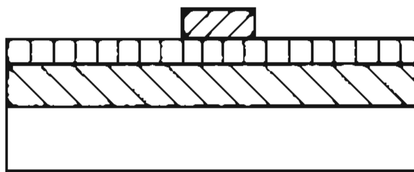

Resist
SOG (Siloxane)
HPR206

SOG developed in
CHF_3/O_2 plasma

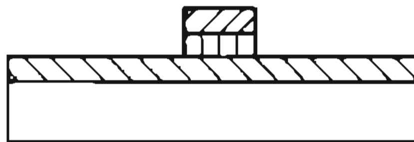

Resist
SOG (Siloxane)
HPR206

O_2 RIE

Figure 7.2 Illustration of a test of the ability of the unimplanted bilayer to transfer a pattern. A standard tri-level optical process was used. The top photoresist was MACDERMID 914, 4000 Å thick.

isotopic abundance was also ignored. Implantations were made both by single line scans 50 μm long and 50 x 50 μm areas using multiple analog raster scans of the target. The dose was controlled by varying the exposure time and can be calculated very simply:

$$D = \frac{IT}{eld}$$

for line scans and

$$D = \frac{IT}{el^2}$$

for area scans, where

I is the beam current, T the exposure time, e the electron charge, l is the line length, d is the spot diameter and D is the dose in ions/cm^2. These simple relations do not consider the current density distribution of the spot. Hence, the variation in dose transverse to the scan direction is not considered either. However, it is easy to show that if

$$Y_{CRT} < M\ d_s\ \frac{\nu_x}{\nu_y}$$

where Y_{CRT} is the monitor dimension along the vertical direction. M is the magnification, d_s is the beam spot size and $\frac{\nu_x}{\nu_y}$ is the ratio of the horizontal to vertical frequency then there will be sufficient overlap of the beam as it scans the surface to deliver a uniform area dose (see Appendix, this chapter). The implants were produced over a range of dose from 10^{14} to 10^{16} ions/cm^2. At a dose of 10^{16} ions/ cm^2 there was 300 Å depression in the SOG. The depression was 130 Å for 10^{15} ions/ cm^2 with similar results for the E. B. Si. The depth profile of Ga in the SOG was measured by Ar sputtering and Auger spectroscopy. The results are shown in Figure

7.3b. Classical predictions place the range at about 100 Å which agrees with the first peak; however the origin of the second peak at about 350 Å is unclear. The depth profile of gallium in the E.B. Si peaks at approximately 100 - 150 Å (Figure 7.3a). The sequence of the experimental exposures and processing is presented in Figure 7.4.

Three sorts of patterns were written into the bi-layers. The first were 50 x 50 μm squares implanted at 10^{16} ions/cm^2. This was used to test the ability to write large features with a uniform dose. Figure 7.5 indicates that this is easily achieved. The second pattern is a series of lines at a fixed dose but with a decreasing distance between adjacent lines. This allows us to examine whether there is any proximity effect. The so-called proximity effect is responsible for the fundamental limitation to the ultimate resolution in electron beam lithography and becomes important for linewidths less than 2 μm. It arises from the fact that the exposure dose at a particular point is the sum of the direct e-beam exposure and the exposure due to the backscattered electrons in the target. For ion beam exposure, the secondary electrons produced by the beam have a relatively short range and there is virtually no ion backscattering in the resist. Furthermore, since the ion range is quite small, (see Figures 7.3a and b) there is no contribution from secondary electron emission from the wafer substrate itself. Therefore, we do not expect to see any significant broadening and indeed, the results bear this out. This is shown in Figures 7.6 and 7.7. The wide line to the right is actually due to accidentally overlapping line exposures and is not related to the proximity effect. A third pattern was used to determine the line width as a function of dose shown in Figure 7.9. We see that the linewidth can be controlled easily by varying the dose between 1.0 and 2.0 x 10^{16} ions / cm^2.

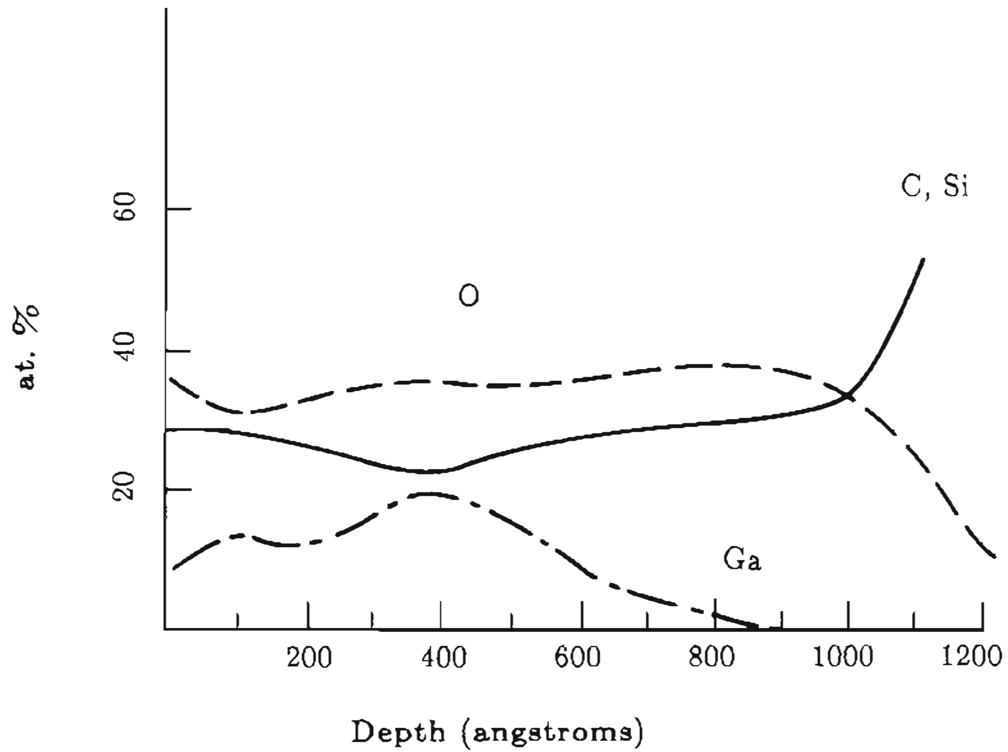

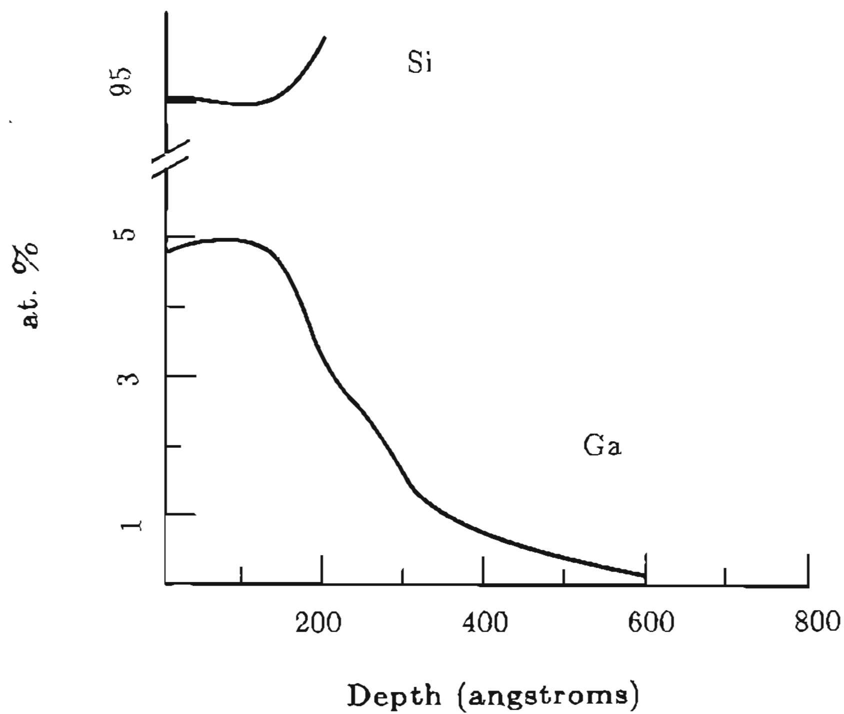

Figure 7.3 Upper: Depth profile by Auger spectroscopy of gallium implanted into SOG. Classical predictions agree with the position of the first peak at approximately 100Å. The origin of the peak at 380Å is unclear but may be due to knock-in by argon ions. Lower: Depth profile by Auger spectroscopy of gallium in electron beam deposited silicon.

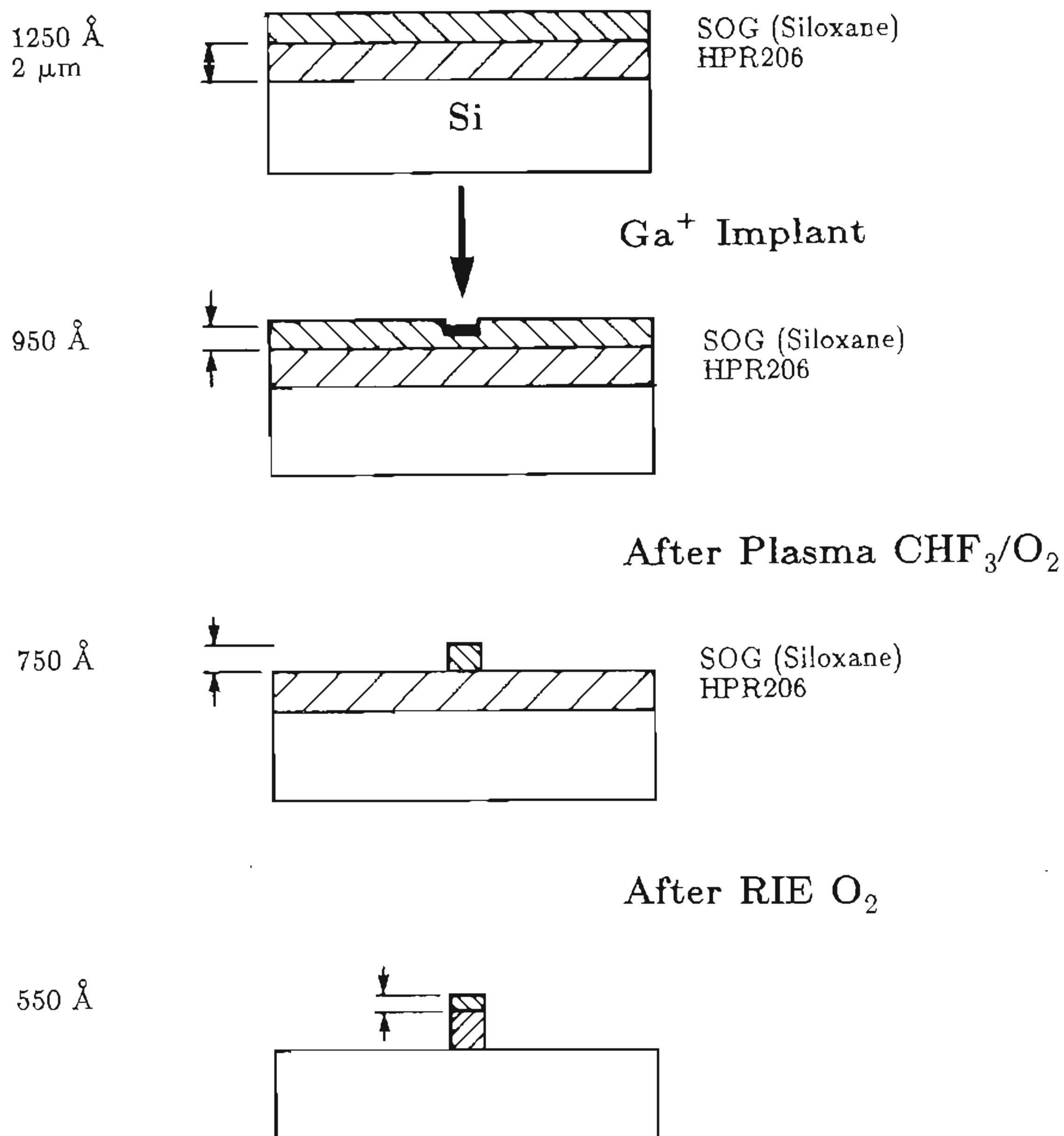

Figure 7.4 Experimental arrangement. Top to bottom: (a) Two level system for FIB ion beam lithography is fabricated. (b) Exposure to Ga^+ implant. 300Å of SOG have been lost due to sputtering. (c) After CHF_3 plasma etching 750Åof SOG remain i.e. 200Å lost during plasma processing. (d) The RIE O_2 consumes 2 μm of unprotected HPR206 while only 200 Å of the implanted etch mask has been consumed i.e. 100:1 selectivity is available. This indicates that a 7.5 μm x 0.4 μm structure could have been fabricated.

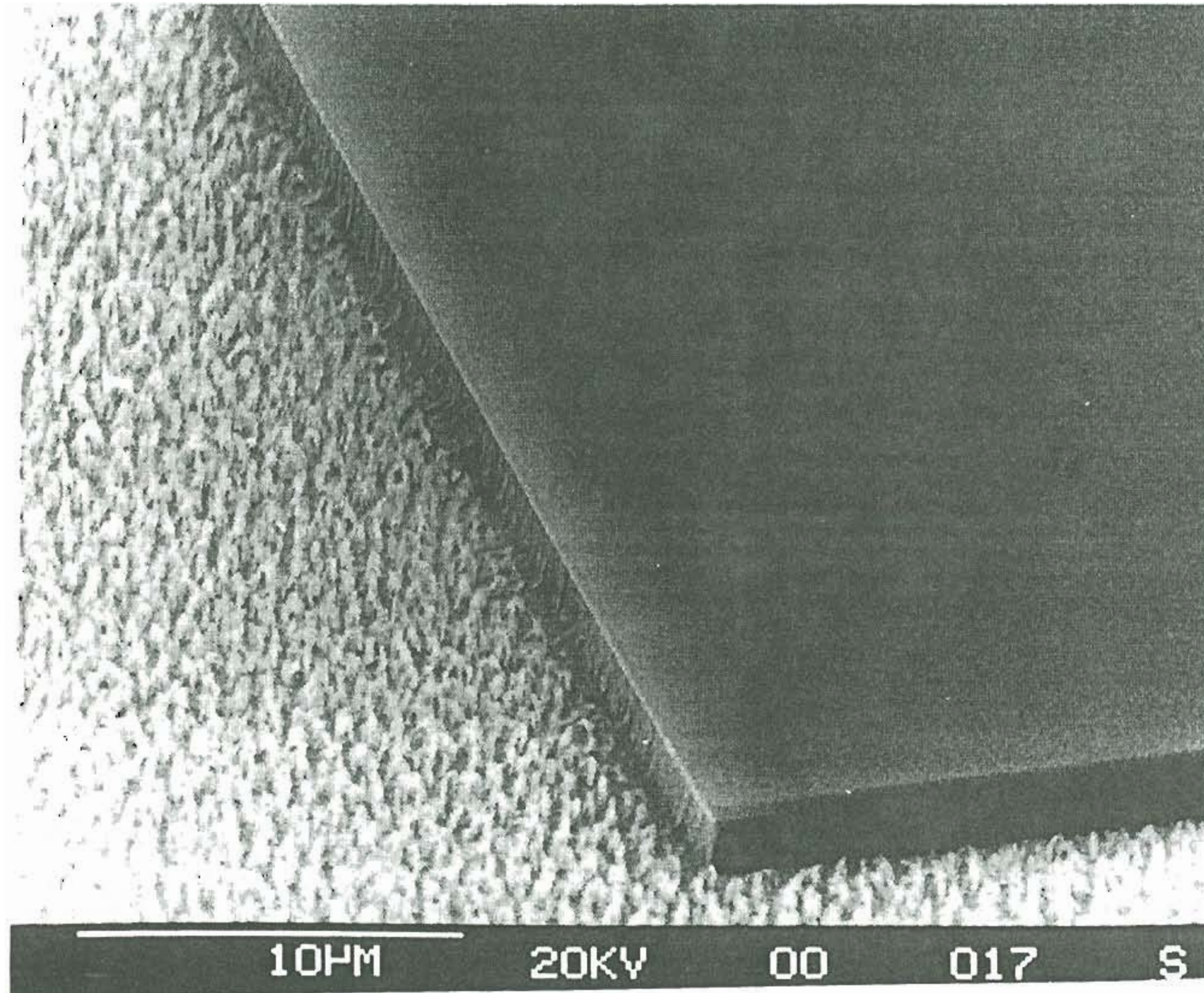

Figure 7.5 $50 \times 50 \mu m$ square implanted at 10^{16} ions/cm^2. Note the smooth flat surface indicating dose uniformity is easily achieved.

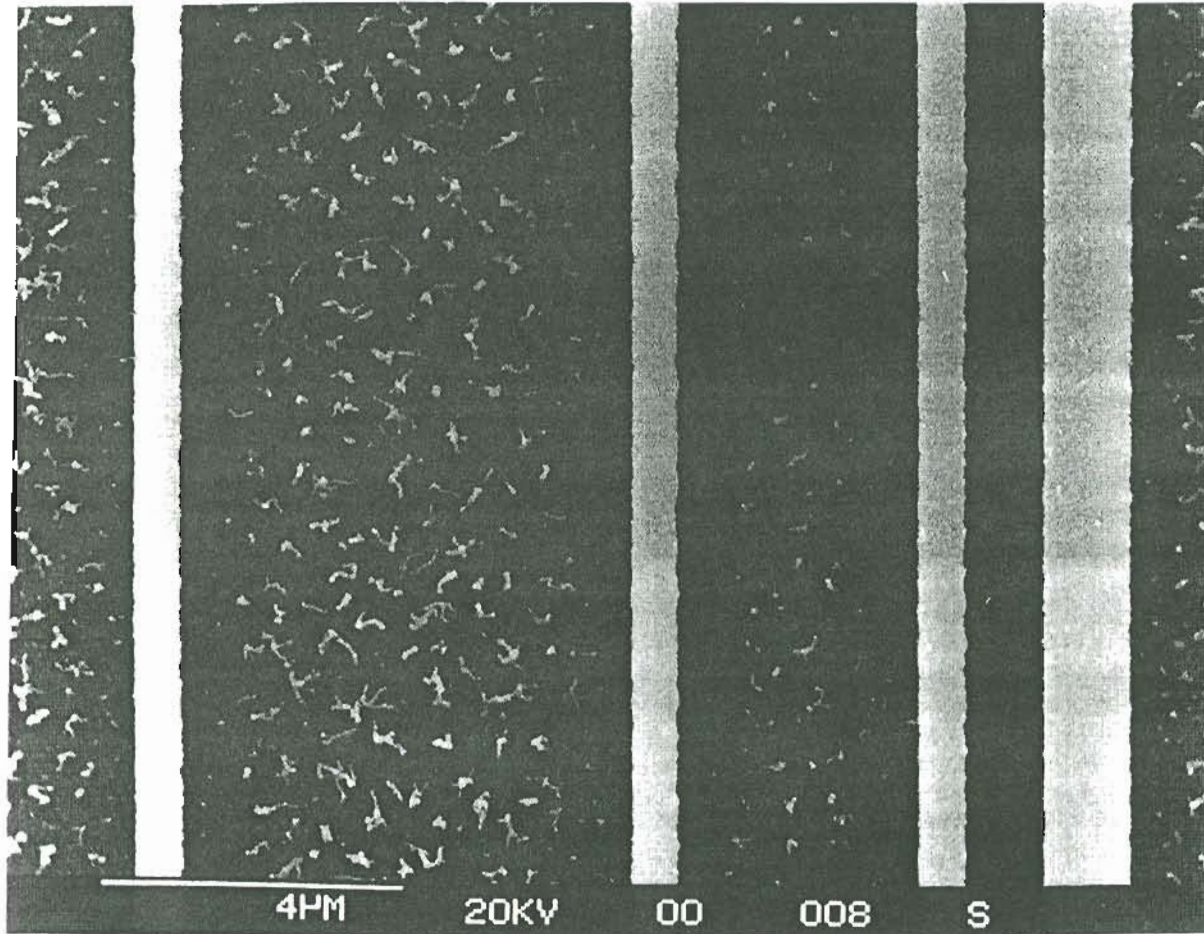

Figure 7.6 Series of fixed dose lines (1×10^{16} ions / cm^2) with decreasing spacing between lines. The line to the right was inadvertently produced by mechanically overlapping two lines.

7.5 Some technical considerations

The various patterns were repeated at many locations over the wafer to ensure reproducible results. At the time these experiments were done, the FIB system was not equipped with a beam blanking capability. This means that as long as the source emitted ions, there was some exposure of the target i.e. the beam could not be "turned off" between segments of a pattern or between different patterns. However, this extraneous exposure was minimized, if not eliminated, by making certain that the duration of the beam retrace was very short compared with the exposure time and that the beam remained stationary only outside the region of interest.

A complete set of patterns consisted of several line scans and a large area raster scan. After four or five sets, the ion current was turned off and the wafer moved manually with a precision of 1 μm to enable the next set of exposures. A Faraday cup mounted on a stage was rotated into place at fixed detents for beam current measurements. This was required since the extracted ion current had a tendency to drift somewhat during the course of several exposures. The stage was then rotated back so the wafer was again under the beam. The ion beam was then turned on again. In view of the desirability of keeping extraneous exposure to a minimum, focusing and astigmatism corrections were somewhat problematic, especially without the beam blanking capability, and particularly since the substrate sometimes exhibited surface charging. When it was possible to obtain a secondary electron image, the focusing and astigmatism adjustments were made. Then the scanning voltages were removed and the wafer quickly moved to a virgin area to begin the next exposure. When the surface charging was strong the image intensity and contrast vanished. Fortunately, it was found that if the ion beam was scanned at the boundary

between a wafer edge and free space there was just sufficient contrast to obtain a rudimentary image with the maximun CEM gain. This was quite difficult and was often done in a darkened room. Patience and visual (i.e. mental) signal processing enabled the focusing and astigmatism adjustments to be done. One may say with confidence that, generally speaking, these adjustments are always difficult at best when such surfaces are smooth, featureless, sometimes exhibit surface charging and are sensitive to the incident radiation.

7.6 Results

Figures 7.6 and 7.7 show typical results after dry etching of the FIB implanted bilayer. The etch produces a 2 μm high vertical wall with a rectangular profile approximately 0.4 μm wide, equal to the beam spot diameter at this energy and working distance. Figure 7.8 shows that smooth side walls result. An important aspect of these results is that the line profiles do not become trapezoidal due to lateral erosion of the (self) mask during RIE O_2 etching. This results from the high etch rate ratio of the HPR206 to SOG in the RIE O_2 plasma. Comparison of this bilevel scheme with that of Kato et al. (see Figure 7.10)[58] shows that their process suffers from substantial mask erosion. We can estimate the effect of induced mask erosion by etching for a time longer than required to develop the patterns i.e. by overetching. After overetching by 50%, there was no apparent linewidth variation. At 150% overetch, the linewidth decreased by about 0.15 μm, although the walls were still rectangular. This proves that there is minimal mask erosion. The linewidth is approximately constant and linewidth variations are a small fraction of the width itself, typically only a few percent. Similar results were obtained for the

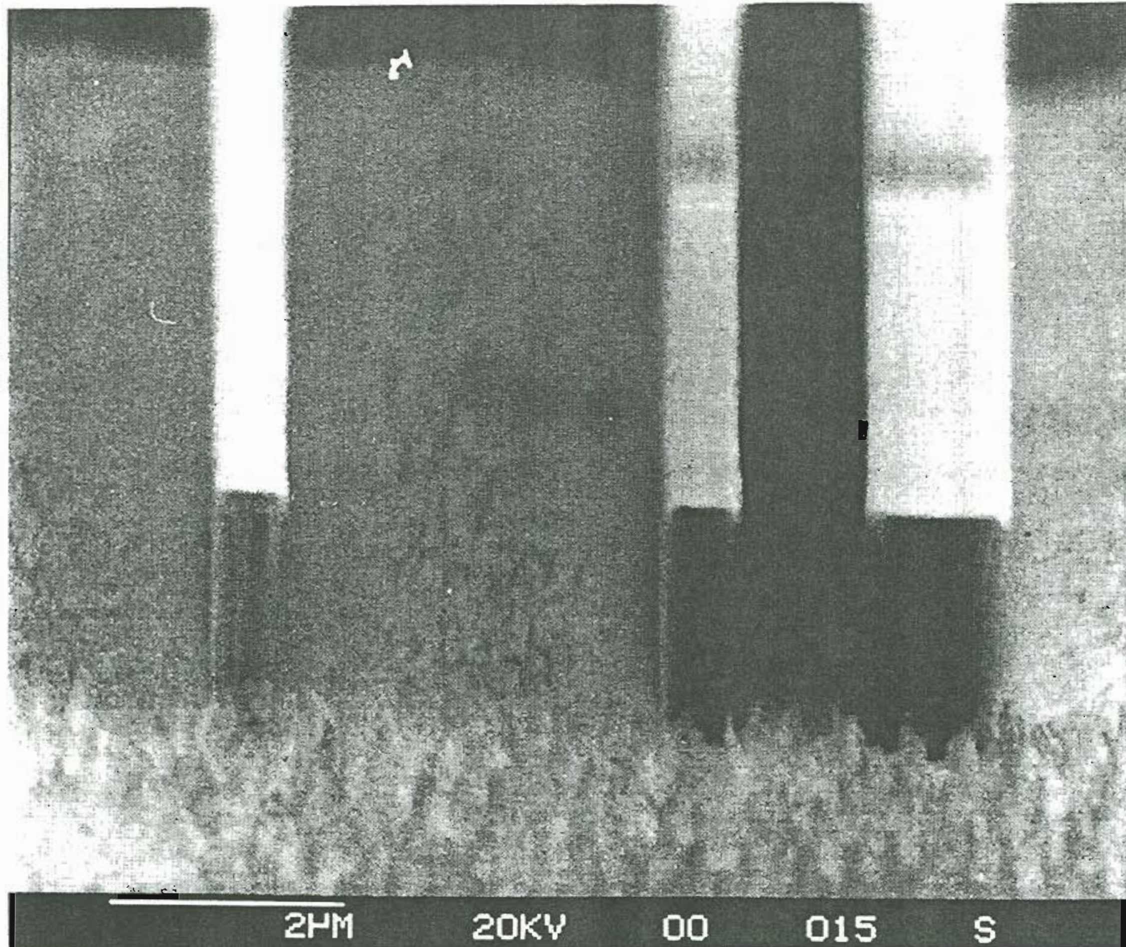

Figure 7.7 Results after dry etching of the implanted bilayer. Smooth vertical walls 2μm high by 0.4μm wide are produced. The beam spot diameter is approximately 0.4μm. Same lines as in Figure 7.6.

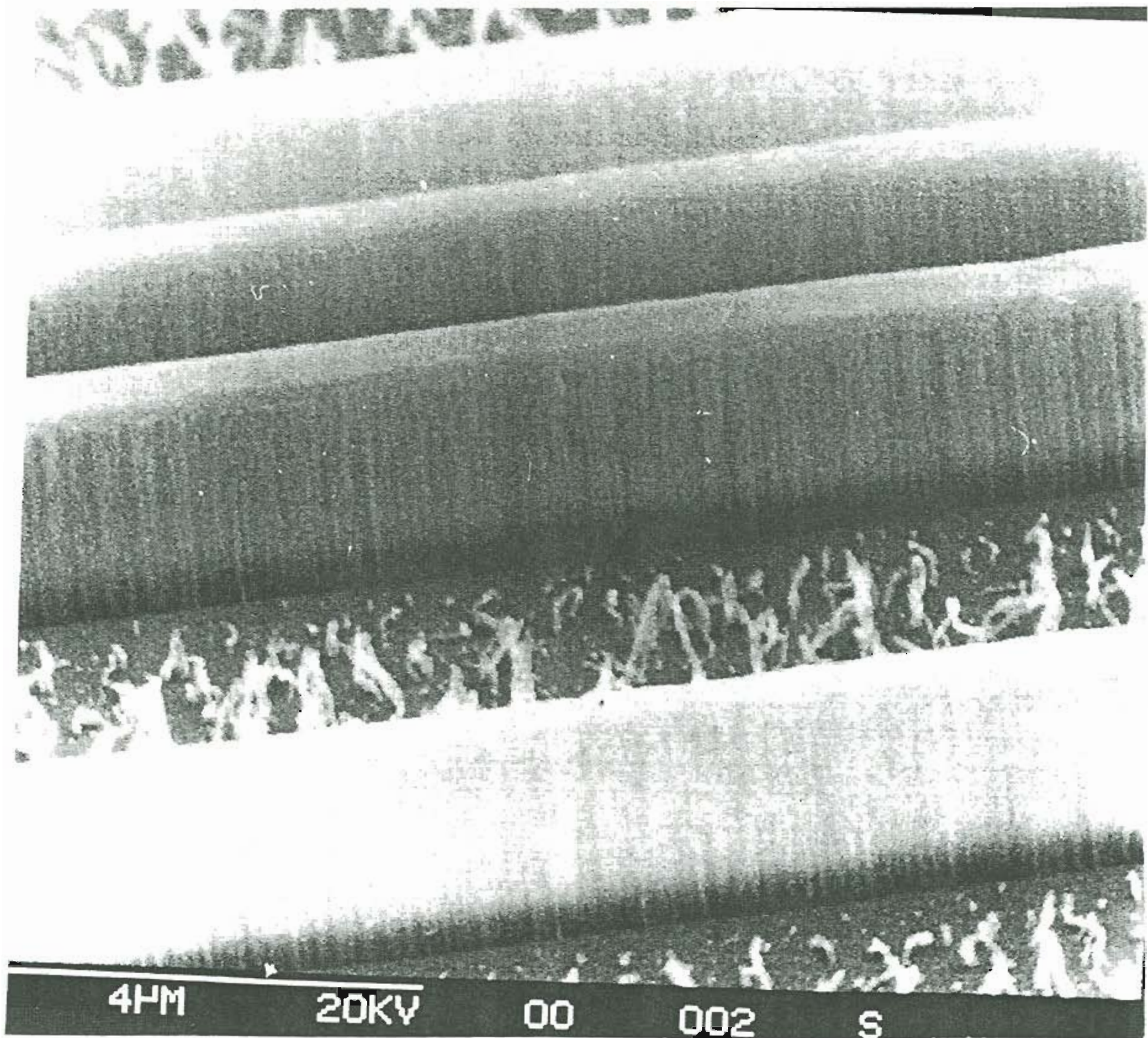

Figure 7.8 High incident angle view showing sidewall smoothness of Figures 7.6 and 7.7 lines.

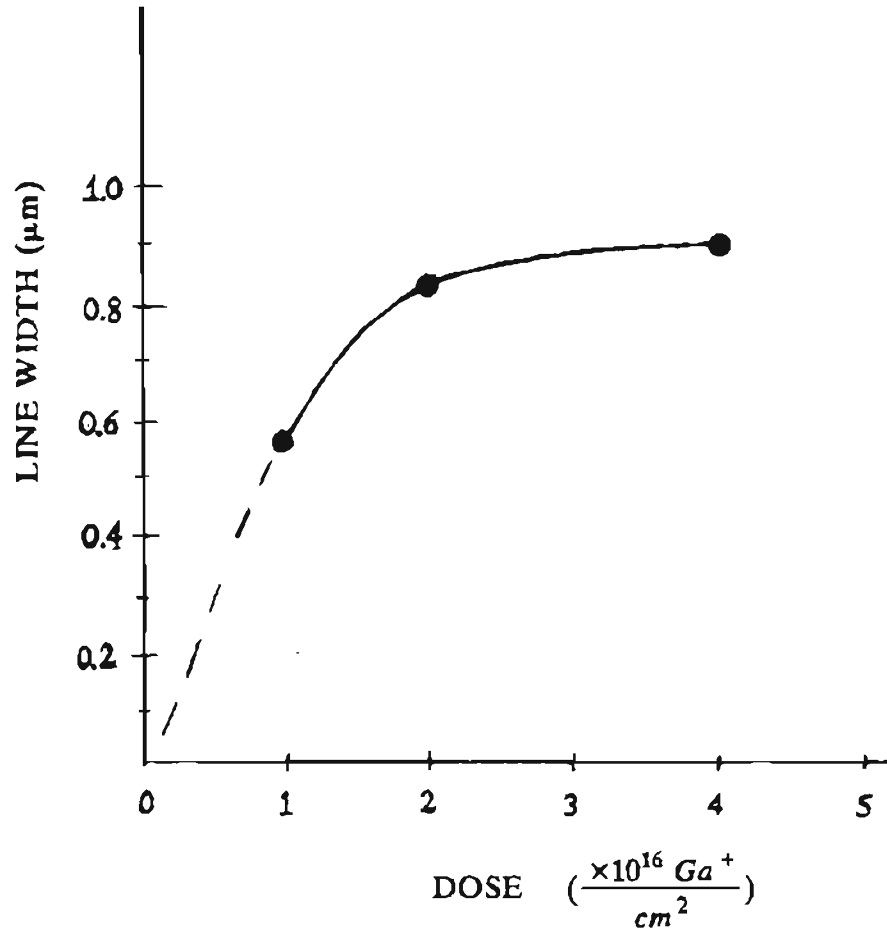

Figure 7.9 Linewidth as a function of dose. Linewidth is easily controlled by varying the dose between 1.0 and 2.0 x 10^{16} ions / cm^2.

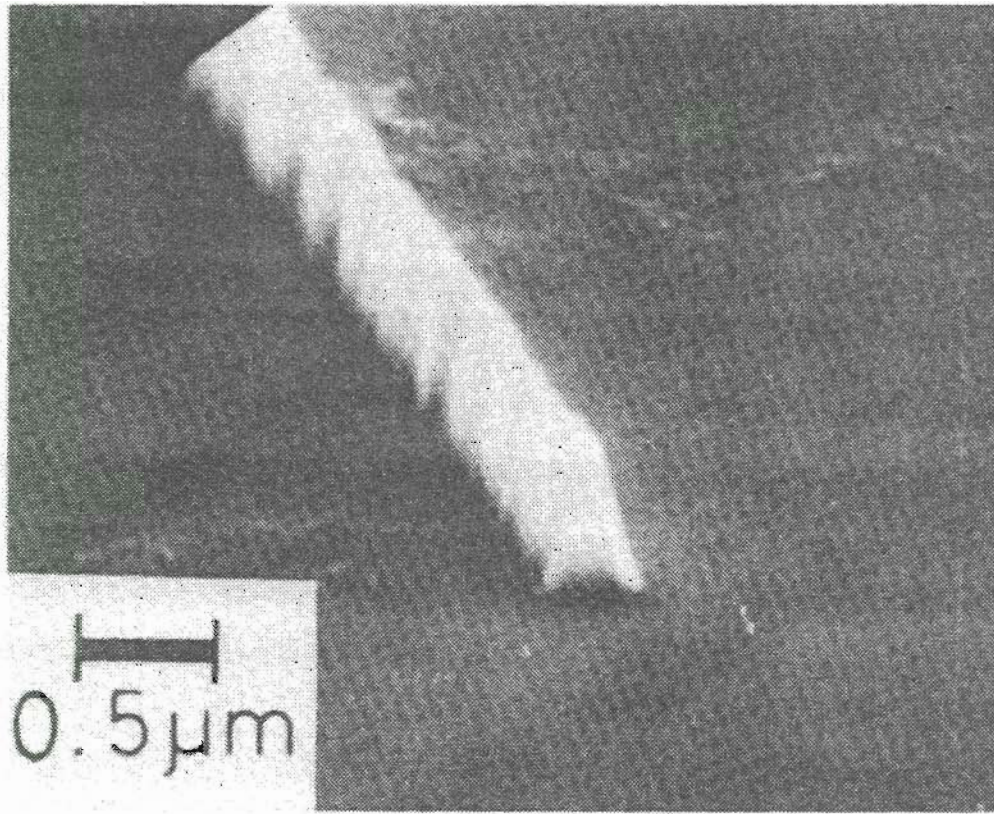

Copyright J.Vac.Sci.& Technol.

Figure 7.10 The bilevel process of Kato et al. results in substantial mask erosion.

E.B. Si / HPR206 bilayer. Figure 7.11 is a view of the developed bilayers in a region where the beam dwelled for approximately 30 seconds before moving the stage manually for the next series of line exposures. The central portion of the spot has sputtered through both layers. This figure and others not shown indicate that the current density in the beam spot is not strictly Gaussian. There appears to be a " halo " around the central spot. Remarkably, the figures show that despite the submicron spot size, within which a Gaussian current density seems appropriate, the exposure by the LMIS affects regions as far as 3 μm or more from the spot center. This may indeed prove to be a fundamental limitation in the use of LMIS for high sensitivity resist exposure or low sensitivity (but high dose) FIB micromachining. Figure 7.12 indicates that the resist is sensitive enough to detect mechanical vibrations of the optical column. These vibrations occurred because the optical column was not vibration isolated at the time. Kuwano's single layer work was repeated by FIB implanting gallium into the HPR206 and developing the pattern by RIE O_2 etching. As indicated in Figures 7.13 and 7.14 this produced 0.5 μm high by 1 μm wide lines with angled walls. The linewidth control is poor and further etching caused the lines to disintegrate.

7.7. Summary

A process has been described which can produce structures of height 2 μm and width 0.4 μm with rectangular profiles with uniform and controlable linewidth. It is likely that narrower lines could have been produced at higher energy but this was not attempted. Referring to Figure 7.4, we see that due to the 100:1 selectivity of HPR206/SOG in the RIE O_2 plasma, the HPR206 could have been patterned up to

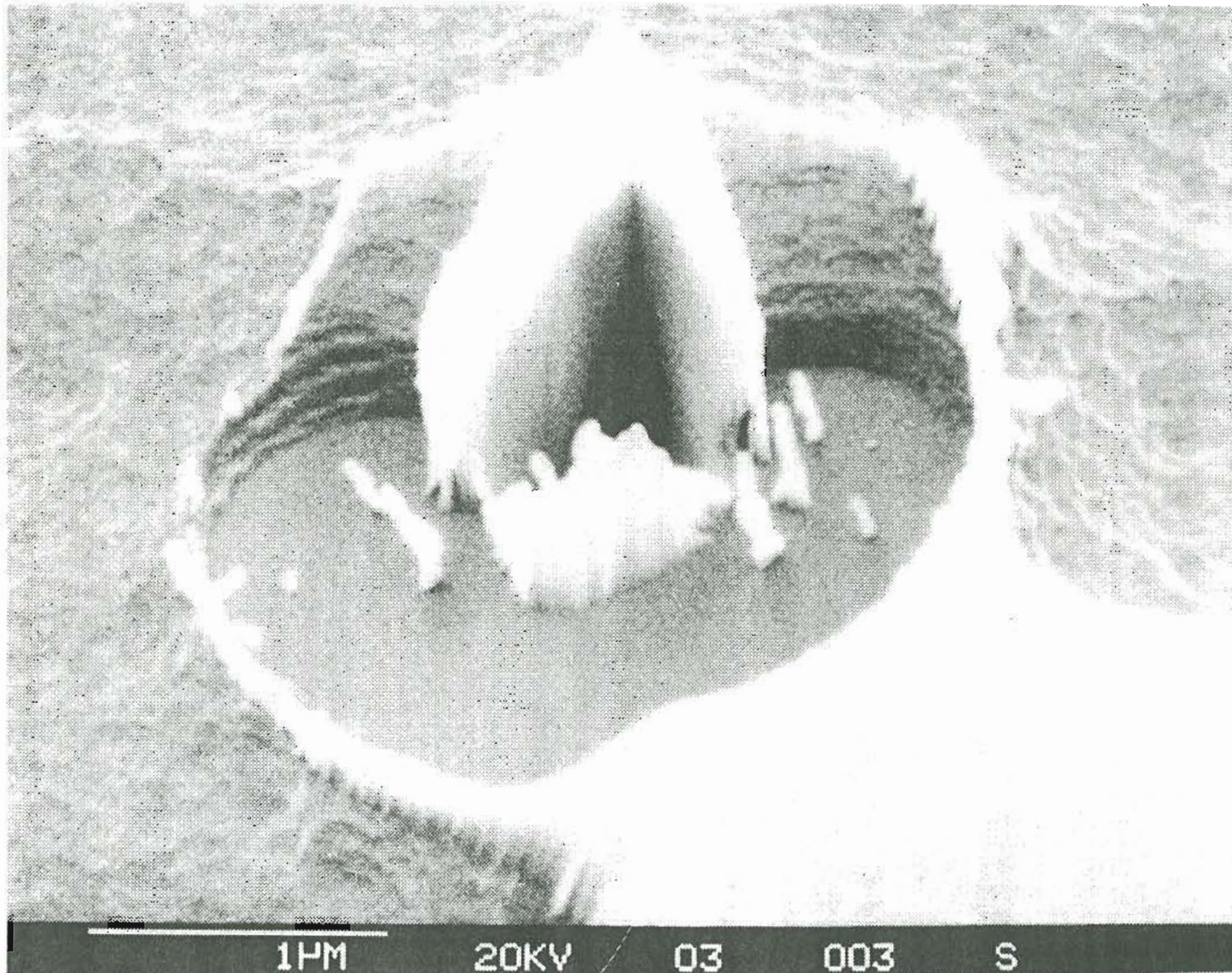

Figure 7.11 The beam dwell was sufficient to reveal some of the non-Gaussian aspects of the current density.

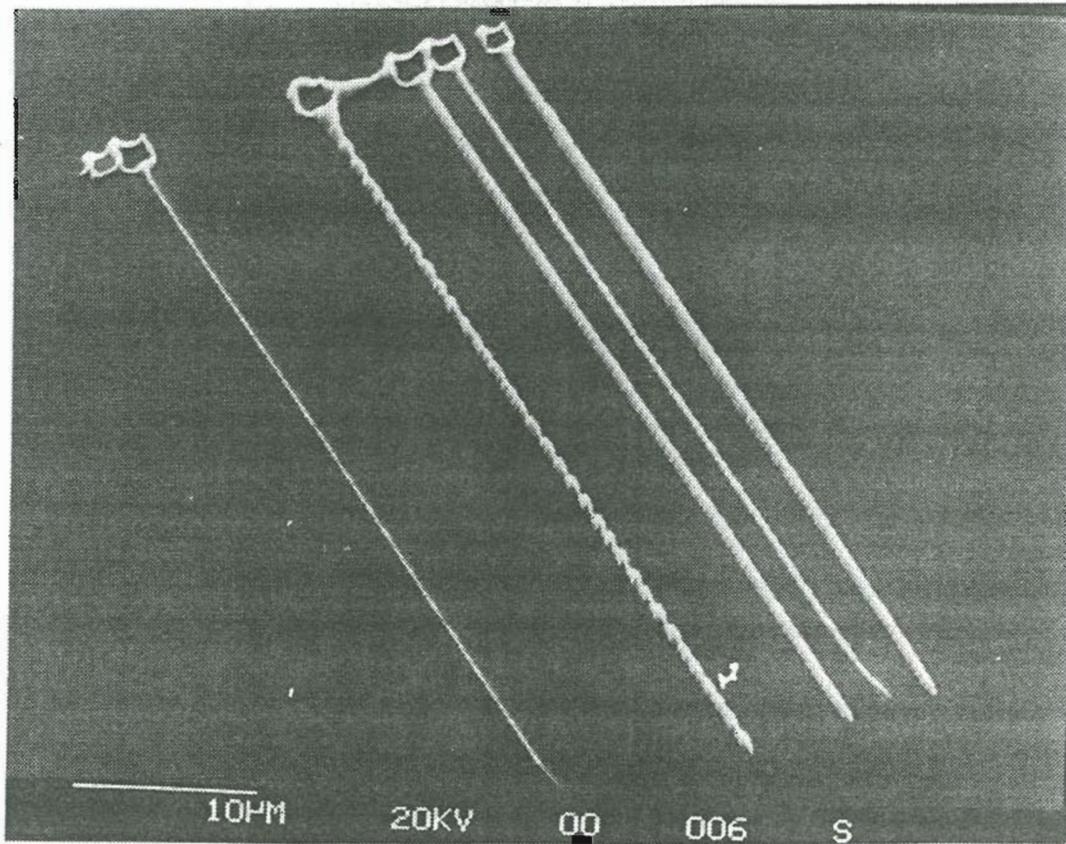

Figure 7.12 Resist sensitivity is sufficient to reveal mechanical vibrations of the optical column which was not vibration isolated at the time.

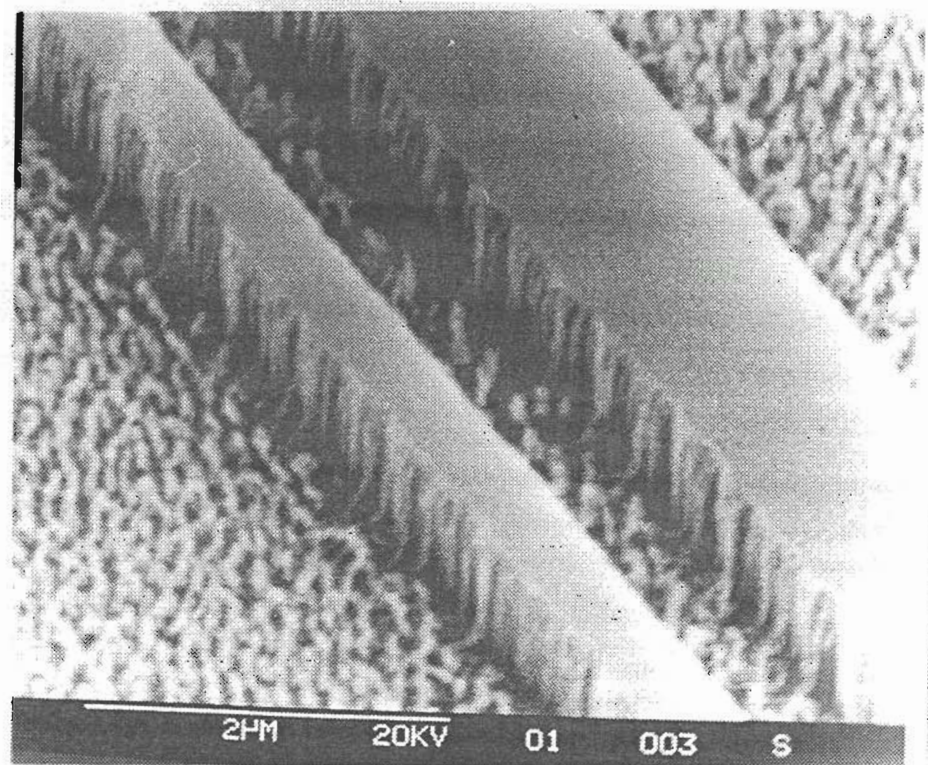

Figure 7.13 Repeat of Kuwano's work. A single layer of HPR206 was implanted by gallium FIB and etched by RIE O_2. The lines are 0.5 µm x 1 µm. The process suffers from poor linewidth control.

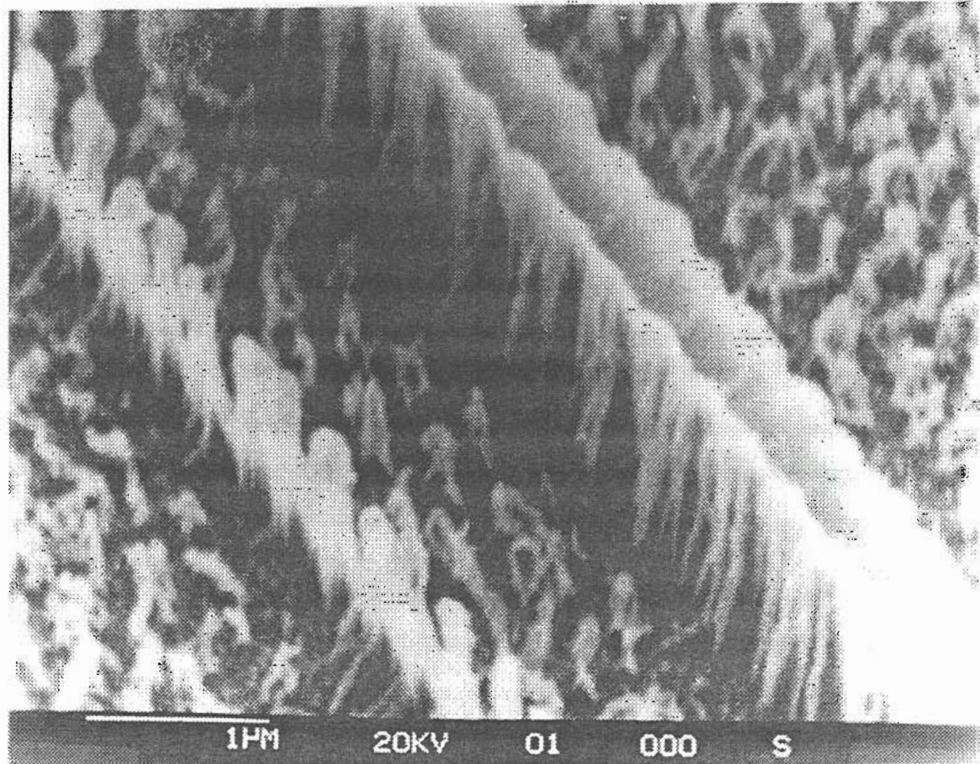

Figure 7.14 Same lines as in Figure 7.13 but after continued etching the lines disintegrate.

7.5 μm thick since 750 Å of SOG remained after the CHF_3 / O_2 plasma etch. This would be useful for commercial application of this bilevel system since thicker resists can protect the underlying substrate for a longer time while etching the surrounding material in a subsequent process. As indicated in Figure 7.10, the line width can be varied by controlling the dose between 1.0 and 2.0 x 10^{16} ions / cm^2. At higher ion doses, the top layer can also be sputtered to form a positive pattern, as in Kato's work[58]. This leads to a pair of narrow high aspect ratio lines separated by less than 0.4 μm. The leftmost lines in Figure 7.15 were formed this way by sputtering through the upper SOG layer. Looking at the processes depicted schematically in Figures 7.2 and 7.4, it is apparent that they can be combined to advantage e.g. the FIB can be used to expose bilayers which themselves have first been patterned optically or by electron beam lithography. This would allow the placement of fine structures created by FIB exposure within larger structures for microfabrication and has been described elsewhere[56, 170].

It should be noted that this process required doses in the 10^{16} ions / cm^2 range which is high by the standards of lithography. However, other materials may be used as a top layer. For example, LaMarche and Levi-Setti[163] report that the threshold sensitivity of amorphous silicon is $\simeq 10^{13}$ ions / cm^2. This could be a desirable material to examine in future experimental work.

While it may appear advantageous to use increasingly senstitive resists for lithography, there is a tradeoff between sensitivity and the exposure error rate due to statistical fluctuations in the beam current. This results in linewidth variations and puts limits on the number of ions required to expose a pixel completely. This has been discussed by Macrander et al.[171], for example. If fluctuations in the beam current are assumed to be due to shot noise then for sufficiently large average current,

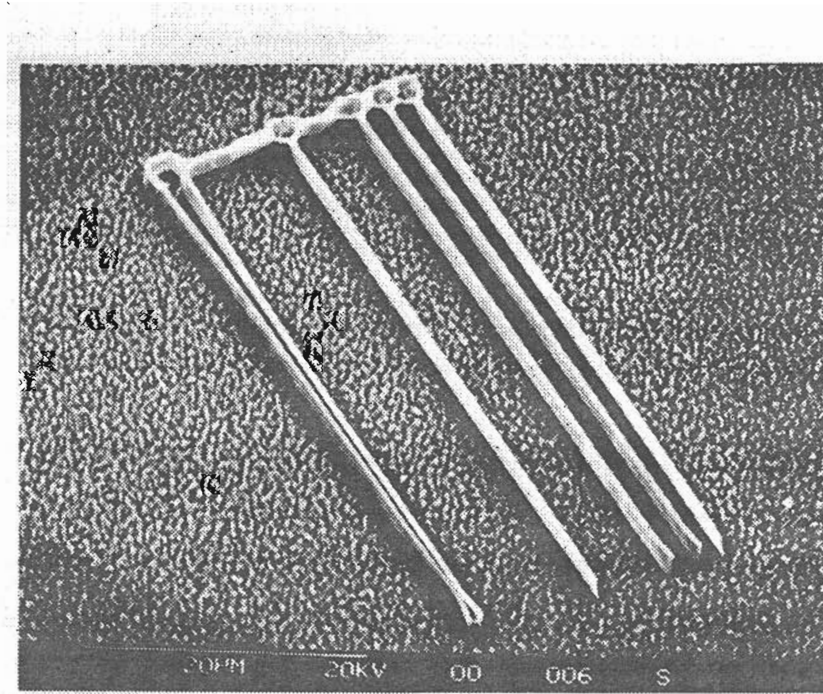

Figure 7.15 As in Kato's work, the top layer can also be sputtered to form a positive resist. The lines at left were produced in this manner and yielded lines separated by less than 0.4 μm.

the Poisson distribution for the shot noise limited emission may be written as a Gaussian distribution giving for the fluctuation:

$$P(\Delta N) = \frac{1}{\Delta N}\left(\frac{2N}{\pi}\right)^{\frac{1}{2}} e^{-\frac{(\Delta N)^2}{2N}}$$

which gives the probability of obtaining a fluctuation of ΔN if N is the number of ions incident on a pixel. A criterion for the fractional variation in linewidth can then be written:

$$\frac{\frac{\Delta W}{W}\ln 10}{\gamma} \geq \frac{\Delta N}{N}$$

where γ is the resist contrast.

For a typical resist like polymethylmethacrylate (PMMA), the authors conclude that 3200 ions per 0.1 μm pixel are necessary to ensure that there will be one error in linewidth per cm^2, an error being defined as variation in linewidth of $\pm$ 10%.

7.8 Appendix

7.8.1 Appendix: Raster scanning for uniform dose

The drawing below represents a target surface of dimensions X_T x Y_T; y_0 is the distance between spots along the y-axis and d_s is the spot diameter.

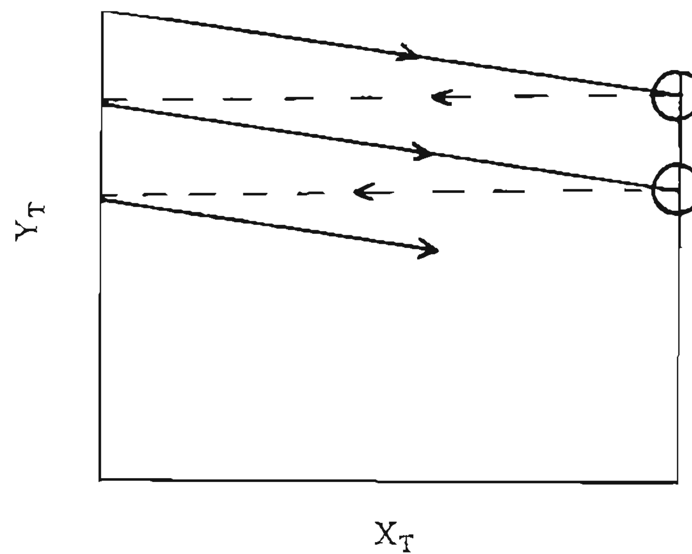

The beam velocity on the target is

$$\bar{v}_b = v_{0x}\hat{i} + v_{0y}\hat{j}$$

This implies that

$$\frac{v_{0y}}{v_{0x}} = \tan\theta = \frac{y_0}{X_T}$$

Now from the figure we see that

$$y_0 < d_s \quad - \quad \text{overlap}$$
$$y_0 = d_s \quad - \quad \text{marginal overlap}$$
$$y_0 > d_s \quad - \quad \text{no overlap}$$

and

$$v_{0x} = \frac{X_T}{T_x} = X_T \nu_x$$

where T_x is the time to sweep across the target along the x-axis and similarly for the y-axis. Therefore, we find

$$Y_{CRT} < Md_s \frac{\nu_x}{\nu_y} \quad - \quad \text{overlap}$$

$$Y_{CRT} = Md_s \frac{\nu_x}{\nu_y} \quad - \quad \text{marginal overlap}$$

$$Y_{CRT} > Md_s \frac{\nu_x}{\nu_y} \quad - \quad \text{no overlap}$$

where M is the magnification and $\frac{\nu_x}{\nu_y}$ is the ratio of the ramp frequencies.

These conditions describe a typical raster scan i.e. continuous velocity along the exposing beam path and blanking during retrace.

8. SPECULATIONS AND POSSIBILITIES FOR FUTURE RESEARCH

The issues surrounding the reproducibility of FIB micromachined structures should be examined closely to determine the effects of small changes in beam qualities like astigmatism and focus. These affect the current density distribution in the spot and would be significant for high dose exposure in (typically) low sensitivity applications like FIBM and in high sensitivity applications such as FIB lithography.

Redeposition results directly from the sputtered material sticking to a surface but it is only identified as a nuisance when it interferes with the final goal or object of the material processing. In fact, sputter deposition for thin film applications relies on precisely the same phenomenon though not identified there as redeposition. This leads naturally to the idea that perhaps the redeposited material may be utilized in a FIB process involving micromachining. Musil et al[172]. appear to be the first to demonstrate that during FIBM of an integrated circuit overlying metal runs separated by an insulator may be deliberately reconnected by the redeposited metal. It may also prove interesting to consider the possibility of controlling the micromachining of the redeposited material itself. This has, as yet, not been attempted. This may be employed for surface contouring, smoothing and for controlled "microdeposition" to produce coatings for monolithic integrated optoelectronic

devices or localized passivation of ICs, for example. This type of application requires a more complete understanding of the basic physics of sputtering under a scanning high current density focused ion beam e.g. the angular distribution of the sputtered neutrals for the particular materials used and of the chemical and physical properties of the deposits including adhesion, density, porosity, and optical properties.

FIB micromachining could also be used in conjunction with optical lithography, FIB lithography and plasma and ion beam formation of "diamondlike" hydrocarbon films to create truly 3D monolithic microelectronic and optoelectronic devices. To the authors knowledge, this suggestion has not yet appeared in the literature. The novel applications of FIB technology are limited mostly by the imagination and will undoubtedly continue to be explored in the future.

References

1. E. W. Müller, *Z. Physik*, vol. 12, p. 136, 1951.

2. E. W. Müller and T. T. Tsong, *Field Ion Microscopy, Principles and Applications,* Elsevier, New York, 1969.

3. R. Levi-Setti, *Scanning Electron Microscopy*, pp. 125-134, Proc. Seventh Annual SEM Symposium, IIT Research Institute, Chicago, IL., 1975.

4. W. Escovitz, T. R. Fox, and R. Levi-Setti, *Proc. Nat. Acad. Sci. USA*, vol. 72(5), pp. 1826-1828, 1975.

5. J. Orloff and L. W. Swanson, *J. Vac. Sci. Technol.*, vol. 12, p. 1209, 1975.

6. J. Orloff and L. W. Swanson, *Scanning Electron Microscopy*, pp. 57-61, Proc. Tenth Annual SEM Symposium, IIT Research Institute, Chicago, IL., 1977.

7. J. Orloff and L. W. Swanson, *J. Vac. Sci. Technol.*, vol. 15, p. 845, 1978.

8. V. E. Krohn, *Prog. Astron. Rocketry*, vol. 5, p. 73, 1961.

9. J. Perel, A. Y. Yahiku, J. F. Mahoney, H. Daley, and A. Sherman, *J. Space Rockets*, vol. 8, p. 702, 1971.

10. J. F. Mahoney, A. Y. Yahiku, H. L. Daley, R. D. Moore, and J. Perel, *J. Appl. Phys.*, vol. 40, p. 5101, 1969.

11. V. E. Krohn, *J. Appl. Phys.*, vol. 45, p. 1144, 1974.

12. V. E. Krohn and G. R. Ringo, *Appl. Phys. Lett.*, vol. 27, p. 479, 1975.

13. V. E. Krohn and G. R. Ringo, *Intl. J. Mass Spectr. Ion Phys.*, vol. 22, p. 307, 1976.

14. P. Marriott, "On-axis energy analysis of Ga^+, Ga^{2+}, Ga_2^+ Ions Emitted from a gallium liquid metal ion source," *Appl. Phys. A*, vol. 44, pp. 329-338, 1987.

15. S. P. Thompson and A von Engel, "Field emission of metal ions and microparticles," *J. Phys. D: Appl. Phys.*, vol. 15, pp. 925-931, 1982.

16. S. P. Thompson and A. von Engel, "Neutral satellites in ion beams from liquid metal ion sources," *J. Phys. D:Appl. Phys.*, vol. 16, pp. 1137-1144, 1983.

17. S. Papadopoulos, "On the energy distribution of doubly charged atomic ions emitted from liquid metal ion sources," *J. Phys. D: Appl. Phys.*, vol. 21, pp. 194-199, 1988.

18. G. L. R. Mair and A. von Engel, "Mass transport in liquid gallium ion beam sources," *J. Phys. D: Appl. Phys.*, vol. 14, pp. 1721-1728, 1981.

19. D. L. Barr, "Gallium clusters from a liquid metal ion source," *J. Vac. Sci. Technol. B*, vol. 5(1), pp. 184-189, Jan/Feb 1987.

20. L. W. Swanson, "Liquid Metal Ion Sources: Mechanism and Applications," *Nucl. Instrum. Methods*, vol. 218, pp. 347-353, 1983.

21. M. Komuro, H. Hiroshima, H. Tanoue, and T. Kanayama, "Maskless etching of a nanometer structure by focused ion beams," *J. Vac. Sci. Technol. B*, vol. 1(4), pp. 985-989, Oct.-Dec. 1983.

22. G. L. R. Mair and T. Mulvey, "Fundamentals of Liquid Metal Ion Sources: Experiment, Theory, and Applications," *SEM 1984/IV*, pp. 1531-1540, 1984.

23. J. Orloff, "The effect of extraction voltage and beam voltage of a liquid metal ion source focused beam system on the current density in a focused spot," *Scanning Electron Microscopy*, vol. IV, pp. 1541-1546, SEM, Inc., Chicago, IL., 1984.

24. A. E. Bell and L. W. Swanson, "The Influence of Substrate Geometry on the Emission Properties of a Liquid Metal Ion Source," *Appl. Phys. A*, vol. 41, pp. 335-346, 1986.

25. N. K. Kang and L. W. Swanson, "Computer simulation of liquid metal ion source optics," *Appl. Phys. A*, vol. 30, pp. 95-104, 1983.

26. D. R. Kingham and L. W. Swanson, "Shape of a Liquid Metal Ion Source: A Dynamic Model Including Fluid Flow and Space Charge Effects," *Appl. Phys. A*, vol. 34, pp. 123-132, 1984.

27. D. R. Kingham and L. W. Swanson, "Theoretical Investigation of Liquid Metal Ion Sources: Field and Temperature Dependence of Ion Emission," *Appl. Phys. A*, vol. 41, pp. 157-169, 1986.

28. L. W. Swanson and D. R. Kingham, "On the Mechanism of Liquid Metal Ion Sources," *Appl. Phys. A*, vol. 41, pp. 223-232, 1986.

29. G. L. R. Mair, "Theoretical determination of current-voltage curves for liquid metal ion sources," *J. Phys. D: Appl. Phys.*, vol. 17, pp. 2323-2330, 1984.

30. A. Wagner, "The hydrodynamics of liquid metal ion sources," *Appl. Phys. Lett.*, vol. 40(5), pp. 440-442, 1 March 1982.

31. G. Benassayag and P. Sudraud, "In Situ High Voltage TEM Observations of an Electrohydro- dynamic (EHD) Ion Source," *Ultramicroscopy*, vol. 16, pp. 1-8, 1985.

32. G. L. R. Mair, "Space Charge Effects in Liquid Metal Ion Sources," *J. Phys. D: Appl. Phys.*, vol. 15, pp. 2523-2530, 1982.

33. G. L. R. Mair, R. G. Forbes, R. V. Latham, and T. Mulvey, "Energy Spread Measurements on a liquid metal ion source," *Microcircuit Engineering*, pp. 171-177, London, 1983.

34. G. L. R. Mair, D. C. Grinrod, M. S. Mousa, and R. V. Latham, "Beam-energy distribution measurements of liquid gallium field ion sources," *J. Phys. D: Appl.*

Phys., vol. 16, pp. L209-L213, 1983.

35. S. Papadopoulos, D. Barr, W. L. Brown, and A. Wagner, "The Energy Spread of Ions from Gold Liquid Metal Ion Sources as a Function of Source Parameters," *J. de Phys.*, vol. 45, 12, pp. C9-217 - C9-226, Dec. 1984.

36. S. P. Thompson and P. D. Prewett, "The dynamics of liquid metal ion sources," *J. Phys. D: Appl. Phys.*, vol. 17, pp. 2305-2321, 1984.

37. T. E. Stern, B. S. Gossling, and R. H. Fowler, *Proc. R. Soc. A*, vol. 124, p. 699, 1929.

38. G. I. Taylor, *Proc. R. Soc. A*, vol. 291, p. 145, 1966.

39. K. L. Aitken, *Proc. Field Emission Day*, p. 23, 1976.

40. K. L. Aitken, D. K. Jeffries, and R. Clampitt, *Culham Lab. Rept.*, vol. CLM/RR/E12, 1975.

41. J. Melngailis, "Focused Ion Beam Technology and Applications," *J. Vac. Sci. Technol.*, vol. B5(2), pp. 469-495, Mar./Apr. 1987.

42. G. L. R. Mair and S. Thoms, "Studies with a capillary ion source," *J. Phys. D: Appl. Phys.*, vol. 19, pp. L203-206, 1986.

43. R. Gomer, *Appl. Phys.*, vol. 19, p. 365, 1979.

44. H. Boersch, *Z. Phys.*, vol. 139, p. 115, 1954.

45. G. H. Jansen, T. R. Groves, and W. Stickel, "Energy Broadening in Electron Beams: A comparison of existing theories and Monte Carlo simulation," *J. Vac. Sci. Technol. B*, vol. 3(1), pp. 190-193, Jan/Feb 1985.

46. P. J. Hoepfner, "A Monte Carlo Calculation of Virtual Source Size and/," *Masters Thesis*, Oregon Graduate Center, January, 1985.

47. W. Knauer, "Energy Broadening in Field Emitted Electron and Ion Beams," *Optik*, vol. 59, 1981.

48. H. Rose and R. Spehr, "Energy Broadening in High-Density Electron and Ion Beams: The Boersch Effect," *Advances in Electronics and Electron Physics*, pp. 475-530, 1 Aug 1984.

49. L. W. Swanson, G. A. Schwind, and A. E. Bell, *Scanning Electron Microscopy*, p. 45, AMF O'Hare, 1979a.

50. L. W. Swanson, G. A. Schwind, A. E. Bell, and J. E. Brady, "Emission characteristics of gallium and bismuth liquid metal field ion sources," *J. Vac. Sci. Technol.*, vol. 16(6), pp. 1864-1867, Nov./Dec. 1979.

51. M. A. Gesley and L. W. Swanson, "Analysis of energy broadening in charged particle beams," *J. de Physique*, vol. 45, pp. C9-167 - C9-172, Dec. 1984.

52. H. Gnaser, F. G. Rudenauer, H. Studnicka, and P. Pollinger, "Application of a liquid metal ion source in ion microprobe analysis ," *Proc. 29th International Field Ion Symposium*, pp. 399-406, Stockholm, 1982.

53. A. R. Bayly, A. R. Waugh, and K. Anderson, "High resolution scanning secondary ion mass spectrometry (SIMS) using liquid metal field - ionization sources," *Scanning Electron Microscopy*, vol. 1, pp. 23-29, 1983.

54. R. Levi-Setti, T. R. Fox, and K. Lam, "Ion channeling effects in scanning ion microscopy with 60KeV Ga probe," *Nucl. Instr. and Methods*, pp. 299-309, 1983.

55. H. Kuwano, K. Yoshida, and S. Yamazaki, *Jpn. J. Appl. Phys.*, vol. 19, L615, 1980.

56. A. Milgram and J. Puretz, "A bilevel resist for ion beam lithography," *J. Vac. Sci. Technol. B*, vol. 3(3), pp. 879-883, May/Jun 1985.

57. H. Morimoto, H. Onoda, T. Kato, Y.Sasaki, K. Saitoh, and T. Kato, "Unique resist profiles with Be and Si focused ion beam lithography," *J. Vac. Sci. Technol. B4(1)*, p. 205, Jan./Feb. 1986.

58. T. Kato, H. Morimoto, K. Saitoh, and H. Nakata, "Submicron pattern fabrication by focused ion beams," *J. Vac. Sci. Technol.*, vol. B 3(1), pp. 50-53, Jan./Feb. 1985

59. E. Miyauchi, T. Morita, A. Takamori, H. Arimoto, Y. Bamba, and H. Hashimoto, "Maskless ion beam writing of precise doping patterns with Be and Si for molecular epitaxially grown multilayer GaAs," *J. Vac. Sci. Technol. B4(1)*, p. 189, Jan./Feb. 1986.

60. L. R. Harriott, R. E. Scotti, K. D. Cummings, and A. F. Ambrose, "Micromachining of integrated optical structures," *Appl. Phys. Lett.*, vol. 48(25), pp. 1704-1706, 23 June 1986.

61. R. K. DeFreez, J. Puretz, R. A. Elliott, J. Orloff, and L. W. Swanson, "CW operation of widely and continuously tunable micromachined-coupled-cavity diode lasers," *Elect. Lett.*, vol. 22, pp. 919-921, 14 August 1986.

62. A. V. Crewe, "Optimization of small electron probes," *Ultramicroscopy*, vol. 23, pp. 159-168, 1987.

63. J. D. Jackson, *Classical Electrodynamics*, pp. 236-240, New York, 1975. Second Edition

64. T. Noda, T. Okutani, K. Yagi, H. Tamura, H. Okanp, and H. Watanabe, "Electrohydrodynamic ion source with a reservoir and an emitter tip heated by

electron bombardment," *Rev. Sci. Instrum.*, vol. 53(9), pp. 1482-1483, September 1982.

65. M. J. Bozack, L. W. Swanson, and A. E. Bell, "Wettability of transition metal boride eutectic alloys to graphite," *J. Mater. Sci.*, vol. 22, pp. 2421-2430, 1987.

66. L. Barofsky. Private Communication

67. H. Arimoto, E. Miyauchi, and H. Hashimoto, "Effects of ambient gases on ion emission stability of liquid-metal ion sources," *J. Vac. Sci. Technol. B*, vol. 5(5), pp. 1368-1371, Sep./Oct. 1987.

68. Y. Ochiai, K. Shihoyama, A. Masuyama, K. Gamo, T. Shiokawa, K. Yoyoda, and S. Namba, "Maskless Ion Beam Assisted Etching of Si Using Chlorine Gas," *Jpn. J. Appl. Phys.*, vol. 24(3), pp. L169-L172, March, 1985.

69. N. Takado, K. Asakawa, H. Arimoto, T. Morita, S. Sugata, E. Miyauchi, and H. Hashimoto, "Chemically-enhanced GaAs maskless etching using a novel focused ion beam etching system with a chlorine molecular and radical beam," *Proceedings of the Materials Research Society Symposium*, Boston, MA., December 1-6 1986.

70. R. C. Weast, *Handbook of Chemistry and Physics,* Chemical Rubber Company, Florida.

71. P. Sudraud, J. Orloff, and G. Benassayag, "The effect of carbon bearing gases and secondary electron bombardment on a liquid metal ion source," *Journ. de Phys.*, vol. 47, C7, pp. 381-387, Nov. 1986.

72. J. Lindhard and M. Scharff, *Phys. Rev.*, vol. 124, pp. 128-130, 1961.

73. W. G. Opyd, J. F. Gibbons, J. C. Bravman, and M. A. Parker, "Damage Calculation and measurement fro GaAs amorphized by Si implantation," *Appl. Phys.*

Lett., vol. 49(15), pp. 974-976, 13 Oct 1986.

74. J. P. Riviere, J. Delafond, C. Jaouen, A. Bellara, and J. F. Dinhut, "Ion-Beam Mixing Kinetics of Fe-Al Multilayers Studied by in situ Electrical Resistivity Measurements," *Appl. Phys. A.*, vol. 33, pp. 77-82, 1984.

75. N. Bohr, *Mat. Fys. Medd. Dan. Vid. Selsk*, vol. 18, p. 8, 1948.

76. J. Lindhard, M. Scharff, and H. E. Schiott, *Mat. Fys. Medd. Dan. Vid. Selsk*, vol. 33, p. 14, 1963.

77. W. A. Grant, D. Dodd, and J. S. Williams, in *Ion Beam Surface Layer Analysis*, ed. F. Kappeler, p. 235, Plenum Press, New York, 1975.

78. J. L. Whitton, *Channeling,* John Wiley, New York, 1973. Chap. 8

79. J. F. Gibbons, "Ion implantation in semiconductors-Part I: Range distribution theory and experiments," *Proc. IEEE*, vol. 56(3), pp. 295-319, March 1968.

80. J. F. Gibbons, "Ion implantation in semiconductors-Part II: Damage production and annealing," *Proc. IEEE*, vol. 60(9), p. 1062, Sept. 1972.

81. K. Winterbon, *Ion Implantation Damage and Energy Deposition Distribution,* Plenum Press, New York, 1975. Vol. II

82. G. H. Kinchin and R. S. Pease, *Rep. Prog. Phys.*, vol. 18(2), 1955.

83. P. Sigmund, *Appl. Phys. Lett.*, vol. 14, p. 114, 1969.

84. P. Sigmund, "Theory of Sputtering. I. Sputtering Yield of Amorphous and Polycrystalline Targets," *Phys. Rev.*, vol. 184(2), p. 383, 10 Aug. 1969.

85. in *Ion Bombardment Modification of Surfaces: Fundamentals and Applications*, ed. R. Kelly, Elsevier, New York, 1984.

86. S. Duncan, R. Smith, D. E. Sykes, and J. M. Walls, "Surface morphology of Si(100), GaAs(100) and InP(100) following oxygen and cesium ion bombardment," *Vacuum*, vol. 34(1-2), pp. 145-151, 1984.

87. I. H. Wilson, *Rad. Eff.*, vol. 18, p. 95, 1973.

88. W. Hauffe, *Phys. Stat. Solidi*, vol. 4a, p. 111, 1971.

89. S. K. Das and M. Kaminsky, "Radiation blistering of polycrystalline niobium by helium-ion implantation," *J. Appl. Phys.*, vol. 44(1), pp. 25-29, January 1973.

90. M. Kaminsky and S. K. Das, "Correlation of blister diameter and blister skin thickness for helium-bombarded V," *J. Appl. Phys.*, vol. 49(11), pp. 5673-5675, November 1978.

91. G. Carter, J. S. Colligon, and M. J. Nobes, *Rad. Eff.*, vol. 31, p. 65, 1977.

92. H. R. Kaufman and R. S. Robinson, "Ion beam texturing of surfaces," *J. Vac. Sci. Technol.*, vol. 16(2), pp. 175-178, Mar/Apr. 1979.

93. R. S. Robinson and S. M. Rossnagel, "Ion-Beam-induced topography and surface diffusion," *J. Vac. Sci. Technol.*, vol. 21(3), pp. 790-797, Sept/Oct 1982.

94. A. Oliva, R. Kelly, and G. Falcone, "Sputtering of Multicomponent Materials: The Diffusion Limit," *Surf. Sci.*, vol. 166, pp. 403 - 418, 1986.

95. N. Hermanne and A. Art, *Rad. Eff.*, vol. 5, p. 203, 1970.

96. R. S. Nelson and D. J. Mazey, *Rad. Eff.*, vol. 18, p. 127, 1973.

97. R. Kelly, *Surf. Sci.*, vol. 100, p. 85, 1980.

98. S. A. Schwartz and C. R. Helms, "A statistical model of sputtering," *J. Appl. Phys.*, vol. 50(8), pp. 5492-5499, Aug. 1979.

99. S. M. Rossnagel and R. S. Robinson, "The time development of impurity generated sputter cones on Cu," *Rad. Eff. Lett.*, vol. 58, pp. 11-16, 1981.

100. N. Biblic, I. H.Wilson, and T. Nenadovic, "The surface topography of Ag/Cu alloys sputtered by bombardment with 35-100KeV argon ions," *J. Appl. Phys.*, vol. 53(7), pp. 5250-5257, July 1982.

101. S. R. Bhattacharya, D. Ghose, D. Basu, and S. B. Karmohapatro, "Surface topography of Ar^+ bombarded GaAs (100) at various temperatures," *J. Vac. Sci. Technol.A*, vol. 5(2), pp. 179-183, Mar/Apr 1987.

102. Y. Homma, H. Okamoto, and Y. Ishii, "Surface microtopography and compositional change of cesium-ion-bombarded semiconductor surfaces," *Jap. J. Appl. Phys.*, vol. 24(8), pp. 934-938, August 1985.

103. D. C. Peacock, "An AES, SAM and RHEED study of InP(110) subjected to ion bombardment and annealing treatements," *Vacuum*, vol. 33, pp. 601-605, 1983.

104. H. Yamaguchi, "Line dose dependence of silicon and gallium arsenide removal by a focused gallium ion beam," *J. de Phys.*, vol. Colloque C6, 48, pp. 165-170, November 1987.

105. T. Ishitani, A. Shimase, and H. Tamura, "Condensation of bombarding gallium ions on a silicon surface," *Appl. Phys. Lett.*, vol. 39(8), pp. 627-628, 1981.

106. V. J. Moore and P. D. Prewett, "Effects of Ga ion bombardment from a liquid metal ion source," *Vacuum*, vol. 34(1-2), pp. 189-191, 1984.

107. F. G. Rudenauer, W. Steiger, E. Wieser, R. Grotzschel, and F. Nahring, "Formation of droplets on Si surfaces bombarded by In from a capillary type liquid metal ion source," *Vacuum*, vol. 35(8), pp. 315-320, 1985.

108. Personal observation.

109. M. Marinov, "Effect of ion bombardment on the initial stages of thin film growth," *Thin Solid Films*, vol. 46, pp. 267-274, 1977.

110. S. P. Thompson, "Neutral emissions from liquid metal ion sources," *Vacuum*, vol. 34(1-2), pp. 223-228, 1984.

111. S. Papadopoulos, *J. Phys. D.: Appl. Phys.*, vol. 20, p. 1302, 1987.

112. C. T. Foxon, J. A. Harvey, and B. A. Joyce, "The evaporation of GaAs under equilibrium and non-equilibrium conditions using a modulated beam technique," *J. Phys. Chem. Solids*, vol. 34, pp. 1693-1701, 1973.

113. M. Lax, "Temperature rise induced by a laser beam," *J. Appl. Physics*, vol. 48(9), pp. 3919-3924, Sept. 1977.

114. M. Lax, "Temperature rise induced by a laser beam II. The nonlinear case," *Appl. Phys. Lett.*, vol. 32(8), pp. 786-788, 15 Oct. 1978.

115. H. S. Carslaw and J. C. Jaeger, *Conduction of heat in solids.*

116. R. Kelly, "Thermal Effects in Sputtering," *Surf. Sci.*, vol. 90, pp. 280-318, 1979.

117. M. Szymonski, "The Sputtering of Gallium Arsenide at Elevated Temperatures," *Appl. Phys.*, vol. 20, pp. 207-211, 1979.

118. M. Tanemura and F. Okuyama, "Cone formation from Mo thin films," *Surf. Sci.*, vol. 181, pp. L193-L199, 1987.

119. S. Morishita, Y. Fujimoto, and F. Okuyama, "Morphological and structural features of Cu seed cones," *J. Vac. Sci. Technol.*, vol. A 6(2), pp. 217-222, Mar./Apr. 1988.

120. F. Okuyama and Y. Fujimoto, "Direct evidence for a thermal effect of Ar^+ ion

bombardment in a conventional sputtering mode," *J. Vac. Sci. Technol. A*, vol. 4(2), pp. 237-238, Mar./Apr. 1986.

121. J. C. C. Tsai and J. M. Morabito, "The Mechanism of Simultaneous Implantation and Sputtering by High Energy Oxygen Ions During Secondary Ion Mass Spectrometry Analysis," *Surf. Sci.*, vol. 44, pp. 247-252, 1974.

122. W. D. Wilson, L. G. Haggmark, and J. P. Biersack, "Calculations of nuclear stopping, ranges, and straggling in the low energy region," *Phys. Rev. B*, vol. 15(5), pp. 2458-2468, 1 March 1977.

123. G. Crow, *Personal communication.*

124. N. Takado, *Personal communication.*

125. V. A. Gunterschultze and W. Tollmein, *Zeit. Physik*, vol. 119, p. 685, 1942.

126. Wehner, *J. Vac. Sci. Technol.*, 1985.

127. Whitton, Holck, and Carter, *Nucl. Instrum. Methods*, 1980.

128. Auciello, *Rad. Eff.*, 1980.

129. H. Betz, A. Heuberger, N. P. Economou, and D. C. Shaver, "Influence of Sputter Effects on the Resolution in X-Ray Mask Repair," *SPIE Conference on Electron Beam, X-Ray and Ion Beam Techniques for Submicrometer Lithography*, Santa Clara, CA., March 11, 1986.

130. J. L. Vossen, "The preparation of substrates for film deposition using glow discharge techniques," *J. Phys. E: Sci. Instrum.*, vol. 12, pp. 159-167, 1979.

131. D. J. Barber, F. C. Frank, M. Moss, J. W. Steeds, and I. S. T. Tsong, *J. Mater. Sci.*, vol. 8, p. 1030, 1973.

132. M. J. Nobes, J. S. Colligon, and G. Carter, *J. Mater. Sci.*, vol. 4, p. 730, 1969.

133. G. Carter, J. S. Colligon, and M. J. Nobes, *J. Mater. Sci.*, vol. 6, p. 115, 1971.

134. J. P. Ducommun, M. Cantagrel, and M. Moulin, *J. Mater. Sci.*, vol. 10, p. 52, 1975.

135. R. Smith and J. M. Walls, "The development of a general three-dimensional surface under ion bombardment," *Phil. Mag. A*, vol. 42(2), pp. 235-248, 1980.

136. R. Smith, S. S. Makh, and J. M. Walls, "Surface morphology during ion etching- The influence of redeposition," *Phil. Mag. A*, vol. 47(4), pp. 453-481, 1983.

137. K. P. Müller and J. Pelka, "Redeposition in ion milling," *Microelectronic Engineering*, vol. 7, pp. 91-101, 1987.

138. G. Crow, J. Puretz, J. Orloff, R. K. DeFreez, and R. A. Elliott, "The Use of Vector Scanning for Producing Arbitrary Surface Contours with a Focused Ion Beam," *J. Vac. Sci. Technol.*, vol. B6(5), pp. 1605-1607, September/October 1988.

139. R. L. Kubena, R. L. Seliger, and E. H. Stevens, "High resolution sputtering using a focused ion beam," *Thin Solid Films*, vol. 92, pp. 165-169, 1982.

140. H. Yamaguchi, A. Shimase, S. Haraichi, and T. Miyauchi, "Characteristics of silicon removal by fine focused gallium ion beam," *J. Vac. Sci. Technol. B*, vol. 3, pp. 71-74, 1985.

141. J. W. Ward, M. W. Utlaut, and R. L. Kubena, "Computer simulation of current density profiles in focused ion beams," *J. Vac. Sci. Technol.*, vol. B5(1), pp. 169-174, Jan./Feb. 1987.

142. Y. Ochiai, K. Gamo, and S. Namba, "Characteristics of Ion Beam Assisted Etching of GaAs Using Focused Ion Beam: Dependence on Gas Pressure," *Jpn.*

J. Appl. Phys., vol. 23(6), pp. L400-L402, June, 1984.

143. J. Puretz, R. K. DeFreez, R. A. Elliott, and J. Orloff, "Focused ion beam micromachined AlGaAs semiconductor laser mirrors," *Elect. Lett.*, vol. 22(13), pp. 700-701, June 19, 1986.

144. T. L. Koch , L. A. Coldren , T. J. Bridges, E. G. Burkhardt, P. J. Corvini, and D. P. Wilt, "1.5 μm monolithic shallow-groove coupled-cavity vapour-phase-transported buried-heterostructure lasers," *Elect. Lett.*, vol. 20, pp. 1001-1002, 1984.

145. K.-L. Chen and S. Wang, "Etched-coupled-cavity InGaAsP/InP lasers," *Elect. Lett.*, vol. 21, pp. 94-95, 1985.

146. L. A. Coldren, K. L. Ebeling, J. A. Rentschler, C. A. Burrus, and D. P. Wilt, "Continuous operation of monolithic dynamic-single-mode coupled-cavity lasers," *Appl. Phys. Lett.*, vol. 44, pp. 368-370, 1984.

147. W. T. Tsang, N. A. Olson, and R. A. Logan, "High-speed single frequency modulation with large tuning rate and frequency excursion in cleaved-coupled-cavity semiconductor lasers," *J. Appl. Phys. Lett.*, vol. 42, pp. 650-652, 15 April 1983.

148. J. Puretz, R. K. DeFreez, R. A. Elliott, J. Orloff, and T. L. Paoli, "300 mW operation of a surface-emitting phase-locked array of diode lasers," *Elect. Lett.*, vol. 23, pp. 130-131, 29 January 1987.

149. Z. L. Liau and J. N. Walpole, "Surface-emitting GaInAsP/InP laser with low threshold current and high efficiency," *Appl. Phys. Lett.*, vol. 46, pp. 115-117, 15 January 1985.

150. R. K. DeFreez, J. Puretz, J. Orloff, R. A. Elliott, H. Namba, E. Omura, and H. Namizaki, "Operating Characteristics and Elevated Temperature Lifetests of Focused Ion Beam Micromachined Straight Transverse Junction Stripe Lasers," *Appl. Phys. Lett.*, vol. 53 (13), 26 Sept. 1988.

151. H. Seiler, "Secondary electron emission in the scanning electron microscope," *J. Appl. Phys.*, vol. 54(11), pp. R1-R18, Nov. 1983.

152. C. K. Crawford, *Scanning Elec. Microsc.*, vol. IV, pp. 11-24, 1980.

153. Y. Ueda and J. Okano, *Mass Spectrosc.*, p. 185, 1972.

154. K. Wittmaack, "Primary-ion charge compensation in SIMS analysis of insulators," *J. Appl. Phys.*, vol. 50(1), pp. 493-497, January 1979.

155. H. Arima, T. Matsukawa, J. Mitsuhashi, H. Morimoto, and H. Nakata, "Electron beam testing of VLSI circuits assisted by focused ion beam etching," *Microelectronic Engineering*, vol. 4, pp. 107-120, 1986.

156. A. Broers, "The Submicron Lithography Labyrinth," *Solid State Technology*, pp. 119-126, June 1985.

157. T. Yamazaki, Y. Suzuki, and H. Nakata, *J. Vac. Sci. Technol.*, vol. 17, p. 1348, 1980.

158. K. Gamo and S. Namba, *Proc. SPIE*, p. 159, 1983.

159. J. I. Pankove, J. T. McGinn, and C. P. Wu, *Appl. Phys. Lett.*, vol. 39, p. 119, 1981.

160. T. Venkatesan, G. N. Taylor, A. Wagner, B. Wilkens, and D. Barr, *J. Vac. Sci. Technol.*, vol. 19, p. 1379, 1981.

161. Palik, Faust, Gray, and Greene, 1982.

162. P. H. LaMarche, R. Levi-Setti, and Y. L. Wang, *J. Vac. Sci. Technol.*, vol. B1, p. 1056, 1983.

163. P. H. LaMarche and R. Levi-Setti, *Proc. SPIE*, vol. 471, p. 60, 1984.

164. I. L. Berry and A. L. Caviglia, *J. Vac. Sci. Technol.*, vol. BI, p. 1059, 1983.

165. I. Adesida, J. D. Chinn, L. Rathbun, and E. D. Wolf, *J. Vac. Sci. Technol.*, vol. 21, p. 666, 1982.

166. H. Hiraoka, *SPIE*, vol. 469, p. 127, 1984.

167. M. Komuro, N. Atoda, and H. Kawakatsu, "Ion Beam Exposure of Resist Materials," *J. Electrochem. Soc.*, vol. 126, pp. 483-490, 3/1979.

168. M. Kaplan, D. Meyerhofer, and L. White, *RCA Review*, vol. 44, p. 135, 1983.

169. L. W. Swanson, "Recent Advances in Liquid Metal Ion Sources," *Microcircuit Engineering 80, International Conference on Microlithography*, Amsterdam, Sept. 30-Oct. 1-2, 1980.

170. A. A. Milgram and J. Puretz, "A multilayer resist for direct write ion beam lithography," *Materials Research Society Symposium*, San Francisco, April 18, 1985.

171. A. Macrander, D. Barr, and A. Wagner, "Resist possibilities and limitations in ion beam lithography," *SPIE Proceedings on Submicron Lithography*, vol. 333, pp. 142-148, 1982.

172. C. R. Musil, J. L. Bartelt, and J. Melngailis, "Focused Ion Beam Microsurgery for Electronics," *IEEE Elect. Dev. Lett.*, vol. EDL-7(5), pp. 285-287, May 1986.

VITA

Joseph Puretz was born in Brussels, Belgium on June 30, 1949. He attended the George W. Hewlett High School on Long Island, New York and received the B.A. degree in Physics from Ithaca College, Ithaca, New York in 1971. He received the ARCS Foundation, Inc. Science Award (achievement rewards for college scientists for continuing excellence) in 1972 and studied in the Physics Department of the George Washington University, Washington, D. C. until the end of 1972. From 1973 to 1977 he was employed as Assistant Physicist in the Chemistry Division of the Illinois Institute of Technology Research Institute (IITRI), a contract research institute in Chicago, Illinois. As a staff member of the Fine Particles Section, a cross-disciplinary group of researchers consisting of chemists, chemical engineers, physicists, mechanical engineers, microscopists, and technicians, he was engaged in experimental work and data analysis for the Section's classified and unclassified sponsored research in diverse areas of basic particle science and technology. This included environmental sampling, aerosol production and transport, filtration studies, light scattering in particle suspensions and inter-particle force of adhesion studies. Two notable achievements during his employment at IITRI were his invention and development of a simple technique for the production of x-ray fluorescence standards for the Environmental Protection Agency (EPA) and invention of a treatment for certain metal powders, enabling their dispersal in vacuum for the Defense Advanced Research Projects Agency (DARPA).

From 1980 to the present, Joseph Puretz has studied in the Applied Physics and Electrical Engineering Department at OGC, initially with the Lasers and Electro-Optics Group and finally in the Surface Physics and Electron Optics Group. He and his co-workers have demonstrated the use of focused ion beam micromachining to create optical quality surfaces for integrated optoelectronics. This work included the manufacture of the first micromachined coupled cavity diode laser and the first micromachined surface-emitting phase-locked array of diode lasers. These achievements have been noted in Optics News, a publication of the Optical Society of America, where the work was cited as one of the 12 most significant achievements in optics for the year 1986. His immediate plans are uncertain but he would like to continue doing research in the general area of LMIS.

PATENTS

J. Puretz, J. H. Orloff, R. K. DeFreez, and R. A. Elliott **Focused Ion Beam Micromachining of Optical Surfaces in Materials** U.S. Patent No. 4,698,129, October 6, 1987.

R. K. DeFreez, R. A. Elliott, and J. Puretz **Longitudinally Coupled Surface Emitting Semiconductor Laser Arrays** U.S. Patent No. 4,797,892, January 10, 1989

R. K. DeFreez, R. A. Elliott, and J. Puretz **Two-Dimensional Phase-Locked Surface Emitting Semiconductor Laser Array** U.S. Patent No. 4,796,268 January 3, 1989

PUBLICATIONS

R. K. DeFreez, J. Puretz, J. Orloff, R. A. Elliott, H. Namba, E. Omura, and H. Namizaki **Operating Characteristics and Elevated Temperature Lifetests of Focused Ion Beam Micromachined Straight Transverse Junction Stripe Lasers** Appl. Phys. Lett. **53**, 26 September 1988, 1153-1155

G. Crow, J. Puretz, J. Orloff, R. K. DeFreez, and R. A. Elliott **The Use of Vector Scanning for Producing Arbitrary Surface Contours with a Focused Ion Beam** J. Vac. Sci. Technol., **B6**(5) September/October 1988, 1605-1607

J. Puretz, R. K. DeFreez, R. A. Elliott, J. Orloff, and T. L. Paoli, **300 mW Operation of a Surface-Emitting Phase-Locked Array of Diode Lasers,** Elect. Lett., **23** 29 January 1987, 130-131

J. Puretz **Dimensional Analysis and Energy Broadening in Particle Beams** J. Phys. D: Appl. Phys.(1986) L237-L240

R. K. DeFreez, J. Puretz, R. A. Elliott, J. Orloff, and L. W. Swanson, **CW Operation of Widely and Continuously Tunable Micromachined-Coupled-Cavity Diode Lasers,** Electron. Lett., **22** 14 August 1986, 919-921

J. Puretz, R. K. DeFreez, R. A. Elliott, and J. Orloff, **Focused-Ion-Beam Micromachined AlGaAs Semiconductor Laser Mirrors**, Electron. Lett., **22** 19 June 1986, 700-702.

J. M. Schroeer and J. Puretz **Secondary Ion Mass Spectrometer with Liquid Metal Field Ion Source and Quadrupole Mass Analyzer** Secondary Ion Mass Spectrometry, SIMS V, Sept. 30 - Oct. 4, 1985

A. Milgram and J. Puretz **A bilevel resist for ion beam lithography** J. Vac. Sci. Technol. B 3(3) May/Jun 1985, 879-883

J. Puretz, J. Orloff, and L. Swanson **An application of focused ion beams to electron beam testing of integrated circuits** Proceedings of the SPIE Electron Beam, X-Ray, and Ion Beam Techniques for Submicrometer Lithographies III Conferences **471** Society of Photo Instrumentation Engineers, 1984, 38-46

R. A. Semmler, R. D. Draftz and J. Puretz **Thin Layer Standards for the Calibration of X-Ray Spectrometers** in X-Ray Fluorescence Analysis of Environmental Samples, ed. Thomas G. Dzubay, Ann Arbor Science 1977

INVITED PAPERS

R. K. DeFreez, J. Puretz, G. A. Crow, G. A. Wilson, H. Ximen, R. A. Elliott, and J. Orloff **Focused-Ion-Beam Micromachined Diode Laser Mirrors**, To be presented at OE LASE '89

R. A. Elliott, R. K. DeFreez, J. Puretz, J. Orloff, and G. A. Crow **Focused-**

Ion-Beam Micromachining of Diode Laser Mirrors and Couplers Proceedings of the SPIE Symposium on Communications Networking in Dense Electromagnetic Environments at the SPIE Symposium on Innovative Science and Technology, January 10-15, 1988, Los Angeles, California, USA, SPIE Proceedings Volume 876, Pages 114-120

R. K. DeFreez, R. A. Elliott, J. Puretz and J. Orloff **Development of Coupled-Cavity Laser Diodes for Remote Sensing** Technical Digest of the Optical Society of America Topical Meeting on Laser and Remote Sensing: Instrumentation and Techniques, North Falmouth, Massachusetts, 28 September to 1 October 1987, Paper WB3.

CONFERENCE PAPERS

J. Orloff, R. K. DeFreez, J. Puretz, R. A. Elliott, H. Namba, E. Omura, and H. Namizaki **The Effect of Micromachining with Focused Ion Beams on the Life and Power Output of AlGaAs TJS Lasers** Microcircuit Engineering, September 20-22, 1988, Vienna, Austria

H. Namba, E. Omura, H. Namizaki, R. K. DeFreez, R. A. Elliott, J. Orloff, and J. Puretz **Reliability and Characteristics of Focused Ion Beam Micromachined TJS Lasers** Accepted for presentation to Optoelectronics Conference (OEC) 1988

R. A. Elliott, R. K. DeFreez, J. Puretz, J. Orloff, H. Namba, E. Omura, and H. Namizaki **Performance and Lifetests of Focused Ion Beam Micromachined Lasers** Accepted for presentation to LEOS '88

G. Crow, J. Puretz, J. Orloff, R. K. DeFreez, and R. A. Elliott **The Use of Vector Scanning for Producing Arbitrary Surface Contours with a Focused Ion Beam** Japan-U.S. Seminar on Focused Ion Beam Technology and Applications, November 1987, Osaka, Japan

R. K. DeFreez, J. Puretz, R. A. Elliott, and J. Orloff **Focused-Ion-Beam Micromachined Coupled-Cavity and Surface-Emitting Arrays of Diode Lasers** Technical Digest of the Conference on Lasers and Electro-Optics Baltimore, Maryland, 26 April to 1 May 1987, Paper WG3

R. Burghard, J. Puretz, and L. W. Swanson **Applying fine-focused ion beams to integrated circuit analysis** SILI-CON Conference, Portland, Oregon 1986

R. K. DeFreez, J. Puretz, R. A. Elliott, and J. Orloff **Semiconductor Lasers Formed by Micromachining with a Focused Ion Beam** Technical Digest of the 1986 Annual Meeting of the Optical Society of America, Seattle, 19-25 October 1986, Paper WR7

A. Milgram and J. Puretz **A multilevel resist for direct write ion beam lithography** Materials Research Society Symposium April 18, 1985 San Francisco

J. Puretz, J. Orloff, and L. Swanson **An application of focused ion beams to electron beam testing of integrated circuits** SPIE Electron Beam, X-Ray, and Ion Beam Techniques for Submicrometer Lithographies III 471 Society of Photo Instrumentation Engineers, 1984, 38-46

R. Davies, M. B. Ranade, J. Puretz, and D. C. Freshwater **Factors Affecting the Ultrasonic Dispersion of Submicron Particles for Size Analysis** PARTEC Conference, Nurenberg, Federal Republic of Germany 1979

J. Puretz **Centrifugal Particle Size Analysis and the Joyce-Loebl Disc Centrifuge** Filtration Day Conference, Filtration Society of England, Midwest Chapter U. S. A., Chicago 24 October 1975